

2013

Polyoxometalates Macroions: From Self-Recognition to Functional Materials

Panchao Yin
Lehigh University

Follow this and additional works at: <http://preserve.lehigh.edu/etd>

 Part of the [Chemistry Commons](#)

Recommended Citation

Yin, Panchao, "Polyoxometalates Macroions: From Self-Recognition to Functional Materials" (2013). *Theses and Dissertations*. Paper 1682.

This Dissertation is brought to you for free and open access by Lehigh Preserve. It has been accepted for inclusion in Theses and Dissertations by an authorized administrator of Lehigh Preserve. For more information, please contact preserve@lehigh.edu.

Polyoxometalates Macroanions: From Self-Recognition to Functional Materials

by

Panchao Yin

A Dissertation

Presented to the Graduate and Research Committee

of Lehigh University

in Candidacy for the Degree of

Doctor of Philosophy

in

Chemistry

Lehigh University

May, 2013

© 2013 Copyright
Panchao Yin

Certificate of Approval

Approved and recommended for acceptance as a dissertation in partial fulfillment of the requirements for the degree of Doctor of Philosophy

Panchao Yin

Polyoxometalates Macroanions: From Self-Recognition to Functional Materials

02-06-2013
Defense Date

Approved Date

Dr. Tianbo Liu
Dissertation Director

Committee Members:

Dr. James E. Roberts

Dr. Kai Landskron

Dr. Daniel Ou-Yang

ACKNOWLEDGMENTS

First, I would like to thank my advisor, Dr. Tianbo Liu, who has given me his continuous help in reading all manuscripts with great care, providing me with valuable advice and informative suggestions. With Dr. Liu's patience, support and great personality, I managed to overcome the obstacles I met with my projects. I found that the past three years at Lehigh University were very enjoyable. He is not only a talented scientist, but also a perfect mentor, who puts necessary but limited control on my experiments while at the same time, teaches me how to do research independently.

I also would like to thank my committee members, Dr. James E. Roberts, Dr. Kai Landskron, and Dr. Daniel Ou-Yang for insightful comments and suggestions for my research. Their professional evaluations of my proposed research projects and my experimental design saved me from unnecessary traps and inspired me with new research ideas. The colleagues in the chemistry department, Dr. Dmitri Vezenov, Dr. Norm Zheng, and Peng Cheng, are acknowledged here for their technical help in running experiments. My thanks also go to members of the Liu group: Dr. Jie Zhang, Dr. Joe Pigga, Dr. Dong Li, Fadi Haso, Baofang Zhang, Lang Hu, and Jill Sledziewski. I would like to also thank the undergraduate students and high school students who worked with me, especially Emily Bitterlich and Joy Wang.

Furthermore, I would like to mention the help and support of external collaborators, Dr. Tao Li and Dr. Xiaobing Zuo, Dr. Zhi-ming Zhang and Dr. En-bo Wang, Dr. Leroy Cronin, and Dr. Zhonghua Peng, for their synthetic and equipment support.

Finally, my sincere thanks should go to my parents, Fasen Yin and Aihua Chen, and my girlfriend, Jing Lin, for their love and encouragement. Without your support, I would not be strong enough to finish my PhD studies.

TABLE OF CONTENTS

LIST OF FIGURES	ix
LIST OF TABLES	xv
ABSTRACT	1
Chapter 1: Introduction to Polyoxometalates Macroions	2
1.1 Introduction of macroions	2
1.2 Introduction to polyoxometalates	4
1.3 Introduction to polyoxometalates-organic hybrid materials	8
1.3.1 Organoimido derivatives of hexamolybdate	9
1.3.2 Organically functionalization of hexavanadate, Anderson-, and vanadium-capped Dawson-type POMs with trisalkoxides	10
Chapter 2: Introduction to the Solution Behavior of POMs and Their Hybrids	14
2.1 Solution behavior of macro-polyoxoanions	15
2.1.1 The discovery of the self-assembly of POM macroanions	16
2.1.2 Driving forces of the self-assembly behavior	17
2.1.3 Source of counter-ion mediated interaction	20
2.1.4 Controlling the assembly/disassembly and blackberry size	26
2.1.5 The unique slow self-assembly process vs. the virus capsid formation	30
2.1.6 Permeability of Blackberry ‘Membrane’ to small cations	34
2.1.7 The self-recognition behavior during self-assembly process	36
2.1.8 Theoretical studies on the polyoxoanionic solutions	38
2.2 Self-assembly of covalently functionalized amphiphilic hybrid POMs	42
2.2.1 Surfactants with POMs as polar head groups	43
2.2.2 Molecular bola from organic-inorganic hybrid POMs	46
2.2.3 Functionality and application of amphiphilic POM-organic hybrid	47
2.3 Conclusion and Outlook	49
Chapter 3: Self-Recognition of Structurally Similar Rod-shaped Macroions during Their Assembly Process	54
3.1 Introduction	54
3.2 Experimental Section	55

3.3	Self-recognition of structurally identical rod-shaped macroions with different central metal atoms during their assembly process	59
3.3.1	Macroionic properties of the molecular rods.....	59
3.3.2	Self-assembly of the molecular rods into blackberries.....	63
3.3.3	Self-recognition behavior of the two molecular rods	66
3.3.4	The mechanisms of self-recognition.....	72
3.3.5	EXAFS studies of the Zn ²⁺ on the surface of molecular rods.....	74
3.3.6	Dissociation of the blackberries leads to the confirmation the role of counterions.....	76
3.4	Self-recognition of rod-shaped macroions with different organic functional groups during their assembly process	77
3.4.1	Molecular structures of two molecular rods with different organic functional groups	77
3.4.2	Self-recognition behavior in their self-assembly process.....	78
3.5	Conclusion and outlook.....	80
Chapter 4: Chiral Recognition and Chiral Discrimination during the Self-Assembly Process of Chiral Polyoxoanions		84
4.1	Introduction	84
4.2	Experimental Section.....	85
4.3	Chiral Recognition and Chiral Discrimination during Their Self-Assembly Process ...	88
4.3.1	Molecular structures and macro-anionic properties of D/L-Fe ₂₈	88
4.3.2	Chiral recognition in the self-assembly process of the chiral clusters.....	91
4.3.3	Chiral discrimination in the self-assembly process of the chiral clusters.....	94
4.3.4	Chiral separation: the combination of chiral recognition and chiral discrimination	98
4.4	Conclusion.....	99
Chapter 5: Self-Assembly of POM-Organic Hybrids to Vesicles with Tunable Sizes and Fluorescence.....		103
5.1	Introduction	103
5.2	Experimental Section.....	104
5.3	Results and Discussion	108
5.3.1	Synthesis and molecular structures.....	108
5.3.2	Critical Association Concentration (CAC).....	110
5.3.3	Effect of Solvent Polarity	112
5.3.4	Effect of Counterions	113

5.3.5	Effect of pH	115
5.3.6	Fluorescence	117
5.3.7	Formation of nano-structures and the stability of the vesicles	119
5.4	Conclusion	120
Chapter 6: Programmed Spontaneous Self-Assembly of Polyoxometalates-Organic Hybrid into Catalytic Active Nano-belt		
125		
6.1	Introduction	125
6.2	Experimental Section	126
6.3	Results and Discussion	127
6.3.1	Synthesis and molecular structure of hybrid 1	127
6.3.2	Morphological characterization of nano-belts	128
6.3.3	Kinetics study of nano-belts formation	131
6.3.4	Oxidative desulfurization Catalysis by nano-belts	135
6.4	Conclusion	137
Chapter 7: Polyoxometalates-Organic Hybrid as Metal-Ion-Driven Molecular Switch with Reversible Folding and Assembly/Disassembly Behaviors		
139		
7.1	Introduction	139
7.2	Experimental Section	140
7.3	Results and Discussion	143
7.3.1	Molecular Structure of the Hybrid Molecular Switch	143
7.3.2	UV-Vis Monitoring the Trans- to Cis- Isomer Transformation Process.	144
7.3.3	¹ H-NMR Monitoring the Reversible Transformation Process	147
7.3.4	The Observation of Folding Behavior of Hybrid during the Transformation Process in SAXS and NOSY	151
7.3.5	Metal-Ion-Driven Self-Assembly/Disassembly behavior of Hybrid in Solution	156
7.4	CONCLUSIONS	159
Chapter 8: Polyoxometalate-Organic Hybrid Molecules as Amphiphilic Emulsion Catalysts for Oxidation Reactions and Nanostructured Polyoxometalate-Polymer Latex Beads.....		
163		
8.1	Introduction	163
8.2	Experimental Section	165
8.3	Polyoxometalate-Organic Hybrid Molecules as Amphiphilic Emulsion Catalysts for Deep Desulfurization	166
8.4	POMs-organic hybrid for building nanostructured POMs-polymer latex beads	173
8.5	Conclusion	176

Chapter 9: Supramolecular Assembly of Conjugated Polymers Containing POM-terminal Side Chains in Polar and Nonpolar Solvents.....	180
9.1 Introduction	180
9.2 Experimental Section.....	181
9.3 Results and Discussion	183
9.3.1 Molecular weight determination.....	183
9.3.2 Self-assembly of the polymers in nonpolar solvent.....	186
9.3.3 Self-assembly of the polymers in polar solvents	188
9.4 Conclusion.....	196
Chapter 10 : Conclusion	199
Author Vita.....	203

LIST OF FIGURES

Figure 1.1 Illustration of the three categories of electrolyte solutions.....	3
Figure 1.2 Ball-stick represented model of negative charged (left) and positively charged (right) nanocage, respectively.....	3
Figure 1.3 POM anions with different topologies and sizes. Reprinted with permission from ref. 5. Copyright 2011 Wiley-VCH.	6
Figure 1.4 Main coordination modes of organic groups covalently linked to POM units via p-block elements. Reprinted with permission from ref. 32. Copyright 2010 American Chemical Society.....	9
Figure 1.5 Structural representation of the obtaining of aryl imido derivatives of hexamolybdate.....	10
Figure 1.6 a) Structural representation of the organic functionalization of Anderson-type POMs; b) Organically functionalized hexavanadate; c) Structural representation of the organic functionalization of Dawson-type POMs. Reprinted with permission from ref. 32. Copyright 2010 American Chemical Society.....	11
Figure 2.1 a) TEM image on dilute aqueous solution of $\{\text{Mo}_{154}\}$ macroions showing the existence of spherical, ~ 45 nm radius assemblies. b) Zimm plot based on the SLS study of the $\{\text{Mo}_{154}\}$ aqueous solutions at pH=3; (inset) CONTIN analysis on the DLS study of the same solution. c) Schematic plot showing the supramolecular blackberry structure formed by $\{\text{Mo}_{154}\}$ macroions in aqueous solution. Reprinted with permission from ref. 27. Copyright 2003 Nature Publishing Group.....	17
Figure 2.2 Transition from discrete macroions (molecules) to blackberries, then to discrete macroions due to the change of solvent content for 1.0 mg/mL $\{\text{Mo}_{132}\}$ in water/acetone mixed solvents. Reprinted with permission from ref. 28. Copyright 2007 American Chemical Society.....	17
Figure 2.3 Plot of the average blackberry radius (in R_h) versus the inversed dielectric constant ($1/\epsilon$) of the solvent for various POM macroions in water/acetone mixed solvents. Linear relationship roughly follows for these systems. Reprinted with permission from ref. 4. Copyright 2010 American Chemical Society.....	19
Figure 2.4 Top: Distance distribution functions based on calculated and experimental scattering data for $\{\text{Mo}_{72}\text{V}_{30}\}$ obtained by using an indirect Fourier transform of the primary SAXS data. (\circ): 0.052 mm $\{\text{Mo}_{72}\text{V}_{30}\}$, (\bullet): 0.013 mm $\{\text{Mo}_{72}\text{V}_{30}\}$, (—): $\{\text{Mo}_{72}\text{V}_{30}\}$ calculated. Bottom: Experimental distance distributions for 0.26 mm $\{\text{Mo}_{72}\text{V}_{30}\}$ in water and acetone/water mixed solvents with various acetone content (in vol %). (—): 75% acetone/water, (\circ): 65% acetone/water, (- - -): 45% acetone/water, (...): 10% acetone/water, (\square): in pure water. Reprinted with permission from ref. 34. Copyright 2009 Wiley-VCH. ..	21
Figure 2.5 Change of blackberry size (in R_h) with added chloride salt concentration (A) and total ionic strength (B) for 0.5 mg/mL $\{\text{Mo}_{72}\text{Fe}_{30}\}$ solutions. For each added cation salt there is a CSC (critical salt concentration), above which the blackberry size increases with increasing salt concentration. Reprinted with permission from ref. 35. Copyright 2010 American Chemical Society.....	23
Figure 2.6 Average hydrodynamic radii (R_h) of the blackberries formed in 0.5 mg/mL aqueous solutions of $\{\text{Mo}_{72}\text{Fe}_{30}\}$ at different pH (adjusted by NaOH or HCl), as measured by DLS at 90° scattering angle. TEM images of aggregates on carbon film formed at pH \sim 3.0 (left; conventional TEM) and pH \sim 4.6 (right; more appropriate cryo-TEM). Reprinted with permission from ref. 30. Copyright 2006 American Chemical Society.....	27
Figure 2.7 (left) Gradually introducing alkyl trimethylammonium halide cationic surfactants into the dilute aqueous solution of $\{\text{Mo}_{72}\text{V}_{30}\}$ cluster can gradually decrease the charge density on the $\{\text{Mo}_{72}\text{V}_{30}\}$ macroions and induce blackberry formation. The average blackberry size increases with increasing surfactant amount (i.e., decreasing charge density on $\{\text{Mo}_{72}\text{V}_{30}\}$). (right) Average hydrodynamic radius (R_h) of the $\{\text{Mo}_{72}\text{V}_{30}\}$ blackberries in aqueous solution containing CTAB or CTAT, measured by DLS. The concentration of $\{\text{Mo}_{72}\text{V}_{30}\}$ is 0.5 mg/mL, equivalent to a molar concentration of 2.6×10^{-5} M. Reprinted with permission from ref. 40. Copyright 2009 American Chemical Society.....	28
Figure 2.8 (Left) Molecular structure of $\{(\text{RSn})_{12}\text{O}_{14}(\text{OH})_6\}^{2+}$. (six-coordinated tin, green; five-coordinated tin, teal; u_3 -oxo, red; u_2 -oxo, purple; R, black; hydrogen, gray). (Right) The formation of large aggregate	

induced by dianions. Reprinted with permission from ref. 48. Copyright 2010 American Chemical Society.	29
Figure 2.9 (left) Change of total scattered intensity of $\{\text{Mo}_{72}\text{Fe}_{30}\}$ solutions at 90° scattering angle. All solutions were kept at 25°C except one at 45°C (the data shown by black triangle). (right) CONTIN analysis of DLS study on $\{\text{Mo}_{72}\text{Fe}_{30}\}$ aqueous solution at different times. Reprinted with permission from ref. 53. Copyright 2005 American Chemical Society.	30
Figure 2.10 Possible mechanisms of $\{\text{Mo}_{72}\text{Fe}_{30}\}$ blackberry formation in dilute aqueous solution. The upper mechanism has been proven to be correct based on SLS and DLS results, while the bottom mechanism can be ruled out. Adapted with permission from ref. 43 and reprinted with permission from ref. 5. Copyright 2010 American Chemical Society.	31
Figure 2.11 (Left) Increment of the scattered intensity (I) from 0.5 mg/mL $\{\text{Mo}_{72}\text{Fe}_{30}\}/\text{H}_2\text{O}$ solutions at different temperatures (22, 35, 45, and 55°C) with time indicates the progress of blackberry formation. (inset) Calculation of the activation energy (E_a) for the blackberry formation. Reprinted with permission from ref. 53. Copyright 2005 American Chemical Society. (Right) Thermodynamic demonstration of the blackberry formation. Reprinted with permission from ref. 57. Copyright 2011 AAAS.	32
Figure 2.12 (left) Comparison of scattered intensity increment (A) and Rh change (B) of two $\{\text{Mo}_{72}\text{Fe}_{30}\}$ samples along reaction time in 0.9wt% NaCl and salt-free solutions Reprinted with permission from ref. 54. Copyright 2010 American Chemical Society. (right) Light scattering study of the assembly of HPV capsid proteins at various HPV concentrations. The lag time, reaction slope, and extent of assembly were dependent upon the initial protein concentration. Changes in scattered light were not observed until minutes later. Reprinted with permission from ref. 55. Copyright 2004 Elsevier.	33
Figure 2.13 Continuous size distribution $c(s)$ analysis of $\{\text{Mo}_{72}\text{Fe}_{30}\}$ solution versus sedimentation coefficient, s . Experiments were performed at a $\{\text{Mo}_{72}\text{Fe}_{30}\}$ concentration of 10 mg/mL in 170 mM NaCl solution at 20°C . Reprinted with permission from ref. 54. Copyright 2010 American Chemical Society.	34
Figure 2.14 (left) Formation of fluorophore-containing $\{\text{Mo}_{72}\text{Fe}_{30}\}$ blackberries in solution. The additional cations, once added into solution, instantly interact with fluorophores in bulk solution and on blackberry surfaces, subsequently enter into the blackberries, and interact with the fluorophores inside. The anions could not cross the membrane. (right) Change in fluorescence quantum yield of Coumarin 1,6-MQ, and CTC with addition of KBr, KCl, and CaCl_2 , respectively; (a) instantaneous change occurs with the addition of salts; (b) change in fluorescence quantum yield with time, once the addition of salt is stopped. Reprinted with permission from ref. 56. Copyright 2008 American Chemical Society.	35
Figure 2.15 (Middle) In mixed dilute aqueous solutions, the clusters (polyhedral representation) $\{\text{Mo}_{72}\text{Fe}_{30}\}$ (top) and $\{\text{Mo}_{72}\text{Cr}_{30}\}$ (bottom) self-assemble into different (i.e., individual) blackberry structures of the Cr30 (yellow) and Fe30 type (blue)—with interfacial water between the macroions (right)—and do not form mixed species (such as the hypothetical structure shown on the left). Reprinted with permission from ref. 57. Copyright 2011 AAAS.	36
Figure 2.16 (A) CONTIN analysis of the DLS studies at 90° scattering angle measured for aqueous solutions containing $\{\text{Mo}_{72}\text{Cr}_{30}\}$ or $\{\text{Mo}_{72}\text{Fe}_{30}\}$ (0.1 mg/ml each), as well as for a solution containing both species (0.1 mg/ml of each) ($\text{pH} = 4.2$). In the mixed solution, the peak due to the larger $\{\text{Mo}_{72}\text{Cr}_{30}\}$ assemblies is dominant because larger structures scatter more light. (B) CONTIN analysis of the DLS experiment carried out on the two components after ultrafiltration of the aqueous solution originally containing both $\{\text{Mo}_{72}\text{Cr}_{30}\}$ and $\{\text{Mo}_{72}\text{Fe}_{30}\}$ (0.1 mg/ml of each) by a series of membranes with different pore sizes; fraction A (red): material retained after filtering by 100,000 dalton-pore size membrane; fraction B (blue): material retained after filtering by 30,000 dalton-pore size membrane. Reprinted with permission from ref. 57. Copyright 2011 AAAS.	37
Figure 2.17 Snapshots of the different simulation boxes after 10 ns. a row, diluted aqueous solution; b row, concentrated aqueous solution; c row, concentrated methanol solution. Reprinted with permission from ref. 60. Copyright 2008 Royal Society of Chemistry.	39
Figure 2.18 a, b, c) Snapshot of water molecules between 2 PW^{3-} , 2 S^{3-} or 2 PW^{3+} ions. d) Snapshot of the $\text{PW}^{3-} \dots \text{Eu}(\text{MeOH})_9^{3+} \dots \text{PW}^{3-}$ pair at a P...P distance of 17.5 Å, corresponding to the free energy minimum along the PMF in methanol. e, f) Highest density region of Eu^{3+} and H_3O^+ , respectively. Adapted with permission from ref. 61. Copyright 2012 Elsevier.	40
Figure 2.19 The formation of vesicles and reverse vesicles structures in polar and nonpolar solvent, respectively. Adapted with permission from ref. 16 and 17. Copyright 2008 American Chemical Society and 2010 Wiley-VCH.	44

Figure 2.20 a) Molecular structure of hexamolybdate-based bola-amphiphiles. b) Molecular structures of Dawson-type POMs-based bola-amphiphiles and its self-assembly into vesicle structures; Monolayer formation for the dumbbell-shaped hybrid surfactants at the water/vapor interface: c) liquid expansion (LE)/G phase, d) LE phase, and e) liquid condensed (LC) phase. Adapted with permission from ref. 8, 14, 15. Copyright 2010 American Chemical Society and 2009, 2011 Wiley-VCH.	47
Figure 3.1 Synthetic procedure of the two molecular rods and the ball-stick representation of molecular structures of the building blocks and the molecular rods. X, center heteroatom; A, hexamolybdate; B, the ring-shaped Anderson-type molecule.	59
Figure 3.2 a) Superimposition of experimental solution wide angle x-ray scattering curve of 1 in its acetonitrile (2 mg/mL) and simulated scattering curve (in blue) using program SolX with the molecular model (c). b) PDDF of 1 in its acetonitrile solution (red curve) obtained using program GNOM and calculated PDDF (green curve) from the molecular model (c) using SolX. The broadening features in the PDDF obtained from GNOM could arise from the configurationally ensemble in solution due to the free rotation of the Mo-N-C bond. c) The build molecular model for fitting.	61
Figure 3.3 SAXS profile of compound 2.	62
Figure 3.4 1H-NMR results of TBA*1 and TBA*I.	63
Figure 3.5 a) Time-resolved SLS results of the solutions of 1 (green dot), 2 (blue dot), and their mixture (red dot) at scattering angle as 90°. b) CONTIN analysis results of the solutions of 1 (green dot), 2 (blue dot), and their mixture (red dot). c) TEM images of assemblies in the solution of 2. d) TEM images of assemblies in the solution of 1. e) Model for the self-assembly process of molecular rods into blackberry structures.	65
Figure 3.6 Time-resolved DLS results of 1's solution with ZnCl ₂	65
Figure 3.7 Time-resolved DLS results of 2's solution with ZnCl ₂	66
Figure 3.8 a) Model of the self-recognition during the self-assembly of two molecular rods in the mixture solution. b) TEM images of the assemblies in the mixture solutions (red rectangle, large assembly; green rectangle, small assembly). c) Zoom in image of the large assembly. d) Zoom in image of the small assembly. e) EDS results of the large assembly. f) EDS results of the small assembly.	67
Figure 3.9 TEM images and EDS results of the assemblies in the mixture solution.	72
Figure 3.10 a) Comparison of XANES data from ZnCl ₂ with data from sample 2; b) comparison of Fourier transformed data of Zn edge from ZnCl ₂ with Zn edge from Sample 2.	75
Figure 3.11 a) Data and fit of EXAFS data from Zn edge of ZnCl ₂ ; b) Data and fit of EXAFS data from Zn edge of Sample 2.	75
Figure 3.12 a) Time-resolved SLS monitoring results of the three solutions after adding TBA*EDTA (Green, 1's solution; Blue, 2's solution; Red, mixture solution). b) Model of the reversibly self-assembly/disassembly process.	77
Figure 3.13 Ball-stick representation of the molecular structures of anion part of 3 and 4.	78
Figure 3.14 DLS results and TEM images of the individual solutions of 3 (up) and 4 (below), respectively.	79
Figure 3.15 a) DLS results of the mixed solution (green) and the individual solutions of 3 (red) and 4 (blue); b) TEM images of the assemblies in the mixed solution.	80
Figure 4.1 a) Ball-stick representation of molecular structures of enantiomers of Fe ₂₈ ; b) c) Side and top view of the molecular structures of L-Fe ₂₈ (Molecular fragments highlighted in blue are tartaric acid fragments). Reprinted with permission from ref. 24. Copyright 2009 Wiley-VCH.	89
Figure 4.2 a) SAXS curves of Ca-D-Fe ₂₈ and Ca-L-Fe ₂₈ ; b) SAXS curve of Ca-L-Fe ₂₈ and the simulated curve based on the molecular structures in crystalline state; c) R _g , measured from SAXS curves, of the solutions with different amount of extra CaCl ₂ ; d) PDDF results of solutions with different amount of extra CaCl ₂ ; e) Model for the counterions association with Fe ₂₈	90
Figure 4.3 SAXS curves of Ba-D-Fe ₂₈ and Ba-L-Fe ₂₈ in the buffer of L-lactic acid, respectively.	91
Figure 4.4 a) SLS results of Ba-D-Fe ₂₈ , Ba-L-Fe ₂₈ and their racemic mixture solutions; b) TEM images of the assemblies in solution Ba-D-Fe ₂₈	92
Figure 4.5 a) Graphical representation of the thermodynamic mechanism of the self-assembly process; b) SLS monitoring of different solutions for 31 hours.	93
Figure 4.6 a) Graphical representation of the chiral discrimination experiments; b) SLS results of Ba-D-Fe ₂₈ in different buffers; c) SLS results of Ba-L-Fe ₂₈ in different buffers.	95
Figure 4.7 SLS monitoring of Ba-D-Fe ₂₈ and Ba-L-Fe ₂₈ in the buffer of L-lactic acid for 400 hrs.	96

Figure 4.8 a) Graphical representation of chiral micro-environment; b) c) TEM images of the assemblies in Ba-D-Fe ₂₈ and Ba-L-Fe ₂₈ in the buffer of L-lactic acid, respectively.....	97
Figure 4.9 a) SLS results of Ba-D-Fe ₂₈ , Ba-L-Fe ₂₈ , and their racemic mixture in the buffer of D-lactic acid respectively; b) SLS results of Ba-D-Fe ₂₈ , Ba-L-Fe ₂₈ , and their racemic mixture in the buffer of L-lactic acid respectively.	99
Figure 4.10 a) Graphical representation of the self-assembly of the two enantiomers in the buffer of D-lactic; b) Graphical representation of ultrafiltration experiment; c) CD spectrum of the solution before ultrafiltration; d) CD spectra of up layer (red) and bottom layer (green) solutions after ultrafiltration; e) CD spectra of aqueous solutions of pure Ba-D-Fe ₂₈ (green) and pure Ba-L-Fe ₂₈ (red).	99
Figure 5.1 The synthesis of the surfactant 1 with Dawson type POMs as polar head group. Polyhedron color code: W, black; P, dark black; V, white. Reprinted with permission from ref. 28. Copyright 2012 Wiley-VCH.	108
Figure 5.2 Reaction route for the synthesis of molecule 2. Reprinted with permission from ref. 20. Copyright 2011 Wiley-VCH.	109
Figure 5.3 Packing diagram of TBA ₂ *1. (Left: ab plane or (001) lattice plane; right: bc plane or (100) lattice plane. Blue sphere represents TBA and red polyhedron represents hexavanadate.) Reprinted with permission from ref. 20. Copyright 2011 Wiley-VCH.	110
Figure 5.4 a) Scattered intensities at 90° scattering angle of the TBA*1 in acetone at different concentrations; b) hydrodynamic radius of the formed vesicle structures in the TBA*1 acetone solution depending on the concentration; c) DLS results of 0.5 (×) and 0.03 (◇) mg/mL TBA*1's acetone solution at 30° scattering angle; d) TEM images of the vesicle structure from the 0.5 mg/mL TBA*1 in acetone solution. Reprinted with permission from ref. 28. Copyright 2012 Wiley-VCH.	111
Figure 5.5 Concentration dependent surface tension of Na ₂ *2's aqueous solution. Reprinted with permission from ref. 20. Copyright 2011 Wiley-VCH.	111
Figure 5.6 a) The plot of the hydrodynamic radius of vesicles vs. the inverse of the dielectric constant of the solvent. ◇ represents the data of Dawson-based surfactant while □ represents that of hexavanadate-based surfactant (V ₆ surfactant); b) TEM images of the vesicle structure formed by TBA*1 in the mixture of water and acetone (v/v=1/1), with a proposed model for the bilayer structure. Reprinted with permission from ref. 28. Copyright 2012 Wiley-VCH.	113
Figure 5.7 DOSY-NMR results of TBA*1 in acetone (a) and acetonitrile (b). A circle, solvent; B circle, tetrabutylammonium; C circle, surfactant anion. Reprinted with permission from ref. 28. Copyright 2012 Wiley-VCH.	113
Figure 5.8 a) The plot of hydrodynamic radius vs. the concentration of added salt. Circle, NaI; Square, ZnCl ₂ ; b) the plot of the reduced scattered intensity at 90° scattering angle vs. the concentration of added salt. Circle, TBA*I; Square, TMDA*Br. Reprinted with permission from ref. 28. Copyright 2012 Wiley-VCH.	115
Figure 5.9 a) DLS results of H*1's aqueous solution at pH = 1.5 (●) and pH= 12 (◆) at 90° scattering angle; b) The plot of hydrodynamic radii of vesicles vs. pH of the hybrid aqueous solution. Reprinted with permission from ref. 28. Copyright 2012 Wiley-VCH.	117
Figure 5.10 (a) H ₂ *2 (left) and TBA ₂ *2 (right) solution under UV light; (b) Fluorescence spectrum of H ₂ *2 excited at 335 nm; (c) Fluorescent image of H ₂ *2 in aqueous solution (By recording the intensity of the red arrow pointed assembly, we are able to analyze the decay of the normalized intensity over time); (d) Total intensity changes with time for a dot marked with an arrow in (c) demonstrating stability of 2's blue fluorescence. Reprinted with permission from ref. 20. Copyright 2011 Wiley-VCH.	119
Figure 5.11 a) SEM image of the micro-needle structures; b) Zoom in image of one needle. Reprinted with permission from ref. 28. Copyright 2012 Wiley-VCH.	120
Figure 5.12 Left: SEM image of micro-sheet structure formed by 1. Right: Zoom in image of the surface of the micro-sheet. Reprinted with permission from ref. 20. Copyright 2011 Wiley-VCH.	120
Figure 6.1 a) Ball-stick representation of the molecular structure of hybrid 1; b) top view of the A-B-A layer structures; c) side view of the A-B-A layer structure.	128
Figure 6.2 a) Pictures of the newly prepared solutions and the solutions became cloudy two hours after their preparation; b) optical microscopy images of the aggregates; c) SEM image of nano-belt structures; d) TEM image of the packing of polar heads on the surface of nano-belt; e) TEM images of the layer structures of nano-belt.	129

Figure 6.3 a) AFM images of nano-belts under wet condition; b) Z-direction graph of the features; c) Z-direction curve of the selected line.	130
Figure 6.4 a) SAXS curve of the nano-belt dispersion solution; b) c) Models of the nanobelts.....	131
Figure 6.6 SEM images of the aggregates in solutions with pH as a) 11.9, b) 10.8, c) 10.5, d) 9.8, e) 9.0, and f) 7.8.	135
Figure 7.1 Ball-stick representation of molecular structure of anions in hybrid 1.	143
Figure 7.2 The reversible transformation process between trans-isomer and cis-isomer of 1.....	144
Figure 7.3 Molecular structure and NMR results of the bipyridine ligand.	145
Figure 7.4 UV-Vis monitoring of the titration of ZnCl ₂ into the DMSO solution of the bipyridine ligand. A bathochromic shift of the bipyridine band from ca. 300 to 330 nm can be observed, which is resulted from the complexation between Zn ²⁺ and the ligand.	145
Figure 7.5 UV-Vis monitoring of hybrid 1 with the titration of ZnCl ₂ in DMSO.....	146
Figure 7.6 Molecular structure of hybrid 2. Cyan polyhedron, WO ₆ ; yellow polyhedron, VO ₆ ; purple polyhedron, PO ₄ ; black sphere, carbon atom; blue sphere, nitrogen atom; red sphere, oxygen atom, gray sphere, hydrogen atom.....	146
Figure 7.7 UV-Vis monitoring of the titration of ZnCl ₂ into the DMSO solution of hybrid 2. No bathochromic shift were observed.	146
Figure 7.8 ¹ H-NMR monitoring of bipyridine ligand with adding ZnCl ₂ and TBA*EDTA. The downfield shift of hydrogen atom of bipyridine and N-H after the adding ZnCl ₂ suggests the transformation of the trans- to cis-. After adding TBA*EDTA to the above solution, the chemical shift move upfield back to their original position, indicating the transformation of cis- to trans-.....	149
Figure 7.9 ¹ H-NMR monitoring results of the titration of ZnCl ₂ to the d ₆ -DMSO solution of 1 (bottom) and adding of (TBA) ₄ *EDTA after the titration of ZnCl ₂ (top).	150
Figure 7.10 ¹ H-NMR monitoring results of the five working cycles of the hybrid 1.	151
Figure 7.11 The possible conformations for trans-isomer and ciso-isomer, respectively.....	153
Figure 7.12 a) SAXS curve of trans-isomer without metal ions (open square), cis-isomer after adding ZnCl ₂ (open circle), and trans-isomer after adding the EDTA into the cis-isomer solution (open triangle). SAXS profiles are vertically offset for clarity. b) Pair distance distribution function, p(r), of the three samples obtained using program GNOM. c) The overlay of calculated p(r) of the three trans-conformations and experimental p(r) of trans-isomer. The calculated p(r) were computed directly from the molecular coordinates using program SolX. d) The overlay of calculated p(r) of the three cis-conformations and experimental p(r) of cis-isomer.	154
Figure 7.13 a) b) 2D NOESY result of hybrid 1's solution without and ZnCl ₂ , respectively. (rectangle-crosspeak code: red, Hd/Hc; green, Hd/He; aqua, Ha/Hb; blue, Hd/Ha) c) Model for the folding and unfolding behavior of the hybrid stimulated by Zn ²⁺	155
Figure 7.14 SAXS data of trans-isomer and cis-isomer measured at 1st day and 30 day. Data are arbitrarily scaled for clarity.	156
Figure 7.15 a) DLS results of the assemblies of Hybrid 1 in Methanol/DMSO mixed solvents at 45° scattering angle. b) TEM image of the large assembly. c) Model for the vesicle structure.	158
Figure 7.16 Model for the parallel packing of trans-isomer of 1.....	158
Figure 7.17 Graphical representation of the trans-isomer to cis-isomers to vesicle structures process.	159
Figure 8.1 Molecular structures for hexavanadate-based hybrid surfactants, 1 and 2. Reprinted with permission from ref.25. Copyright 2012 Wiley-VCH.	167
Figure 8.2 The equation for the catalytic oxidation reaction of thiophene. Reprinted with permission from ref.25. Copyright 2012 Wiley-VCH.	168
Figure 8.3 a) Picture of the emulsion catalytic system of surfactant with the pH of aqueous solution at 6; b) Models for the catalytic system; c) Model for the biphasic catalytic reactions. Reprinted with permission from ref.25. Copyright 2012 Wiley-VCH.	168
Figure 8.4 DLS results of the diluted emulsion solution. (Rh = ca. 400 nm). Reprinted with permission from ref.25. Copyright 2012 Wiley-VCH.	168
Figure 8.5 Oxidation decomposition conversion of thiophene for 1 and 2 catalyzed reactions at 80 min. (Control groups: V6 as catalyst, the conversion is ca. 0% even after 1 day; SDS (sodium dodecyl sulfate) as catalyst, the conversion is ca. 6% at 80 min at pH = 1.7, 4.8, and 6.5, and achieved 40 % after 12 hrs.) Reprinted with permission from ref.25. Copyright 2012 Wiley-VCH.	169

Figure 8.6 Pictures of hybrid 1's the catalytic systems with aqueous solutions at different pH values. The organic phases for pH = 5 and 6 are colorless while the pH is lower than 5, the organic phases are of yellow color. Reprinted with permission from ref.25. Copyright 2012 Wiley-VCH.	171
Figure 8.7 a) UV-Vis results of the hexanes phases with aqueous solutions at different pH values (Blue, pH=6; Green, pH=4; Red, pH=2); b) TEM images of the rod-like reverse emulsions; c) EDS results taken from the rod-like structures in b) in TEM, indicating large abundance of vanadium; d) Model for the rod-like reverse emulsion; e) SEM images of the precipitation. Reprinted with permission from ref.25. Copyright 2012 Wiley-VCH.	172
Figure 8.8 a) The freshly separated organic phase of catalytic reactions with the pH value of aqueous solutions as 2; b) sample a) overnight.	173
Figure 8.9 Molecular structure of hybrid 3.	174
Figure 8.10 top) Typical experiment for emulsion polymerization; bottom) model for hybrid stabilized emulsion and the particles after polymerization.	175
Figure 8.11 top) TEM images of the POM-polymer latex; bottom) EDS results of the surface area of the latex beads.	176
Figure 9.1 Molecular structures of polymers 1, 2, 3, and 4. Reprinted with permission from ref.22. Copyright 2012 Wiley-VCH.	184
Figure 9.2 The change in scattered intensities monitored at 90° scattering angle as the concentration of polymer 1 in toluene is continuously lowered through solvent titration. The CMC was determined to be 0.04 mg/mL.	184
Figure 9.3 Zimm plot for the calculation of molecular weight of polymer 1.	185
Figure 9.4 Topography of the surface of a spin-coated polymer 1 film.	185
Figure 9.5 a) CONTIN analysis results of DLS data of polymer 1's 0.1 mg/mL toluene solution at the scattering angle of 30°; b) the scattering intensities versus time monitored at 90° scattering angle for polymer 1's 0.1 mg/mL toluene solution. Reprinted with permission from ref.22. Copyright 2012 Wiley-VCH.	187
Figure 9.6 a) TEM image of the assembly of polymer 1 in toluene; b) fluorescence microscope image of a 0.1 mg/mL toluene solution of polymer 1 (scale bar, 30 um); c) model of the reverse vesicle structure in toluene. Reprinted with permission from ref.22. Copyright 2012 Wiley-VCH.	187
Figure 9.7 Dynamic light scattering (DLS) results of 2 (blue) and 3 (red) at scattering angle of 30 degree. $R_h=R_g=200$ nm for 2 and $R_h=R_g=110$ nm for 3.	188
Figure 9.8 Images taken under fluorescence for a) assemblies in 1's 0.1 mg/mL acetone solution; b) assemblies in 1's 0.1 mg/mL DMSO solution. Scale bar, 10 um. Reprinted with permission from ref.22. Copyright 2012 Wiley-VCH.	189
Figure 9.9 Fluorescence image of a DMSO solution of polymer 1, showing the rod structure (up right corner) and small dots of single chains.	190
Figure 9.10 TEM images for a) assemblies in acetone; b) zoom in image of the feature in a); c) another rod structure in acetone; d) assemblies in DMSO (inset: zoom in image for the tube structure). e) Model for the tube-like assemblies. Reprinted with permission from ref.22. Copyright 2012 Wiley-VCH.	190
Figure 9.11 EDS taken under TEM for a) aggregates in toluene; b) aggregates in acetone; c) aggregates in DMSO. The peak at 17.4 KeV indicates the existence of Mo.	191
Figure 9.12 TEM images for the tube-like structures in 1's 10 mL 0.5 mg/mL DMSO solution with 0.5 mg ZnCl ₂ . Diameter = 58 nm. Light Scattering results indicate the R_h and R_g values for the aggregates being 69 nm and 80 nm, respectively.	192
Figure 9.13 TEM images for the tube-like structures in 1's 10 mL 0.5 mg/mL DMSO solution with 2 mg tetramethyl ammonium bromide. Diameter = 55 nm. Light Scattering results indicate R_h and R_g values for the aggregates are 60 nm and 73 nm, respectively.	193
Figure 9.14 Excitation (blue) and emission (red) spectra of 0.005 mg/mL solution of 1 in acetone.	194
Figure 9.15 Excitation (blue) and emission (red) spectra of 0.1 mg/mL solution of 1 in acetone.	195
Figure 9.16 Excitation (blue) and emission (red) spectra of 0.005 mg/mL of 1 in DMSO solution.	195
Figure 9.17 Excitation (blue) and emission (red) spectra of 0.1 mg/mL of 1 in DMSO solution.	196
Figure 10.1 Different functional devices derived from the assemblies of POM-organic hybrids.	200

LIST OF TABLES

Table 2-1 Information on the structure, charge density, and self-assembly behavior of macro-polyoxoanions in aqueous solutions.	15
Table 2-2 Critical salt concentrations needed for precipitating $\{\text{Mo}_{72}\text{Fe}_{30}\}$ blackberries from different $\{\text{Mo}_{72}\text{Fe}_{30}\}$ concentrations. Reprinted with permission from ref. 38. Copyright 2010 Elsevier.	25
Table 2-3 Formulas and molecular structures of the hybrid surfactants studied in our group.	43
Table 3-1 List of fit parameters obtained from modeling the data for Zn edge of ZnCl_2 and 2: SO_2 was obtained by fitting the Zn foil whose EXAFS was measured before data collection on samples was started. R factors for all the fits are less than 0.03.	75
Table 8-1 Oxidation decomposition conversion ratio of thiophene for 1 and 2 catalyzed experiments and control experiments at 80 min.	169

ABSTRACT

Large, hydrophilic polyoxoanions with high solubility in water and/or other polar solvents demonstrate unique solution behavior by self-assembling into single layer, hollow, spherical “blackberry”-like structures, which are obviously different from small, simple ions. These macroions cannot be treated as insoluble colloidal suspensions either because they form stable “real solutions”. These inorganic macroions demonstrate some features usually Pobelieved to belong only to complex biological molecules, such as the self-recognition, chiral recognition, and chiral selection in dilute solutions. Highly negatively-charged molecular rods with almost identical structures were observed to self-assemble into their individual ‘blackberry’ structures, demonstrating tiny differences (e.g. charge, charge distribution, and organic ligands) could lead to self-recognition behavior. Chiral recognition behavior was understood by studying the self-assembly process in the racemic mixture solutions. Moreover, chiral organic molecules (lactic acid and tartaric acid) can be used to selectively inhibit the self-assembly process of one of the enantiomers. Meanwhile, polyoxometalate-based organic-inorganic hybrid materials demonstrate amphiphilic properties by self-assembling into vesicles and reverse vesicles in polar and non-polar solvents, respectively, and form catalytic emulsions in biphasic environments. Designed hybrid molecules can be programed to different devices with applications in fluorescence, photo-electronic conversion, molecular switch, and catalyst.

Chapter 1: Introduction to Polyoxometalates Macroions

1.1 Introduction of macroions

It was believed that electrolyte solutions can be classified into two categories based on the electrolyte's sizes, that is, solutions of simple ions (< 1 nm, e.g. NaCl) and colloid suspensions (10 nm \sim 100 nm, e.g. highly charge polystyrene latex dispersed in aqueous solution).¹ The solutions of simple ions are well understood by the Debye-Hückel theory and its extended form, in which an ionic atmosphere model is used to explain the solution behavior of simple ions and the ions are believed to be homogeneously distributed in the solutions.² Meanwhile, the colloid suspensions can be described by the Derjaguin-Landau-Verwey-Overbeek theory (DLVO theory), which suggests that the stability of colloid suspensions is the co-effect of van der Waals force (attractive force) and the static charge repulsion force.^{3,4} However, the missing gap between simple ions and colloids raises a quite interesting question: what happens when soluble ions reach the nanometer size scale? Our experimental results suggest that the highly charge large ions (1 nm \sim 10 nm) behave different from either simple ions or colloids in the solution state by self-assembling into thermodynamically-stable supramolecular structures.^{1,5,6} Therefore, we believe that solutions of large ions open a new research area by filling the gap between simple ions and colloids. These new members were named as macroions. Macroions are mainly composed of three groups of compounds: nanocages, bio-macromolecules, and polyoxometalates (POMs).

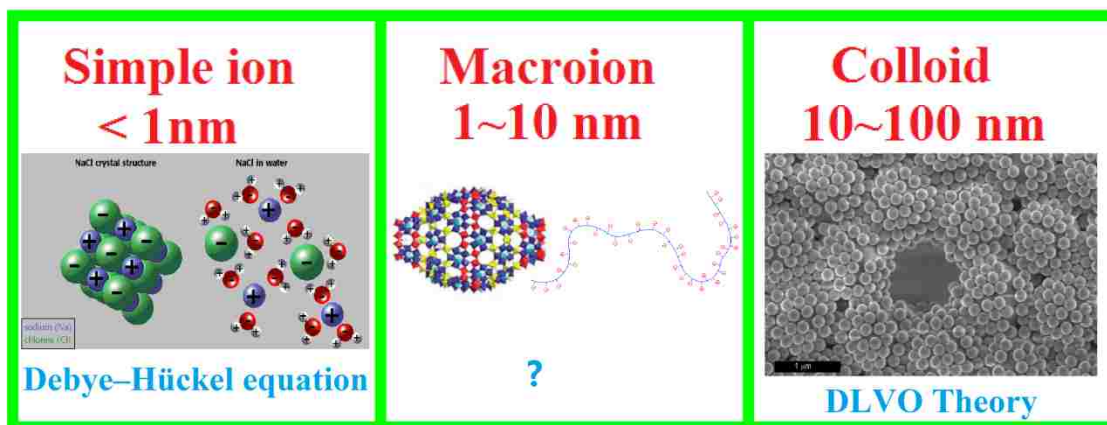


Figure 1.1 Illustration of the three categories of electrolyte solutions.

Nanocages are a large group of metal organic complex clusters at the nanometer scale with applications in adsorption, separation, and catalysis.⁷ The clusters are synthesized by coordinating multi-functional organic ligands with metal ions, which are also named as metal-organic polyhedron (MOP). The cluster can be either highly positively charged (with neutral organic ligands) or negatively charged (negatively charged organic ligands).⁷

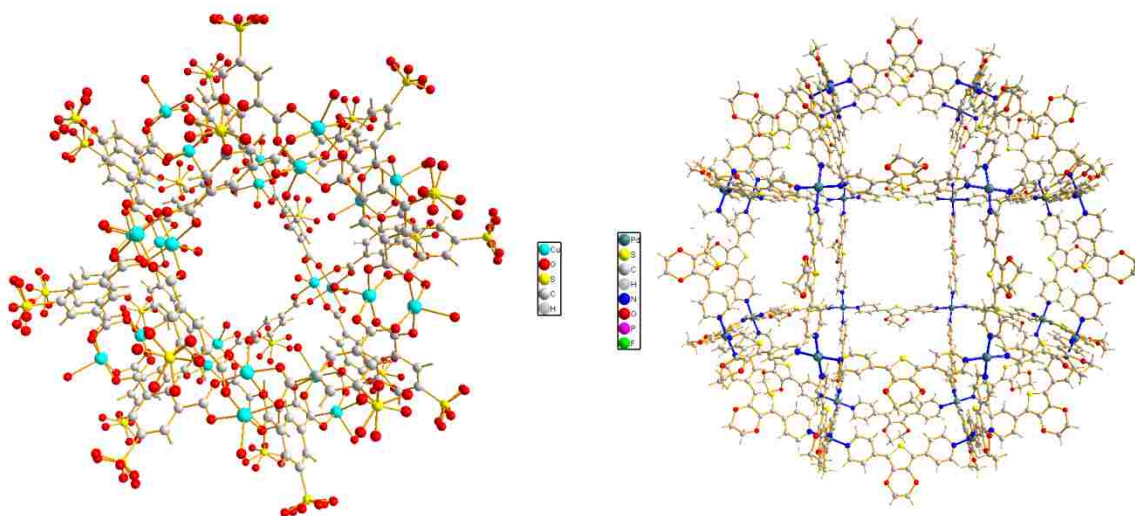


Figure 1.2 Ball-stick represented model of negative charged (left) and positively charged (right) nanocage, respectively.

The well-known bio-macromolecules, such as DNA, RNA, and proteins, could be highly charged and behave as macroions in solution. DNA and RNA are usually negatively charged due to the

existence of phosphate while proteins can be charged in both ways since they have both positively and negatively charged amino acids. Probably due to their macro-ionic properties, these bio-macromolecules are quite sensitive to the introduction of metal ions in solution by showing controllable folding and self-assembly behavior.⁸⁻¹⁰

POMs, as the largest group of macroions, are the major topic of my dissertation and are introduced in the following section.

1.2 Introduction to polyoxometalates

Polyoxometalates are a large class of metal-oxide cluster anions consisting of early transition metals (usually Mo, W, V, Nb, and Ta) in their high oxidation states and oxo ligands.^{11,12} POMs usually are anions that consist of three or more transition metal-oxo polyhedron linked together through shared oxygen atoms to form a large, closed 3-dimensional framework. Due to the multiple valences and coordination formats of the center metal ions and various kinds of connections of these metal oxide polyhedron units, POMs demonstrate extremely rich topological structures, sizes, and charges, and can be structurally classified into several different types (see Figure 1.3).¹¹ Based on the elemental and molecular structural analysis, POMs can be classified into isopolyoxometalates, with general formula as $[M_mO_y]^{p-}$, and heteropolyoxometalates, with general formula as $[X_xM_mO_y]^{q-}$ (M is the early transition metals and X is hetero atoms such as phosphorus or silicon). For both kinds of POMs, the MO_6 octahedron is the basic building unit of the POM framework. According to Lipscomb's principle, no MO_6 octahedron can have more than two unshared oxygen atoms (terminal oxo ligand).¹³ The MO_6 with only one terminal oxo ligand is called type I octahedron and the one with two terminal oxo ligands is called type II octahedron. Since type I MO_6 octahedron can accommodate addenda metal atoms with d^0 , d^1 , and d^2 electronic configurations, whereas type II octahedron are restricted to d^0 metals only, there is a

structural limitation upon the reducibility of POMs. The reduction of POMs must be accompanied by only minor structural changes, which can be achieved if the POM is constructed only by type I MO_6 octahedron (type I POM) since an electron added to metal centers enters an orbital that is predominantly non-bonding with minimal subsequent bond length alternation. On the other hand, if the MO_6 of POM have two cis terminal oxo ligand (type II POM), the added electron must enter an anti-bonding orbital and will result in large structural changes.¹⁴

As the major types of POMs- Keggin, Lindqvist, Dawson, and Anderson type POMs- have been synthesized and characterization several decades ago, they are still hot topics in catalysis and organic-inorganic hybrid materials. Keggin type POMs, first reported by Keggin in 1933 with formula $[\text{XO}_4\text{M}_{12}\text{O}_{36}]^{n-}$, have overall Td symmetry and are based on a central XO_4 tetrahedron surrounded by twelve MO_6 octahedron (all type I) arranged in four groups of three edge-shared octahedron, M_3O_{13} .¹⁵ Lindqvist type POMs, with the formula $[\text{M}_6\text{O}_{19}]^{m-}$, are a super octahedron composed of six type I MO_6 octahedron through edge-sharing linking.¹⁶ Anderson type POMs, $[\text{XO}_6\text{M}_6\text{O}_{18}]^{r-}$, show planar structures with D_{3d} symmetry. The center octahedron, XO_6 , is surrounded by six type II edge-sharing linked MO_6 octahedron.¹⁷ The Wells-Dawson POM, first characterized by Dawson, is considered as the second best known POM. Dawson-type POMs are of cylinder-shape with length and diameter as 1.3 and 1.0 nm, respectively. Their structures are derivate from Keggin-type POMs by symmetrically linking two tri-lacunary Keggin-type POMs. Therefore, Dawson-type POMs show very similar chemical properties (e.g. spectroscopic, redox, and catalytic properties) with Keggin POMs even though their stability is weaker.^{18,19} Keggin, Dawson, and Lindqvist-type of POMs are type I POMs while Anderson type POMs are type II.

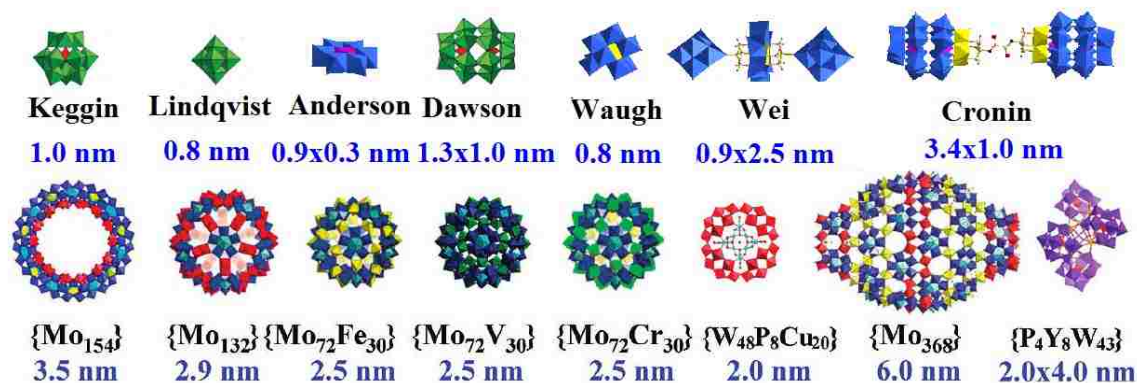


Figure 1.3 POM anions with different topologies and sizes. Reprinted with permission from ref. 5. Copyright 2011 Wiley-VCH.

Compared to simple ions, POM anions have much larger sizes and lower charge densities. They are highly soluble and form real solutions, which is different from thermodynamically unstable colloids. Thus, the solution behavior of POM anions, especially their interaction with counterions, is different from the previous two types of systems. On the other hand, POM macroions can be used as initial candidates for understanding polyelectrolyte solutions. The polyelectrolyte solutions are very complex and still poorly understood because both intermolecular and intramolecular interactions need to be considered. POM macroions with well-defined molecular structure, mass, shape and charge density are ideal, simplified model systems where only intermolecular interactions need to be considered.^{1,20} As the result, the POM macroions are extremely valuable systems for understanding the transition from simple ions to colloids, and particularly important for exploring the macroion-counterion interaction when the two parts have negligible, but still not significant size differences.

Having been known for centuries, POMs still attract a lot of interest due to their outstanding properties in catalysis, medicine, and photo-electronic responses.¹² Due to the ability to reversibly change oxidation states of metal centers with minor structural change and acidic properties, POMs are considered to be good catalytic materials with high stability and wide working range, including oxidation, hydroxylation, esterification, polymerization, and C-H bond activation

reaction.²¹ Currently, more than 80% of the patent applications concerning the application and properties of POMs are related to catalysis.²² Recent years have witnessed great development of POMs' application as catalysts. 'Sandwich' type POMs have been developed as the fastest, carbon-free molecular water oxidation catalyst to date, which is of significance in artificial photosynthesis.²³ POMs with complicated structure were developed to selectively catalyze functionalization of certain positions of target molecules.^{24,25} What is more, POMs were incorporated into metal organic framework (MOF) and were used as high efficiency and selective catalytic materials.^{26,27} As early as the 1970s, heteropolyoxometalates that catalyzed the hydration of propene had been industrialized in Japan with the production as 50,000 t per year. After that, the hydration of isobutene and n-butene were realized with large production. With the catalyst as phosphomolybdate, methacrolein was oxidized to produce methacrylic acid (220,000 t per year) in 1982.²²

Although most of the current POM catalysts show high efficiency during the reaction process, most of them are homogeneous systems and share the common drawbacks, that is, catalyst/product separation and catalyst reuse are difficult. The immobilization of catalytically active species onto solid supports can solve the catalyst recovery and recycle process. With the help of noncovalent interactions, POMs can be loaded onto inert solid supports such as zeolites²⁸, ionic polymers^{29,30}, and ionic liquid functionalized silicon substrates³¹. Another way for the preparation of such heterogeneous system is to incorporate POMs into MOF structures.^{26,27} However, these systems have disadvantages. For the former type of heterogeneous catalysts, the leaching of POMs due to the non-covalent interaction and the high price for the substrate are two weak points for such kinds of materials.³¹ POM-MOF structures actually are the ideal heterogeneous catalytic materials with high efficiency, stability and selectivity. However, the design and preparation of such structures are quite difficult with rare examples and are currently not so easy to be industrialized. On the other hand, as an important issue in research on catalysts,

two or more immiscible liquid phases reaction systems cannot be catalyzed with high efficiency by either the homogeneous or heterogeneous catalytic materials referred above.

1.3 Introduction to polyoxometalates-organic hybrid materials

POMs, generally speaking, are completely hydrophilic, and therefore are not compatible with organic media. The rigid nature of POMs, as well as their incompatibility with organic media hinders the development of POM-based functional materials. Thus, organic functionalization of POMs has been becoming a hot topic and attracting more and more interest, which is able to enhance POMs' compatibility and processibility.^{32,33} Currently, two major different ways are provided for the organic functionalization of POMs: 1) non-covalently grafting organic ligands onto POMs' surface through electrostatic, hydrogen bonding or van der Waals interactions; 2) covalently or iono-covalently linking organic fragments to POMs' surface.³² Due to the advantages of covalent functionalization in stability and controllability, the application of the corresponding products has extended from self-assembly research, constructing framework materials to building catalytic-active devices.^{32,33}

Dolbecq *et al.* summarized the previous research on covalent functionalization of POMs and suggested six different modes for organic groups to be covalently linked to POM units.³² In this dissertation, the functionalization of Lindqvist, Anderson, and Dawson type POMs is presented in the following section since most of the current synthetic and materials design research start from them.

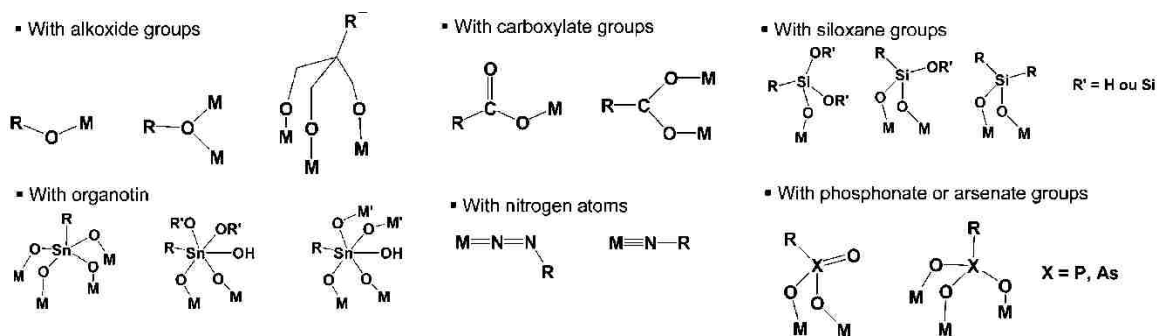


Figure 1.4 Main coordination modes of organic groups covalently linked to POM units via p-block elements. Reprinted with permission from ref. 32. Copyright 2010 American Chemical Society.

1.3.1 Organoimido derivatives of hexamolybdate

The organoimido derivatives of hexamolybdate were formed by replacing one or more oxo ligands on the surface of hexamolybdate with the nitrogen atom of organic fragments. The organic ligands conjugated link to the surface of hexamolybdate through a Mo≡N triple bond. Zubieta et al. first mentioned the synthesis of aryl imido derivatives of hexamolybdate in 1988 through the reaction of [MoCl₄(NNMePh)] with [(n-Bu₄N)₂[Mo₂O₇]].³⁴ Since then, Maatta, Errington, Proust, and Peng have developed different synthetic protocols, which significantly increased the number of organic imido derivatives with varied functional groups.³³

Due to its special conjugated linkage, Neumann and Maatta studied the electron transfer properties from organic fragments to hexamolybdate and proposed their potential applications in photo-catalysis.^{35,36} Peng succeeded in incorporating hexamolybdate in the main chains and side chains of conductive polymers, respectively through such covalent functionalization and the obtained hybrid materials were claimed to be good candidates for research in photo-catalysis, solar cell, and electronic devices.^{37,38} Wei et al. observed the C-H bond activation by hexamolybdate in its alkyl imido derivatives.³⁹

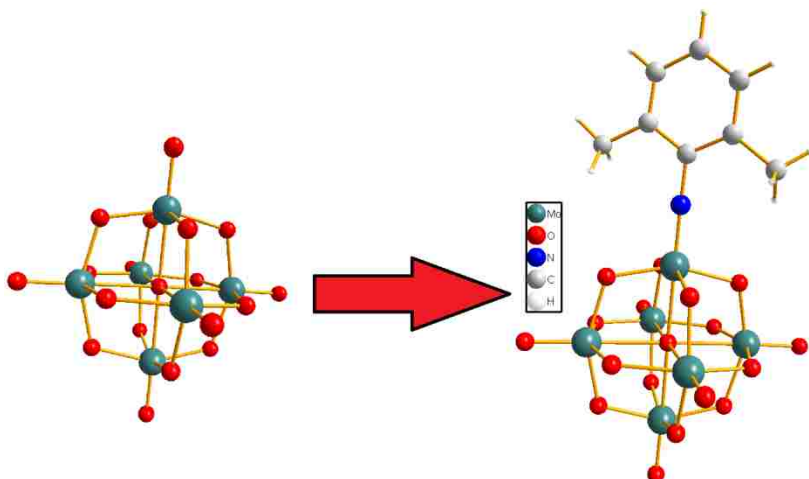


Figure 1.5 Structural representation of the obtaining of aryl imido derivatives of hexamolybdate.

1.3.2 Organically functionalization of hexavanadate, Anderson-, and vanadium-capped Dawson-type POMs with trisalkoxides

In the molecular structures of hexavanadate, Anderson- and vanadium-capped Dawson-type POMs, the three neighbor u_3 -oxo ligands are comparatively more highly negatively charged than the other oxo ligands, which are either protonated or coordinated with metal ions without organic functionalization. Being similar to the esterification reactions, the three protonated u_3 -oxo groups can react with organic trisalkoxides and form three C-C single bonds by removing three molecules of water. Due to the strong stability of the linkages and the multiple functional groups that can be attached on the organic fragments, the obtained hybrid materials have been widely studied for their applications.³²

Cronin et al. designed 3D porous crystalline materials and cell selective adhesive matrix from organically functionalized Anderson-type POMs.^{40,41} Hill and Cronin built POM-based catalytic-active dendrimer and dimer materials from functionalized Dawson-type POMs.^{42,43} Surfactants with POMs as polar head groups were designed and synthesized through the introduction of alkyl tails or hydrophobic aromatic groups into organic fragments of the three different types of POMs' hybrids.^{41,44-46}

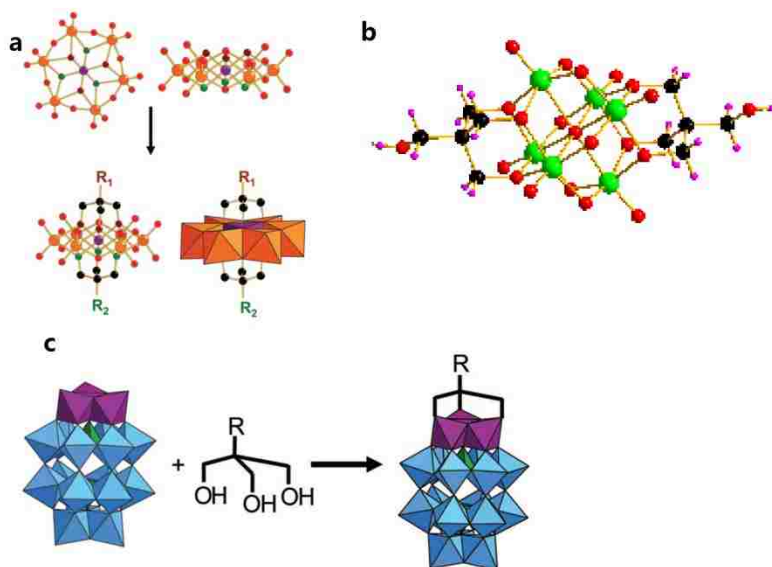


Figure 1.6 a) Structural representation of the organic functionalization of Anderson-type POMs; b) Organically functionalized hexavanadate; c) Structural representation of the organic functionalization of Dawson-type POMs. Reprinted with permission from ref. 32. Copyright 2010 American Chemical Society.

Reference

- (1) Liu, T. B. *Langmuir* **2010**, *26*, 9202.
- (2) Debye, P. J.; Huckel, E. *Phys. Z.* **1923**, *24*, 185.
- (3) Derjaguin, B. V.; Landau, L. *Acta. Physicochim. URSS* **1941**, *89*, 555.
- (4) *Theory of the Stability of Lyophobic Colloids*; Verwey, E. J.; Overbeek, J. T. G., Eds.; Elsevier: Amsterdam, 1948.
- (5) Yin, P.; Li, D.; Liu, T. *Isr. J. Chem.* **2011**, *51*, 191.
- (6) Yin, P.; Li, D.; Liu, T. *Chem. Soc. Rev.* **2012**, *41*, 7368.
- (7) Dalgarno, S. J.; Power, N. P.; Atwood, J. L. *Coord. Chem. Rev.* **2008**, *252*, 825.
- (8) Stigter, D. *Biophys. J.* **1995**, *69*, 380.
- (9) Zlotnick, A.; Aldrich, R.; Johnson, J. M.; Ceres, P.; Young, M. J. *Virology* **2000**, *277*, 450.
- (10) Roh, J. H.; Behrouzi, R.; Briber, R. M.; Guo, L.; Thirumalai, D.; Woodson, S. A. *Biophys. J.* **2009**, *96*, 575a.
- (11) Long, D.-L.; Burkholder, E.; Cronin, L. *Chem. Soc. Rev.* **2007**, *36*, 105.

- (12) Hill, C. L. *Chem. Rev.* **1998**, *98*, 1.
- (13) *Comprehensive Inorganic Chemistry*; Sneed, M. C., Ed.; Van Nostrand: New York, 1953; Vol. 1.
- (14) Pope, M. T. *Heteropoly and Isopoly Oxometalates*; Springer-Verlag: Berlin, Heidelberg, New York, Tokyo, 1983.
- (15) Keggin, J. F. *Proceedings of the Royal Society of London. Series A* **1934**, *144*, 75.
- (16) Lindqvist, I. *Arkiv. Kemi.* **1952**, *2*, 325.
- (17) Anderson, J. S. *Nature* **1937**, *140*, 850.
- (18) Wells, A. F. *Structural Inorganic Chemistry*; 1st ed.; Oxford University Press: Oxford, 1945.
- (19) Dawson, B. *Acta. Crystallogr.* **1953**, *6*, 113.
- (20) Muller, A.; Peters, F.; Pope, M. T.; Gatteschi, D. *Chem. Rev.* **1998**, *98*, 239.
- (21) Moffat, J. B. *Metal-Oxygen Cluster: The Surface and Catalytic Properties of Heteropoly Oxometalates*; Kluwer Academic/Plenum Publishers: New York, 2001.
- (22) Kozhevnikov, I. V. *Catalysts for Fine Chemical Synthesis: Catalysis by Polyoxometalates*; Wiley: Berlin, 2002; Vol. 2.
- (23) Yan, Y.; Wang, H.; Li, B.; Hou, G.; Yin, Z.; Wu, L.; Yam, V. W. W. *Angew. Chem. Int. Ed.* **2010**, *49*, 9233.
- (24) Sloboda-Rozner, D.; Witte, P.; Alsters, P. L.; Neumann, R. *Adv. Syn. Cata* **2004**, *346*, 339.
- (25) Mizuno, N.; Hikichi, S.; Yamaguchi, K.; Uchida, S.; Nakagawa, Y.; Uehara, K.; Kamata, K. *Cata. Today* **2006**, *117*, 32.
- (26) Ma, F.-J.; Liu, S.-X.; Sun, C.-Y.; Liang, D.-D.; Ren, G.-J.; Wei, F.; Chen, Y.-G.; Su, Z.-M. *J. Am. Chem. Soc* **2011**, *133*, 4178.
- (27) Sun, C.-Y.; Liu, S.-X.; Liang, D.-D.; Shao, K.-Z.; Ren, Y.-H.; Su, Z.-M. *J. Am. Chem. Soc* **2009**, *131*, 1883.
- (28) Maksimchuk, N. V.; Kholdeeva, O. A.; Kovalenko, K. A.; Fedin, V. P. *Isr. J. Chem* **2011**, *51*, 281.

- (29) Qi, W.; Wu, L. *Polymer Int.* **2009**, *58*, 1217.
- (30) Zhou, T.; Li, H.; Liu, G.; Zhang, L.; Yao, D.; Hu, D. *J. App. Polymer. Sci.* **2009**, *114*, 4000.
- (31) Yamaguchi, K.; Yoshida, C.; Uchida, S.; Mizuno, N. *J. Am. Chem. Soc.* **2004**, *127*, 530.
- (32) Dolbecq, A.; Dumas, E.; Mayer, C. d. R.; Mialane, P. *Chem. Rev.* **2010**, *110*, 6009.
- (33) Proust, A.; Thouvenot, R.; Gouzerh, P. *Chem. Commun.* **2008**, 1837.
- (34) Kang, H.; Zubietta, J. *J. Chem. Soc., Chem. Commun.* **1988**, 1192.
- (35) Stark, J. L.; Young, V. G., Jr.; Maatta, E. A. *Angew. Chem. Int. Ed.* **1995**, *34*, 2547.
- (36) Bar-Nahum, I.; Narasimhulu, K. V.; Weiner, L.; Neumann, R. *Inorg. Chem.* **2005**, *44*, 4900.
- (37) Xu, B.; Lu, M.; Kang, J.; Wang, D.; Brown, J.; Peng, Z. *Chem. Mater.* **2005**, *17*, 2841.
- (38) Lu, M.; Xie, B.; Kang, J.; Chen, F.-C.; Yang, Y.; Peng, Z. *Chem. Mater.* **2005**, *17*, 402.
- (39) Li, Q.; Wei, Y.; Hao, J.; Zhu, Y.; Wang, L. *J. Am. Chem. Soc.* **2007**, *129*, 5810.
- (40) Song, Y. F.; Long, D. L.; Cronin, L. *Angew. Chem. Int. Ed.* **2007**, *46*, 3900.
- (41) Song, Y.-F.; McMillan, N.; Long, D.-L.; Kane, S.; Malm, J.; Riehle Mathis, O.; Pradeep Chullikkattil, P.; Gadegaard, N.; Cronin, L. *J. Am. Chem. Soc.* **2009**, *131*, 1340.
- (42) Zeng, H.; Newkome, G. R.; Hill, C. L. *Angew. Chem. Int. Ed.* **2000**, *39*, 1772.
- (43) Pradeep, C. P.; Misdrahi, M. F.; Li, F.-Y.; Zhang, J.; Xu, L.; Long, D.-L.; Liu, T.; Cronin, L. *Angew. Chem. Int. Ed.* **2009**, *48*, 8309.
- (44) Song, Y.-F.; McMillan, N.; Long, D.-L.; Thiel, J.; Ding, Y.; Chen, H.; Gadegaard, N.; Cronin, L. *Chem. Eur. J.* **2008**, *14*, 2349.
- (45) Yin, P.; Wu, P.; Xiao, Z.; Li, D.; Bitterlich, E.; Zhang, J.; Cheng, P.; Vezenov, D. V.; Liu, T.; Wei, Y. *Angew. Chem. Int. Ed.* **2011**, *50*, 2521.
- (46) Yin, P.; Pradeep, C. P.; Zhang, B.; Li, F.-Y.; Lydon, C.; Rosnes, M. H.; Li, D.; Bitterlich, E.; Xu, L.; Cronin, L.; Liu, T. *Chem. Eur. J.* **2012**, *18*, 8157.

Chapter 2: Introduction to the Solution Behavior of POMs and Their Hybrids

Polyoxometalates (POMs), a large group of metal oxide clusters, are important due to their wide application as catalysts, photo-electronic/magnetic materials, and biologically active materials.^{1,2} The self-assembly of POMs at different scales ranging from nanometer to micrometer has been recognized as a hot topic since it is well-known that the performance of POMs-based devices and materials depends strongly on their self-assembly structures. Currently, various ways are available to assemble POMs into nano-, micro-, or framework structures.³ Moreover, the nano-scaled, uniform POMs may also be applied as valuable model systems to address fundamental scientific issues.⁴

Metal oxide polyhedra of POMs (MO_x , $\text{M}=\text{Mo}$, W , V , and Nb ; $x=4\sim 7$, e.g. the different colors of the POMs in Table 1 represent different types of metal oxide polyhedra; light blue, MoO_7 pentagon bi-pyramid polyhedron; dark blue, MoO_6 octahedron; yellow, FeO_6 octahedron; light green, CrO_6 octahedron; dark green, VO_6 octahedron) can be considered as ‘monomers’ while they are linked with each other through corner-, edge-, or face-sharing manners, which enable synthetic chemists to build POMs with different topologies and sizes.²

Due to the excess of oxo ligands over metal ions, POMs are usually highly negatively charged, i.e., they exist as soluble macro-anions in solution. This feature makes the POMs unique, as such macroions have well-defined molecular structures, uniform shapes, tunable charges and no intra-molecular charge interactions, and demonstrate completely different behaviors than regular small ions or large, unstable colloidal suspensions. These polyoxoanions are ideal models for understanding the broadly defined macroionic solutions including polyelectrolytes and biomacromolecular systems, e.g., the interaction between DNA and proteins and the formation of virus capsids.^{4,5}

Meanwhile, organic functional groups can be covalently grafted to the surface of POMs, resulting in a new type of amphiphilic hybrid materials.⁶⁻⁸ The solvophobic interaction of the amphiphilic molecules in appropriate solvents can trigger the formation of micelles, vesicles, and reverse-vesicle structures,⁹⁻¹⁷ which expands the compatibility of the POMs in organic media.

2.1 Solution behavior of macro-polyoxoanions

Table 2-1 Information on the structure, charge density, and self-assembly behavior of macro-polyoxoanions in aqueous solutions.

Polyoxoanion	{Mo ₇₂ Fe ₃₀ }			{Mo ₇₂ Cr ₃₀ }	{Mo ₁₅₄ }	{Cu ₂₀ P ₈ W ₄ ₈ }	{P ₄ Y ₉ W ₄ ₃ }	{Mo ₁₃₂ }	{Mo ₇₂ V ₃₀ }
Molecular structure									
Negative Charge	0 ~ 1	1 ~ 29	29~30	5	15	25	30	42	31
Size (nmx)	2.5			2.5	3.6 X 1.2	2.2 X 1.1	4 X 2 X 2	2.9	2.5
Charge Density (nm ⁻²)	0 ~ 0.051 pH<2.9	0.051 ~ 1.477 2.9<pH<6.6	unstable pH>6.6	0.255	0.543	1.291	1.08	1.590	1.579
Self-Assembly in aqueous solution	No	Yes	unstable	Yes	Yes	Yes	Yes	Yes at high conc.	No
Rh of Blackberry (nm)		48 ~ 15		60	45	38	46		

x represents the dimension of size.

	Formula	ref
{Mo ₇₂ Fe ₃₀ }	[Mo ^{VI} ₇₂ Fe ^{III} ₃₀ O ₂₅₂ (CH ₃ COO) ₁₂ {Mo ₂ O ₇ (H ₂ O)} ₂ {H ₂ Mo ₂ O ₈ (H ₂ O)} ₁ (H ₂ O) ₉₁]* ca.150H ₂ O	21
{Mo ₇₂ Cr ₃₀ }	[{Na(H ₂ O) ₁₂ } ₂ {Mo ^{VI} ₇₂ Cr ^{III} ₃₀ O ₂₅₂ (CH ₃ COO) ₁₉ (H ₂ O) ₉₄ }]*ca.120H ₂ O	25
{Mo ₁₅₄ }	Na ₁₅ [Mo ₁₅₄ O ₄₆₂ H ₁₄ (H ₂ O) ₇₀] _{0.5} [Mo ₁₅₂ O ₄₅₇ H ₁₄ (H ₂ O) ₆₈] _{0.5} * ca.400H ₂ O	18
{Cu ₂₀ P ₈ W ₄₈ }	K ₁₂ Li ₁₃ [Cu ₂₀ Cl(OH) ₂₄ (H ₂ O) ₁₂ (P ₈ W ₄₈ O ₁₈₄)]* 22H ₂ O	24
{P ₄ Y ₉ W ₄₃ }	K ₁₅ Na ₆ (H ₃ O) ₉ [(PY ₂ W ₁₀ O ₃₈) ₄ (W ₃ O ₁₄)]*39H ₂ O	23
{Mo ₁₃₂ }	(NH ₄) ₄₂ [{(Mo ^{VI})Mo ^V ₁₅ O ₂₁ (H ₂ O) ₆ }] ₁₂ {Mo ₂ O ₄ (CH ₃ COOH)} ₃₀]* ca.300H ₂ O* ca.10CH ₃ COONH ₄	19
{Mo ₇₂ V ₃₀ }	Na ₈ K ₁₄ (VO) ₂ [{(Mo ^{VI})Mo ^{VI} ₅ O ₂₁ (H ₂ O) ₃ }] ₁₀ {(Mo ^{VI})Mo ^{VI} ₅ O ₂₁ (H ₂ O) ₃ (SO ₄) ₂ }{V ^{IV} O(H ₂ O)} ₂₀ {V ^{IV} O} ₁₀ {KSO ₄ }] ₅]* ca.150H ₂ O	22

The past decades witnessed significant development in the synthesis of giant POMs with sizes ranging from *ca.* 2 nm to 6 nm (Table 2-1).¹⁸⁻²⁵ From physical chemists' point of view, these macroanions are valuable models to understand the transition of solution behavior from simple ionic solution (e.g. NaCl solutions, described by Debye-Hückel theory) to colloidal suspensions (Derjaguin-Landau-Verwey-Overbeek theory, or DLVO theory).⁴

2.1.1 The discovery of the self-assembly of POM macroanions

Large, anionic POMs were observed to slowly form large structures in aqueous solution even though the POMs were highly soluble.²⁶ Laser light scattering (LLS), a powerful technique for analyzing particles or polymers (including bio-macromolecules) in solution, is used to monitor the dilute POM solutions. By measuring the scattered intensity from solutions at different scattering angles, static light scattering (SLS) can be used to determine the average molecular weight (\overline{Mw}) and radius of gyration (R_g) of the aggregates. Dynamic light scattering (DLS) measures the intensity-intensity time correlation function from the scattered light, which is analyzed by the CONTIN method to calculate the average hydrodynamic radius (R_h) of the particles and the particle size distribution.⁴ The LLS results indicated that large structures were detected in various POM solutions, which took a long time to reach equilibrium at room temperature.⁴ A typical CONTIN analysis from the DLS study of {Mo₁₅₄} aqueous solution at pH=3.0 showed the formation of large assemblies with an average R_h of 45 nm and a narrow size distribution (Fig. 1b). SLS study analyzed by the Zimm plot indicated that the assemblies had an average \overline{Mw} of 2.54×10^7 g/mol (*ca.* 1150 {Mo₁₅₄}) and an average R_g of 45 nm. The relation of $R_h/R_g \approx 1$ for spherical objects (TEM image in Figure 2.1a) and the low mass suggested a hollow, single-layered vesicular structure with the average inter-{Mo₁₅₄} distance ~ 0.9 nm. Since {Mo₁₅₄} was fully hydrophilic, the assemblies were formed due to different driving forces from the surfactant vesicles where hydrophobic interaction was critical. A nickname “blackberry” was

given to the new aggregates due to the similarities between the two species (Figure 2.1c).²⁷ The free-energy favored stable blackberry structures have been observed in appropriate polar solvents of different POM macroanions.⁴

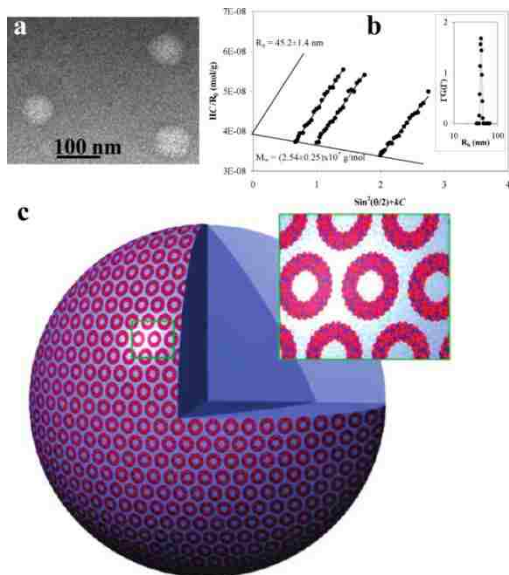


Figure 2.1 a) TEM image on dilute aqueous solution of $\{Mo_{154}\}$ macroions showing the existence of spherical, ~ 45 nm radius assemblies. b) Zimm plot based on the SLS study of the $\{Mo_{154}\}$ aqueous solutions at pH=3; (inset) CONTIN analysis on the DLS study of the same solution. c) Schematic plot showing the supramolecular blackberry structure formed by $\{Mo_{154}\}$ macroions in aqueous solution. Reprinted with permission from ref. 27. Copyright 2003 Nature Publishing Group.

2.1.2 Driving forces of the self-assembly behavior

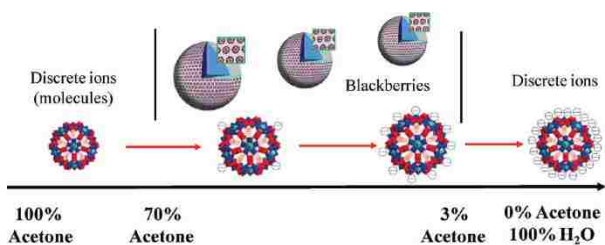


Figure 2.2 Transition from discrete macroions (molecules) to blackberries, then to discrete macroions due to the change of solvent content for 1.0 mg/mL $\{Mo_{132}\}$ in water/acetone mixed solvents. Reprinted with permission from ref. 28. Copyright 2007 American Chemical Society.

The blackberries represent a new type of self-assembled structures in solution, formed by hydrophilic ions with large size and moderate charges. The most critical issue is the driving force behind the assembly process. A simple experiment can help clarify this issue and distinguish the macroions from other types of solutes. LLS results revealed the presence of $\{Mo_{132}\}$ blackberries

in water/acetone mixed solvents containing 3 to 70 vol% acetone, with the average R_h of blackberries increasing from 45 to 100 nm with increasing acetone content (Figure 2.2).²⁸ Only discrete $\{\text{Mo}_{132}\}$ clusters were found in solutions containing <3 vol % and >70 vol % acetone, under which circumstances the discrete macroanions were of very high and very low charge density, respectively.²⁸ In an acetone-rich solvent, the strong counterion condensation made the effective charge of $\{\text{Mo}_{132}\}$ very low. In such a case, $\{\text{Mo}_{132}\}$ clusters existed as single clusters without any assemblies. With increasing water content, the effective charge of the macroions increased, which should increase the electrostatic repulsion between individual $\{\text{Mo}_{132}\}$ macroanions. Instead, the $\{\text{Mo}_{132}\}$ macroanions started to attract strongly with each other and form blackberries. This observation rules out the possibility that van der Waals forces are the major driving force for the self-assembly process.⁴

On the other hand, in various macroionic solutions, the blackberry size shows a linear relationship with the inverse of the dielectric constant of the solvent, which implies a charge-regulated self-assembly process for blackberry formation (Figure 2.3).²⁹ The assumption of such a ‘charge-regulated’ self-assembly process was further confirmed by the pH-controlled self-assembly behavior of $\{\text{Mo}_{72}\text{Fe}_{30}\}$. $\{\text{Mo}_{72}\text{Fe}_{30}\}$ can be treated as a weak nano-acid by partially deprotonating of 30 water ligands coordinated to the 30 Fe(III) centers on its surface.²¹ The chemical equilibrium for deprotonation and protonation of $\{\text{Mo}_{72}\text{Fe}_{30}\}$ could be tuned by changing the pH of the aqueous environment, which finally affected the net charge of the POMs.³⁰ LLS studies indicated that the blackberry formation could be observed in solution with $\text{pH} > 2.9$, however, no aggregates formed in solutions with $\text{pH} < 2.9$ (Table 2-1).³⁰ The experimental results suggested that the charge density of $\{\text{Mo}_{72}\text{Fe}_{30}\}$ was too low in solution with low pH to form blackberry structures, which not only ruled out the major contribution of van der Waals forces, but also confirmed the importance of charge effects in blackberry formation.⁴

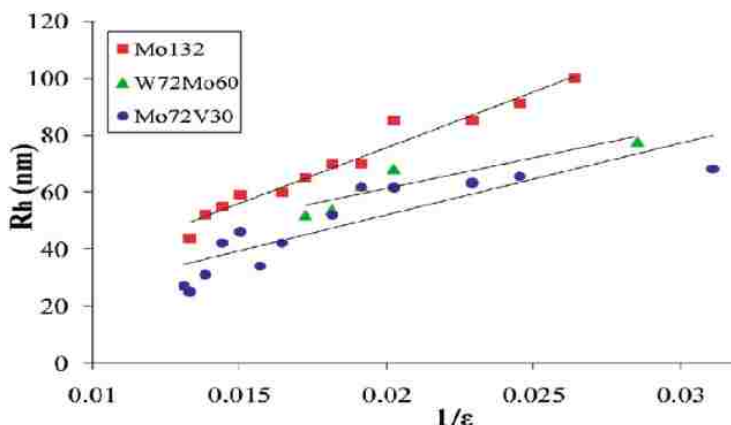


Figure 2.3 Plot of the average blackberry radius (in R_h) versus the inversed dielectric constant ($1/\epsilon$) of the solvent for various POM macroions in water/acetone mixed solvents. Linear relationship roughly follows for these systems. Reprinted with permission from ref. 4. Copyright 2010 American Chemical Society.

The study of $\{\text{Mo}_{132}\}$ and $\{\text{Mo}_{72}\text{Fe}_{30}\}$ solutions suggested that the charge density of the macroanions should be neither too low nor too high in order to form blackberry structures. The explanation might be that the counterion-mediated attraction is not strong enough to overcome the repulsion between POMs with too high charges, while POMs with too low charges are not able to hold counterions as ion-pairing structures, which will largely reduce the attractive force.⁴ The data on the molecular structures and solution behaviors of macroanions can be used to estimate the proper charge density range for the self-assembly behavior (Table 2-1). Basically, the charge density of macroions with the size of 2~4 nm should be within the range of $0.051\sim 1.471 \text{ nm}^{-2}$ in order to be able to self-assemble into blackberry structures in aqueous solution. However, the macroanions with charge densities $< 0.051 \text{ nm}^{-2}$ or $> 1.579 \text{ nm}^{-2}$ are supposed to stay as discrete single anions or molecules. Obviously, this charge density range will change when the macroionic size varies.

2.1.2.1 Counterion-mediated attraction

By realizing the importance of charge in the blackberry formation and the uniqueness of the macroionic solutions, we tried to seek for the possible contributions of the counterion-mediated attractions as the possible driving force. Similar cases were reported in polyelectrolyte and

biomacromolecular (proteins and DNAs) solutions, although usually multivalent counterions are needed (in our current cases monovalent counterions already can achieve this).³¹ Inspired by the formation of bound pairs of highly charged polystyrene latex in aqueous environment, Ise and Sogami confirmed the counterion-mediated attraction between like-charged colloidal particles experimentally and theoretically (although it is still controversial in the colloid community since van der Waals forces among colloidal particles are so dominant).³²

2.1.3 Source of counter-ion mediated interaction

Due to their high charges and size disparity between them and their counterions, macropolyoxoanions can strongly associate with their counterions and form ion-pairs, which are considered to play a significant role in the formation of blackberry structures.

2.1.3.1 Small-angle X-ray scattering

Small-angle X-ray scattering (SAXS) can be used to explore the information on the shape and size of macromolecules, characteristic distances of partially ordered materials, pore sizes, and other data, such as the determination of the microscale or nanoscale structure of particle systems in terms of such parameters as averaged particle sizes, shapes, distribution, and surface-to-volume ratio.³³ SAXS is appropriate for studying the POMs in dilute solution because of their giant sizes and well-defined structures.^{34,35} Within appropriate concentration range, SAXS curves are quite sensitive to the changes of radius of gyration (R_g) and shape of POM anions.^{34,35} Either counterion association around POMs or the self-assembly of POMs will lead to noticeable changes in SAXS curves, which can be further quantitatively interpreted by calculating the R_g value and the distance pair distribution functions.^{34,35}

2.1.3.2 Counterion distribution around polyoxoanions

$\{\text{Mo}_{72}\text{V}_{30}\}$ stays as discrete anions in dilute aqueous solution due to its high charge density, which makes it a good model for studying the counterion distribution around macroanions.^{34,36}

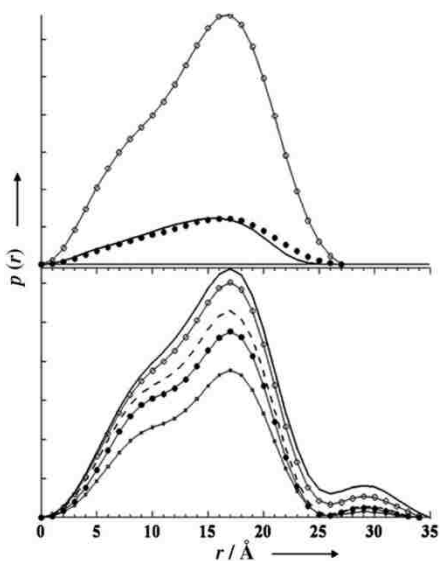


Figure 2.4 Top: Distance distribution functions based on calculated and experimental scattering data for $\{\text{Mo}_{72}\text{V}_{30}\}$ obtained by using an indirect Fourier transform of the primary SAXS data. (○): 0.052 mM $\{\text{Mo}_{72}\text{V}_{30}\}$, (●): 0.013 mM $\{\text{Mo}_{72}\text{V}_{30}\}$, (—): $\{\text{Mo}_{72}\text{V}_{30}\}$ calculated. **Bottom:** Experimental distance distributions for 0.26 mM $\{\text{Mo}_{72}\text{V}_{30}\}$ in water and acetone/water mixed solvents with various acetone content (in vol %). (—): 75% acetone/water, (○): 65% acetone/water, (- - -): 45% acetone/water, (...): 10% acetone/water, (□): in pure water. Reprinted with permission from ref. 34. Copyright 2009 Wiley-VCH.

$\{\text{Mo}_{72}\text{V}_{30}\}$ macroanion theoretically can carry ~ 31 negative charges with the counterions being 14 K^+ , 8 Na^+ , 2 VO^{2+} , and 5 H^+ in its very dilute solutions (the protons might be partially associated with surface oxo ligands). The corresponding SAXS curve identified several peaks which could be fit by the form factor of single $\{\text{Mo}_{72}\text{V}_{30}\}$ cluster. The distance pair distribution $p(r)$, the probability of finding the vector length r in a molecule, could be generated from the Moore analysis of the SAXS curve to provide a physically meaningful description of the particle morphology.³⁴ For $\{\text{Mo}_{72}\text{V}_{30}\}$ in dilute aqueous solution, the $p(r)$ curves shown in Figure 2.4(top) correspond to single $\{\text{Mo}_{72}\text{V}_{30}\}$ clusters (a core-shell spherical particle with a maximum linear dimension of 26 Å) with no counterion association around macroions. However, when the concentration was over 0.052 mM or a certain amount of acetone was introduced into the solution, another new peak appeared (centered at ~ 30 Å and extends the effective distribution to ~ 34 Å) in the $p(r)$ plot (Figure 2.4). The original distribution remained unchanged, suggesting that the macroions still existed as discrete ions. This additional peak suggested that some metal counterions were closely associated with the macroions and distributed in the range of 0.2-0.9 nm

to the surface of macroions. The peak due to the associated counterions became more and more significant with increasing POM concentration or acetone content. Meanwhile, Guinier plots indicated that the average R_g value of the $\{\text{Mo}_{72}\text{V}_{30}\}$ macroions also increases, accordingly. The appearance of the peak due to associated counterions was consistent with the appearance of the blackberry structures, indicating the direct connection between these two issues and the role of counterions on the blackberry formation.³⁴

The counterion effect is critical in the current case because the size disparity between the macroions and counterions is obvious, but not significant (like in the case of colloids). In other words, in macroionic solutions, the counterions cannot be treated as point charges (in colloidal suspensions it has no problem) and consequently the hydrated size of the counterions becomes important. This introduces more challenges to theoretical approaches because the mean field approach cannot be applied for the macroionic solutions quantitatively.^{4,34}

2.1.3.3 Counterion exchange around macranions

The appropriate size disparity between macroions and their counterions also renders the macroions another important feature—it can accurately distinguish monovalent counterions with different hydrated sizes, and has a corresponding preference sequence. In other words, the exchange of monovalent counterions around such macroions can be achieved. A simple observation was the change of blackberry size when a small amount of proper extra salt was added (Figure 2.5). For $\{\text{Mo}_{72}\text{Fe}_{30}\}$, the original counterions were protons. Its blackberry size did not change from the salt-free solutions when 1-20 mM LiCl or NaCl was added. However, when 0.1-10 mM KCl was added, the blackberry size became considerably larger ($R_h \sim 34.6$ nm). Same result was observed when RbCl was introduced ($R_h \sim 35.7$ nm). A reasonable explanation is that K^+ and Rb^+ ions (smaller hydrated sizes) could replace the protons around $\{\text{Mo}_{72}\text{Fe}_{30}\}$, which would increase the attractive force between macroions and lead to larger blackberries, while large hydrated ions such as Li^+ and Na^+ could not replace the protons due to their lower priority.³⁵

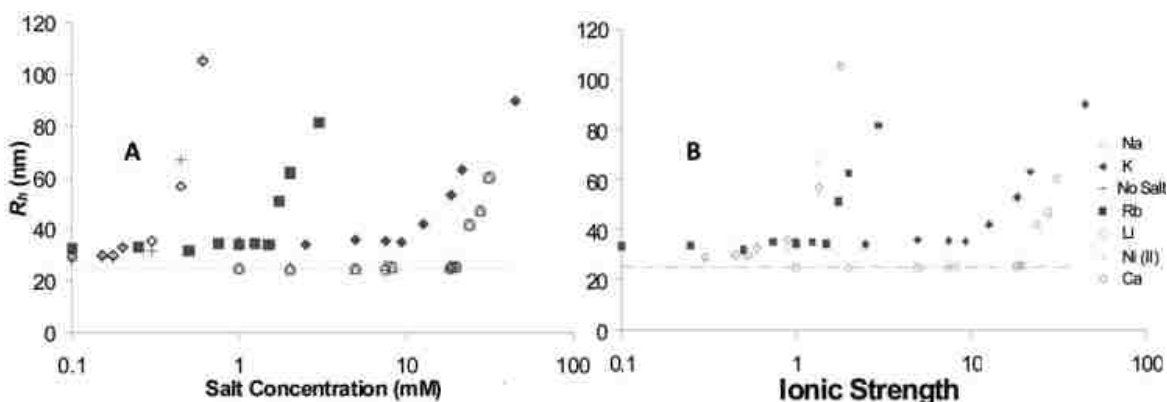


Figure 2.5 Change of blackberry size (in R_h) with added chloride salt concentration (A) and total ionic strength (B) for 0.5 mg/mL $\{Mo_{72}Fe_{30}\}$ solutions. For each added cation salt there is a CSC (critical salt concentration), above which the blackberry size increases with increasing salt concentration. Reprinted with permission from ref. 35. Copyright 2010 American Chemical Society

This speculation was confirmed by isothermal titration calorimetry (ITC) studies. By adding NaCl to the aqueous solution of $\{Mo_{72}Fe_{30}\}$, there was no measurable binding of Na^+ ions to macroions even with the molar ratio of Na^+ to POM of 1000:1. The titration curve for KCl indicated that binding between the K^+ ions and the $\{Mo_{72}Fe_{30}\}$ macroions was present. 50-60 K^+ were needed for completely saturating the binding sites (~ 6) on $\{Mo_{72}Fe_{30}\}$. Instead, < 10 Rb^+ ions were needed for saturation, suggesting that the binding to $\{Mo_{72}Fe_{30}\}$ macroions was much stronger for Rb^+ than for K^+ . The ITC studies provided direct confirmation that the binding strength between $\{Mo_{72}Fe_{30}\}$ and monovalent cations followed the order of $(Li^+, Na^+) < H_3O^+ < K^+ < Rb^+ < Cs^+$, which was completely consistent with the observed corresponding blackberry formation processes.³⁵

Direct evidence for the counter-cation exchange was obtained from anomalous small-angle X-ray scattering (ASAXS) studies. When Rb^+ was present in $\{Mo_{72}V_{30}\}$ solution, there was an obvious difference between the $I(Q)$ response obtained at different energies. The difference indicated that Rb^+ distributed homogeneously and isotropically around the macroions, which meant that the replacement of K^+ by Rb^+ in $\{Mo_{72}V_{30}\}$ solution was possible. Furthermore, pH value of the aqueous solution decreased due to the release of more free protons resulted from counterion

replacement. The capability of distinguishing different monovalent cations in dilute solution is unique for these hydrophilic macroions.³⁵

2.1.3.4 Water-bridged Hydrogen Bonding

$\{\text{Mo}_{72}\text{Fe}_{30}\}$ and $\{\text{Mo}_{72}\text{Cr}_{30}\}$ are two POMs with the same size and morphology.^{21,25} They can be of the same charge density by carefully tuning the pH of their individual aqueous solutions, however, their assembly sizes are very different (even with the same charge density), which implies the existence of another strong inter-POM force besides charge interaction (Table 2-1).³⁶ $\{\text{Mo}_{154}\}$, a wheel-shape molecule with 70 water ligands on its surface, was applied for dielectric relaxation measurements to directly uncover the role of ‘the force’, hydrogen bonding in the formation of blackberry structures.³⁷ The conductance-corrected dielectric spectra and difference spectra of a freshly prepared solution and ‘aged’ solution (two weeks after the preparation) were comparatively studied, which indicates that ‘the strength of the hydration extends as cluster association takes place with more water molecules being more strongly bound between the wheels and the presence of relatively fewer less strongly bound water molecules’.³⁷ Simply put, the water can stay between the macroanions with higher viscosity than pure water, which can support additional hydrogen bonds help to bind the POMs together. However, pH-dependent self-assembly of $\{\text{Mo}_{72}\text{Fe}_{30}\}$ and $\{\text{Mo}_{72}\text{Cr}_{30}\}$ in aqueous solution indicated that the two clusters were not able to self-assemble into blackberry at low pH, suggesting that water-bridged hydrogen bonding might not be the major driving force for the blackberry formation, but the force to strengthen the interaction between macroions.^{30,36}

2.1.3.5 Stability of polyoxoanions in salt-containing aqueous solutions

The stability of polyoxoanions and blackberry structures has been explored at high salt concentrations. Basically, the stability of blackberries can be studied in the same way as we do for colloidal systems due to their larger sizes than discrete POM anions. As the fundamental

theory in colloidal science, DLVO theory reveals that charge repulsion stabilized the charged particles while van der Waals force leads to the coagulation of the particles.⁴ Usually adding extra ions can be used to destabilize the colloidal system since it significantly screens the repulsive interactions. Different types of cations were added to the aqueous solutions of $\{\text{Mo}_{72}\text{Fe}_{30}\}$ with different concentrations, respectively (Table 2-2). Precipitation, indication of the instability, can be observed when the concentrations of added salts passed a critical salt concentration (CSC). The monovalent cations with small hydrated radii had lower CSC values. The cations with higher valence showed much lower CSC values. Interestingly, there was no trend among different divalent cations like that observed among the monovalent cations. In this respect, the valence of the divalent cations was so dominant on determining the stability of blackberries which made other factors, e.g., the hydration of the cations, negligible. Macroanionic concentration dependence was found where the stability of the $\{\text{Mo}_{72}\text{Fe}_{30}\}$ solution increased with increasing macroanionic concentration. This behavior is likely attributed to the close association of monovalent counter-ions around macroions existing in aqueous solution which is facilitated at higher macroionic concentrations. The precipitates from $\{\text{Mo}_{72}\text{Fe}_{30}\}$ solutions could be re-dissolved in solution (except for solutions containing Cs^+ or Rb^+) when adjusting the solution $\text{pH} < 1.5$ so that the $\{\text{Mo}_{72}\text{Fe}_{30}\}$ clusters became almost neutral and fully protonated.³⁸

Table 2-2 Critical salt concentrations needed for precipitating $\{\text{Mo}_{72}\text{Fe}_{30}\}$ blackberries from different $\{\text{Mo}_{72}\text{Fe}_{30}\}$ concentrations. Reprinted with permission from ref. 38. Copyright 2010 Elsevier.

Ion	Critical concentration (mM) 0.1 mg/mL $\{\text{Mo}_{72}\text{Fe}_{30}\}$	Critical concentration (mM) 0.25 mg/mL $\{\text{Mo}_{72}\text{Fe}_{30}\}$	Critical concentration (mM) 0.5 mg/mL $\{\text{Mo}_{72}\text{Fe}_{30}\}$
Li^+	25	50	95
Na^+	8.5	36	70
K^+	6	25	50
Rb^+	0.5	1	4
Cs^+	0.2	0.3	0.5
NH_4^+	2.5	12	27.5
Mg^{2+}	0.25	0.5	1
Ca^{2+}	0.25	0.5	1
Ba^{2+}	0.25	0.5	1
Ni^{2+}	0.25	0.5	1
Al^{3+}	<0.005	0.02	0.05

2.1.4 Controlling the assembly/disassembly and blackberry size

The assembly and disassembly of blackberries, as well as the transition between the blackberries with different sizes, can be achieved by properly adjusting parameters such as the macroionic charge density, solvent polarity, and extra salt concentration.

2.1.4.1 *'Power on/off' the self-assembly process and accurately controlling the blackberry size*

The charge density of macroions can be tuned by changing the concentration or temperature of the macroionic solutions besides the effects of solution pH and solvent polarity that discussed earlier. The charge density is too low for macroions to self-assemble when the pH of 0.5 mg/mL $\{\text{Mo}_{72}\text{Fe}_{30}\}$ aqueous solution is < 2.9 ; or for $\{\text{Mo}_{132}\}$ in acetone/water solution the acetone content is over 70%vol. The self-assembly process can be triggered by adding base into the aqueous solution of $\{\text{Mo}_{72}\text{Fe}_{30}\}$, or adding appropriate amount of water to the acetone/water solution of $\{\text{Mo}_{132}\}$.^{28,30} On the other hand, the disassembly of the blackberries can be achieved by applying the reverse procedures. $\{\text{Mo}_{72}\text{Cr}_{30}\}$ shows the similar pH-controlled self-assembly behavior with $\{\text{Mo}_{72}\text{Fe}_{30}\}$ by displaying the 'switch' point at $\text{pH}=2.7$.³⁶ $\{\text{Mo}_{72}\text{V}_{30}\}$ is able to self-assembly into blackberry within the range 2-90 vol% acetone in acetone/water mixed solvents.³⁶ Meanwhile, due to the capturing of counterions (ammonium) in the nano-pores on the surface of $\{\text{Mo}_{72}\text{Fe}_{30}\}$, its charge density is lowered and appropriate for counterion-mediated self-assembly. However, the total scattered intensity dropped, which meant the blackberry disassembled, after mild heating of the solution from room temperature to 40 °C.³⁹ The 'power off' process can be explained by exceeding the critical charge density of $\{\text{Mo}_{72}\text{Fe}_{30}\}$ resulted from the temperature enhanced release of the ammonium ions from the pores into the bulk solution.³⁹

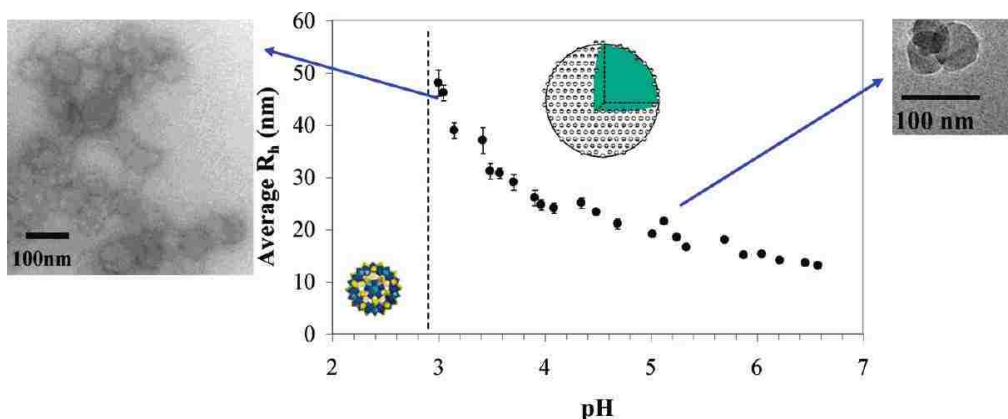


Figure 2.6 Average hydrodynamic radii (R_h) of the blackberries formed in 0.5 mg/mL aqueous solutions of $\{Mo_{72}Fe_{30}\}$ at different pH (adjusted by NaOH or HCl), as measured by DLS at 90° scattering angle. TEM images of aggregates on carbon film formed at pH \sim 3.0 (left; conventional TEM) and pH \sim 4.6 (right; more appropriate cryo-TEM). Reprinted with permission from ref. 30. Copyright 2006 American Chemical Society.

By continuously tuning the pH of the weak acid type POMs' solutions, the solvent polarity of strong electrolyte POMs' solutions or adding cationic surfactants to macroionic solutions in the range that the formation of blackberry can be observed, the charge densities of macro-anions are supposed to be varied, which shows a significant effect in the size of the assemblies.⁴ In the aqueous solution of $\{Mo_{72}Fe_{30}\}$, self-assembly occurs with the blackberry size decreasing with increasing pH, from $R_h \sim 50$ nm at pH = 3.0 to $R_h \sim 15$ nm at pH = 6.0 (Figure 2.6).³⁰ The blackberry size of $\{Mo_{72}Cr_{30}\}$ decreases from 70 to 40 nm within the pH range 2.7~7.0.³⁶ LLS revealed the presence of the $\{Mo_{132}\}$ blackberry structures in water/acetone mixed solvents containing 3 to 70 vol% acetone, with their average R_h increasing from 45 to 100 nm with increasing acetone content (Figure 2.2). The average blackberry size increased linearly with increasing $1/\epsilon$, with ϵ being the solvent's dielectric constant (Figure 2.3).²⁸ Similar trends have also been identified in $\{Mo_{72}V_{30}\}$ and $\{W_{72}Mo_{60}\}$ in water/acetone mixed solvents.²⁹ A charge regulated self-assembly process was given to explain the formation of blackberries, which predicted that the vesicle size is proportional to the inverse of the dielectric constant of the solvent.²⁹

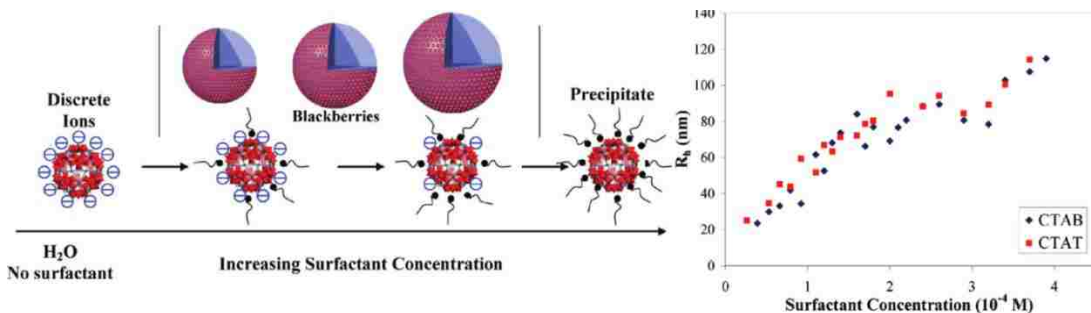


Figure 2.7 (left) Gradually introducing alkyl trimethylammonium halide cationic surfactants into the dilute aqueous solution of {Mo₇₂V₃₀} cluster can gradually decrease the charge density on the {Mo₇₂V₃₀} macroions and induce blackberry formation. The average blackberry size increases with increasing surfactant amount (i.e., decreasing charge density on {Mo₇₂V₃₀}). (right) Average hydrodynamic radius (R_h) of the {Mo₇₂V₃₀} blackberries in aqueous solution containing CTAB or CTAT, measured by DLS. The concentration of {Mo₇₂V₃₀} is 0.5 mg/mL, equivalent to a molar concentration of 2.6 X 10⁻⁵M. Reprinted with permission from ref. 40. Copyright 2009 American Chemical Society.

Cationic surfactants with long enough alkyl chains can interact with macroanions stoichiometrically and therefore be used to accurately decrease the macroionic effective charge (Figure 2.7). A typical study was carried out with {Mo₇₂V₃₀}, which does not show self-assembly behavior in dilute aqueous solution due to its high charge density.⁴⁰ After introducing a small amount of water-soluble cationic surfactants, such as cetyltrimethylammonium bromide (CTAB), trimethyltetradecylammonium chloride (CTAT), dodecyltrimethylammonium bromide (DTAB), and octyltrimethylammonium bromide (OTAB), the charge density on {Mo₇₂V₃₀} macroions was expected to decrease so that the {Mo₇₂V₃₀} macroions will enter the blackberry-formation regime (Figure 2.7). The average R_h of the blackberries continued to increase with increasing surfactant concentration, as shown in Figure 2.7.⁴⁰ CTAB and CTAT strongly interacted with the macroions stoichiometrically while shorter OTAB had much weaker interaction with the macroions.⁴⁰

Represented by {Mo₇₂V₃₀} and {P₄Y₈W₄₃}, weak acid salt type POMs carry a considerable amount of charges in crystals but still further deprotonate some surface water ligands when dissolved in a solvent.^{34,41} For these macroions, their self-assembly processes can be controlled by either changing solvent content or changing solution pH (in aqueous solution). Consequently, such POMs are valuable for directly comparing the effects of solvent content and solution pH on the blackberry size. The yttrium-containing lacunary polyoxotungstate {P₄Y₈W₄₃} macroanions

could form $R_n \sim 53$ nm blackberries in 0.3 mg/mL aqueous solution. The blackberry size increased with increasing amount of acetone added into the solution, which was quantitatively similar to the case of $\{Mo_{132}\}$ as described above. Changing solution pH could also alter the blackberry size. However, since the pH change only affected the amount of protons released from the macroions, the change of blackberry size due to pH was smaller than the change caused by changing solvent content.⁴¹

2.1.4.2 Size limit of the ‘macroanions’

The size disparity between highly-charged particles and their counter-ions is considered to be the source for ion-pairing and like-charge interaction.⁴² The static charge interaction is stronger than the thermal motion of small counterions, however, weaker than the thermal motion of large particles. In that way, it can hold counterions around the highly charged particles. As a quite important but unsolved issue, what is the critical size for the macroion that can self-assemble into blackberry structures? Currently, the smallest polyoxoanions that were proved to be able to self-assemble is $\{Cu_{20}P_8W_{48}\}$ with size as 2.2 X 1.1 nm (Table 2-1).⁴³ Further exploration on POMs with different sizes have been undergoing in our lab to determine the critical size.

2.1.4.3 Controlling the morphology of the assemblies

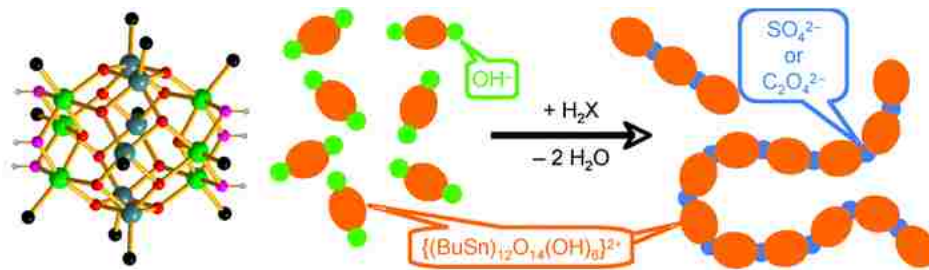


Figure 2.8 (Left) Molecular structure of $\{(RSn)_{12}O_{14}(OH)_6\}^{2+}$. (six-coordinated tin, green; five-coordinated tin, teal; u_3 -oxo, red; u_2 -oxo, purple; R, black; hydrogen, gray). (Right) The formation of large aggregate induced by dianions. Reprinted with permission from ref. 48. Copyright 2010 American Chemical Society.

The macroions with anisotropic charge distribution can also assemble into non-spherical objects with low symmetry. The tin-12 oxo cluster (Figure 2.8), $\{(RSn)_{12}O_{14}(OH)_6\}^{2+}$, first reported in

1989, is an interesting, positively charged organic-inorganic cluster. The football-shaped cluster exhibits two positive charges that are located at the poles of the cluster, defined by the six-coordinated Sn ions and the u^2 ligands.^{44,45} Because of the location of the two positive charges, the cluster can interact with dianions to show some interesting assembly behaviors. Very recently, Ribot et al. applied pulsed field gradient NMR spectroscopy to probe the anions mediated associative behavior of $\{(R\text{Sn})_{12}\text{O}_{14}(\text{OH})_6\}^{2+}$. The counterion can only interact with the two poles of the $\{\text{Sn}_{12}\}$, which finally direct the formation of a worm-like structure in organic solvents (Figure 2.8).^{44,45}

2.1.5 The unique slow self-assembly process vs. virus capsid formation

Blackberries are thermodynamically stable, which is quite different from colloidal systems.^{4,46-49} However, different from the comparatively fast self-assembly behavior of amphiphilic molecules, the macroanions need a long period of time, sometimes even several months at room temperature, to reach equilibrium state.^{4,43,50} The unique slow self-assembly process have been studied by long-time monitoring results and kinetic studies, which shared similarities with the self-assembly of virus capsid proteins.⁴

2.1.5.1 The kinetic properties of the self-assembly

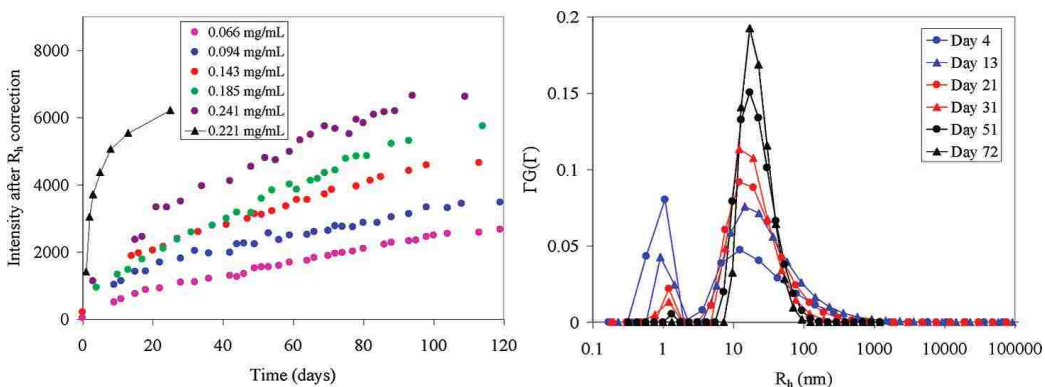


Figure 2.9 (left) Change of total scattered intensity of $\{\text{Mo}_{72}\text{Fe}_{30}\}$ solutions at 90° scattering angle. All solutions were kept at 25°C except one at 45°C (the data shown by black triangle). **(right)** CONTIN analysis of DLS study on $\{\text{Mo}_{72}\text{Fe}_{30}\}$ aqueous solution at different times. Reprinted with permission from ref. 53. Copyright 2005 American Chemical Society.

The slow blackberry formation under certain circumstances enables detailed study on the mechanism of the self-assembly. Figure 2.9 demonstrates a typical SLS and DLS study on the formation of $\{\text{Mo}_{72}\text{Fe}_{30}\}$ blackberries in aqueous solution at different macroionic concentrations. The scattered intensity recorded by SLS continued to increase with time, suggesting the continuous formation of large structures in solution. At the same time, DLS studies indicated that there exist two modes (corresponding to two different types of particles) in solution: discrete macroions ($R_h \sim 1.2$ nm) and blackberries (average $R_h \sim 25$ nm). The first peak became smaller and smaller while the second one grew larger with time, indicating that the discrete macroions were continuously forming blackberries while the average blackberry size remained almost unchanged during the whole process. Combining the above information, we concluded that the formation mechanism of the blackberry should follow upper route in Figure 2.10. That is, at the beginning, the unimers slowly associated into dimers (or oligomers). This was the rate-determining step. Once enough oligomers were available, they quickly assembled into large blackberries. This step was fast so that no “small” blackberries were observed during the whole process.^{43,50}

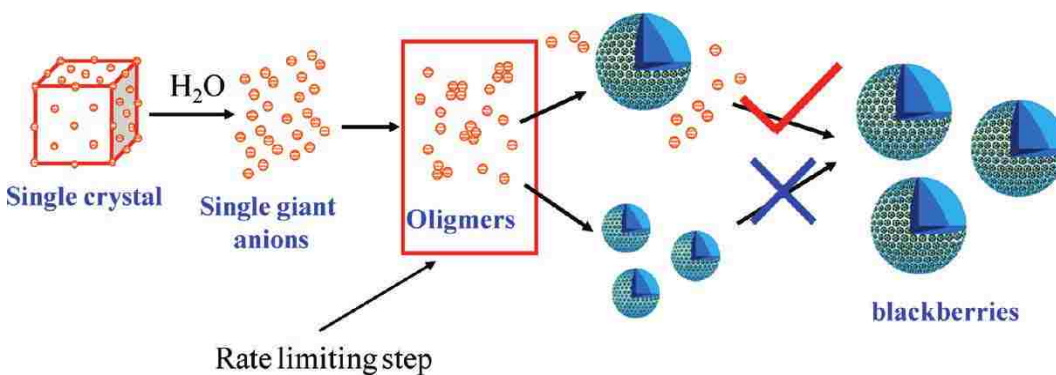


Figure 2.10 Possible mechanisms of $\{\text{Mo}_{72}\text{Fe}_{30}\}$ blackberry formation in dilute aqueous solution. The upper mechanism has been proven to be correct based on SLS and DLS results, while the bottom mechanism can be ruled out. Adapted with permission from ref. 43 and reprinted with permission from ref. 5. Copyright 2010 American Chemical Society.

The slow blackberry formation is attributed to the high energy barrier for the transition from single macroions to blackberries. Time-resolved SLS studies were used to determine the initial “reaction” rates in $\{\text{Mo}_{72}\text{Fe}_{30}\}$ aqueous solutions at different temperatures. The ‘rate’ could be

significantly enhanced by increasing the temperature of the solutions. By using the Arrhenius equation $\ln(k) = -E_a/RT + \ln A$, the activation energy of the oligomer formation could be calculated as $\sim 115 \pm 8$ kJ/mol, which was indeed very high (Figure 2.11).⁵⁰

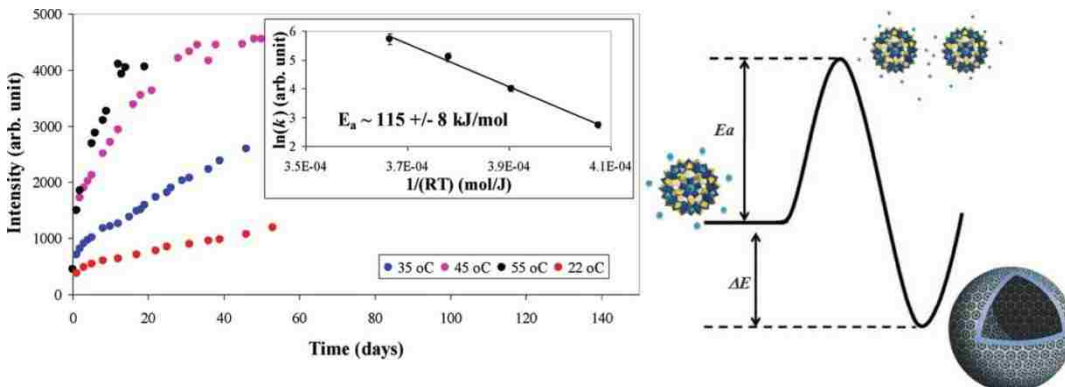


Figure 2.11 (Left) Increment of the scattered intensity (I) from 0.5 mg/mL $\{\text{Mo}_{72}\text{Fe}_{30}\}/\text{H}_2\text{O}$ solutions at different temperatures (22, 35, 45, and 55 °C) with time indicates the progress of blackberry formation. **(inset)** Calculation of the activation energy (E_a) for the blackberry formation. Reprinted with permission from ref. 53. Copyright 2005 American Chemical Society. **(Right)** Thermodynamic demonstration of the blackberry formation. Reprinted with permission from ref. 57. Copyright 2011 AAAS.

2.1.5.2 Lag Phase during the Blackberry Formation

In aqueous solution containing no or small amounts of extra monovalent cations (e.g., NaCl, NaBr, NaI, and Na_2SO_4 at concentrations of 0.017 mol/L), the $\{\text{Mo}_{72}\text{Fe}_{30}\}$ blackberry formation process, recorded by SLS studies as the time-resolved intensity curve, showed a linear relationship with time, similar to a first-order reaction.⁵⁰ However, a lag phase was observed in the SLS studies of the dilute solutions of $\{\text{Cu}_{20}\text{P}_8\text{W}_{48}\}$ ⁴³ and $\{\text{Mo}_{72}\text{Fe}_{30}\}$ ⁵⁰ (in minutes). This lag phase became significant when the extra salt concentration was higher or introducing glycerol, a viscous and water-miscible solvent, as shown in Figure 2.12. The initial scattered intensity from this solution was very low, suggesting that almost all the $\{\text{Mo}_{72}\text{Fe}_{30}\}$ macroanions existed as discrete anions. After a lag period of ~ 20 days, the intensity suddenly started to increase until it was stabilized after months at a very high level, indicating a slow formation of blackberries. Overall, the whole kinetic curve is sigmoidal.⁵¹

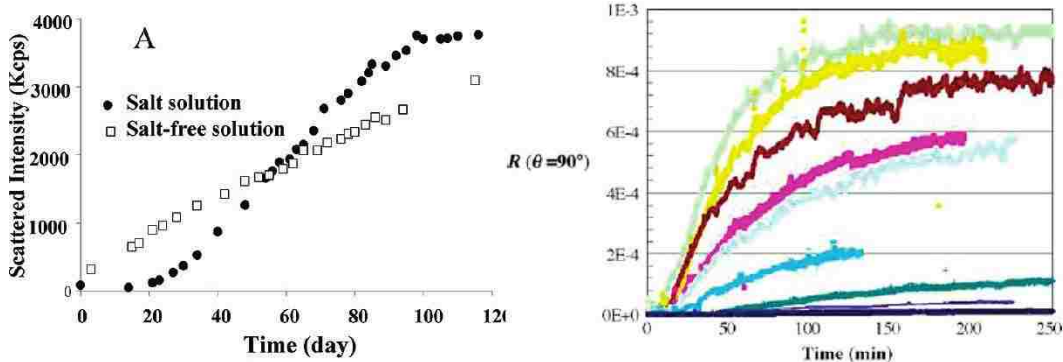


Figure 2.12 (left) Comparison of scattered intensity increment (A) and Rh change (B) of two $\{\text{Mo}_{72}\text{Fe}_{30}\}$ samples along reaction time in 0.9wt% NaCl and salt-free solutions Reprinted with permission from ref. 54. Copyright 2010 American Chemical Society. (right) Light scattering study of the assembly of HPV capsid proteins at various HPV concentrations. The lag time, reaction slope, and extent of assembly were dependent upon the initial protein concentration. Changes in scattered light were not observed until minutes later. Reprinted with permission from ref. 55. Copyright 2004 Elsevier.

The sigmoidal curve for a self-assembly process has also been reported in other systems such as virus capsid formation (Figure 2.12)⁵², ester hydrolysis, vesicle formation, and nanoparticle preparation. In general, it is considered to be a typical feature of a two-step process: in the initial lag period, the “reaction” begins with the slow formation of oligomer nucleus; once the amount of the rate limiting nucleus has reached a critical value, subsequent oligomers or monomers are quickly added to the growing assembly structures at a time until it is complete.⁵¹

To identify the oligomeric species during the lag period, sedimentation velocity (SV) experiments were performed on the 18th day after the $\{\text{Mo}_{72}\text{Fe}_{30}\}$ solution was prepared, corresponding to the final stage of the lag period in the kinetic curve (Figure 2.13). In a typical SV experiment, the experimental curves were fitted using the Lamm equation to deduce the sedimentation coefficients (s) of sedimentating species and their corresponding sedimentation coefficient distributions $c(s)$ (Figure 2.13).⁵¹ For the $\{\text{Mo}_{72}\text{Fe}_{30}\}$ solution on the 18th day, the results showed the coexistence of two species: $s \sim 6.6$ S with the dominant abundance (56%) and $s \sim 9.5$ S (10%), corresponding to $\{\text{Mo}_{72}\text{Fe}_{30}\}$ monomers and dimers, respectively. In addition, the measurement also suggested the possible existence of a small amount of larger oligomers (such as trimers) in solution. Besides the concentration of additional salts, the length of the lag period also

depended on temperature, the valence state of the cations and the anions, as well as the solvent content.⁵¹

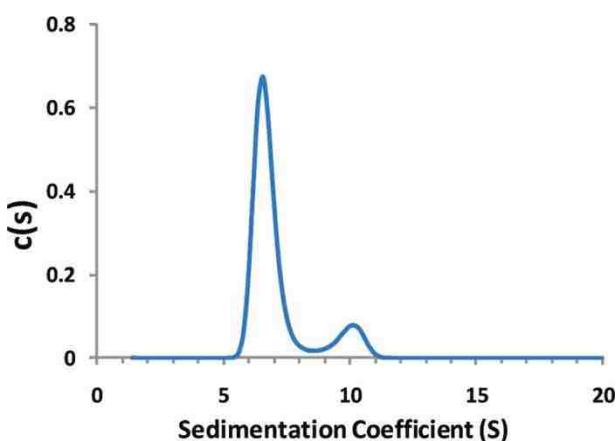


Figure 2.13 Continuous size distribution $c(s)$ analysis of $\{\text{Mo}_{72}\text{Fe}_{30}\}$ solution versus sedimentation coefficient, s . Experiments were performed at a $\{\text{Mo}_{72}\text{Fe}_{30}\}$ concentration of 10 mg/mL in 170 mM NaCl solution at 20 °C. Reprinted with permission from ref. 54. Copyright 2010 American Chemical Society.

The assembly structures and formation processes of blackberries and virus capsids (mostly spherical, single-layered structures formed by the ordered assembly of capsid protein units which are also soluble macroanions) demonstrate interesting structural similarities. Furthermore, the sigmoidal curves suggested that their self-assemblies might share similar mechanisms.^{4,5} The hydrophobic interaction is widely believed as the dominant driving force for the virus capsid formation. However, for the POMs, they do not contain any hydrophobic moieties, and thus, hydrophobic interaction does not play a role in the blackberry formation. Then the question is: is it possible that the electrostatic interaction might be underestimated in the virus shell formation? Ideally and potentially, the POM macroions might be useful as simple model systems to study the more complicated bio-macromolecular systems.^{4,42}

2.1.6 Permeability of Blackberry ‘Membrane’ to small cations

Advanced AFM technology can realize in-situ detection of blackberry structures in solution state. A Si substrate was first modified with ammonium, which can positively charge the surface of substrate under low pH. Then the substrate was immersed in the solution of $\{\text{Mo}_{72}\text{Fe}_{30}\}$ (vol

water/acetone = 1). The single POM anions and the formed aggregates were supposed to be negative charged, which favor to interact with the positively charged surface. Interestingly, ring-like structures were found when the AFM tip tapped the surface immersed in solution. The size of the ring was about the same of the size of assemblies observed from LLS studies. As time went by, more and more ‘rings’ were detected, which was due to the comparatively slow adsorption of self-assembled structures on the surface. The AFM results confirmed that blackberries were likely negatively charged hollow structures and the shell of the sphere can be broken by AFM tips.⁴²

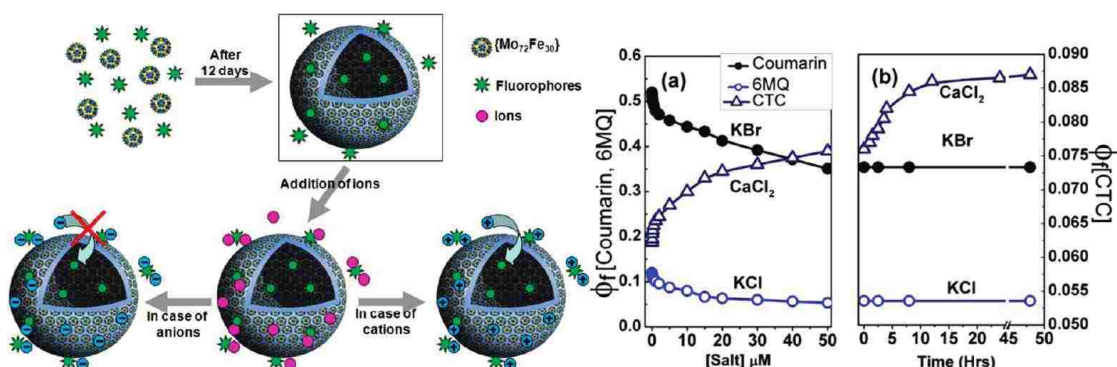


Figure 2.14 (left) Formation of fluorophore-containing {Mo₇₂Fe₃₀} blackberries in solution. The additional cations, once added into solution, instantly interact with fluorophores in bulk solution and on blackberry surfaces, subsequently enter into the blackberries, and interact with the fluorophores inside. The anions could not cross the membrane. (right) Change in fluorescence quantum yield of Coumarin 1,6-MQ, and CTC with addition of KBr, KCl, and CaCl₂, respectively; (a) instantaneous change occurs with the addition of salts; (b) change in fluorescence quantum yield with time, once the addition of salt is stopped. Reprinted with permission from ref. 56. Copyright 2008 American Chemical Society.

As the in-situ AFM results proved that the membranes of blackberry were quite soft, permeability tests indicated that the membranes selectively allowed cationic species to pass through (Figure 2.14).⁵³ The permeability tests were based on the monitoring of fluorescence spectroscopy of water-soluble dyes that are specifically sensitive for one (or two) type of ions. Chlorotetracycline (CTC) (sensitive to Ca²⁺ and Mg²⁺), 6-methoxyquinoline (6-MQ) (sensitive to Cl⁻) and Coumarin 1 (sensitive to Br⁻) were added to the freshly prepared {Mo₇₂Fe₃₀} aqueous solution. The fluorophores would be partly incorporated into the inner areas of blackberries during the self-assembly process, which was confirmed by the 18 nm shift of their fluorescent signals.⁵³ Specific ions sensitive to the dye were introduced to the solution after the completion of blackberry

formation. A sudden jump in fluorescence signal suggested that the CTC molecules staying in bulk solution were immediately saturated after dominant amount of Ca^{2+} ions were added. Interestingly, there was a very slow, continuous increment in the fluorescence signal after the initial process, suggesting a slow, continuous binding between Ca^{2+} ions and CTCs. The results could be explained as that Ca^{2+} ions could slow pass the blackberry membranes and bind with CTC molecules inside. However, anions such as Cl^- and Br^- could not pass through the membrane.⁵³

2.1.7 The self-recognition behavior during self-assembly process

The previous studies on the lag phase period in the self-assembly process, the POMs-based host-guest interaction, and modular redox-active inorganic chemical cells indicate that POMs are good models to understand some fascinating behaviors of biological systems in solution. For example, self-recognition is a general and significant phenomenon in biological units which directly connects to many biological functions. It is important to understand the critical forces for the self-recognition. Biological systems are too complicated while the POM macroions are ideal simple models.^{4,51}

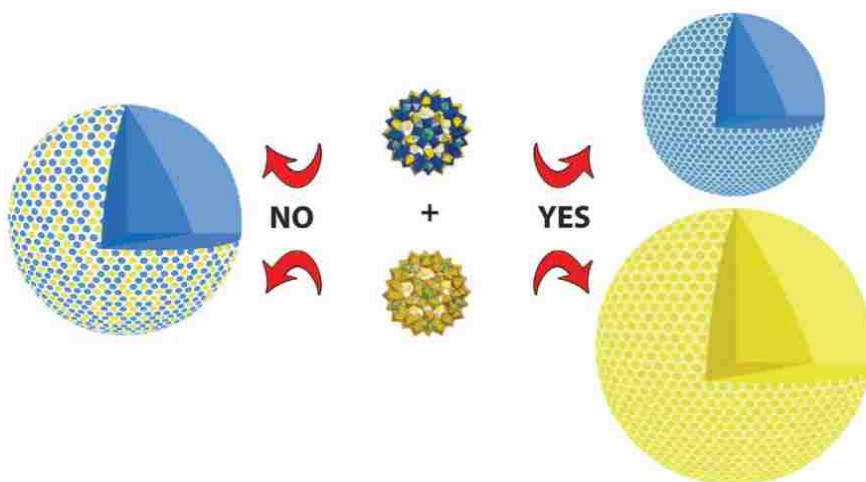


Figure 2.15 (Middle) In mixed dilute aqueous solutions, the clusters (polyhedral representation) $\{\text{Mo}_{72}\text{Fe}_{30}\}$ (top) and $\{\text{Mo}_{72}\text{Cr}_{30}\}$ (bottom) self-assemble into different (i.e., individual) blackberry structures of the Cr30 (yellow) and Fe30 type (blue)—with interfacial water between the macroions (right)—and do not form mixed species

(such as the hypothetical structure shown on the left). Reprinted with permission from ref. 57. Copyright 2011 AAAS.

The aqueous solutions containing the mixture of two spherical polyprotic clusters: $\{\text{Mo}_{72}\text{Fe}_{30}\}$ and $\{\text{Mo}_{72}\text{Cr}_{30}\}$ are studied. The clusters have 30 characteristic and active $\text{M}(\text{H}_2\text{O})$ groups coordinated to the non-Mo atoms, different mobilities of their surface hydration layers as well as degrees of deprotonation. Our previous discussion suggests that the water ligands (weak Brønsted acids) release protons, i.e., about seven for $\{\text{Mo}_{72}\text{Fe}_{30}\}$ and about five for $\{\text{Mo}_{72}\text{Cr}_{30}\}$ in aqueous solution.³⁶

The mixed aqueous solutions of the $\{\text{Mo}_{72}\text{Cr}_{30}\}$ - and $\{\text{Mo}_{72}\text{Fe}_{30}\}$ -type POMs were studied to determine whether they form homogeneous or heterogeneous blackberry structures (Figure 2.15). The two separated modes in the DLS study indicated the presence of two types of large species with different sizes (Figure 2.16). The two peaks corresponded to those of the individual solutions containing either $\{\text{Mo}_{72}\text{Cr}_{30}\}$ or $\{\text{Mo}_{72}\text{Fe}_{30}\}$ at the same pH value. More convincing evidence for such self-recognition behavior could be obtained by individually analyzing the elements of the two assemblies corresponding to the two peaks. The two assemblies could be separated from the parent solution by filtration.⁵⁴

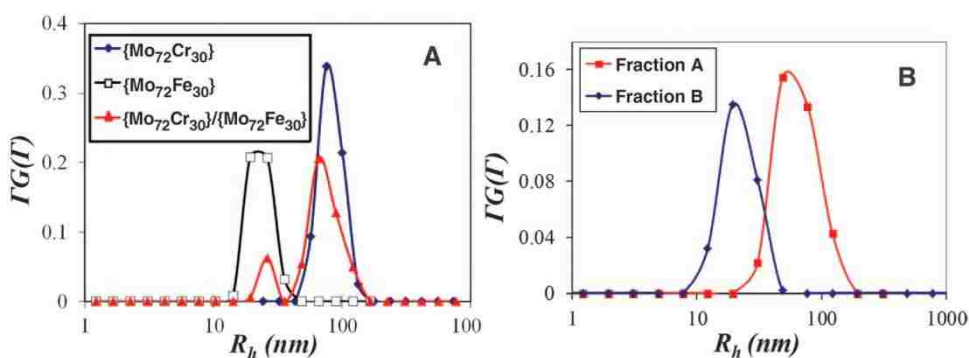


Figure 2.16 (A) CONTIN analysis of the DLS studies at 90° scattering angle measured for aqueous solutions containing $\{\text{Mo}_{72}\text{Cr}_{30}\}$ or $\{\text{Mo}_{72}\text{Fe}_{30}\}$ (0.1 mg/ml each), as well as for a solution containing both species (0.1 mg/ml of each) (pH = 4.2). In the mixed solution, the peak due to the larger $\{\text{Mo}_{72}\text{Cr}_{30}\}$ assemblies is dominant because larger structures scatter more light. (B) CONTIN analysis of the DLS experiment carried out on the two components after ultrafiltration of the aqueous solution originally containing both $\{\text{Mo}_{72}\text{Cr}_{30}\}$ and $\{\text{Mo}_{72}\text{Fe}_{30}\}$ (0.1 mg/ml of each) by a series of membranes with different pore sizes; fraction A (red): material retained after filtering by 100,000 dalton-pore size membrane; fraction B (blue): material retained after filtering by 30,000 dalton-pore size membrane. Reprinted with permission from ref. 57. Copyright 2011 AAAS.

As described in section 2.1.5, the formation of oligomers is the rate-determining step for the blackberry formation. Time-resolved SLS studies at the early stage of the self-assembly (still in lag phase period) showed that the curves for the freshly prepared solutions of $\{\text{Mo}_{72}\text{Cr}_{30}\}$ and $\{\text{Mo}_{72}\text{Fe}_{30}\}$ were almost identical in slope and both show minor lag periods, suggesting that two dimer/oligomer formation processes in the solutions are kinetically similar. More importantly, SLS studies at both early stage and after the whole self-assembly process indicated that the individual species assembled faster than their mixtures at a given concentration, which meant that the self-recognition started as early as the oligomer formation. The large energy barrier in the oligomer formation probably enabled the self-recognition even for species with minor differences. In the current case, the most critical factor of generating the self-recognition was due to the small charge density difference between these two types of macroions. Additionally, the 30 identical $\text{Cr}^{\text{III}}(\text{H}_2\text{O})$ and $\text{Fe}^{\text{III}}(\text{H}_2\text{O})$ groups differ greatly in the lability (i.e., residence time) of their water ligands. As a result, the interfacial water mobilities and heterogeneities of the macroions in the two superstructures differ significantly, and the hydrogen bonding network for the $\{\text{Mo}_{72}\text{Cr}_{30}\}$ -type blackberries was more dense and stable. The different mobilities of the interfacial water networks can be confirmed by the fact that the transport of Ca^{2+} through the $\{\text{Mo}_{72}\text{Cr}_{30}\}$ blackberry membranes was slower than that through the $\{\text{Mo}_{72}\text{Fe}_{30}\}$ -type system by a factor of 3 to 4.⁵⁴

2.1.8 Theoretical studies on the polyoxoanionic solutions

Bo and Poblet et al. calculated the radial distribution functions of Li^+ , Na^+ , and K^+ with Keggin ions bearing 3-, 4-, and 5- charges, and the diffusion coefficients of these Keggin ions.^{55 56} The effect of the microscopic molecular details of the solvent was a key aspect to interpret the simulation results due to the competition between electrostatic interaction among the ions and the stability of the solvation shell. Further analysis showed that the solvent-shared structures weakly bound to the POM anions played a crucial role in the determination of the dynamic properties of the

anions. The authors also suggested that the image of the ion pair as a well-defined molecular conformation had to be substituted by a more dynamic picture in which the paired ions moved inside the region bounded by Bjerrum's length, with some preferred locations that were the result of the more stable balance between electrostatic interactions, entropic effects, as well as the solvent effect.^{55 56}

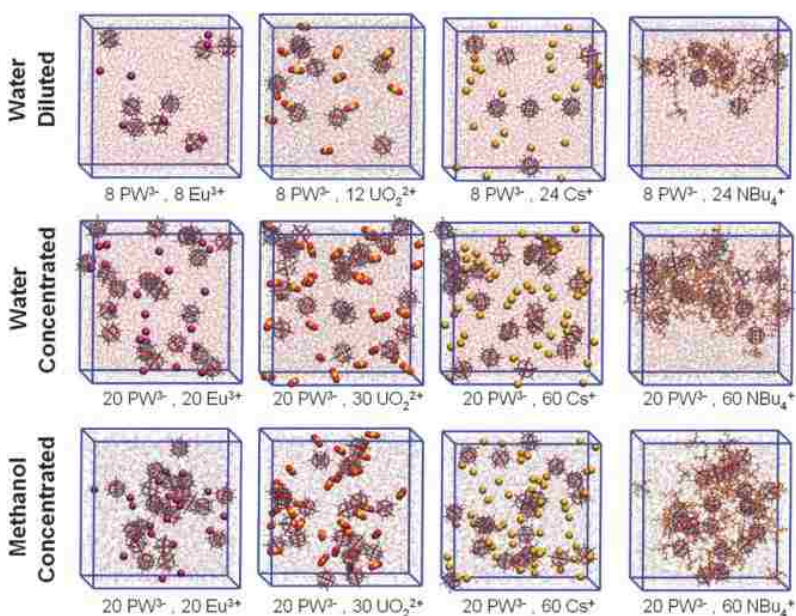


Figure 2.17 Snapshots of the different simulation boxes after 10 ns. a row, diluted aqueous solution; b row, concentrated aqueous solution; c row, concentrated methanol solution. Reprinted with permission from ref. 60. Copyright 2008 Royal Society of Chemistry.

Wipff et al. performed theoretical simulations on the aggregation of Keggin anions ($\text{PW}_{12}\text{O}_{40}^{3-}$) in aqueous and methanol solutions.⁵⁷ Aqueous solutions of Keggin anions were simulated at two anionic concentrations with Cs^+ , NBu_4^+ , UO_2^{2+} , Eu^{3+} , H_3O^+ , and H_5O_2^+ being counterions, respectively (Figure 2.17). They revealed significant counterion effects related to the degree of salt dilution, as well as the cation-anion and anion-anion interactions. The hydrophobic NBu_4^+ cations tended to surround POMs via loose contacts and created a “phase separation” between water and a humid, salty, overall neutral domain where all ions were concentrated. More hydrophilic cations were generally separated from the POM anions. The most important finding was the aggregation of POMs, mostly into dimers with short inter-POM distances ($\text{P}\cdots\text{P} < 12\text{\AA}$),

but also into oligomers in concentrated solutions where *ca.* 9 to 46% of the POMs formed aggregates, depending on the type of counterions. While Eu^{3+} and UO_2^{2+} were fully hydrated and interacted at short distances with POM anions as solvent-separated ion pairs, Cs^+ could form contact ion pairs, as well as solvent-separated ions. Among the monovalent counterions, H_3O^+ led to the most serious aggregation, due to the influence of the protons. The POMs' dynamic properties were also dependent on the counterions: their diffusion coefficients were the lowest with NBU_4^+ , and highest with Cs^+ , reflecting the degree of ion condensation in water. The role of water on the solution state of the POM salts was further demonstrated by simulating the most concentrated systems in methanol solution. Methanol solvated the counter-cations poorer than water did and could not form bridges between POMs, therefore a higher portion of anion-cation contacts, and no oligomers with short contacts could be found in methanol.⁵⁷

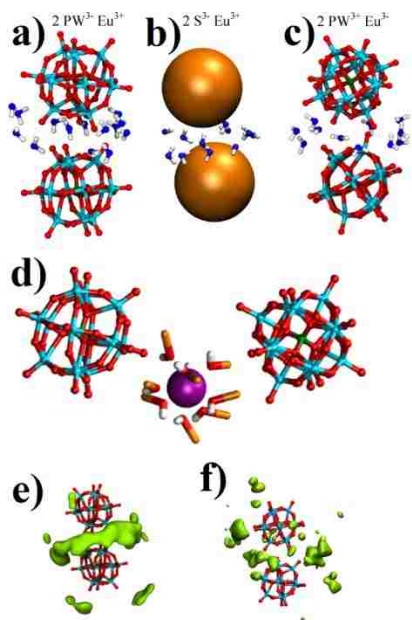


Figure 2.18 a), b), c) Snapshot of water molecules between 2 PW^{3-} , 2 S^{3-} or 2 PW^{3+} ions. d) Snapshot of the PW^{3-} . . . $\text{Eu}(\text{MeOH})_9^{3+}$. . . PW^{3-} pair at a P . . . P distance of 17.5 Å, corresponding to the free energy minimum along the PMF in methanol. e), f) Highest density region of Eu^{3+} and H_3O^+ , respectively. Adapted with permission from ref. 61. Copyright 2012 Elsevier.

Further detailed theoretical simulations were carried out to understand the like-charge attraction between Keggin type POMs. Wipff and co-workers calculated the changes in free energy $\Delta G(d)$

as a function of the P··P distance d , which represented the inter-POM distance.⁵⁸ As the POM anions approached each other, the free energy profiles were found to be quite flat, with a tiny minimum at *ca.* 11 Å, showing that the anions can form “contact ion pairs” in the presence of either H₃O⁺, UO₂²⁺ or Eu³⁺ counterions. The appearance of minimum energy around 10 Å and contact ion pairs were observed no matter what methodological variants were used, which supported the above finding that Keggin anions could form dimers or oligomers in water. The importance of stabilizing bridging water molecules was demonstrated by comparing Keggin anion (PW³⁻) to its spherical analogues (S³⁻) and to Keggin cations (PW³⁺, with all atomic charges of regular Keggin inverted) (Figure 2.18a, b, and c). The water bridged hydrogen bonds were specific in the dimer of Keggin anions, which was much stronger than the non-specific ones in the dimer of S³⁻. Water could not afford bridging H-bonds with the cationic dimer but solvated the contact region of this dimer via its O_{H2O} oxygens. The role of water was further demonstrated by comparing the simulation results in water and in methanol solution where there was no contact ion pair, but a free energy minimum at *ca.* 17 Å, corresponding to an ion separated pair PW³⁻··Eu(MeOH)₉³⁺··PW³⁻ (Figure 2.18d). These findings were important for understanding processes, such as condensation and assembling of POMs and macro-ions in water or at aqueous interfaces. Analysis of the distribution of counterion around the Keggin-dimer structures revealed that the counterions were in the bridge area of the dimers and acted like a ‘cationic glue’ (Figure 2.18e, f).⁵⁸

Wipff’s studies on comparatively small POMs confirmed the counterion-mediated attraction as driving force and the existence of water-bridged hydrogen bonding interaction for like-charge attraction and further self-assembly behavior of macroions.⁵⁸ Meanwhile, Kegel et al. claimed that only direct-contact hydrogen bonding contributed to the formation of POM shells while electrostatic repulsion played a role only in the folding of the sheet-like structures into shell, based on a simplified model.⁵⁹ Their simulation results seemed to be inconsistent with the

experimental results that the blackberry structures were disassembled into monomers without precipitation when $\{\text{Mo}_{72}\text{Fe}_{30}\}$ was uncharged (at $\text{pH} < 2.9$)³⁰ while the hydrogen bonding remained. Kegel's simulation would give opposite results, which could be due to the ignorance of the role of water molecules, such as solvation effect of the macroions and the induced polarization of water molecules in their simulation. Second, the strength of hydrogen bonding is highly dependent on the deprotonation of the water ligands, the distance between donor (D) and acceptor (A) atoms and the D-H...A angles, which require more complex models.

It might be difficult to do detailed simulations on giant POMs nowadays. Therefore, thermodynamic studies on the blackberry structures help reveal the key factor that might determine the size of blackberry structures. A simplified half empirical equation was presented by Kegel et al.²⁹ A charge-regulated self-assembly process was given to explain the formation of blackberry with a general expression for the blackberry radius R is expressed as

$$R \sim -48\lambda_{\text{B}}u/\psi^2 \quad (\text{Equation 2.1})$$

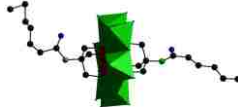

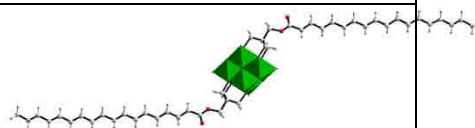
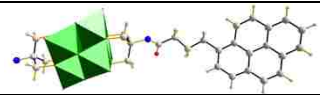
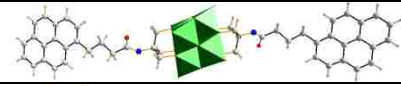
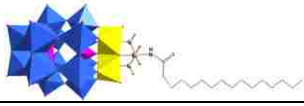
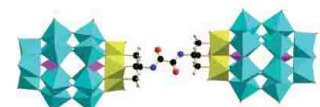
with $\lambda_{\text{B}} \sim 56/\epsilon$. Consequently, the size of the blackberries is determined by three parameters: the solvent content (in ϵ), the effective charge on the blackberries (described by the zeta potential ψ), and the magnitude of the attractive force among the macroions (u).²⁹

2.2 Self-assembly of covalently functionalized amphiphilic hybrid POMs

Chemical functionalization with organic components can effectively tune POMs' electronic structures and improve their compatibility and processibility.⁶ Due to their negative charges and the large amount of oxo ligands on their surfaces, POMs, generally speaking, are hydrophilic and therefore many of them are not compatible with organic media. Covalently functionalization by hydrophobic organic ligands renders the clusters amphiphilic features, which can be reflected in their self-assembly behavior in water/air and water/oil interface, polar and nonpolar solvents.^{7-9,11-}

Different from the self-assembly of macroions into blackberry structures, the driving force for the self-assembly of amphiphilic hybrid POMs is mostly solvophobic interaction. Being more complicated than the self-assembly of common amphiphilic surfactants, the study of the assembly of hybrid POMs needs to take the counterion effect and the bulky, charged polar head group into account besides the effect of molecule topology, solvent polarity, concentration, and hydrophobicity of the organic ‘tails’.⁷ The current research on all the effects will be summarized in the following sections.

Table 2-3 Formulas and molecular structures of the hybrid surfactants studied in our group.

Abbreviation	Hybrid surfactants formula	Molecular structure
S1	$(\text{TBA})_3[\text{MnMo}_6\text{O}_{18}\{(\text{OCH}_2)_3\text{CNHCO}(\text{CH}_2)_4\text{CH}_3\}_2]$	
S2	$(\text{TBA})_3[\text{MnMo}_6\text{O}_{18}\{(\text{OCH}_2)_3\text{CNHCO}(\text{CH}_2)_{14}\text{CH}_3\}_2]$	
S3	$(\text{TBA})_2[\text{V}_6\text{O}_{13}\{(\text{OCH}_2)_3\text{CCH}_2\text{OOC}(\text{CH}_2)_{16}\text{CH}_3\}_2]$	
S4	$(\text{TBA})_2[\text{V}_6\text{O}_{13}\{(\text{OCH}_2)_3\text{CNHOC}(\text{CH}_2)_3\text{C}_{16}\text{H}_9\} \{(\text{OCH}_2)_3\text{CNH}_2\}]$	
S5	$(\text{TBA})_2[\text{V}_6\text{O}_{13}\{(\text{OCH}_2)_3\text{CNHOC}(\text{CH}_2)_3\text{C}_{16}\text{H}_9\}_2]$	
S6	$((\text{TBA})_5\text{H}[\text{P}_2\text{V}_3\text{W}_{15}\text{O}_{59}(\text{OCH}_2)_3\text{CNHCOC}_{15}\text{H}_{31}])$	
S7	$\text{TBA}_{10}\text{H}_2[\{\text{P}_2\text{V}_3\text{W}_{15}\text{O}_{59}(\text{OCH}_2)_3\text{CNHCO}\}_2]$	

2.2.1 Surfactants with POMs as polar head groups

Conventional surfactants usually have one polar head group covalently linked with one or several hydrophobic (e.g., alkyl) tails. Packing parameter (P), defined from a surfactant’s geometrical

parameters, can be used to predict the assemblies of the surfactants in polar and nonpolar solvents.⁷ The polar head groups of our hybrids have higher negative charge and much larger sizes. Our studies indicate that the POM-based hybrid surfactants show complicated but controllable self-assembly behavior.^{12,60}

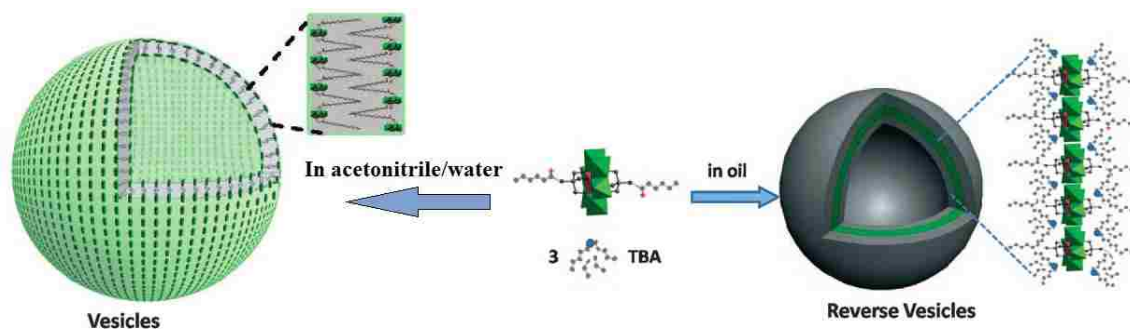


Figure 2.19 The formation of vesicles and reverse vesicles structures in polar and nonpolar solvent, respectively. Adapted with permission from ref. 16 and 17. Copyright 2008 American Chemical Society and 2010 Wiley-VCH.

Due to the convenience in synthesis, the original counterions of the anionic polar head groups are usually bulky organic cations, such as tetrabutylammonium (TBA).⁶ TBAs are strongly associated with polar head groups through static charge interactions in nonpolar solvents, which significantly reduces the polar heads' hydrophilic properties. Consequently, the amphiphilic properties of the hybrids are not obvious.¹³ However, the association between TBAs and POM head groups becomes weaker when the polarity of solvent is higher, which is confirmed by the difference in diffusion speed between TBA and anionic hybrids calculated from NMR results.¹³ The hybrids show amphiphilic properties by self-assembly into vesicle structures in appropriate polar solvents (Figure 2.19).¹³ The vesicle size of S3 and S6 showed a linear relationship with the inverse of the dielectric constant of the solvent, indicating a charge-regulated process. Hybrid S3 showed a much more negative slope than that of S6, which could be related to the less negative charge of hexavanadate (V_6) (-2) compared to Dawson-type POM (-6).^{13,60} The counterion disassociation is controlled by factors such as static charge interaction, solvent polarity and solvation of ions. Static charge force is proportional to the number of charges of the ions and

thus, TBA could be easier to diffuse away from the surface of the S3's polar head groups than from Dawson clusters (S6). Therefore, the effective charge on the S3 increases more significantly when the solvent polarity increases, which finally results in a more negative slope.^{13,60} For S3, vesicles could only be observed when 20~35 vol% of water was added to its acetone solution.¹³ However, due to the high negative charge (-6) and much larger polar head group, S6 can form vesicle structures in less polar solvents such as pure acetone.^{13,60} Additionally, two of the hybrids (S1 and S2) were proved to be able to form reverse vesicles in nonpolar solvents (Figure 2.19).¹⁷ The sizes of the assemblies could be continuously increased by decreasing the polarities of the solvents, which is due to the increasing solvophobic interaction.^{13,16}

Different salts, ZnCl₂, CuCl₂, NaI, tetrabutylammonium iodide (TBA*I) and dodecyltrimethylammonium bromide (DTMA*Br), which are soluble in acetonitrile, were added to acetonitrile solutions of S6, respectively, to study the role of the counterions on the vesicle formation and vesicular sizes. The vesicle size decreased gradually with increasing concentration of ZnCl₂. Interestingly, the vesicle size remained unchanged at first upon addition of NaI, but gradually increased when the NaI concentration exceeds 0.03 mg/mL. ZnCl₂, which is quite solvated in acetonitrile, preferred coordinating to the terminal or bridging oxo ligands on the surface of the Dawson clusters, forcing the polar domains to be exposed to the solvent-environment, which in turn increased the curvature of the vesicle, i.e. the vesicle size became smaller. Upon the addition of NaI, on the other hand, the sodium ions contributed to shielding the high negative charges of the polar head groups from each other, and thus reduced the repulsion between the polar heads on the surface of the vesicle. The curvature of the vesicle decreased, and as a result the vesicle size increased. The additions of CuCl₂, TBA*I or DTMA*Br showed no obvious effect on the vesicle size as those cations were not able to replace the TBA cations that surrounded the polar Dawson clusters. However, TBA*I and DTMA*Br were observed to cause the disassembly of the vesicles and this was confirmed by the fact that the scattered intensities

from corresponding solutions dropped increasingly when more of these salts were added.⁶⁰

The hybrids can be water-soluble when the original counterions, TBAs, are replaced by protons through ion-exchange resin.^{12,13} In aqueous solution, the POM head groups can work as nano-acid by reversibly releasing and associating protons with their surface oxo ligands. The assembly sizes were quite sensitive to pH of the aqueous solution. The increasing of pH will further release the protons from the surface of POMs, which increases the net charges of the head groups. The resulted increasing repulsion between POMs on the surface of vesicles increases the curvature of assemblies, e.g., smaller vesicle sizes.^{12,13}

Wang and co-workers were able to functionalized Dawson type POMs with polystyrene chain. They claimed that the hybrid aggregated into micro-spherical particles and precipitated from organic solvent when the POM polar head (Dawson POMs)'s original counterions, TBAs, were replaced by proton through ion-exchange resin.¹⁰ Meantime, the surfactants with Keggin type POM as polar head groups were found by Polarz et al. to be able to self-assembly into micelles and lyotropic phases.¹¹ The surfactants were later observed to self-assembly into a hexagonal lattice in air/water interface.⁹

2.2.2 Molecular bola from organic-inorganic hybrid POMs

Bola-amphiphiles are a type of molecules with a hydrophobic skeleton and two hydrophilic end groups. The synthetic technology rendered us the ability to apply Lindqvist and Dawson type POMs as the hydrophilic end groups (Figure 2.20a and b).^{8,15} Based on the molecular structure and packing parameter analysis, the POM-based amphiphiles, theoretically, are able to self-assembly to form only bi-layer structure with POMs heads staying outsides, e.g. regular vesicles, which means only polar solvents are appropriate for them. In our research, the polarity of solvents was carefully tuned and the bola-amphiphiles were observed to form bilayer vesicle structures with POMs on the outside surface while the organic linkers stayed inside the shell (Figure 2.20b). The sizes of the assemblies depended largely on the polarity of the solvents by showing a

continuous increasing trend when the polarities of the solvents were tuned to be lower,^{8,15} which showed the opposite trend with that of POM-organic hybrid surfactants. Five Bola-amphiphiles with different central linker groups were systematically studied for comparison. The vesicle formation was found to be an entropy-driven process, and the entropy term $T\Delta S$ was much larger compared with conventional surfactants, such as the ionic Gemini surfactants. In addition, the length of the organic linker might show a direct relation to the $T\Delta S$ value, as for a longer linker the entropy gain tended to be more negative because more hydrogen bonds needed to be broken.¹⁴

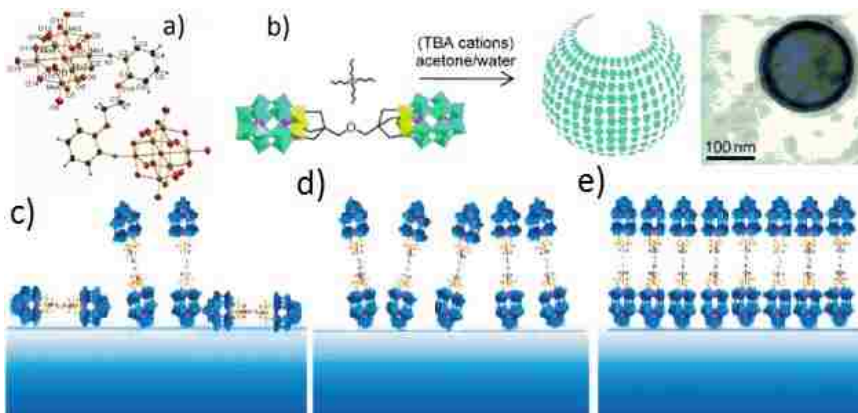


Figure 2.20 a) Molecular structure of hexamolybdate-based bola-amphiphiles. b) Molecular structures of Dawson-type POMs-based bola-amphiphiles and its self-assembly into vesicle structures; Monolayer formation for the dumbbell-shaped hybrid surfactants at the water/vapor interface: c) liquid expansion (LE)/G phase, d) LE phase, and e) liquid condensed (LC) phase. Adapted with permission from ref. [8](#), [14](#), [15](#). Copyright 2010 American Chemical Society and 2009, 2011 Wiley-VCH.

These Bola-amphiphilic hybrids also showed the formation of LB films at the air-water interface with TBA as counter-cations (Figure 2.20c,d,e). The air/water interfacial behaviors, obtained from the π -A isotherms, for hybrids with linear alkyl chain linkers are relatively similar. However, hybrids with bipyridine and ether linkers present different air/water behavior. The liquid expanded and liquid condensed phases are clearly located and connected through a plateau. We believe that the hydrophobicity and composition of the organic linkers play dominant roles.¹⁴

2.2.3 Functionality and application of amphiphilic POM-organic hybrid

Being similar to the common amphiphiles, POM-organic hybrids were observed to be able to reduce the surface tension in the air/water interface. S3 was studied to show a critical micelle

concentration (CMC) of 0.23 mg/mL in the surface tension vs. concentration curve.¹³ Therefore, the hybrids could be treated as novel surfactants. Furthermore, the surfactants with POMs as polar head groups could help form stable emulsions in immiscible water/organic solvents system.^{11,60} Due to the high catalytic activity of POM polar head groups, the hybrid surfactants, actually, can work as emulsion catalysts in biphasic reaction systems.⁶¹ Polarz *et al.* applied the surfactants with Keggin-type POM as polar head groups in the emulsion polymerization reaction environment. The route provided a convenient way to synthesize POM-based nano-scale catalytic particles.²⁰

Another interesting feature is the controllable fluorescent properties of the hybrids' assemblies. Recently, Hill *et al.* synthesized two amphiphilic hybrid POMs with two pyrene groups attached to the central polyoxovanadate, indicated as S5 in Table 3.¹² It was found that S5 could form fluorescent-active vesicular structures in water/DMSO mixed solvents by folding the pyrene groups into the middle hydrophobic layer. By replacing the original bulky TBA (TMA or TEA) counterions with protons, obvious emission peak shifts were noticed in the fluorescence spectra, which were attributed to the formation of pyrene excimers. Since it is well documented that the formation of pyrene excimers largely depends on spatial distance of two pyrene monomers (<0.5 nm), an estimation of the distance of adjacent S5 molecules could be made through monitoring the change of emission pattern. Indeed, the emission spectra of pyrene gradually changed with the solution pH values, and so did the vesicle size and zeta potential value of the vesicles. Moreover, from the 2D NOESY NMR study, for the first time, it was observed that the amphiphilic TBA counterions interact with pyrene groups in the hydrophobic layer of vesicles. This information is important to understand how the hybrid surfactants arrange themselves to form closely packed regions in the supramolecular structures and could be used to explain how the counter-ions perturbs the solvent-phobic layer formation.¹²

2.3 Conclusion and outlook

The past decades has witnessed the significant advancement of the research on the synthesis and application of POMs-based materials. Those large polyoxoanions represent the transitional area between simple ions and colloids, and are perfect models for understanding the solution behavior of polyelectrolytes. Their unique slow self-assembly process and smart recognition behavior uncover the probable mechanism for the self-assembly of bio-macroanions, e.g. virus capsid proteins. Our further researches will extend the studying on the recognition behavior between polyoxoanions with tiny differences. Meanwhile, the previous research is heavily involved with macroanions with high symmetries. Based on the blackberry model, macroanions with anisotropic shapes or anisotropic charge distribution might assemble into non-spherical objects. The anisotropic macroanions are currently undergoing study in our lab.

Meanwhile, the amphiphilic POM-based hybrids are actually surfactants with catalytic active polar head groups. Our previous study suggests that the hybrids able to form stable emulsions in oil/water interface, which support micro-environment for catalytic reactions of the POMs polar heads.

Reference

- (1) Hill, C. L. *Chem. Rev.* **1998**, *98*, 1.
- (2) Long, D.-L.; Burkholder, E.; Cronin, L. *Chem. Soc. Rev.* **2007**, *36*, 105.
- (3) Long, D.-L.; Tsunashima, R.; Cronin, L. *Angew. Chem. Int. Ed.* **2010**, *49*, 1736.
- (4) Liu, T. B. *Langmuir* **2010**, *26*, 9202.
- (5) Zlotnick, A.; Johnson, J. M.; Wingfield, P. W.; Stahl, S. J.; Endres, D. *Biochemistry* **1999**, *38*, 14644.
- (6) Dolbecq, A.; Dumas, E.; Mayer, C. d. R.; Mialane, P. *Chem. Rev.* **2010**, *110*, 6009.

- (7) Li, D.; Yin, P.; Liu, T. *Dalton* **2012**, *41*, 2853.
- (8) Xiao, F.; Misdrahi, M. F.; Zhang, J.; Yin, P.; Hao, J.; Lv, C.; Xiao, Z.; Liu, T.; Wei, Y. *Chem. Eur. J.* **2011**, *17*, 12006.
- (9) Giner-Casares, J. J.; Brezesinski, G.; Möhwald, H.; Landsmann, S.; Polarz, S. *J. Phys. Chem. Lett.* **2012**, *3*, 322.
- (10) Han, Y.; Xiao, Y.; Zhang, Z.; Liu, B.; Zheng, P.; He, S.; Wang, W. *Macromolecules* **2009**, *42*, 6543.
- (11) Landsmann, S.; Lizandara-Pueyo, C.; Polarz, S. *J. Am. Chem. Soc.* **2010**, *132*, 5315.
- (12) Li, D.; Song, J.; Yin, P.; Simotwo, S.; Bassler, A. J.; Aung, Y.; Roberts, J. E.; Hardcastle, K. I.; Hill, C. L.; Liu, T. *J. Am. Chem. Soc.* **2011**, *133*, 14010.
- (13) Yin, P.; Wu, P.; Xiao, Z.; Li, D.; Bitterlich, E.; Zhang, J.; Cheng, P.; Vezenov, D. V.; Liu, T.; Wei, Y. *Angew. Chem. Int. Ed.* **2011**, *50*, 2521.
- (14) Misdrahi, M. F.; Wang, M.; Pradeep, C. P.; Li, F.-Y.; Lydon, C.; Xu, L.; Cronin, L.; Liu, T. *Langmuir* **2011**, *27*, 9193.
- (15) Pradeep, C. P.; Misdrahi, M. F.; Li, F.-Y.; Zhang, J.; Xu, L.; Long, D.-L.; Liu, T.; Cronin, L. *Angew. Chem. Int. Ed.* **2009**, *48*, 8309.
- (16) Zhang, J.; Song, Y.-F.; Cronin, L.; Liu, T. *J. Am. Chem. Soc.* **2008**, *130*, 14408.
- (17) Zhang, J.; Song, Y.-F.; Cronin, L.; Liu, T. *Chem. Eur. J.* **2010**, *16*, 11320.
- (18) Müller, A.; Das, S. K.; Fedin, V. P.; Krickemeyer, E.; Beugholt, C.; Bögge, H.; Schmidtman, M.; Hauptfleisch, B. *ZAAC* **1999**, *625*, 1187.
- (19) Müller, A.; Krickemeyer, E.; Bögge, H.; Schmidtman, M.; Peters, F. *Angew. Chem. Int. Ed.* **1998**, *37*, 3359.
- (20) Müller, A.; Roy, S. *Coord. Chem. Rev.* **2003**, *245*, 153.

- (21) Müller, A.; Sarkar, S.; Shah, S. Q. N.; Bögge, H.; Schmidtman, M.; Sarkar, S.; Kögerler, P.; Hauptfleisch, B.; Trautwein, A. X.; Schünemann, V. *Angew. Chem. Int. Ed.* **1999**, *38*, 3238.
- (22) Botar, B.; Kogerler, P.; Hill, C. L. *Chem. Commun.* **2005**, 3138.
- (23) Howell, R. C.; Perez, F. G.; Jain, S.; DeW. Horrocks, J. W.; Rheingold, A. L.; Francesconi, L. C. *Angew. Chem. Int. Ed.* **2001**, *113*, 4155.
- (24) Mal, S. S.; Kortz, U. *Angew. Chem. Int. Ed.* **2005**, *44*, 3777.
- (25) Todea, A. M.; Merca, A.; Bögge, H.; van Slageren, J.; Dressel, M.; Engelhardt, L.; Luban, M.; Glaser, T.; Henry, M.; Müller, A. *Angew. Chem. Int. Ed.* **2007**, *46*, 6106.
- (26) Muller, A.; Diemann, E.; Kuhlmann, C.; Eimer, W.; Serain, C.; Tak, T.; Knochel, A.; Pranzas, P. K. *Chem. Commun.* **2001**, 1928.
- (27) Liu, T.; Diemann, E.; Li, H.; Dress, A. W. M.; Muller, A. *Nature* **2003**, *426*, 59.
- (28) Kistler, M. L.; Bhatt, A.; Liu, G.; Casa, D.; Liu, T. *J. Am. Chem. Soc.* **2007**, *129*, 6453.
- (29) Verhoeff, A. A.; Kistler, M. L.; Bhatt, A.; Pigga, J.; Groenewold, J.; Klokkenburg, M.; Veen, S.; Roy, S.; Liu, T.; Kegel, W. K. *Phys. Rev. Lett.* **2007**, *99*, 066104.
- (30) Liu, T. B.; Imber, B.; Diemann, E.; Liu, G.; Cokleski, K.; Li, H. L.; Chen, Z. Q.; Muller, A. *J. Am. Chem. Soc.* **2006**, *128*, 15914.
- (31) Stevens, M. J. *Biophys. J.* **2001**, *80*, 130.
- (32) Sogami, I.; Ise, N. *J. Chem. Phys.* **1984**, *81*, 6320.
- (33) Chu, B.; Hsiao, B. S. *Chem. Rev.* **2001**, *101*, 1727.
- (34) Pigga, J. M.; Kistler, M. L.; Shew, C. Y.; Antonio, M. R.; Liu, T. B. *Angew. Chem. Int. Ed.* **2009**, *48*, 6538.
- (35) Pigga, J. M.; Teprovich, J. A.; Flowers, R. A.; Antonio, M. R.; Liu, T. B. *Langmuir* **2010**, *26*, 9449.

- (36) Kistler, M. L.; Liu, T. B.; Gouzerh, P.; Todea, A. M.; Muller, A. *Dalton* **2009**, 5094.
- (37) Oleinikova, A.; Weingärtner, H.; Chaplin, M.; Diemann, E.; Bögge, H.; Müller, A. *ChemPhysChem* **2007**, *8*, 646.
- (38) Pigga, J. M.; Liu, T. *Inorg. Chim. Acta.* **2010**, *363*, 4230.
- (39) Todea, A. M.; Merca, A.; Bögge, H.; Glaser, T.; Pigga, J. M.; Langston, M. L. K.; Liu, T.; Prozorov, R.; Luban, M.; Schröder, C.; Casey, W. H.; Müller, A. *Angew. Chem. Int. Ed.* **2010**, *49*, 514.
- (40) Kistler, M. L.; Patel, K. G.; Liu, T. B. *Langmuir* **2009**, *25*, 7328.
- (41) Mishra, P. P.; Jing, J.; Francesconi, L. C.; Liu, T. B. *Langmuir* **2008**, *24*, 9308.
- (42) Yin, P.; Li, D.; Liu, T. *Isr. J. Chem.* **2011**, *51*, 191.
- (43) Liu, G.; Liu, T. B.; Mal, S. S.; Kortz, U. *J. Am. Chem. Soc.* **2006**, *128*, 10103.
- (44) Ribot, F.; Escax, V.; Martins, J. C.; Biesemans, M.; Ghys, L.; Verbruggen, I.; Willem, R. *Chem. Eur. J.* **2004**, *10*, 1747.
- (45) Van Lokeren, L.; Willem, R.; van der Beek, D.; Davidson, P.; Morris, G. A.; Ribot, F. *J. Phys. Chem. C* **2010**, *114*, 16087.
- (46) Liu, G.; Cai, Y. G.; Liu, T. B. *J. Am. Chem. Soc.* **2004**, *126*, 16690.
- (47) Liu, G.; Kistler, M. L.; Li, T.; Bhatt, A.; Liu, T. B. *J. Cluster Sci.* **2006**, *17*, 427.
- (48) Liu, T. B. *J. Am. Chem. Soc.* **2002**, *124*, 10942.
- (49) Liu, T. B. *J. Am. Chem. Soc.* **2003**, *125*, 312.
- (50) Liu, G.; Liu, T. *Langmuir* **2005**, *21*, 2713.
- (51) Zhang, J.; Li, D.; Liu, G.; Glover, K. J.; Liu, T. B. *J. Am. Chem. Soc.* **2009**, *131*, 15152.
- (52) Casini, G. L.; Graham, D.; Heine, D.; Garcea, R. L.; Wu, D. T. *Virology* **2004**, 325, 320.

- (53) Mishra, P. P.; Pigga, J.; Liu, T. *J. Am. Chem. Soc.* **2008**, *130*, 1548.
- (54) Liu, T.; Langston, M. L. K.; Li, D.; Pigga, J. M.; Pichon, C.; Todea, A. M.; Müller, A. *Science* **2011**, *331*, 1590.
- (55) Leroy, F.; Miro, P.; Poblet, J. M.; Bo, C.; Avalos, J. B. *J. Phys. Chem. B* **2008**, *112*, 8591.
- (56) Lopez, X.; Nieto-Draghi, C.; Bo, C.; Avalos, J. B.; Poblet, J. M. *J. Phys. Chem. A* **2005**, *109*, 1216.
- (57) Chaumont, A.; Wipff, G. *Phys. Chem. Chem. Phys.* **2008**, *10*, 6940.
- (58) Chaumont, A.; Wipff, G. *Comptes Rendus Chimie* **2012**, *15*, 107.
- (59) Mani, E.; Groenewold, J.; Kegel, W. K. *Inorg. Chim. Acta.* **2010**, *363*, 4295.
- (60) Yin, P.; Pradeep, C. P.; Zhang, B.; Li, F.-Y.; Lydon, C.; Rosnes, M. H.; Li, D.; Bitterlich, E.; Xu, L.; Cronin, L.; Liu, T. *Chem. Eur. J.* **2012**, *18*, 8157.
- (61) Yin, P.; Wang, J.; Xiao, Z.; Wu, P.; Wei, Y.; Liu, T. *Chem. Eur. J.* **2012**, *18*, DOI: 10.1002/chem.201201551.

Chapter 3: Self-Recognition of Structurally Similar Rod-shaped Macroions during Their Assembly Process

3.1 Introduction

Biomolecules rarely function in isolation; hence a thorough understanding of biological process is highly dependent upon an examination of assemblies of biomolecules and the interaction driving the assembly process.¹⁻³ When two different assemblies are in the same solution they may coexist and remain self-sorted or they may hybridize.^{3,4} Self-recognition and self-assembly of biomolecules contribute to the formation of biomolecules complexes with uniqueness and specific functionality, which are the chemical basis of diverse phenomena such as cell signaling, the immune response, and gene regulatory interaction.⁵⁻⁸

Non-covalent interactions, e.g. hydrogen bonding⁹, π - π stacking¹⁰, coordination¹¹, static charge interaction¹², and solvophobic interaction¹³, are responsible for the self-assembly and self-recognition of bio-macromolecules.^{11,14-16} Especially, counterion-mediated like-charge attraction and water-bridged hydrogen bonding were found to play significant roles in the folding, assembly, and recognition behavior of proteins, RNA, and DNA.^{17,18} Meantime, polyoxometalates (POMs) can be considered as ‘inorganic polyelectrolyte’ composed of negatively-charged metal oxide polyhedra with well-defined molecular structures, uniform shapes, and negligible intramolecular charge interaction, which are ideal models for studying the intermolecular interaction of polyelectrolytes, e.g. the interaction between DNA and protein and the formation of virus capsids.¹⁹⁻²¹ Our previous research helps us understand and control the counterion-mediated attraction between macroions through the study of the self-assembly process of the macroions into hollow ‘blackberry’-type structures in their dilute solutions.²⁰⁻²² Our recent study on an assembly process in a homogeneous dilute aqueous solution of two nano-scaled,

spherical polyprotic metal oxide-based macroions demonstrates the self-recognition among these two macroions by forming homogeneous ‘blackberries’-type structures.²³ The role of charge density difference in such two macroions is believed to be the dominant factor in the self-recognition process.²³ However, the original study was based on an obvious difference while we hope to push the limit by studying highly similar mixtures, which might help explain the general phenomenon in biological systems. Herein, we report the study of the solution behavior of a mixture of two highly charged molecular rods with almost identical structures and charge densities except the difference of their encapsulated central metal atoms. Time-resolved light scattering, TEM, and energy dispersive X-ray spectroscopy (EDS) were utilized to analyze the self-recognition behavior among the two molecular rods. Density function theory (DFT) calculation and kinetic monitoring of the disassembly process of the formed ‘blackberry’ structures in the individual solutions of the two molecular rods and their mixture solution, respectively, were combined to uncover the mechanism for their self-recognition behavior.

3.2 Experimental Section

General. TBA*OH solution (40%, wt), EDTA, acetonitrile, anhydrous ZnCl₂, d₃-acetonitrile and d₆-acetone were purchased from Sigma-Aldrich and used without further purification. Filters were purchase from Millipore for solution preparation. G300 Copper grids were purchased from SPI. A commercial Brookhaven Instrument LLS spectrometer equipped with a solid-state laser operating at 532 nm was used for measurement for both SLS and DLS. NMR spectra were recorded on a Bruker 500 spectrometer and were calibrated to the residual proton resonance of the solvent. The TEM images were taken on a JEOL JEM-2000 electron microscope operated at 200 kV with EDS attachment (Oxford). Samples for the TEM analysis were prepared by dropping a small volume of the solution sample onto a carbon film on copper grid.

Synthesis of nanorods. The synthesis was done according to the previous procedure.^{24,25} The samples were put in air to get rid of the solvent molecular after the crystalline compounds were obtained.

Synthesis of TBA*EDTA. 5 mL TBA*OH (40%,wt) solution was mixed with 0.274g EDTA. The mixture was kept sonicating until EDTA was fully dissolved. The obtained solution was kept at 50°C with reduced pressure for one week. Colorless ionic liquid was obtained.

Static light scattering. A commercial Brookhaven Instrument LLS spectrometer equipped with a solid-state laser operating at 532 nm was used for measurement of both SLS and DLS. SLS experiments were performed at scattering angles (θ) between 20 and 100°, at 2° intervals. However, due to the large fluctuations in scattered intensities at low scattering angles, we removed the data from 20-40° in the final analysis. Derived from Rayleigh-Gans-Debye equation²⁶, partial Zimm plot was used to analyze the SLS data to obtain the radius of gyration (R_g). The partial Zimm plot stems from the following approximate formula: $1/I = C(1+R_g^2*q^2/3)$. Here R_g is determined from the slope and the intercept of a plot of $1/I$ vs. q^2 .

Dynamic light scattering. DLS measures the intensity–intensity time correlation function by means of a BI-9000AT multi-channel digital correlator. The field correlation function $|g^{(1)}(\tau)|$ was analyzed by the constrained regularized CONTIN method²⁷ to yield information on the distribution of the characteristic linewidth Γ from $|g^{(1)}(\tau)| = \int G(\Gamma) \exp(-\Gamma\tau) d\Gamma$. The normalized distribution function of the characteristic linewidth, $G(\Gamma)$, so obtained, can be used to determine an average apparent translational diffusion coefficient, $D_{app} = \Gamma/q^2$. The hydrodynamic radius R_h is related to D via the Stokes–Einstein equation: $R_h = kT/(6\pi\eta D)$ where k is the Boltzmann constant and η the viscosity of the solvent at temperature T . From DLS measurements, we can obtain the particle-size distribution in solution from a plot of $\Gamma G(\Gamma)$ versus R_h . The R_h of the particles is obtained by extrapolating $R_{h,app}$ to zero scattering angle.

TEM and EDS. The TEM images were taken on a JEOL JEM-2000 electron microscope operated at 200 kV with EDS attachment (Oxford). Samples for the TEM analysis were prepared by dropping a small volume of the solution sample onto a carbon film on copper grid.

1D NMR and 2D DOSY. All the NMR spectra were recorded on Bruker Avance 500 spectrometer equipped with a BBO probe at 25 °C. 2.0 mg compound **1** and 1.1 mg TBA*I were dissolved in 1 mL d₆-acetone, respectively for ¹H-NMR experiments.

DOSY was performed on a Bruker 500 MHz spectrometer with the magnetic field gradient (g) varying from 0 to 32 G/cm in 16 ~ 32 steps. The length of the gradient (d) was from 6000 ms to 8000 ms, and the time interval between two pulsed gradients (D) was from 0.1 s to 0.15 s. All spectra were taken at room temperature. After the data collection, FIDs were processed and analyzed with the NMR software TopSpin 2.0 provided by Bruker. Both T1/T2 relaxation and CONTIN methods were used to fit the raw data. The observed proton signal I in a standard DOSY spectrum is expressed through equation 1:

$$I = I_0 \exp \left[-(2\pi\gamma\delta)^2 \left(\Delta - \frac{\delta}{3} \right) D g^2 \right]$$

Equation (3-1)

where I₀ is the reference intensity, γ is the gyromagnetic ratio of the proton. If only one diffusive component exists in the solution, a straight line will occur in a plot of ln(I/I₀) versus g², and the apparent diffusion coefficient (D) can be calculated from the slope using linear regression analysis.

SAXS experimental section. The SAXS experiments were performed at 12-ID-B station with X-ray energy of 12 KeV at the Advanced Photon Source of the Argonne National Laboratory. The sample to detector distance was about 2 m. A 2D CCD detector was used to acquire images with typical exposure times in the range of 1.0 s.

X-ray absorption near edge structure (XANES) and extended x-ray absorption fine structure (EXAFS). The Zn K-edge (9,659 eV) EXAFS and XANES measurements were carried

out at the MRCAT 10-ID beam line at the Advanced Photon Source, Argonne National Laboratory in order to study the local environment around the Zn atoms in the NPs.²⁸ EXAFS and XANES measurements of the samples were done in fluorescence mode with the ion chamber in Stern Heald geometry and the samples were loaded in plastic cuvettes for the measurements. Zn foil EXAFS was measured with help of the reference ion chamber for every scan taken on the samples for the purpose of energy calibration. EXAFS measurements were done in transmission geometry on ZnCl₂ solution which was used as standards. Data was collected from -250 eV below Zn edge to 1,000 eV above Zn edge at step size of 0.35 eV and measurement time 0.1 sec per point. Several scans were taken on each sample and merged for better statistics.

The spot size of the incident x-ray beam on the sample was 500 micron by 500 micron. Data collected was processed using Athena software²⁹ by extracting the EXAFS oscillations $\chi(k)$ as a function of photoelectron wave number k following standard procedures. The theoretical paths were generated using FEFF6³⁰ and the models were done in the conventional way using the fitting program called Artemis³¹. Fitting parameters were obtained by modeling the EXAFS data of each sample in R-space until a satisfactory fit describing the system was obtained. Data sets were simultaneously fitted in R-space with k -weights of 1, 2 and 3.

3.3 Self-recognition of structurally identical rod-shaped macroions with different central metal atoms during their assembly process

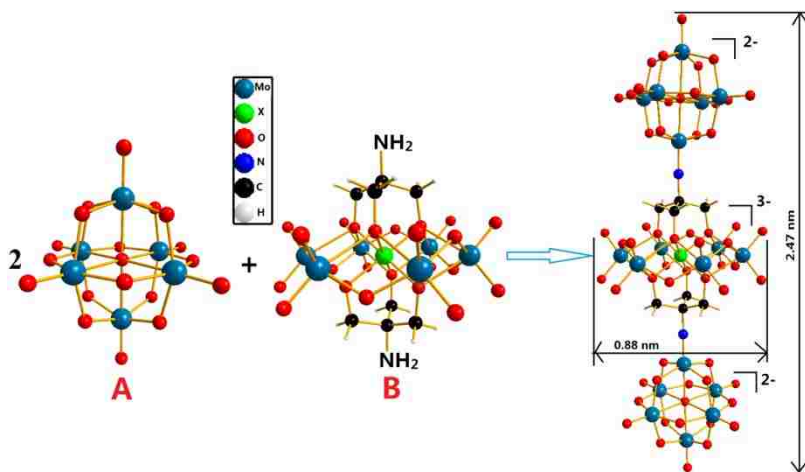


Figure 3.1 Synthetic procedure of the two molecular rods and the ball-stick representation of molecular structures of the building blocks and the molecular rods. X, center heteroatom; A, hexamolybdate; B, the ring-shaped Anderson-type molecule.

3.3.1 Macroionic properties of the molecular rods

Two molecular rods, $((C_4H_9)_4N)_7[Mo_6O_{18}NC(OCH_2)_3XMo_6O_{18}(OCH_2)_3CNMo_6O_{18}]$ ($X = Mn^{III}(1)$, $Fe^{III}(2)$), were synthesized and fully characterized in previous paper.²⁴ These two compounds were synthesized by covalently linking two super-octahedron-shaped hexamolybdate (A) onto the two sides of a ring-shaped Anderson-type POM (B) (Figure 3.1). Basically, the two molecular rods are almost identical except that the center heteroatom of the ring-like molecule is different: Mn^{III} for rod 1 and Fe^{III} for rod 2. Both molecular rods are highly charged (-7) with tetrabutylammonium (TBA) as counterion, and hydrophilic with surface composed of molybdenum oxide. Due to the non-conjugative nature of the linkage between A and B units, they retain their original charges as -2 and -3, respectively (Figure 3.1). Molecular rods 1 and 2 have identical lengths and diameters being *ca.* 2.47 nm and 0.88 nm, respectively. The actual structures of the molecular rods in solution (acetonitrile) have been investigated through solution small angle X-ray scattering (SAXS) with a spatial resolution of 2.9 Å.³² The two molecular rods show identical SAXS curves (Figure 3.2a and Figure 3.3), suggesting they have identical molecular

structures in solution state. The calculated SAXS profile for the rod-shape molecular model fits well with the experimental data of **1**, indicating that the rod-shape survives while the crystals of **1** dissolve in acetonitrile (Figure 3.2a).³³ Radius of gyration (R_g) of the molecule is 0.73 nm, calculated from small angle region using Guinier equation. Further exploration of the scattering data with program GNOM generates pair distance distribution functions (PDDF) in real space, $p(r)$.³⁴ The PDDF exhibit the feature of rod-shaped molecular triads, where the first peak centered at *ca.* 0.25 nm describes the intra-subunit (A or B) atom-pair distances, while the second peak at *ca.* 0.90 nm and the third peak at *ca.* 1.70 nm represent the separations of A to B and A to A, respectively (Figure 3.2b and 2c). Time-resolved solution x-ray scattering studies and scattering measurements on aged samples suggest that the molecular rods are quite stable at least within two months. As a general feature for the solution physical chemistry of macroions, the ion-pairing of the molecular rods with its counterions, TBA, were investigated by ¹H-NMR and 2D diffusion ordered ¹H-NMR spectroscopy (DOSY).³⁵ The four proton peaks of TBA in *d*₆-acetone solution of **1** were much broader than that in *d*₆-acetone solution of TBA*I (tetrabutylammonium iodide), suggesting possible strong association of TBAs with large structures in **1**'s acetone solution (Figure 3.4). DOSY results indicated that TBAs in the solution of **1** diffuse much slower (diffusion coefficient (D) = 2.8×10^{-9} m²/s) than the 'free' TBAs in TBA*I (tetrabutylammonium iodide) solution ($D = 4.4 \times 10^{-9}$ m²/s), suggesting strong association of TBAs with the molecular rods. The charge density of the molecular rods is $-1.06 e \cdot \text{nm}^{-2}$, which is a little higher than the range that might be appropriate for the counterion-mediated static charge-regulated self-assembly.

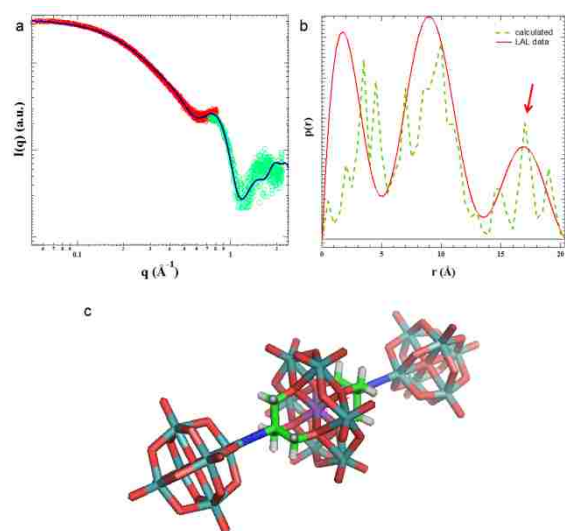


Figure 3.2 a) Superimposition of experimental solution wide angle x-ray scattering curve of **1** in its acetonitrile (2 mg/mL) and simulated scattering curve (in blue) using program SolX with the molecular model (c). b) PDDF of **1** in its acetonitrile solution (red curve) obtained using program GNOM and calculated PDDF (green curve) from the molecular model (c) using SolX. The broadening features in the PDDF obtained from GNOM could arise from the configurationally ensemble in solution due to the free rotation of the Mo-N-C bond. c) The build molecular model for fitting.

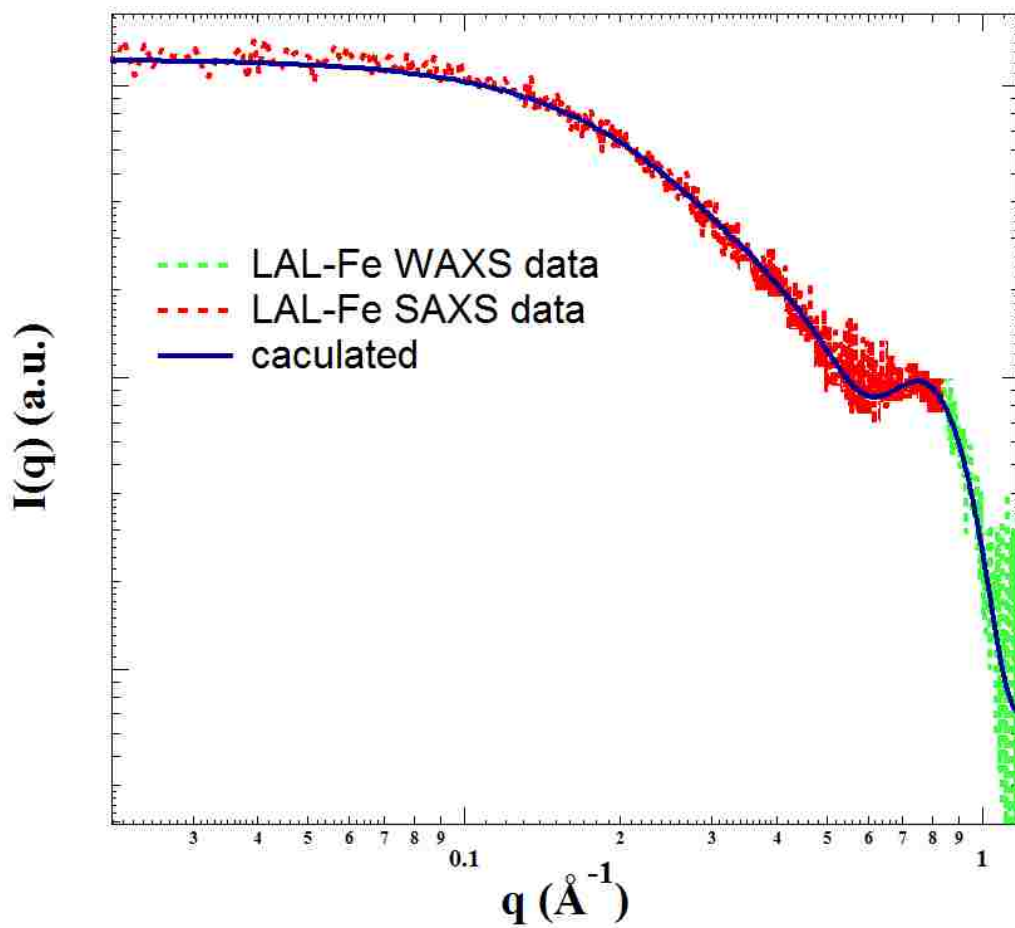


Figure 3.3 SAXS profile of compound 2.

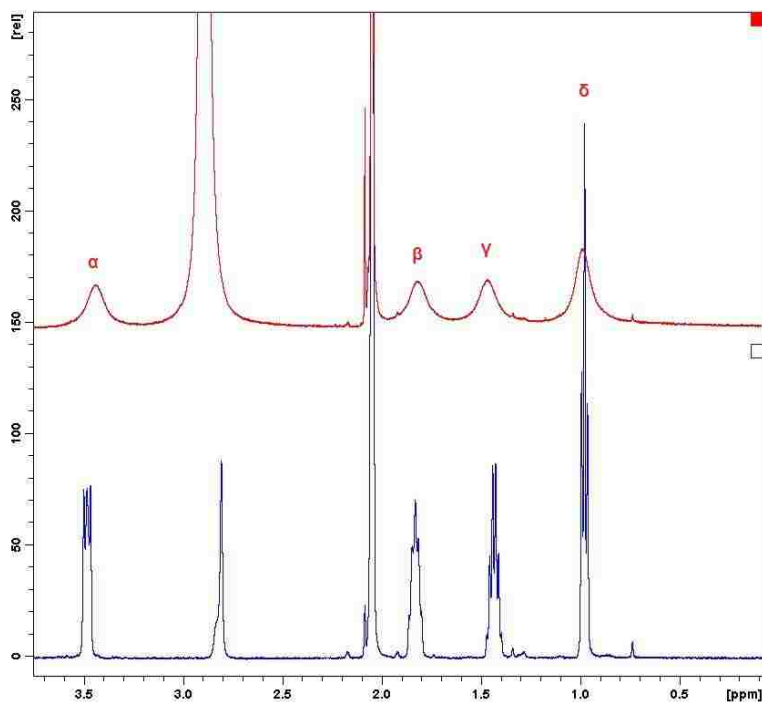


Figure 3.4 $^1\text{H-NMR}$ results of TBA*1 and TBA*I.

3.3.2 Self-assembly of the molecular rods into blackberries

The two rod-like molecules are quite soluble in acetonitrile, however are not able to self-assemble into larger supramolecular structures in dilute solution with the bulky and hydrophobic counterions, TBA, due to their too high surface charge densities. The addition of ZnCl_2 to their acetonitrile solution of the individual molecular rods, respectively, could trigger the self-assembly process since Zn^{2+} has higher priority to interact with rod-like macroanions. Time-resolved static light scattering results (SLS) indicated that the scattered intensities at 90° scattering angle for both macroionic solutions at room temperature showed a linear increment as time and reached equilibrium at *ca.* 37 days (Figure 3.5a). Dynamic light scattering (DLS) results indicated that the hydrodynamic radii of the assemblies in the individual solution of two molecular rods did not change in the whole self-assembly process (Figure 3.6 and Figure 3.7 in supporting information). The combination of the DLS and SLS suggested that it was the number of the assemblies, not size of the assemblies that increased during the self-assembly process. A typical CONTIN analysis from DLS study of individual solutions of the compounds indicated that R_h of large assemblies

showed no angular dependence with narrow distribution and average values as 80 ± 4 and 27 ± 2 nm (Figure 3.5b), respectively, for the solutions of **1** and **2**. SLS study analyzed by Zimm plot indicated that the assemblies had average R_g of 76 ± 4 and 30 ± 2 nm, respectively. The ratio of $R_h/R_g \sim 1.0$ suggest a hollow spherical structure for the assemblies of **1** and **2**, respectively, which is also confirmed by TEM results (Figure 3.5c and d). The counterion (Zn^{2+})-mediated attraction among the highly charged molecular rods is responsible for the formation of the assemblies (blackberries), which shows some obvious similarities with natural biomacromolecules, such as viral capsid proteins.^{36,37} Both of the blackberry and spherical viral capsid are nanoscaled single-layer hollow shells, which are quite different from the vesicles of lipid molecules (Figure 3.5e). Moreover, the two assemblies demonstrate similar kinetic features: the rate-limiting oligomers formation followed a rapid formation of the large assemblies from the oligomers. The formed blackberry-type structures of **1** and **2**, respectively, are of obviously different sizes although the two macroanions are almost identical in both shape and charge density. It is believed that the encapsulated central metal ions lead to the distortion of Anderson-type POM framework and therefore affect the charge distribution of unit B. The different charge distributions of the two macroions play a vital role in the bind strength of added counterion (Zn^{2+}) onto the surface of the macroions, which finally determines the size of the assemblies. More details on the mechanism are introduced in the next section.

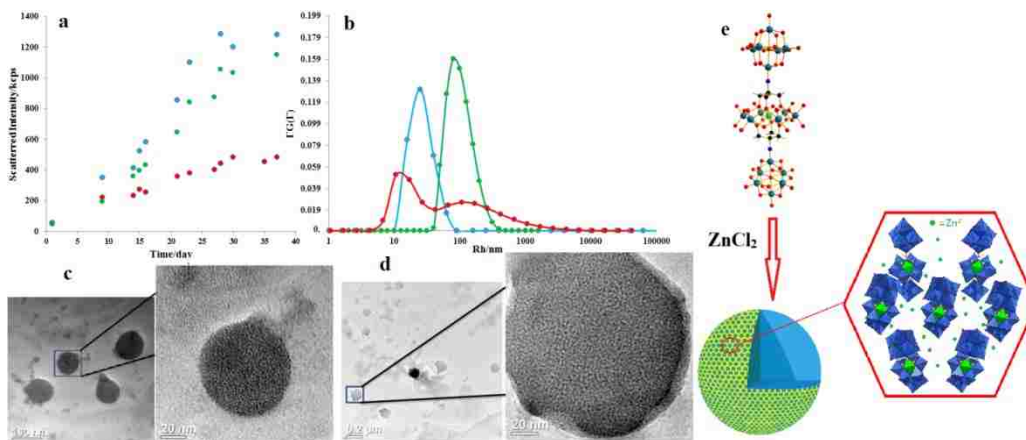


Figure 3.5 a) Time-resolved SLS results of the solutions of 1 (green dot), 2 (blue dot), and their mixture (red dot) at scattering angle as 90° . b) CONTIN analysis results of the solutions of 1 (green dot), 2 (blue dot), and their mixture (red dot). c) TEM images of assemblies in the solution of 2. d) TEM images of assemblies in the solution of 1. e) Model for the self-assembly process of molecular rods into blackberry structures.

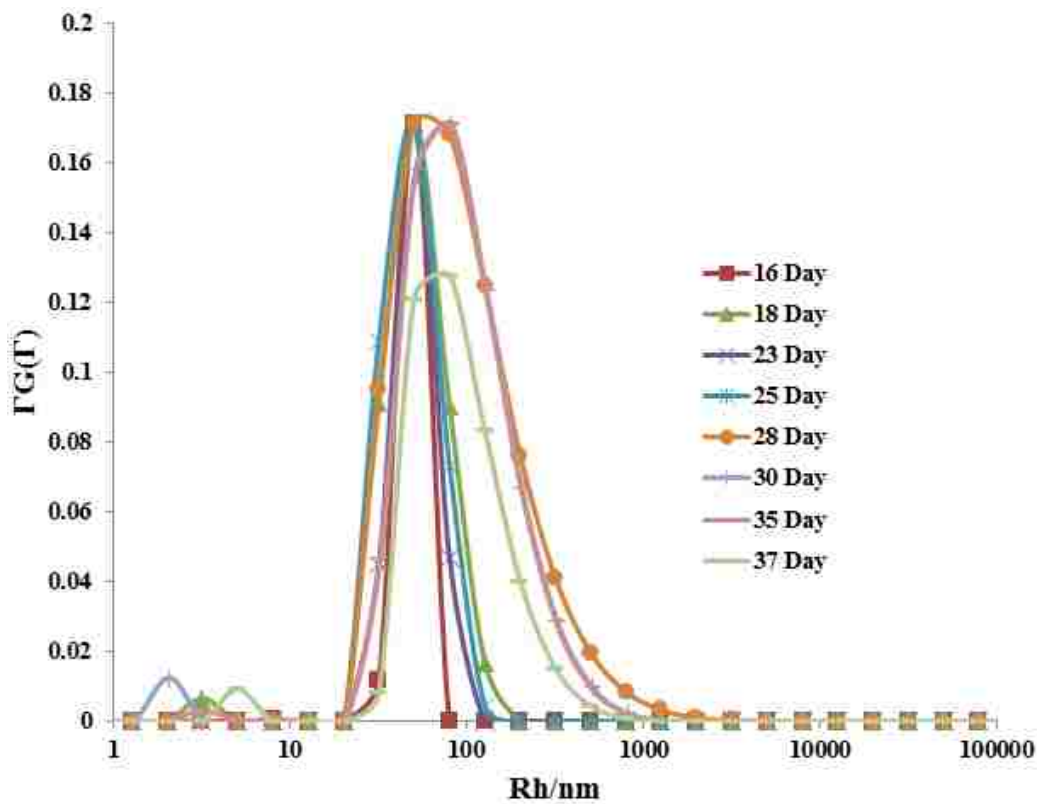


Figure 3.6 Time-resolved DLS results of 1's solution with $ZnCl_2$.

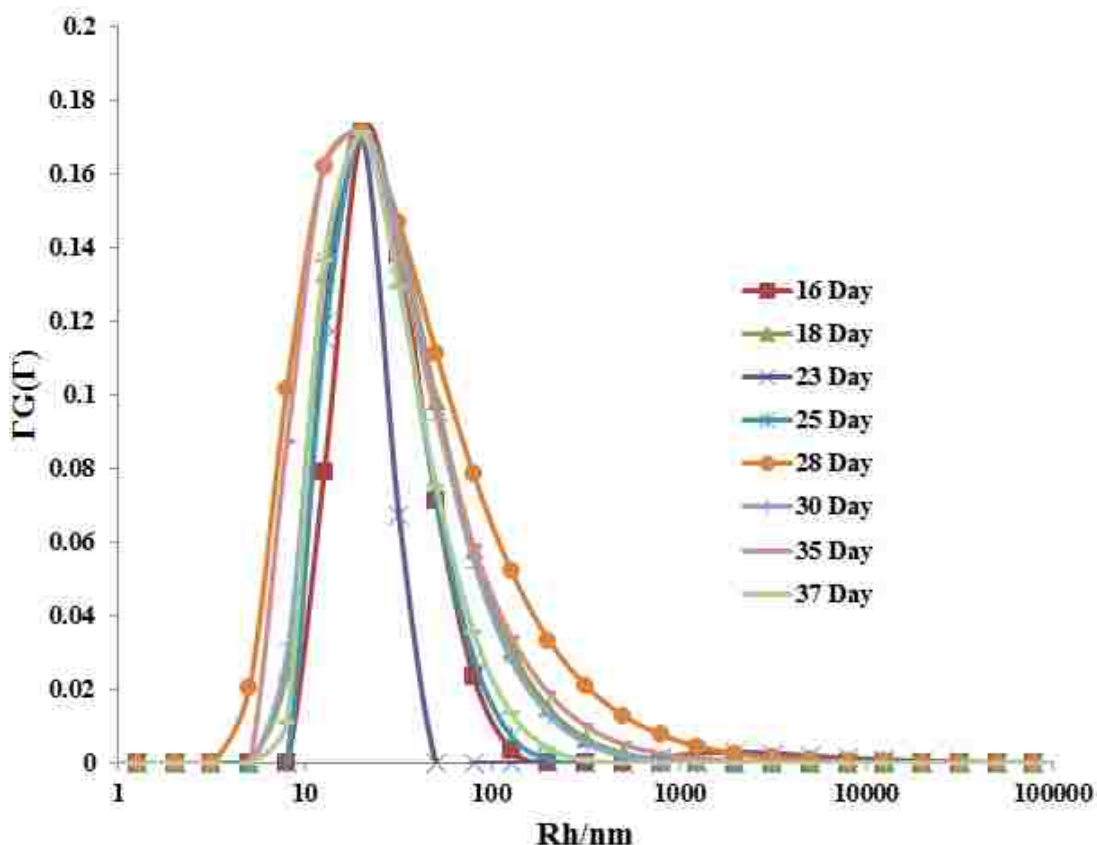


Figure 3.7 Time-resolved DLS results of 2's solution with $ZnCl_2$.

3.3.3 Self-recognition behavior of the two molecular rods

Impressively, the two inorganic molecular rods show self-recognition behavior by self-assembling into two types of individual blackberry-type structures instead of mixed ones in their mixed solution. The macroions' shapes, surface composition, charges, and counterions are expected to play vital roles in their self-assembly process based on our previous research. However, for the two molecular rods, all the above factors look identical, making the possible self-recognition challenging and intriguing. It thus provides a good opportunity to uncover the mechanism for this phenomenon. The mixed solution of **1** and **2** (1:1 mass ratio, concentration 0.25 mg/mL each) was prepared for studying their self-recognition behavior. The resulting two separated modes in the CONTIN analysis of DLS study of the mixed solution indicated the presence of two differently sized large species (Figure 3.5b). The two peaks, within the error limit of the CONTIN analysis, correspond to those assemblies from the individual solutions containing

either molecular rod **1** or **2** with the same concentration and added ZnCl_2 amount, which indicated that the molecular rods might recognize each other and assemble into their individual homogeneous blackberry structures (Figure 3.5b).

Additionally, time-resolved SLS results indicated that two molecular rods self-assembled at almost the same speed in their individual solution with the same concentration (0.5 mg/mL, Figure 3.5a), which rules out the possibility that the self-recognition is primarily due to kinetic effects (i.e., that one type of molecular rods assembles faster). Meantime, the mixture solution of **1** and **2** (1:1 mass ratio, concentration 0.25 mg/mL each) showed a much slower self-assembly process than the individual solution of **1** and **2**, respectively (Figure 3.5a), which confirms that the molecular rods favor to be self-sorted in the mixture solution.

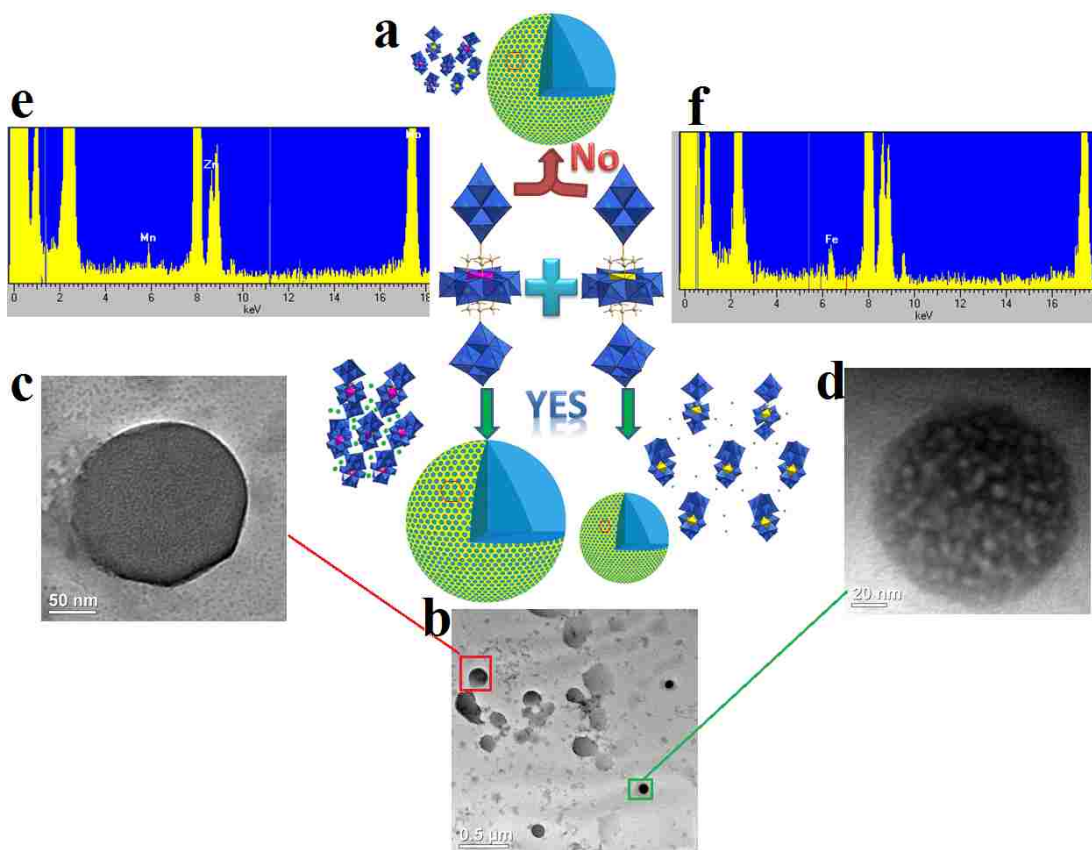
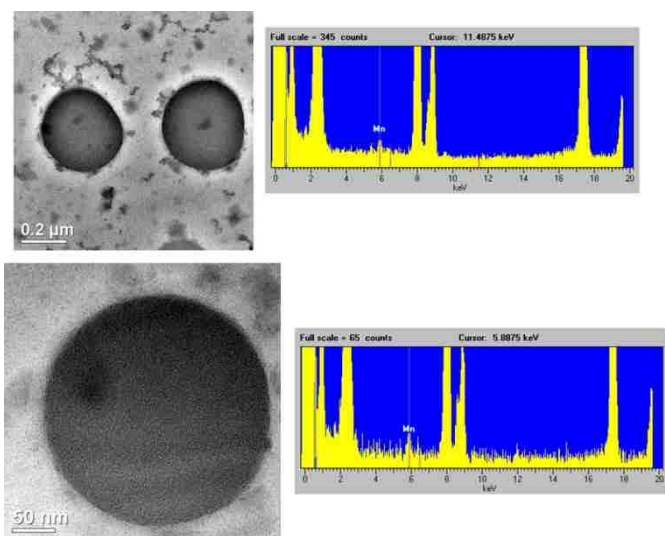
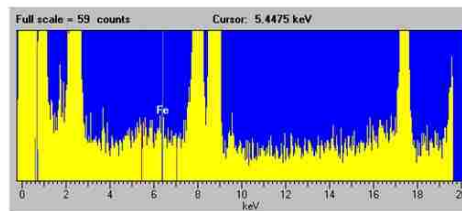
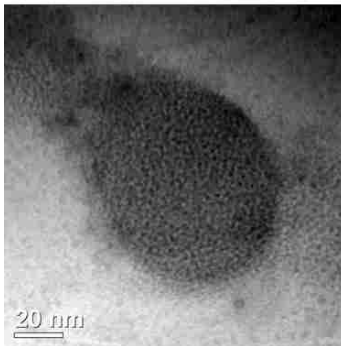
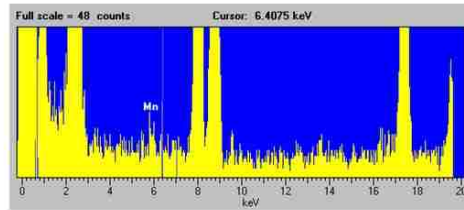
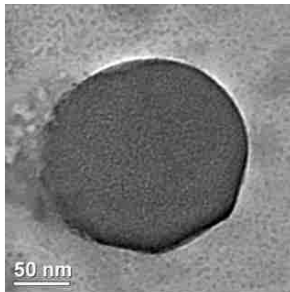
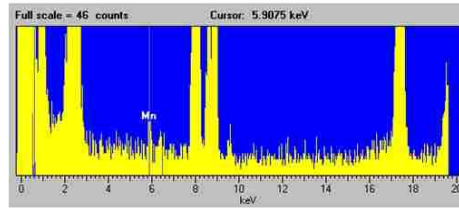
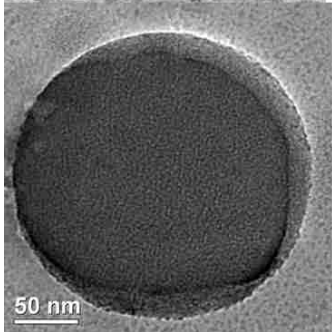
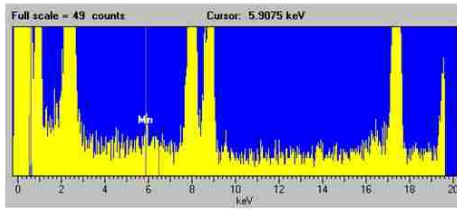
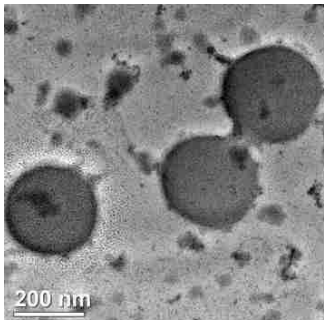
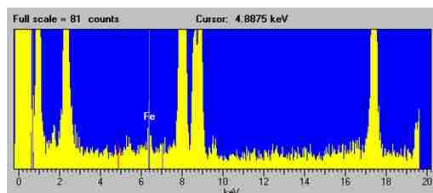
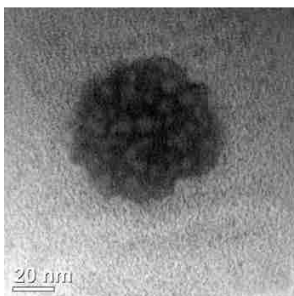
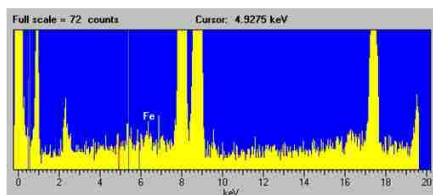
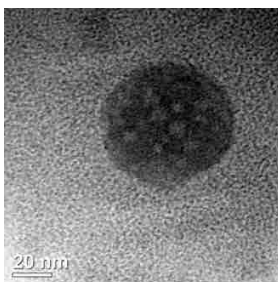
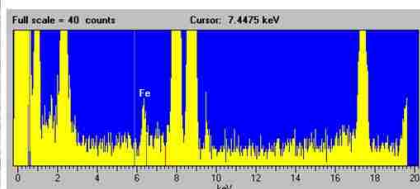
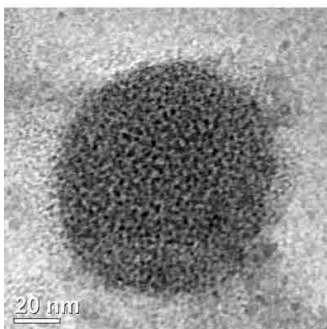
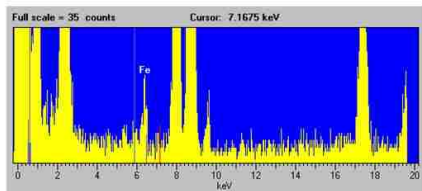
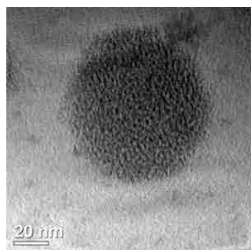


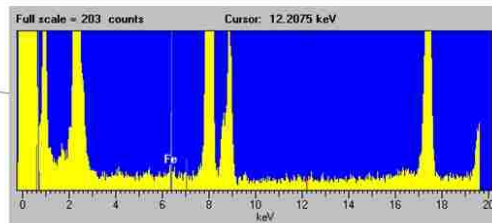
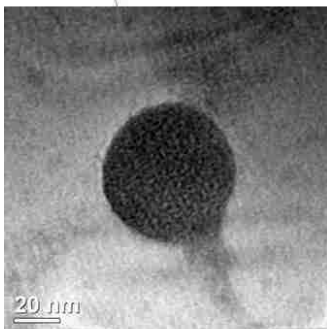
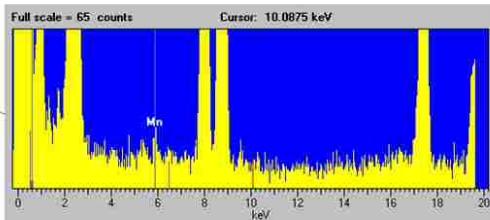
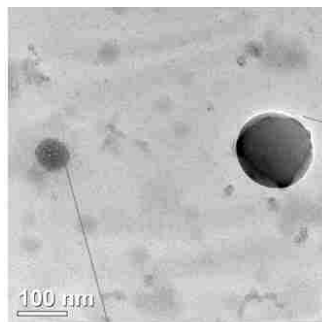
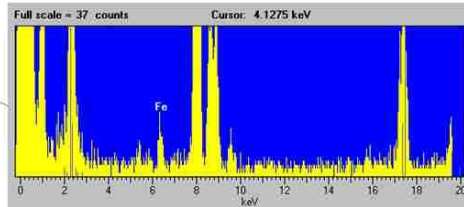
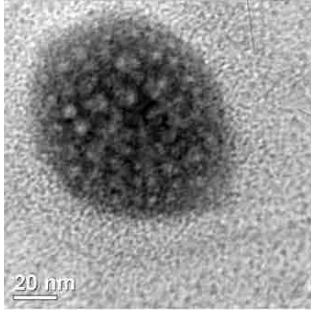
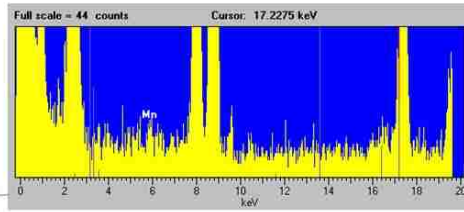
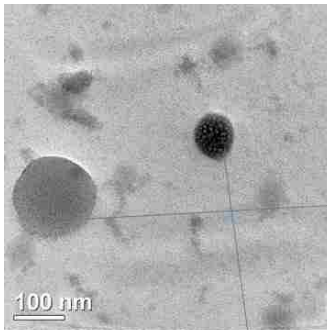
Figure 3.8 a) Model of the self-recognition during the self-assembly of two molecular rods in the mixture solution. b) TEM images of the assemblies in the mixture solutions (red rectangle, large assembly; green rectangle, small assembly). c) Zoom in image of the large assembly. d) Zoom in image of the small assembly. e) EDS results of the large assembly. f) EDS results of the small assembly.

The critical evidence for the self-recognition comes from the combination of TEM and EDS technology. TEM images of the assemblies in the mixed solution indicated that vesicles with two different sizes co-existed (Figure 3.8b, c, d), whose sizes were close to that of corresponding homogeneous blackberries assembled from the molecular rods, respectively, confirming the existence of two species in DLS results of the mixture solution. Moreover, EDS results of the individual vesicles suggested that the dominant metal elements for larger vesicles (size *ca.* 160 nm) and smaller vesicles (size *ca.* 60 nm) are Mn and Fe, respectively, besides Mo and Zn (Figure 3.8e, f), which confirmed that molecule **1** and **2** assembled into the larger and smaller vesicles, respectively. To rule out the possibility that the EDS results are random, another 18 vesicles with different sizes were selected for EDS analysis, which were consistent with the previous results and supportive to the model of homogeneous blackberry structures (Figure 3.9).









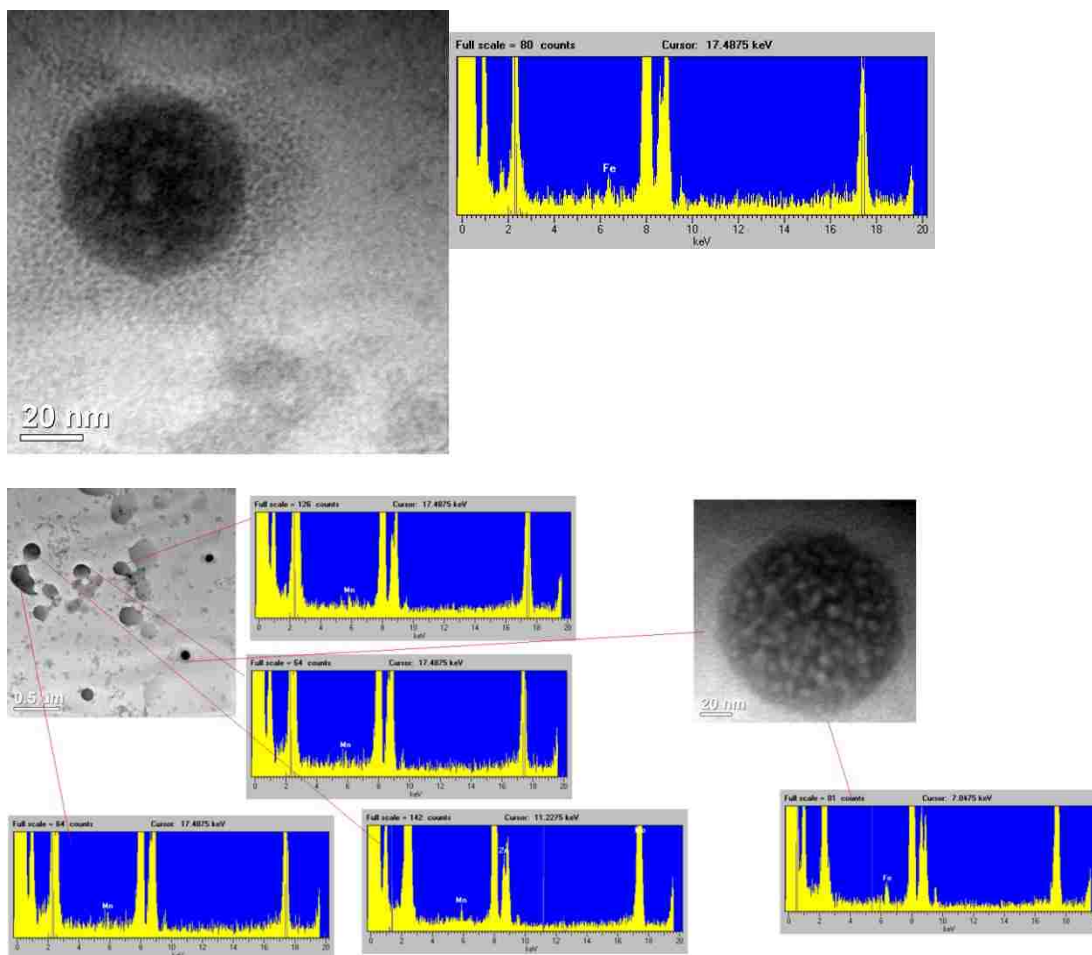


Figure 3.9 TEM images and EDS results of the assemblies in the mixture solution.

3.3.4 The mechanisms of self-recognition

Our previous study on the self-assembly of macroions suggest that the formation of oligomers at the beginning of the assembly process is the rate-limiting step with high activation energy barrier, which enables the preference to the formation of self-sorted oligomers in the mixture of **1** and **2**.²³ In other words, the formation process is slow compared to the self-assembly of amphiphiles; however, it provides the situation for recognition among macro-ions with minor differences. The formation energy for homo-oligomers is slightly lower than the hybrid oligomers, however enough to lead to the discrimination of homogeneous blackberry structures over heterogeneous ones. Additionally, the heteroatoms encapsulated inside the inorganic molecular rods are the only difference between the two molecules and supposed to direct the self-recognition behavior

(Figure 3.1 and Figure 3.8). DFT calculation indicates that the central atom of molecule **1** (heteroatom, Mn) is more positively charged than that of molecule **2** (Fe) and the perimeter of the planar molecular unit (B) of **1** is more negatively charged than that of **2** although their net charges are identical for the two macroanions. Owing to the difference in their charge distribution, **1** is more negative on its surface and able to interact with counterion much stronger to strengthen the counterion-mediated attraction, which consequently results in the smaller curvature of the assemblies of **1**, e.g. larger sizes for blackberry structures (Figure 3.8).

Due to the anhydrous solution environment, zinc chloride favors to bind onto the oxo ligand-enriched surface of the molecular rods, which enables the formation of blackberries of compound **1** and **2** and projects their differences of charge distribution into the size differences of their assemblies. Different from the solvation model of ions in aqueous solution, zinc chloride prefer to direct bind/coordination onto the surface oxo ligands of POMs since solvent molecules (acetonitrile) are comparatively weak ligands.^{38,39} Thus, the negative charge density of oxo ligand of the molecular rods, which determines the binding strength of oxo-zinc association, has significant effect on the size of formed blackberry structures and self-recognition behavior. As discussed above, the terminal oxo ligands of **1** carry higher negative charges than that of **2**, which strengthen **1**-ZnCl₂ binding and therefore decrease the curvature of assemblies, e.g. larger sizes for blackberries. Moreover, in the anhydrous acetonitrile solution of the molecular rods, zinc chloride could become partially positively charged by replacing its chloride ligand with solvent molecule or surface oxo ligand of POMs. The binding of Zn complex on the surface of molecular rods can lower their net charge density to the range appropriate for self-assembly and thus the formation of blackberries can be observed when ZnCl₂ is added to the original solutions of the molecular rods. **1** is supposed to be more negative charged on its surface and therefore able to bind more Zn complex than **2**, which lowers the net charge of **1** more and makes its blackberries with larger sizes. The ability of **1** to strongly bind with more zinc ions than **2** can be further

confirmed by the following study which monitors the disassembly process of blackberries in the solutions of the molecular rods respectively after removing ZnCl_2 .

3.3.5 EXAFS studies of the Zn^{2+} on the surface of molecular rods

XANES and EXAFS spectroscopy was employed to probe the local environment around Zn atoms in the solutions. XANES is used to determine the oxidation state and electronic transitions and fingerprint the element of interest. EXAFS is used for determination of local structure i.e. interatomic distances, coordination numbers and the types of neighboring atoms with few angstroms around the element of interest which is Zn in this case. Figure 3.10a shows the normalized absorption coefficient data for ZnCl_2 's acetonitrile solution plotted along with the samples. The figure clearly show that the spectra for ZnCl_2 is different from that of the samples as observed from the shift in peak position and the nature of the oscillations indicated by the arrows. Figure 3.10b shows comparison of the Fourier transformed EXAFS data in r-space for the samples and ZnCl_2 solution. It is obvious that the local structure around Zn atoms is different in ZnCl_2 solution and the samples. For **2**'s solution, the first shell peak is observed at 1.5 Å, whereas for ZnCl_2 it is at 1.7 Å. This would imply presence of slightly higher bond lengths for Zn atoms in ZnCl_2 when compared to the sample. Figure 3.11a and b show the data and fit of the EXAFS data from ZnCl_2 and **2**'s acetonitrile solution (with Zinc ion) and the fit parameters are listed in Table 3-1.

From Table 3-1, we observe that ZnCl_2 solution has Zn-low Z atom bonds (in our case, mostly is the N atom from acetonitrile solvent) along with Zn-Cl bonds.⁴⁰ **2**'s solution has only Zn-O bonds while Zn-Cl bonds were not necessary to fit the data. The shift of the first shell peak to high value of r in Figure 3.10b for ZnCl_2 may due to the presence of Zn-Cl bonds.

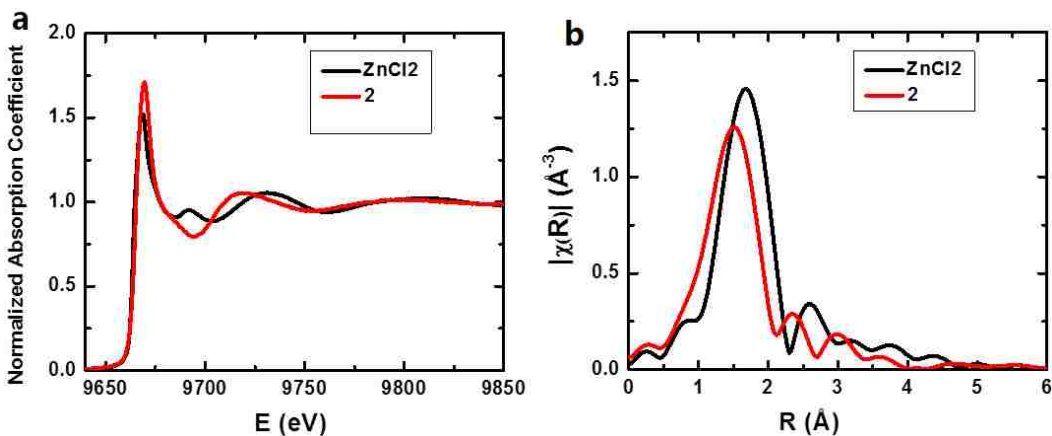


Figure 3.10 a) Comparison of XANES data from ZnCl_2 with data from sample 2; b) comparison of Fourier transformed data of Zn edge from ZnCl_2 with Zn edge from Sample 2.

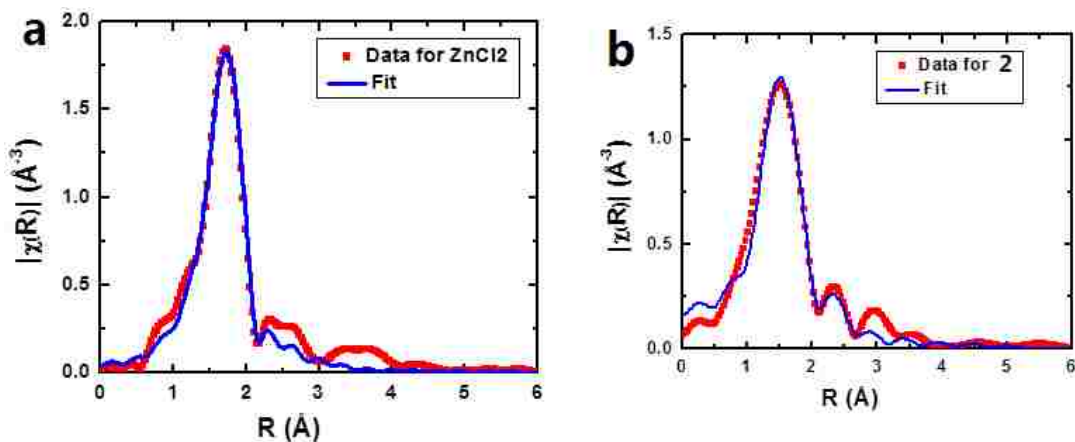


Figure 3.11 a) Data and fit of EXAFS data from Zn edge of ZnCl_2 ; b) Data and fit of EXAFS data from Zn edge of Sample 2.

Table 3-1 List of fit parameters obtained from modeling the data for Zn edge of ZnCl_2 and 2: So_2 was obtained by fitting the Zn foil whose exafs was measured before data collection on samples was started. R factors for all the fits are less than 0.03.

Edge	Sample Name	Paths	Bond length R (ang)	Coordination Number (n)	Debye Waller Factor (ang ²)	Energy Shift ΔE (eV)
Zn edge $S_0^2=1.04$	ZnCl₂ R=1.0-3.0 Å k= 2.5-12 Å ⁻¹	Zn-O	2.04 ± 0.05	2.5 ± 1.4	0.008 ± 0.003	2.5 ± 2.6
		Zn-N	2.20 ± 0.03	2.9 ± 1.2	0.008 ± 0.003	
	Sample 2 R=1.1-2.6 Å k=2.3-8.2 Å ⁻¹	Zn-O	2.03 ± 0.01	3.5 ± 0.3	0.007 ± 0.002	2.1 ± 0.9

3.3.6 Dissociation of the blackberries leads to the confirmation the role of counterions

Time-resolved SLS results of individual solutions of **1** and **2** and their mixtures (with ZnCl_2 added) at equilibrium state indicated that the scattering intensity kept going down exponentially to less than 200 kcps (scattered intensity for benzene, 113 kcps) when $(\text{TBA})_4\text{*EDTA}$ (tetrabutylammonium*ethylenediaminetetraacetate, see experimental section, molar ratio of $(\text{TBA})_4\text{*EDTA}$ to added Zn^{2+} is *ca.* 1) was added to each of the solutions, respectively, suggesting the disassembly of the blackberry structures. EDTA is a strong chelating agent that can almost stoichiometrically coordinate with metal ions. In our case, EDTA can extract the Zn^{2+} from the blackberry structures, which will become thermodynamically unstable and consequently disassemble into monomers. The half-life of the disassembly process could be used to estimate the robustness of macroion- Zn^{2+} interaction and the blackberry structures. Being consistent with the DFT calculation results that **1** can more strongly interact with Zn^{2+} , **1**'s solution showed longer half-life (2893 s) than that of **2**'s solution (597 s) (Figure 3.12a). The molecular rods self-assembled in self-sorted ways in their mixture solution and the formed two types of homogeneous blackberry structures should have different robustness according to the above discussions. Therefore, the half-life of the mixture solution should be longer than that of individual **2**'s solution due to the existence of **1**'s robust vesicles, however, shorter than that of **1** because of lower concentration of **1**'s blackberry structures, which was consistent with our experiment results (half-life of mixture solution, 1585 s). The monitoring results confirm that molecular rod **1** can bind more zinc complex strongly than **2**. Interesting, SLS and DLS results of the three solutions suggested that larger assemblies with similar sizes as that of their original solutions, respectively, were observed again in their solution when ZnCl_2 was added to each of the solutions, which not only confirm the stability of monomers during self-assembly/disassembly process, but also provide us a way to reversibly control the self-assembly/disassembly of macroions in their solutions (Figure 3.12).

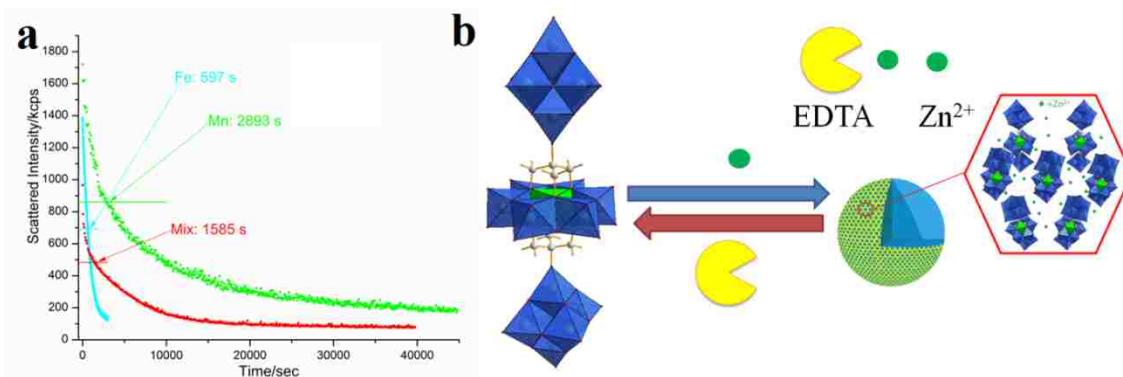


Figure 3.12 a) Time-resolved SLS monitoring results of the three solutions after adding TBA*EDTA (Green, 1's solution; Blue, 2's solution; Red, mixture solution). b) Model of the reversibly self-assembly/disassembly process.

3.4 Self-recognition of rod-shaped macroions with different organic functional groups during their assembly process

3.4.1 Molecular structures of two molecular rods with different organic functional groups

Aryl imido ligands can be used to replace terminal oxo ligands on the surface of unit A in molecular rod of **1** through the further reactions of rod **1** with aromatic amines. Organic ligands (naphthyl and 1-methylnaphthyl) with tiny differences were grafted onto the surface of molecular **1** and two new molecular rods **3** and **4** were obtained. Molecular structures of the two compounds show that two organic ligands are attached on the surface of two A units, respectively (Figure 3.13). There is obviously change in their molecular shape and size after the organic modification and the charges of them remained unchanged. However, the surface of the new compounds became partially hydrophobic due to the introduction of these bulky aromatic groups.²⁵

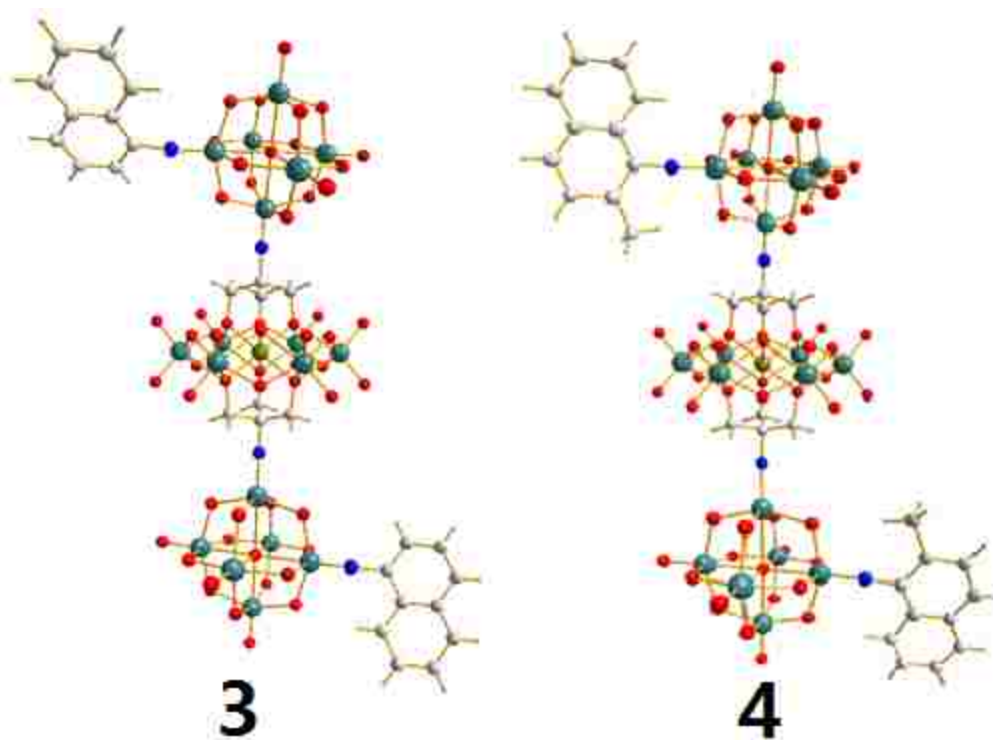


Figure 3.13 Ball-stick representation of the molecular structures of anion part of **3** and **4**.

3.4.2 Self-recognition behavior in their self-assembly process

Being similar with the self-assembly behavior of macroanion **1** and **2**, the new compounds slowly self-assembled into hollow spherical supramolecular assemblies in their diluted acetonitrile solutions with the addition of extra ZnCl_2 . DLS analysis on the individual solutions of **3** and **4** (0.5 mg/mL) at equilibrium state of the self-assembly process indicate that large structures with Rh as 30 ± 2 nm and 110 ± 6 nm were formed in the solution of **3** and **4**, respectively. SLS results show that the ratio of $R_g/R_h \sim 1$ for both of the two solutions, suggesting hollow spherical model for the formed large assemblies, which, as well as their size information, were confirmed by the TEM images of the corresponding assemblies (Figure 3.14). Interestingly, DLS results of the mixed solution of **3** and **4** (1:1 mixture, 0.25 mg/mL for either of them) indicate that two assemblies with Rh as 30 ± 2 and 120 ± 6 nm, respectively, which correspond to the sizes of assemblies in the individual solutions of **3** and **4** within the error limit of CONTIN analysis. The analysis of the TEM images of the assemblies in the mixture solution provides solid evidence for

the formation of two types of assemblies by showing that two types of hollow spherical features with obviously different sizes coexist (Figure 3.15).

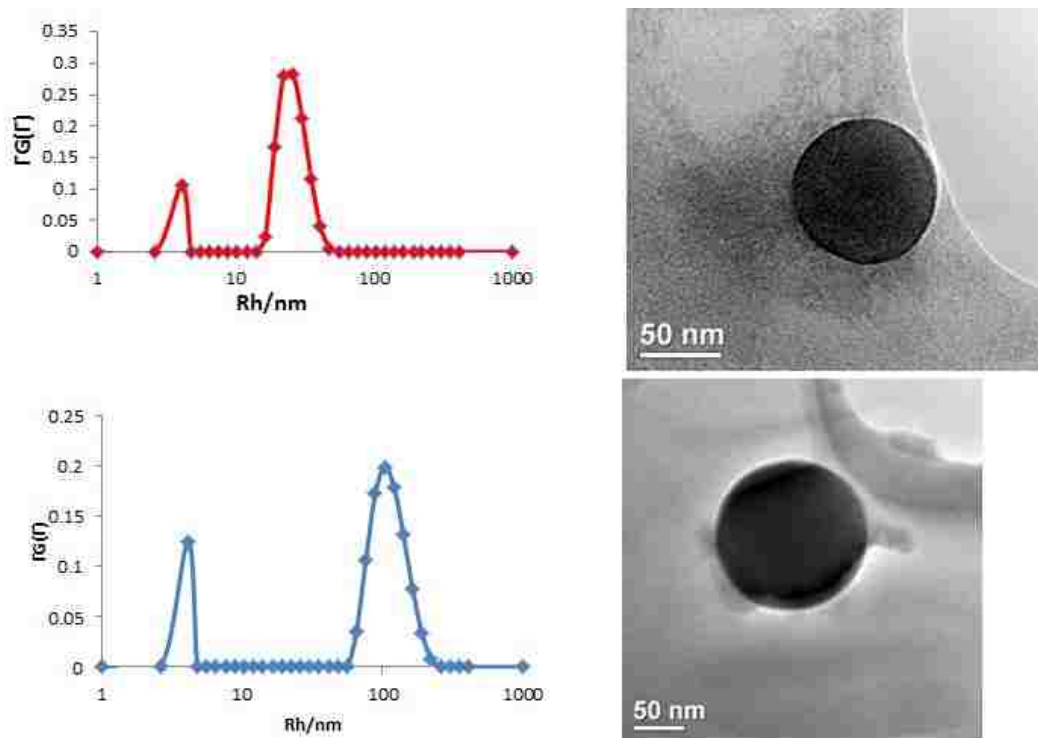


Figure 3.14 DLS results and TEM images of the individual solutions of **3** (up) and **4** (below), respectively.

The formation of their individual blackberry structures suggests the self-recognition behavior of **3** and **4** in the mixture solutions. The tiny difference of their organic fragments (methyl group) is supposed to lead to the self-recognition behavior. Being different from the self-assembly of **1** and **2**, hydrophobic interaction should be counted as partial driving force besides counterion mediated attraction because of the introduction of organic ligands. Thus, the difference of methyl groups in compound **3** and **4** could have effect in the hydrophobic interaction between monomers during their self-assembly behavior, which finally results in different sizes of the two compounds' blackberry structures and their self-recognition behavior.

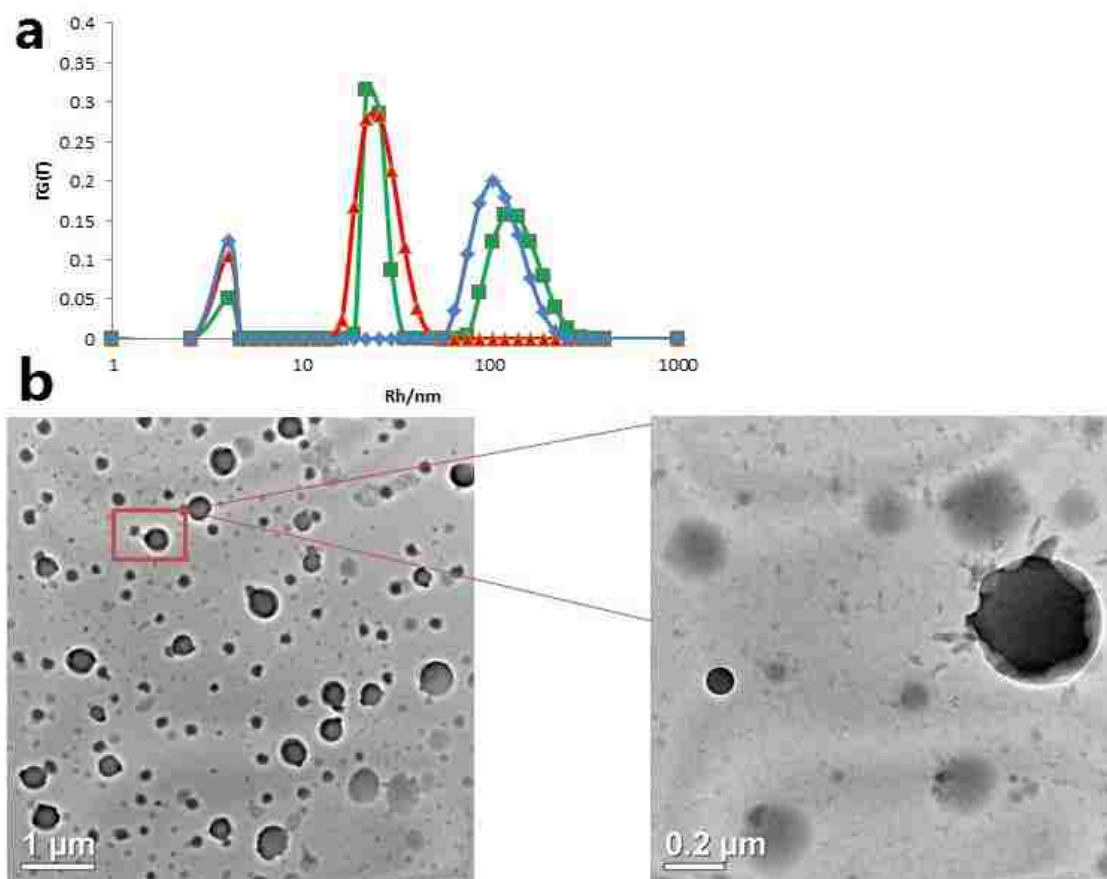


Figure 3.15 a) DLS results of the mixed solution (green) and the individual solutions of 3 (red) and 4 (blue); b) TEM images of the assemblies in the mixed solution.

3.5 Conclusion and outlook

In both of the cases with two very similar macroionic molecular rods, they were observed to self-assemble into hollow spherical blackberry structures and showed self-recognition behavior by assembling into homogeneous blackberries in their mixture solutions. By controlling the addition and removal of the counterions, Zn^{2+} , the self-assembly/disassembly of the molecular rods can be controlled. The counterion-mediated like-charge interaction plays important roles in the formation of bio-molecular complex and self-assembly of polyelectrolyte into functional materials. Our research on self-recognition and self-assembly/disassembly of macro-ions could be helpful to understand recognition behavior and self-assembly of biomolecules and direct the design of polyelectrolyte materials.

Reference

- (1) Lehn, J.-M. *Proc. Natl. Acad. Sci. USA* **2002**, *99*, 4763.
- (2) Olson, A. J.; Hu, Y. H. E.; Keinan, E. *Proc. Natl. Acad. Sci. USA* **2007**, *104*, 20731.
- (3) Rebek, J. *Proc. Natl. Acad. Sci. USA* **2009**, *106*, 10423.
- (4) Caulder, D. L.; Raymond, K. N. *Angew. Chem. Int. Ed.* **1997**, *36*, 1440.
- (5) Mann, S. *Nature* **1988**, *332*, 119.
- (6) Martin, B.; Becourt, C.; Bienvenu, B.; Lucas, B. *Blood* **2006**, *108*, 270.
- (7) Misevic, G. N.; Guerardel, Y.; Sumanovski, L. T.; Slomianny, M. C.; Demarty, M.; Ripoll, C.; Karamanos, Y.; Maes, E.; Popescu, O.; Strecker, G. *J Biol Chem* **2004**, *279*, 15579.
- (8) *Cellular and Biomolecular Recognition*; Jelinek, R., Ed.; Wiley-VCH: Weinheim, 2009.
- (9) Hanessian, S.; Simard, M.; Roelens, S. *J. Am. Chem. Soc.* **1995**, *117*, 7630.
- (10) Salonen, L. M.; Ellermann, M.; Diederich, F. *Angew. Chem. Int. Ed.* **2011**, *50*, 4808.
- (11) Langner, A.; Tait, S. L.; Lin, N.; Rajadurai, C.; Ruben, M.; Kern, K. *Proc. Natl. Acad. Sci. USA* **2007**, *104*, 17927.
- (12) Feng, J.; Ruckenstein, E. *J. Chem. Phys.* **2006**, *124*, 124913.
- (13) Snyder, P. W.; Mecinović, J.; Moustakas, D. T.; Thomas, S. W.; Harder, M.; Mack, E. T.; Lockett, M. R.; Héroux, A.; Sherman, W.; Whitesides, G. M. *Proc. Natl. Acad. Sci. USA* **2011**, *108*, 17889.
- (14) Lehn, J.-M. *Angew. Chem. Int. Ed.* **1990**, *29*, 1304.
- (15) So, C. R.; Kulp, J. L.; Oren, E. E.; Zareie, H.; Tamerler, C.; Evans, J. S.; Sarikaya, M. *ACS Nano* **2009**, *3*, 1525.

- (16) Harada, A.; Kobayashi, R.; Takashima, Y.; Hashidzume, A.; Yamaguchi, H. *Nat. Chem.* **2011**, *3*, 34.
- (17) Heilman-Miller, S. L.; Thirumalai, D.; Woodson, S. A. *J. Mol. Bio.* **2001**, *306*, 1157.
- (18) Roh, J. H.; Behrouzi, R.; Briber, R. M.; Guo, L.; Thirumalai, D.; Woodson, S. A. *Biophys. J.* **2009**, *96*, 575a.
- (19) Cronin, L.; Muller, A. *Chem. Soc. Rev.* **2012**, *41*, 7333.
- (20) Liu, T. B. *Langmuir* **2010**, *26*, 9202.
- (21) Yin, P.; Li, D.; Liu, T. *Chem. Soc. Rev.* **2012**, *41*, 7368.
- (22) Yin, P.; Li, D.; Liu, T. *Isr. J. Chem.* **2011**, *51*, 191.
- (23) Liu, T.; Langston, M. L. K.; Li, D.; Pigga, J. M.; Pichon, C.; Todea, A. M.; Müller, A. *Science* **2011**, *331*, 1590.
- (24) Zhang, J.; Hao, J.; Wei, Y.; Xiao, F.; Yin, P.; Wang, L. *J. Am. Chem. Soc.* **2009**, *132*, 14.
- (25) Zhang, J.; Yin, P.; Hao, J.; Xiao, F.; Chen, L.; Wei, Y. *Chem. Eur. J.* **2012**, *18*, 13596.
- (26) Hiemenz, P. C.; Rajagopalan, R. *Principles of Colloid and Surface Chemistry*; Marcel Dekker: New York, 1997.
- (27) Provencher, S. W. *Comput. Phys. Commun.* **1982**, *27*, 229.
- (28) Segre, C. U.; Leyarovska, N. E.; Chapman, L. D.; Lavender, W. M.; Plag, P. W.; King, A. S.; Kropf, A. J.; Bunker, B. A.; Kemner, K. M.; Dutta, P.; Duran, R. S.; Kaduk, J. In *SYNCHROTRON RADIATION INSTRUMENTATION: SRI99: Eleventh US National Conference*; American Institute of Physics: Stanford, California (USA), 1999; Vol. 521, p 419.
- (29) Newville, M. *J Synchrotron Radiat* **2001**, *8*, 322.
- (30) Rehr, J. J.; Albers, R. C. *Rev. Modern Phys.* **2000**, *72*, 621.

- (31) Ravel, B.; Newville, M. *J Synchrotron Radiat* **2005**, *12*, 537.
- (32) Zhang, R.; Thiyagarajan, P.; Tiede, D. M. *J. App. Cryst.* **2000**, *33*, 565.
- (33) Svergun, D. I.; Koch, M. H. J. *Rep. Prog. Phys.* **2003**, *66*, 1735.
- (34) Svergun, D. *J. App. Cryst.* **1992**, *25*, 495.
- (35) Stigter, D. *Biophys. J.* **1995**, *69*, 380.
- (36) Zhang, J.; Li, D.; Liu, G.; Glover, K. J.; Liu, T. B. *J. Am. Chem. Soc.* **2009**, *131*, 15152.
- (37) Zlotnick, A.; Aldrich, R.; Johnson, J. M.; Ceres, P.; Young, M. J. *Virology* **2000**, *277*, 450.
- (38) Libus, W.; Puchalska, D.; Szuchnicka, T. *J. Phys. Chem.* **1968**, *72*, 2075.
- (39) Evans, J. C.; Lo, G. Y. S. *Spectrochim. Acta.* **1965**, *21*, 1033.
- (40) D'Angelo, P.; Zitolo, A.; Ceccacci, F.; Caminiti, R.; Aquilanti, G. *J Chem Phys* **2011**, *135*, 154509.

Chapter 4: Chiral Recognition and Chiral Discrimination during the Self-Assembly Process of Chiral Polyoxoanions

4.1 Introduction

Molecular chirality was primarily demonstrated by Louis Pasteur's famous experiments on separating tartaric acid with different handedness under microscope in 1848.^{1,2} It was not until 25 years later that J. H. van't Hoff and J. A. Lebel simultaneously but independently provided the explanation that there are two different ways in which four different objects can be arranged at the corners of a tetrahedron, and that the two arrangements are mirror images of one another.³ The term 'chiral' is derived from the Greek name kheir meaning 'hand' and was firstly mentioned by Lord Kelvin in 1904 in his Baltimore Lectures on Molecular Dynamics and the Wave Theory of Light in which he stated that 'I call any geometrical figure, or group of points, chiral, and say it has chirality, if its image in a plane mirror, ideally realized, cannot be brought to coincide with itself.'⁴⁻⁶ Thanks to their opening work in molecular chirality, chirality-related research has been attracting more and more interest and. It extended from asymmetric synthesis in organic chemistry, chiral separation in analytical chemistry, chiral surfaces and supramolecular assemblies, to homo-chirality in the origin of life.^{7,8} In the meantime, the theories on chirality have been being updated and now chemists believe that chirality in molecules can result from not only chiral building blocks or guest, but also asymmetric arrangements of achiral building blocks, or an intrinsically asymmetric molecular structure.⁹

Chiral recognition and chiral discrimination (selection) are the two major topics in chiral research.¹⁰⁻¹² Currently, the study of the two topics were explored mainly in the study of physical properties of solid samples (including crystallization)^{10,11}, amino acid clusters in gas phase¹³, molecular interaction on surfaces^{14,15}, and supramolecular assemblies¹⁶. However, very limited

methods with high cost could be applied for asymmetric synthesis and chiral separation until now. Meanwhile, the homo-chirality of biological molecules, as one of the biggest puzzles in understanding how life began, is still remained unsolved. The two major building units of bio-macromolecules, amino acids and sugars, exist only in L- and D-type, respectively. A few sketchy theories have been proposed to explain the originality of homo-chirality; however, none of them were convincing enough to be widely accepted by the community.^{17,18} Our group mainly focuses on the research on solution behaviors of macro-ions, including polyoxometalates, nanocages, and bio-macromolecules, by studying their self-assembly process in their dilute solutions.¹⁹⁻²¹ Inorganic macro-ions demonstrate similar self-assembly behavior with that of one type of early life, viral capsid proteins in both kinetic properties and assembly morphology (single-layer hollow spheres). Therefore, chiral inorganic macroions were used in this work, as simple models for chiral bio-macromolecules to help us understand chiral recognition and chiral discrimination in biological systems.^{19,22} Meanwhile, our recent study on the assembly process of two different nano-scaled, spherical polyprotic metal oxide-based macroions with the same size but different charge density in dilute solution, demonstrated that the the two macroions can self-recognize each other by forming homogeneous ‘blackberry’-type structures.²³ The role of charge density difference in such systems is believed to be the dominant factor in the self-recognition process.²³ However, the original study was based on an obvious difference. Here, we hope to push the limit by studying highly similar mixtures, which might help explain the general phenomenon of self-recognition in biological systems.

4.2 Experimental section

General. D- and L-Lactic acid were purchased from Sigma-Aldrich and used without further purification. Macrosep Advance Centrifugal Device, 30K MWCO was purchased from Pall Corporation. 200 and 450 nm filters were purchased from Millipore for solution preparation.

G300 Copper grids were purchased from SPI. A commercial Brookhaven Instrument LLS spectrometer equipped with a solid-state laser operating at 532 nm was used for measurement of both SLS and DLS. The TEM images were generated on a JEOL JEM-2000 electron microscope operated at 200 kV with EDS attachment (Oxford). Samples for the TEM analysis were prepared by dropping a small volume of the solution sample onto a carbon film on copper grid. J-815 from JASCO was used to take CD spectra of samples.

Synthesis. The two pairs of enantiomers, $\text{Ca}_{10}\text{Fe}_{28}(\text{u}_3\text{-O})_8(\text{D-Tart})_{16}(\text{HCOO})_{24}$ (Ca-D-Fe₂₈) and $\text{Ca}_{10}\text{Fe}_{28}(\text{u}_3\text{-O})_8(\text{L-Tart})_{16}(\text{HCOO})_{24}$ (Ca-L-Fe₂₈), $\text{Ba}_{10}\text{Fe}_{28}(\text{u}_3\text{-O})_8(\text{D-Tart})_{16}(\text{HCOO})_{24}$ (Ba-D-Fe₂₈) and $\text{Ba}_{10}\text{Fe}_{28}(\text{u}_3\text{-O})_8(\text{L-Tart})_{16}(\text{HCOO})_{24}$ (Ba-L-Fe₂₈) were synthesized and fully characterized previously.²⁴

Static light scattering. A commercial Brookhaven Instrument LLS spectrometer equipped with a solid-state laser operating at 532 nm was used for measurement of both SLS and DLS. SLS experiments were performed at scattering angles (θ) between 20 and 100°, at 2° intervals. However, due to the large fluctuations in scattered intensities at low scattering angles, data from 20-40° in the final analysis were removed. Derived from Rayleigh-Gans-Debye equation²⁵, partial Zimm plot was used to analyze the SLS data to obtain the radius of gyration (R_g). The partial Zimm plot stems from the following approximation: $1/I = C(1+R_g^2*q^2/3)$. Here R_g is determined from the slope and the intercept of a plot of $1/I$ vs. q^2 .

Dynamic light scattering. DLS measures the intensity–intensity time correlation function by means of a BI-9000AT multi-channel digital correlator. The field correlation function $|g^{(1)}(\tau)|$ was analyzed by the constrained regularized CONTIN method²⁶ to yield information on the distribution of the characteristic linewidth Γ from $|g^{(1)}(\tau)| = \int G(\Gamma)e^{-\Gamma*\tau}d\Gamma$. The normalized distribution function of the characteristic linewidth, $G(\Gamma)$, so obtained, can be used to determine an average apparent translational diffusion coefficient, $D_{app} = \Gamma/q^2$. The hydrodynamic radius R_h is related to D via the Stokes–Einstein equation: $R_h = kT/(6\pi\eta D)$ where k is the Boltzmann constant

and η the viscosity of the solvent at temperature T . From DLS measurements, we can obtain the particle-size distribution in solution from a plot of $\Gamma G(\Gamma)$ versus R_h . The R_h of the particles is obtained by extrapolating $R_{h,app}$ to zero scattering angle.

CD spectrum. Solution samples were put in cuvette (thickness, 1 cm) and the solutions were diluted by DI water until the HT in the whole wavelength range is lower than 800 mV. The solutions with appropriate concentrations were scanned from 600 to 220 nm for 5 times and the obtained data were averaged after subtracting the baseline of pure solvent (water).

Ultrafiltration. Ultrafiltration was performed using Macrosep Advance Centrifugal Device (30 K MWCO) to separate blackberry structure and discrete polyoxometalate. A sample solution was poured into the device and the device is rotated at a speed of 4000 xg for 50 minutes. The upper layer and bottom layer were collected for CD spectrum testing, respectively.

Small angle X-ray Scattering. The SAXS experiments were performed at 12-ID-B station with X-ray energy of 12 KeV at the Advanced Photon Source of the Argonne National Laboratory. The sample to detector distance was about 2 m. A 2D CCD detector was used to acquire images with typical exposure times in the range of 1.0 s.

Preparation of the solutions for SAXS studies. Ca-D/L-Fe₂₈ were dissolved in D.I. water, respectively (2.0 mg/mL). CaCl₂ stock solution was prepared as 21.8 mg/mL and titrated to 1 mL of prepared Ca-D/L-Fe₂₈ solutions, respectively with 0 uL, 5 uL, 5 uL, and 5 uL step by step. 2 mg of Ba-D/L-Fe₂₈ were dissolved in 1 mL buffer of D- or L-lactic acid (2 mg/mL), respectively.

4.3 Chiral recognition and chiral discrimination during their self-assembly process

4.3.1 Molecular structures and macro-anionic properties of D/L-Fe₂₈

Single-crystal X-ray diffraction analyses reveal that the two compounds are enantiomers and show chiral wheel-type structures. The anionic ferric wheel [Fe₂₈(u₃-O)₈(Tart)₁₆(HCOO)₂₄]²⁰⁻ consists of 29 six-coordinate iron(III) centers linked by 8 u₃-oxo bridges, 16 Tart linkers, and 24 formic acid ligands. The Fe₂₈ wheel contains a cross-like inner cavity with the shortest and longest diameter of circa 8.4 and 11.5 Å, respectively; its external diameter is about 26.5 Å and the thickness is circa 9.5 Å (Figure 4.1). Seven Fe³⁺ centers coordinate with three Tart ligands to form the {Fe₇} cluster, which is further linked with another three identical clusters through Tart ligands to create the wheel-type macroanions. If the Tart ligands are visualized as ‘amino acids’, the Fe₂₈ cluster can be considered as a protein- or peptide-like molecule because 16 ‘amino acids’ will be connected together through Fe³⁺ metal centers.²⁴ Therefore, it is straightforward to understand chiral recognition and chiral discrimination among bio-macromolecules from the corresponding study of Fe₂₈ chiral clusters

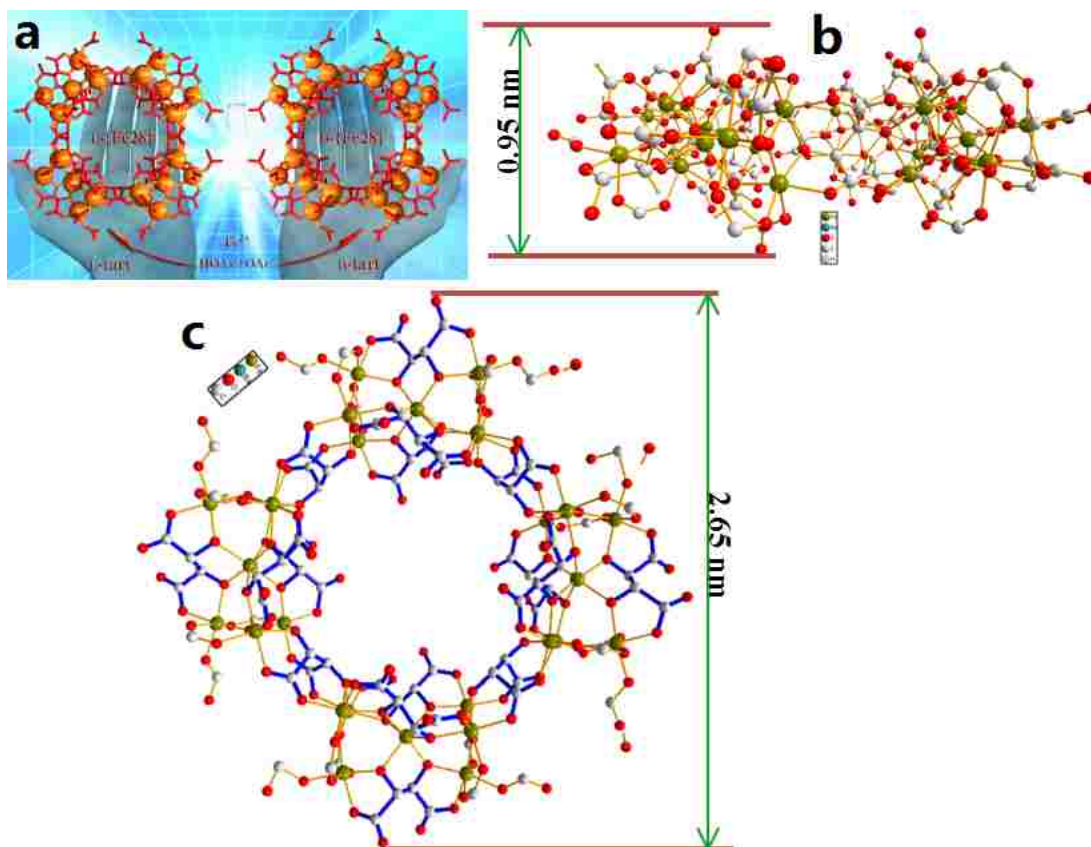


Figure 4.1 a) Ball-stick representation of molecular structures of enantiomers of Fe₂₈; b) c) Side and top view of the molecular structures of L-Fe₂₈ (Molecular fragments highlighted in blue are tartaric acid fragments). Reprinted with permission from ref. 24. Copyright 2009 Wiley-VCH.

Small angle X-ray scattering (SAXS) was utilized to study the molecular structures of the chiral wheel in solution state along with counterion (Ca²⁺) association. The Ca-D-Fe₂₈ and Ca-L-Fe₂₈ were observed to stay as discrete clusters in their dilute solutions by showing low and stable scattering intensity (ca. 15.0 kcps at scattering angle 90°; the scattered intensity for pure benzene and water are 116 and 13 kcps, respectively at that situation) in time-resolved static light scattering (SLS) results. Therefore, this pair of enantiomers is appropriate for studying solution properties of single clusters. The two enantiomers show identical SAXS curves, suggesting they have ‘identical’ molecular structure in solution state, which is consistent with the structural similarity between the enantiomers in crystalline state (Figure 4.2a). The calculated SAXS profile based on Fe₂₈ cluster structure in crystalline state fits well with the experimental data of Ca-L-

Fe₂₈, indicating that the wheel-structure survives and remains stable as the enantiomeric crystals dissolve in water (Figure 4.2b). Extra Ca²⁺ was titrated into the homogeneous solutions of both of the two enantiomers and radius of gyration (R_g) of the clusters, calculated from the small angle region using Guinier equation, was observed to increase with more and more CaCl₂ solution being titrated (Figure 4.2c). Meantime, further exploration of the scattering data with program GNOM generates pair distance distribution functions (PDDF) in real space, p(r). The intensity keep increasing at the range from 2.5 nm to 3.5 nm, suggesting the association of counterions on the surface of the chiral clusters (Figure 4.2d and e).^{27,28}

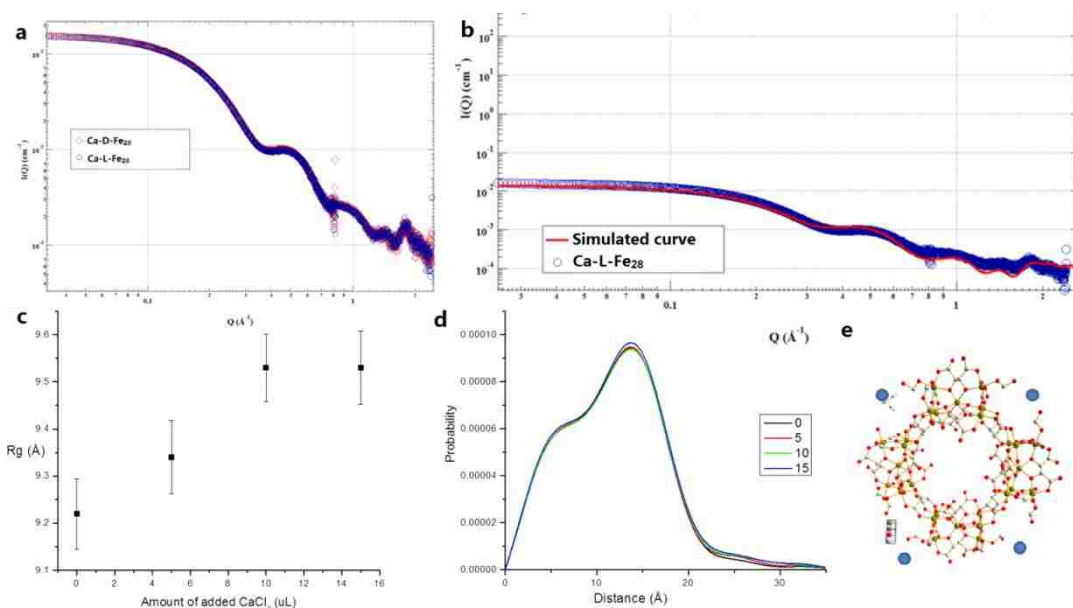


Figure 4.2 a) SAXS curves of Ca-D-Fe₂₈ and Ca-L-Fe₂₈; b) SAXS curve of Ca-L-Fe₂₈ and the simulated curve based on the molecular structures in crystalline state; c) R_g, measured from SAXS curves, of the solutions with different amount of extra CaCl₂; d) PDDF results of solutions with different amount of extra CaCl₂; e) Model for the counterions association with Fe₂₈.

The enantiomers with Ba²⁺ as counterions (Ba-D-Fe₂₈ and Ba-L-Fe₂₈) were observed to self-assemble into large supramolecular structures, however, only exist as discrete clusters in the buffer of lactic acid (2mg/mL). Routine analysis of SAXS data of the two enantiomers in both buffers of D and L-lactic acid indicates that the wheel-shaped cluster structures remain stable in the buffer solutions. More importantly, the two enantiomers show almost identical SAXS curves

in both buffers, suggesting the chiral type of co-anion (lactic acid) have no effect in counterion association of the chiral clusters (Figure 4.3).

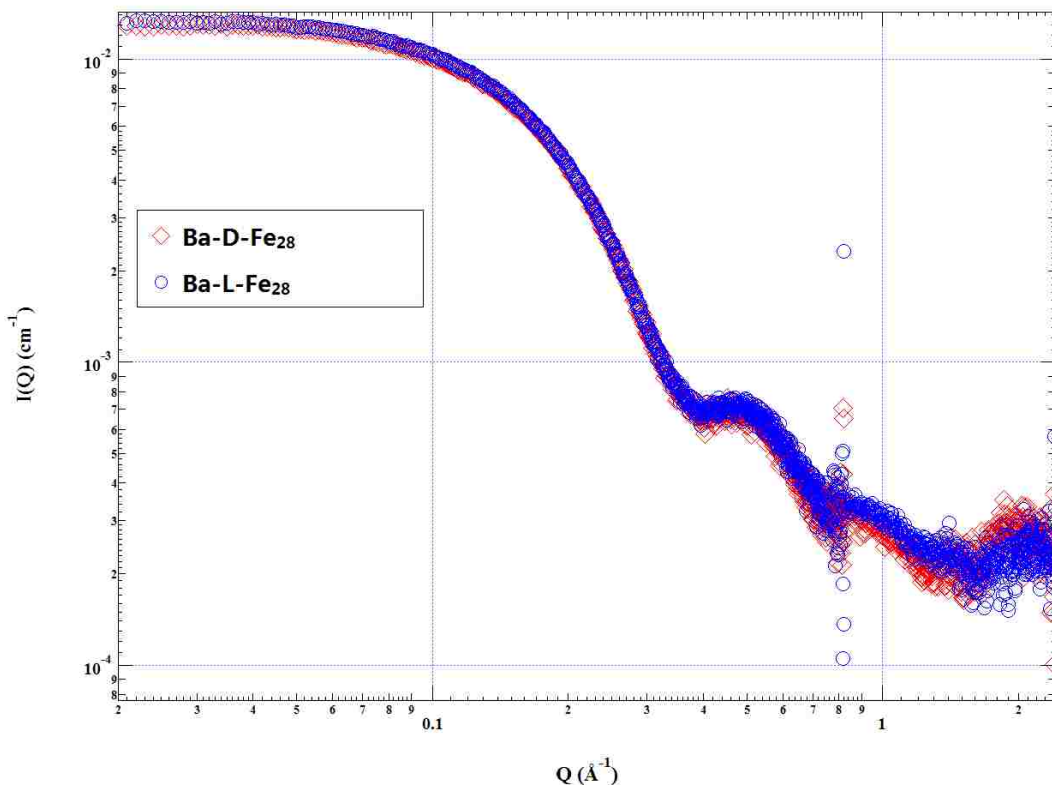


Figure 4.3 SAXS curves of Ba-D-Fe₂₈ and Ba-L-Fe₂₈ in the buffer of L-lactic acid, respectively.

4.3.2 Chiral recognition in the self-assembly process of the chiral clusters

With Ba²⁺ as counterions, Ba-D-Fe₂₈ (0.5 mg/mL), Ba-L-Fe₂₈ (0.5 mg/mL), and their mixture (D/L = 1:1, D, 0.25 mg/mL; L, 0.25 mg/mL) in water, as monitored by SLS, showed a slow self-assembly process and reached equilibrium state at ca. 60 days, which is the typical character of self-assembly of macroions into ‘blackberry’-type structures.^{19,20} The two enantiomers show almost identical kinetic curves, suggesting that they self-assemble at the same speed. The total concentration of the macroions in the mixture solution is actually identical with the individual solutions of the enantiomers (0.5 mg/mL). Thus the kinetic properties of the mixture solution should be similar with the enantiomer solutions if there is no chiral recognition between the two enantiomers in their racemic mixtures. However, the mixture shows slower self-assembly speed

and equilibrates at much lower scattered intensity compared to that of the individual enantiomer solutions. This implies that the two enantiomers can self-recognize each other since both of the kinetic parameters are highly dependent on the concentration of macroions (Figure 4.4). A typical CONTIN analyses on dynamic light scattering (DLS) results of the three solutions indicate that assemblies of hydrodynamic radius (R_h) as ca. 65 ± 4 nm form during the self-assembly process in solutions, respectively. SLS results indicate that R_g is close to their corresponding R_h values, which is consistent with the hollow spherical model of blackberry structures confirmed by further TEM studies (Figure 4.4).

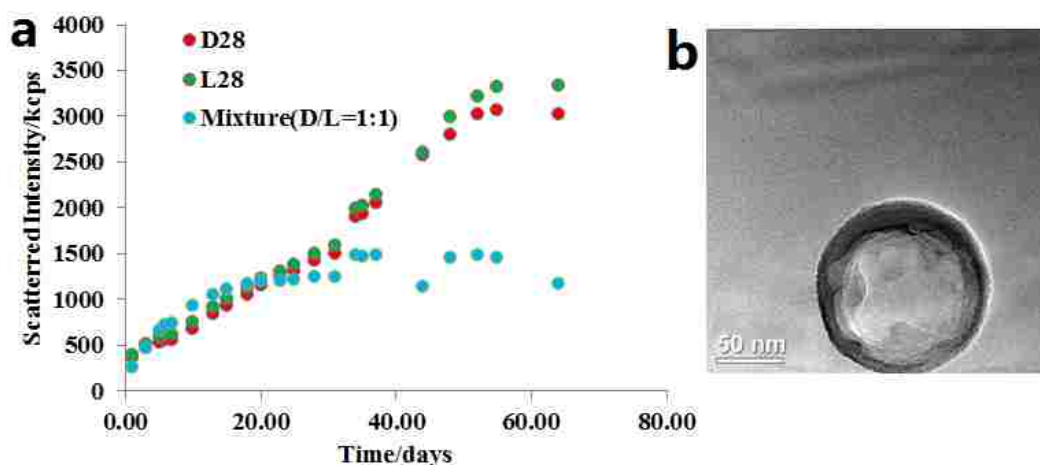


Figure 4.4 a) SLS results of Ba-D-Fe₂₈, Ba-L-Fe₂₈ and their racemic mixture solutions; b) TEM images of the assemblies in solution Ba-D-Fe₂₈.

As confirmed by a previous study on self-assembly of macroions, the lag phase period, claimed as dimer/oligomer formation state, during the self-assembly process is responsible for the self-recognition behavior.^{23,29} The two individual enantiomer solutions and their mixture solution were monitored by SLS at the first 31 hrs (Figure 4.5). Obviously, the two individual solutions self-assemble at almost the same speed and much faster than that of the mixture solution, confirming the self-recognition of the two enantiomers in their mixture solution. Meantime, after the confirmation of the chiral-recognition behavior, the above mentioned mixture solution can be now considered as ‘real’ mixtures of two species: D- and L-Fe₂₈. Here comes the next question: how independently do the two species self-assemble in their mixture solution? In order to answer

the question, another two solutions of individual Ba-D- and Ba-L-Fe₂₈ were prepared at 0.25 mg/mL, respectively, which is the half of the concentration of the original ones, and monitored during the same period. The sum of scattered intensity of the two new solutions was represented by curve of black dots. Ideally, D- and L-Fe₂₈ self-assemble independently into larger structures in their mixture and scattered intensity of mixture should be exactly the sum of individual enantiomer solutions (0.25 mg/mL). Experimentally, the curve of summed intensity showed larger slope than that of mixture solution, suggesting that D- and L-Fe₂₈ form non-ideal mixture solution and they have negative effect in the self-assembly process of each other.

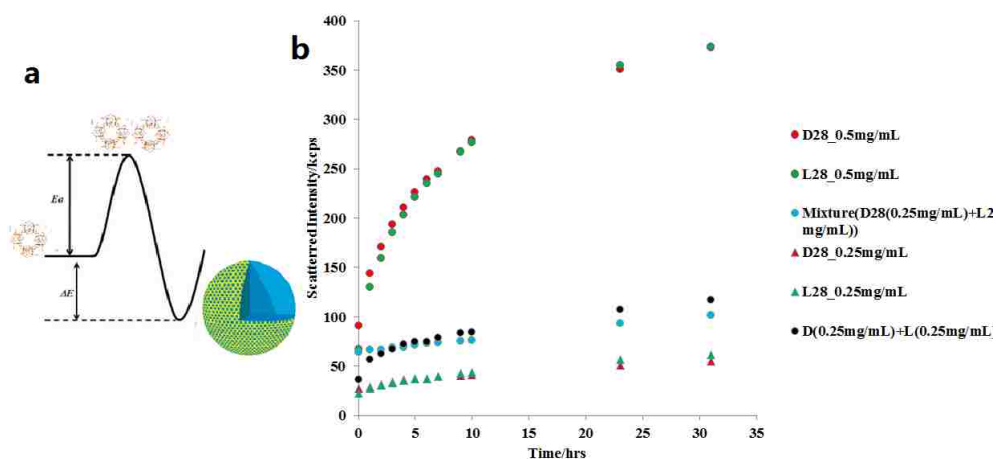


Figure 4.5 a) Graphical representation of the thermodynamic mechanism of the self-assembly process; b) SLS monitoring of different solutions for 31 hours.

The high symmetry of the assemblies (blackberry structures), strong counterion-mediated attraction, and rigid nature of molecular structure are supposed to lead to low tolerance on the morphology difference between building units (macroion monomers). Olson et al. have studied the viral capsid self-assembly through theoretical simulation and they happened to mention chiral recognition in their modeling story.³⁰ In the video of the assembly process of Olson's macroscopic models, only oligomers with homo-chiral units were observed at beginning, which is consistent with one of our conclusions that the self-recognition starts as early as lag phase period. Dimers or oligomers were considered as the intermediate state in the self-assembly process of discrete macroions to blackberry structures. Due to the morphological compatibility, the

formation energy for homo-oligomers is slightly lower than the hybrid oligomers. However, this tiny difference seems to be enough to lead to the discrimination of homogeneous blackberry structures over heterogeneous ones. Moreover, typical blackberry structures are almost perfect hollow spherical objects and therefore, their high symmetries cannot permit the tiny defects of the insertion of heter-chiral monomers.

4.3.3 Chiral discrimination in the self-assembly process of the chiral clusters

Chiral organic molecules, e.g. lactic acid, can be used to tune the self-assembly process of Ba-D/L-Fe₂₈ in their dilute solution. Ba-D-Fe₂₈ and Ba-L-Fe₂₈ (0.5 mg/mL) were dissolved three different buffers, D-lactic acid (33 ug/mL in water), L-lactic acid (33 ug/mL in water), and D/L-lactic acid (D-lactic acid, 16.5 ug/mL; L-lactic acid, 16.5 ug/mL), respectively (Figure 4.6). Interestingly, D-Fe₂₈ macroanions were observed to self-assemble rapidly in buffer of L-lactic acid with very short lag phase period, however self-assemble very slowly in the buffer of D-lactic acid with long lag phase of ca. 10 day. The self-assembly speed of the D-Fe₂₈ in buffer of D/L-lactic buffer is in the middle of the above two solutions with lag phase as ca. 6 days. In the meantime, the self-assembly process of L-Fe₂₈ is the fastest in the buffer of D-lactic acid with shortest lag phase time and slowest in the buffer of L-lactic acid with longest lag phase time (ca. 5 days). Moreover, the self-assembly speed and the lag phase time of L-Fe₂₈ in the buffer of D/L-lactic acid lies in the middle. The explanation for the observations is that D-lactic acid suppresses the self-assembly of D-Fe₂₈ while L-lactic acid suppresses the self-assembly of L-Fe₂₈. The suppression effect depends on the concentration of lactic acid and probably that is the reason that Fe₂₈ in D/L-lactic acid is always in the middle in self-assembly speed. On the other hand, the comparison of the self-assembly rate of the two enantiomers in the same buffer indicates that L-Fe₂₈ self-assembles much faster than D-Fe₂₈ for the buffer of D-lactic acid while D-Fe₂₈ self-assembles faster than L-Fe₂₈ in the buffer of L-lactic acid.

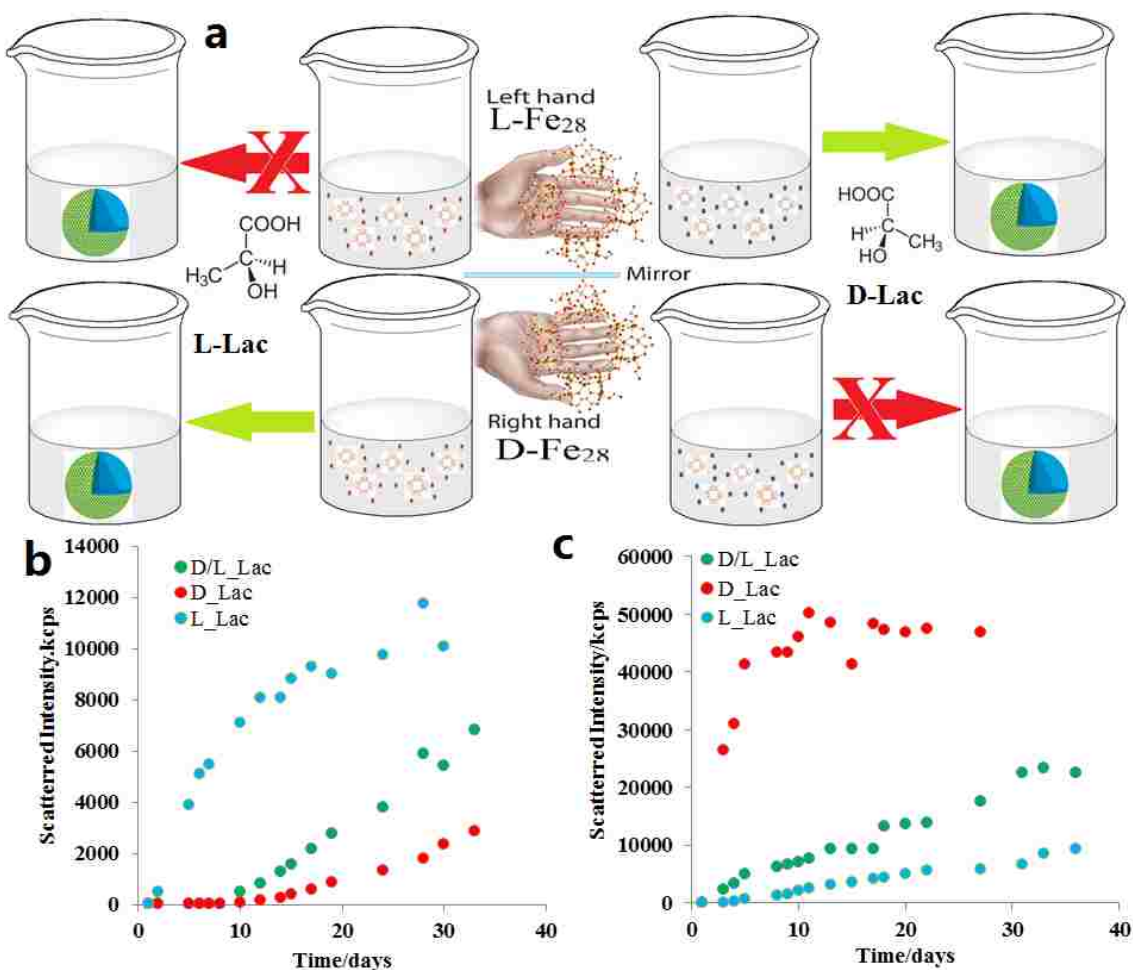


Figure 4.6 a) Graphical representation of the chiral discrimination experiments; b) SLS results of Ba-D-Fe₂₈ in different buffers; c) SLS results of Ba-L-Fe₂₈ in different buffers.

Being similar with the chiral recognition study, chiral discrimination starts at lag phase period of the self-assembly process. The solution behavior of D-Fe₂₈ and L-Fe₂₈ (0.5 mg/mL) were studied in the buffer of L-lactic acid (33 ug/mL) for the first 400 hrs of their self-assembly process (Figure 4.7). The lag phase time for the solution of D-Fe₂₈ and L-Fe₂₈ could be roughly determined as ca.50 and ca. 266 hrs (longer than 266 hours and less than 400 hrs), respectively. In the buffer of L-lactic acid, the formation of D-Fe₂₈ dimers/oligomers at the beginning of self-assembly process is much easier than that of L-Fe₂₈.

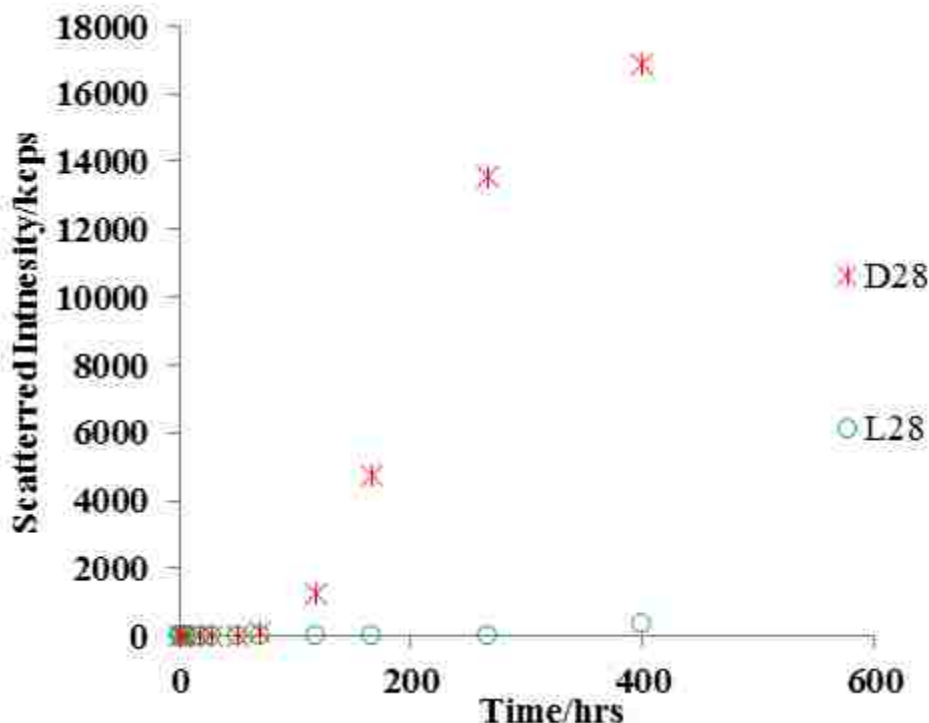


Figure 4.7 SLS monitoring of Ba-D-Fe₂₈ and Ba-L-Fe₂₈ in the buffer of L-lactic acid for 400 hrs.

The chiral discrimination during the chiral macroions' self-assembly process is believed to result from the compatibility between chiral co-anions (lactic acid) and the chiral micro-environment confined by chiral POMs. At the lag phase period, discrete macroionic clusters meet with each other to form dimer (or oligomer) structures, which is the rate-determine step with high activation barrier for the self-assembly process.²⁹ The confined space between the clusters is the so-called chiral micro-environment. Counterions (Ba²⁺) and their co-anions (lactic acid) are supposed to exist in this area to mediate the attraction between the two like-charge clusters. Therefore, the compatibility of lactic acid and the chiral micro-environment determines the activation energy of the formation of dimers/oligomers (Figure 4.8a). Experimental results suggest L-, and D-lactic acid are compatible with the chiral micro-environments of D-, and L-Fe₂₈, respectively and thus 'like' pairs (D-lactic acid/L-Fe₂₈; L-lactic acid/D-Fe₂₈) could have lower activation energy in formation dimers than that of 'dislike' pairs (D-lactic acid/D-Fe₂₈; L-lactic acid/L-Fe₂₈), which explains why the 'like' pairs show shorter lag phase periods. Such compatibility was also

believed to have effect in the formation of complete blackberry structures. The area painted in yellow in blackberry model was actually also chiral micro-environment confined by chiral POMs (Figure 4.8b). The compatibility of lactic acid in the buffer with such area could determine the rate of the formation of blackberry and its size. Obviously, the ‘dislike’ pairs show much slower process in formation of blackberry than that of ‘like’ pairs. CONTIN analyses on the DLS results on the solutions of ‘like’ and ‘dislike’ pairs indicates that ‘like’ pairs form larger blackberry structures ($R_h \sim R_g = 63$ nm) than ‘dislike’ pairs do ($R_h \sim R_g = 40$ nm), confirming that POMs in ‘like’ pairs interact stronger with each other (Figure 4.8).

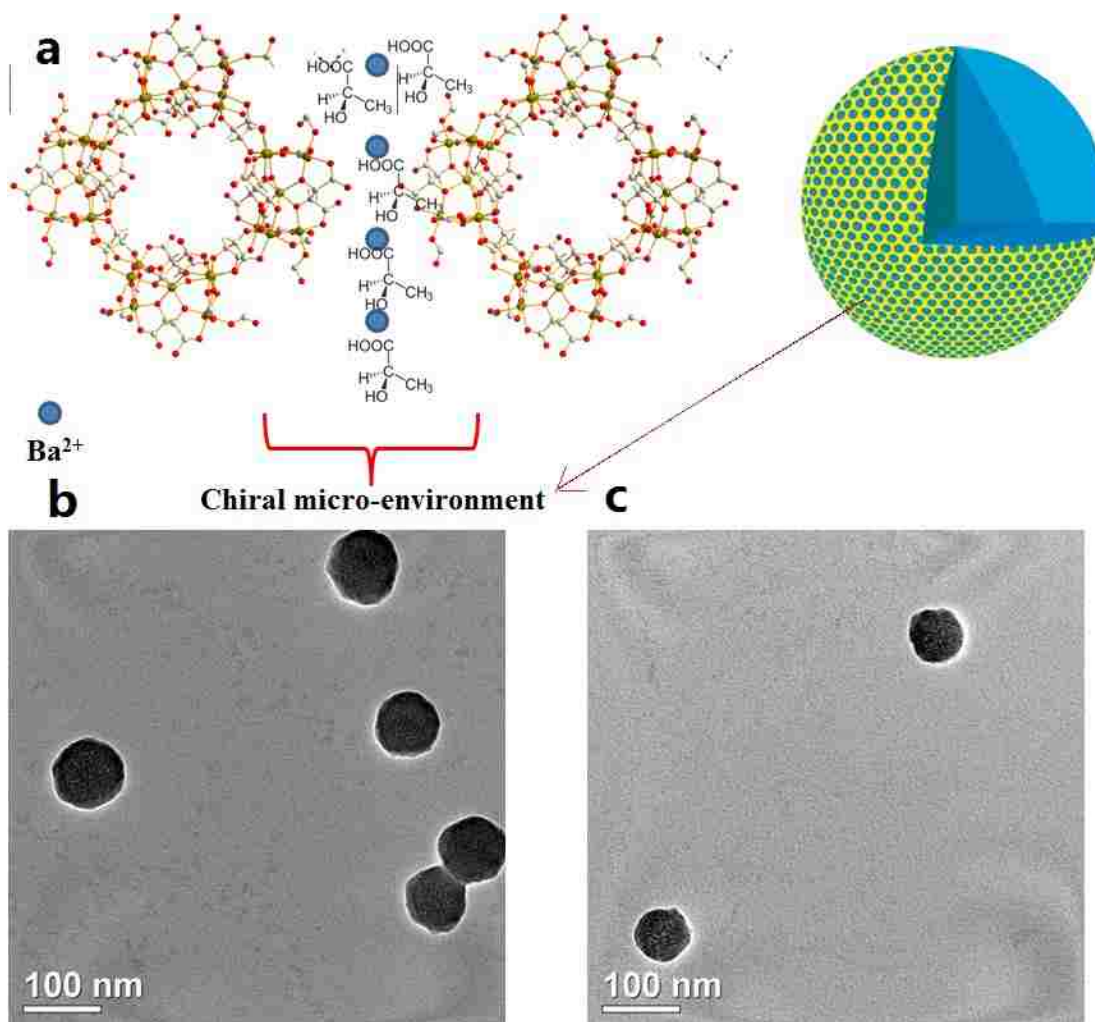


Figure 4.8 a) Graphical representation of chiral micro-environment; b) c) TEM images of the assemblies in Ba-D-Fe₂₈ and Ba-L-Fe₂₈ in the buffer of L-lactic acid, respectively.

4.3.4 Chiral separation: the combination of chiral recognition and chiral discrimination

Chiral separation could be carried out if chiral recognition and chiral discrimination can work together. The monitoring of individual enantiomer solutions and their racemic mixture in the buffer with D- and L-lactic acid, respectively, might provide evidence for the assumption. Different from the results regarding the self-recognition study, the blackberry formation speed of the racemic mixture is in the middle of 'like' pairs and 'dislike' pairs in both D- and L-lactic acid buffers (Figure 4.9). The plausible explanation is that lactic acids specifically suppresses the self-assembly of their 'dislike'-pair partners while their 'like'-pair partners are able to self-assemble into larger structures, which contributes largely to the scattered intensities increment in the racemic mixture solutions.

More convincing evidences for the co-existence of chiral recognition and discrimination are from ultrafiltration experiments. Theoretically, based on the above assumption, the addition of certain type of lactic acid (let's take D-lactic acid as an example.) to the racemic mixture of Ba-D/Ba-L-Fe₂₈ would favor the self-assembly of L-Fe₂₈ and suppress the self-assembly of D-Fe₂₈ and most of L-Fe₂₈ would exist as assemblies while most of D-Fe₂₈ stays as discrete clusters. The enantiomers could easily be separated since the blackberry structures and monomers are of quite different sizes (monomer, 2.65nm; blackberry, 80~120 nm) and can be separated by filtration. The racemic mixture with added D-lactic acid was experimentally filtered by passing the solution through membrane with cut off molecular weight as 30K. Amazingly, the upper layer solution, supposed to be full of large assemblies, shows the signal of L-Fe₂₈ while the bottom layer solution, supposed to be dominated by monomers, shows the signal of D-Fe₂₈, which support the our assumption that L-Fe₂₈ and D-Fe₂₈ dominantly exist as blackberry structures and discrete clusters, respectively in the separated solutions (Figure 4.10). Therefore, chiral recognition and discrimination were experimentally confirmed to work together, which not only strongly supports

the above study on self-recognition and self-discrimination, but also provides possible way for chiral separation.

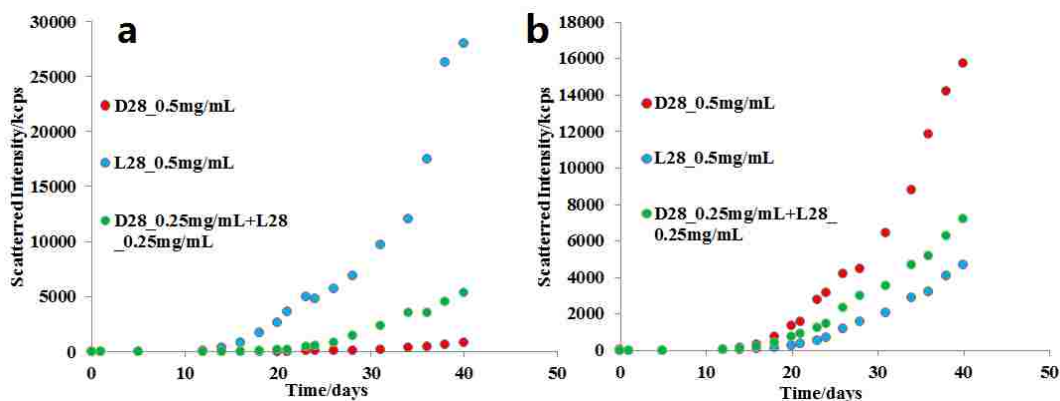


Figure 4.9 a) SLS results of Ba-D-Fe₂₈, Ba-L-Fe₂₈, and their racemic mixture in the buffer of D-lactic acid respectively; b) SLS results of Ba-D-Fe₂₈, Ba-L-Fe₂₈, and their racemic mixture in the buffer of L-lactic acid respectively.

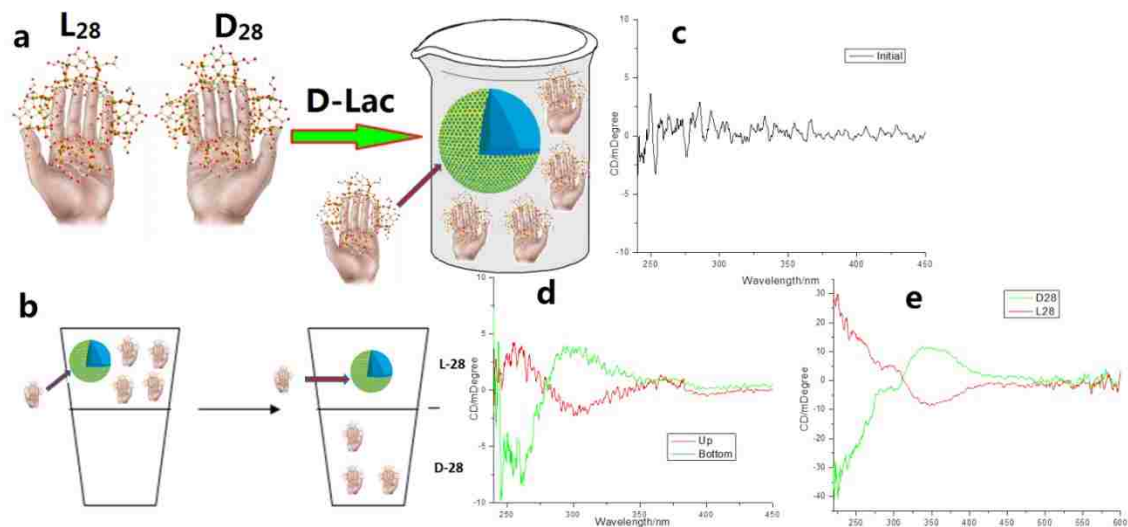


Figure 4.10 a) Graphical representation of the self-assembly of the two enantiomers in the buffer of D-lactic; b) Graphical representation of ultrafiltration experiment; c) CD spectrum of the solution before ultrafiltration; d) CD spectra of up layer (red) and bottom layer (green) solutions after ultrafiltration; e) CD spectra of aqueous solutions of pure Ba-D-Fe₂₈ (green) and pure Ba-L-Fe₂₈ (red).

4.4 Conclusion

Chiral macro-polyoxoanions were observed to show chiral recognition behavior by forming homogeneous blackberry structure of the individual enantiomers in their racemic mixtures. Their self-assembly behavior can be tuned by addition of lactic acid with the ‘like’-pairs and ‘dislike’-

pair rules. The study on chiral recognition and chiral discrimination provides us with insightful ideas on the nature of interaction between macroions, which not only sheds light on the basic research on homo-chirality and chiral selection, but also provides new way for chiral separation and sensing.

Reference

- (1) Gal, J. *Chirality* **2011**, *23*, 1.
- (2) Flack, H. *Acta Cryst. A* **2009**, *65*, 371.
- (3) *The Cambridge History of Science*; Nye, M. J., Ed.; Cambridge University Press: Cambridge, 2003; Vol. 5.
- (4) Lough, W. J.; Wainer, I. *Chirality in Natural and Applied Science*; Blackwell Science Ltd-CRC Press: USA and Canada, 2002.
- (5) Clayden, J.; Greeves, N.; Warren, S. *Organic chemistry*; 2nd ed.; Oxford University Press: USA, 2012.
- (6) Kelvin, W. T. *Baltimore Lectures on Molecular Dynamics and the Wave Theory of Light*; C. J. Clay: London, 1904.
- (7) *Chiral Recognition in Separation Methods: Mechanisms and Applications*; 1st ed.; Berthod, A., Ed.; Springer, 2010.
- (8) Cline, D. B. *Eur. Rev.* **2005**, *13*, 49.
- (9) Zang, H.; Miras, H. N.; Yan, J.; Long, D.-L.; Cronin, L. *J. Am. Chem. Soc.* **2012**, *134*, 11376.
- (10) Kuhnle, A.; Linderoth, T. R.; Hammer, B.; Besenbacher, F. *Nature* **2002**, *415*, 891.
- (11) Meyer, V. R.; Rais, M. *Chirality* **1989**, *1*, 167.
- (12) Alkorta, I.; Picazo, O.; Elguero, J. *Curr. Org. Chem.* **2006**, *10*, 695.

- (13) Dwivedi, P.; Wu, C.; Matz, L. M.; Clowers, B. H.; Siems, W. F.; Hill, H. H., Jr. *Anal Chem* **2006**, *78*, 8200.
- (14) Suh, I.-H.; Park, K. H.; Jensen, W. P.; Lewis, D. E. *J. Chem. Educ.* **1997**, *74*, 800.
- (15) Addadi, L.; Weiner, S. *Nature* **2001**, *411*, 753.
- (16) *Supramolecular chirality*; 1st ed.; Crego-Calama, M.; Reinhoudt, D. N., Eds.; Springer, 2006.
- (17) Blackmond, D. G. *Cold Spring Harb Perspect Biol.* **2010**, *2*, a002147.
- (18) Breslow, R. *Tetrahedron Lett.* **2011**, *52*, 2028.
- (19) Liu, T. B. *Langmuir* **2010**, *26*, 9202.
- (20) Yin, P.; Li, D.; Liu, T. *Isr. J. Chem.* **2011**, *51*, 191.
- (21) Yin, P.; Li, D.; Liu, T. *Chem. Soc. Rev.* **2012**, *41*, 7368.
- (22) Zlotnick, A.; Aldrich, R.; Johnson, J. M.; Ceres, P.; Young, M. J. *Virology* **2000**, *277*, 450.
- (23) Liu, T.; Langston, M. L. K.; Li, D.; Pigga, J. M.; Pichon, C.; Todea, A. M.; Müller, A. *Science* **2011**, *331*, 1590.
- (24) Zhang, Z. M.; Li, Y. G.; Yao, S.; Wang, E. B.; Wang, Y. H.; Clerac, R. *Angew. Chem. Int. Ed.* **2009**, *48*, 1581.
- (25) Hiemenz, P. C.; Rajagopalan, R. *Principles of Colloid and Surface Chemistry*; Marcel Dekker: New York, 1997.
- (26) Provencher, S. W. *Comput. Phys. Commun.* **1982**, *27*, 229.
- (27) Svergun, D. *J. Appl. Crystallogr.* **1992**, *25*, 495.
- (28) Svergun, D. I.; Koch, M. H. J. *Rep. Prog. Phys.* **2003**, *66*, 1735.
- (29) Zhang, J.; Li, D.; Liu, G.; Glover, K. J.; Liu, T. B. *J. Am. Chem. Soc.* **2009**, *131*, 15152.

(30) Olson, A. J.; Hu, Y. H. E.; Keinan, E. *Proc. Nat. Acad. Sci. USA* **2007**, *104*, 20731.

Chapter 5: Self-Assembly of POM-Organic Hybrids to Vesicles with Tunable Sizes and Fluorescence

5.1 Introduction

Polyoxometalates (POMs) are a large group of anionic metal oxide clusters with varied topologies, sizes and charge densities, composed of early transition metal ions in high oxidation states and oxo ligands.^{1,2} POMs have been widely studied for their applications in the development of magnetic and photo-electronic materials, catalysts and medicines.¹⁻³ POMs are also used in industry as catalysts and electrode materials.⁴ In recent years, the self-assembly behavior of POMs has received continuous interest as it helps to incorporate POMs into nano-devices with desired morphology and functionality, which consequently expands the applicability of POMs.⁵⁻⁸

Various methods are available to assemble POMs into nano- and micro-structures. As a well-developed protocol, supramolecular interaction-driven self-assembly, including coordination and hydrogen bonding, has been used to obtain oligomers of POMs,^{9,10} POM based nano-cages,¹¹ nano-rods,^{12,13} and 3D frameworks^{14,15}. Due to the macroionic feature of POM anions, counterion-mediated self-assembly leads to the formation of hollow, spherical ‘blackberry’ structures in solutions as well as monolayers of close-packed POM clusters on surfaces.^{5-7,16} Self-assembly of POMs based on solvophobic interactions has also been achieved by using surfactant-encapsulated POMs^{17,18} and/or POM-organic hybrids¹⁹. In the latter approach, several types of POM hybrids with different molecular architectures (dumb-bells, POMs functionalized with single or double alkyl chains, etc.) have been successfully explored for their amphiphilic properties in solution and at interfaces.^{19,20} Therefore, these POM based hybrids can be considered as unique types of surfactants with bulky polar head groups.

So far, hybrids containing several types of POM clusters have been explored. Anderson-type POMs functionalized with two long alkyl chains were found to form bilayer vesicle structures in acetonitrile/water mixed solvents, and reverse vesicle structures in acetonitrile/toluene mixed solvents.^{21,22} The vesicle size can be tuned by solvent composition. Moreover, the vesicles of a Lindqvist hexavanadate-based hybrid surfactant were found to demonstrate interesting fluorescence properties associated with the self-assembly process.²⁰ The surfactants with Keggin type POM as polar head groups were found by Polarz et al. to be able to self-assemble into micelles and lyotropic phases.¹⁹ The surfactants were later observed to self-assemble into a hexagonal lattice at the air/water interface.²³ However, the research in this area has only just started and is still far from achieving the aim of rationally controlling the self-assembly process of hybrids by designing their architectures to facilitate their applications. One important POM type lacking detailed studies as a polar head group in single cluster hybrid surfactants is the Dawson cluster. Earlier studies on single Dawson based hybrids were carried out mainly on bulk samples and/or at interfaces, leaving their detailed solution behavior unexplored.²⁴ Herein, we report the synthesis of a single Dawson cluster based organic-inorganic hybrid and its concentration-, polarity-, counterion- and pH-dependent self-assembly behaviors in solution, determined by using laser light scattering (LLS), electron microscopy, and ¹H-NMR techniques.

5.2 Experimental section

General. Acetonitrile, acetone, anhydrous ZnCl₂, d₃-acetonitrile and d₆-acetone were purchased from Sigma-Aldrich and used without further purification. 200 nm filters were purchased from Millipore for solution preparation. Copper grids were purchased from SPI. A commercial Brookhaven Instrument LLS spectrometer equipped with a solid-state laser operating at 532 nm was used for measurement of both SLS and DLS. NMR spectra were recorded on a Bruker 500 spectrometer and were calibrated to the residual proton resonance of the solvent. The TEM images were taken on a JEOL JEM-2000 electron microscope operated at 200 kV with EDS

attachment (Oxford). Samples for the TEM analysis were prepared by dropping a small volume of the solution sample onto a carbon film on copper grid. H*1's aqueous solutions with concentrations ranging from 0 to 1.75 mg/mL were prepared for surface tension measurement. The measurement was carried out in AR-G2 using Du Noüy Ring method. Differential scanning calorimetry (DSC) were done in STA (TA).

Sample 1 preparation. $\text{TBA}_5\text{H}_4[\text{P}_2\text{V}_3\text{W}_{15}\text{O}_{62}]$ was synthesized according to the previous literature.^[27] $\text{TBA}_5\text{H}_4[\text{P}_2\text{V}_3\text{W}_{15}\text{O}_{62}]$ (1.0 g, 0.19 mmol) was dissolved in 30 mL of MeCN, then L^1 (0.107 g, 0.3 mmol) was added to the solution. The reaction mixture was refluxed for 6 days in the dark. The resulting yellow solution was filtered and added drop-wise to an excess of diethyl ether with vigorous stirring. The resulting yellow solid was collected and re-dissolved in minimum volume of MeCN, then re-precipitated by addition of diethyl ether. The yellow precipitate thus obtained was isolated by filtration, dried overnight under vacuum and recrystallized from acetonitrile by ether diffusion. Yield 0.90 g (0.16 mmol, 81.4 %, based on $\text{TBA}_5\text{H}_4[\text{P}_2\text{V}_3\text{W}_{15}\text{O}_{62}]$).

Elemental analysis (%) calcd for $\text{C}_{116}\text{H}_{254}\text{N}_7\text{O}_{63}\text{P}_2\text{V}_3\text{W}_{15}$ ($5727.64 \text{ g mol}^{-1}$): C 24.32, H 4.47, N 1.71; found: C 25.20, H 4.65, N 1.80. $^1\text{H NMR}$ (400 MHz; CD_3CN): $\delta = 6.11$ (s, 1H, -NH-), 5.72 (s, 6H, - $\text{CH}_2\text{-O}$), 2.15 (t, 2H, -CO- $\text{CH}_2\text{-}$), 1.30 (m, 24H, alkyl), 0.917 (t, 3H, - CH_3) ppm in addition to the TBA and solvent resonances. FT-IR (KBr): 3444 (w), 2960 (m), 2929 (m), 2873 (m), 1483 (m), 1465 (w), 1379, 1083 (s), 1064, 946 (s), 906 (s), 887 (s), 788 (s), 786 (w), 719 cm^{-1} . ESI (CH_3CN , m/z): 2621.7 [$\text{TBA}_4\mathbf{1}$]²⁻, 1666.7 [$\text{TBA}_3\mathbf{1}$]³⁻, 1586.5 [$\text{TBA}_2\mathbf{H1}$]³⁻.

Sample 2 preparation. $(\text{TBA})_2[\text{V}_6\text{O}_{13}\{(\text{OCH}_2)_3\text{CCH}_2\text{OH}\}_2]$ was prepared according to previous literature.^[9] $(\text{TBA})_2[\text{V}_6\text{O}_{13}\{(\text{OCH}_2)_3\text{CCH}_2\text{OH}\}_2]$ (1mmol, 1.26g) DCC (0.44g) and stearic acid (4mmol, 1.14g) were dissolved in 50 mL acetonitrile. When they dissolved completely, 0.2g DMAP was added to the solution. The mixture was stirred at 80°C for 72h and then filtered. 0.17g

Red thin plate-like crystals of TBA₂***1** were collected from the filtrate within two days (yield, 10%).

TBA₂***2** (Bu₄N)₂[V₆O₁₃{(OCH₂)₃CCH₂OOC(CH₂)₁₆CH₃}₂] Yield: 0.17g (10%). Elemental anal. for C₇₈H₁₅₈N₂O₂₃V₆: Calc. (%) C, 52.11; N, 1.56; H, 8.86. Found: C, 52.14; N, 1.61; H, 8.80. ¹HNMR (500MHz, Acetone-d₆, 300K): δ = 0.8640(t, 6H, CH₃-, tail), 0.9745(t, 24H, CH₃-, [Bu₄N]⁺), 1.2708(m, 52H, -(CH₂)₁₃-, tail), 1.4641(m, 16H, -CH₂-, [Bu₄N]⁺), 1.5487(m, 4H, -CH₂-, tail), 1.8425(m, 16H, -CH₂-, [Bu₄N]⁺), 2.2000(m, 4H, OOC-CH₂-, tail), 3.5113(t, 16H, NCH₂-, [Bu₄N]⁺), 3.9401(t, 4H, COO-CH₂-, tail), 5.0630(s, 12H, (OCH₂)₃CR). IR (KBr pellet, cm⁻¹): 2961 (s), 2922 (s), 2872(s), 2852 (s), 1752(s), 1485(m), 1469(s), 1384(m), 1159(m), 1132(m), 1062(s), 961(s), 942(vs), 881(w), 812(m), 720(s), 582(m), 513(w). UV/Vis (MeCN): λ_{max} = 350nm. ESI (MeCN): 656.35 (2²⁻), 1313.22 ({2+H}⁻), 1554.50 ({2+TBA}⁻).

Static light scattering: A commercial Brookhaven Instrument LLS spectrometer equipped with a solid-state laser operating at 532 nm was used for measurement of both SLS and DLS. SLS experiments were performed at scattering angles (θ) between 20 and 100°, at 2° intervals. However, due to the large fluctuations in scattered intensities at low scattering angles, we removed the data from 20-40° in the final analysis. Derived from Rayleigh-Gans-Debye equation²⁵, partial Zimm plot was used to analyze the SLS data to obtain the radius of gyration (R_g). The partial Zimm plot stems from the following approximate formula: 1/I = C(1+R_g²*q²/3). Here R_g is determined from the slope and the intercept of a plot of 1/I vs. q².

Dynamic light scattering: DLS measures the intensity–intensity time correlation function by means of a BI-9000AT multi-channel digital correlator. The field correlation function |g⁽¹⁾(τ)| was analyzed by the constrained regularized CONTIN method²⁶ to yield information on the distribution of the characteristic line width Γ. The normalized distribution function of the characteristic line width, G(Γ), so obtained, can be used to determine an average apparent translational diffusion coefficient, D_{app} = Γ/q². The hydrodynamic radius R_h is related to D via the

Stokes–Einstein equation: $R_h = kT/(6\pi\eta D)$ where k is the Boltzmann constant and η the viscosity of the solvent at temperature T . From DLS measurements, we can obtain the particle-size distribution in solution from a plot of $\Gamma^*G(\Gamma)$ versus R_h . The R_h of the particles is obtained by extrapolating $R_{h,app}$ to zero scattering angle. The normalized distribution function of the characteristic line width, $G(\Gamma)$, so obtained, can be used to determine an average apparent translational diffusion coefficient, $D_{app} = \Gamma/q^2$. The hydrodynamic radius R_h is related to D via the Stokes–Einstein equation: $R_h = kT/(6\pi\eta D)$ where k is the Boltzmann constant and η the viscosity of the solvent at temperature T . From DLS measurements, we can obtain the particle-size distribution in solution from a plot of $\Gamma^*G(\Gamma)$ versus R_h . The R_h of the particles is obtained by extrapolating $R_{h,app}$ to zero scattering angle.

1D NMR and 2D DOSY. All the NMR spectra were recorded on Bruker Avance 500 spectrometer equipped with a BBO probe at 25 °C. DOSY was performed on a Bruker 500 MHz spectrometer with the magnetic field gradient (g) varying from 0 to 32 G/cm in 16 ~ 32 steps. The length of the gradient (d) was from 6000 ms to 8000 ms, and the time interval between two pulsed gradients (D) was from 0.1 s to 0.15 s. All spectra were taken at room temperature. After the data collection, FIDs were processed and analyzed with the NMR software TopSpin 2.0 provided by Bruker. Both T1/T2 relaxation and CONTIN methods were used to fit the raw data. The observed proton signal I in a standard DOSY spectrum is expressed through equation 1:

$$I = I_0 \exp \left[- (2\pi\gamma\delta)^2 \left(\Delta - \delta/3 \right) D g^2 \right] \quad \text{Equation (3-1)}$$

where I_0 is the reference intensity, γ is the gyromagnetic ratio of the proton. If only one diffusive component exists in the solution, a straight line will occur in a plot of $\ln(I/I_0)$ versus g^2 , and the apparent diffusion coefficient (D) can be calculated from the slope using linear regression analysis.

5.3 Results and discussion

5.3.1 Synthesis and molecular structures

Due to the existence of symmetrical functional positions on the surfaces of Anderson, Lindqvist, and Keggin clusters, the hybrid surfactants containing such polar head groups usually have two alkyl tails.¹⁹⁻²¹ However, the two caps of the substituted Dawson cluster, $[P_2V_3W_{15}O_{62}]^{9-}$, are asymmetrical, with the vanadate cap comparatively more reactive than the tungstate one. Therefore, it is only possible to synthesize single-tailed hybrids based on this cluster. Similar to the synthesis of Dawson-based dumb-bell molecules,²⁷ the organic ligand L^1 with a 15-carbon alkyl chain and tris(hydroxymethyl)amidomethane moiety was initially synthesized and then reacted with $[P_2V_3W_{15}O_{62}]^{9-}$ obtaining the target molecule $((C_4H_9)_4N)_5H[P_2V_3W_{15}O_{59}(OCH_2)_3CNHCOC_{15}H_{31}]$, TBA***1**, (TBA, $((C_4H_9)_4N)^+$; **1**, the surfactant anion) (Figure 5.1). The original counterions, five TBA molecules, can be replaced with protons by passing an acetonitrile solution of TBA***1** through a column filled with a cation exchange resin. The resulting new compound $H_6[P_2V_3W_{15}O_{59}(OCH_2)_3CNHCOC_{15}H_{31}]$, H***1**, is soluble in both acetonitrile and water.

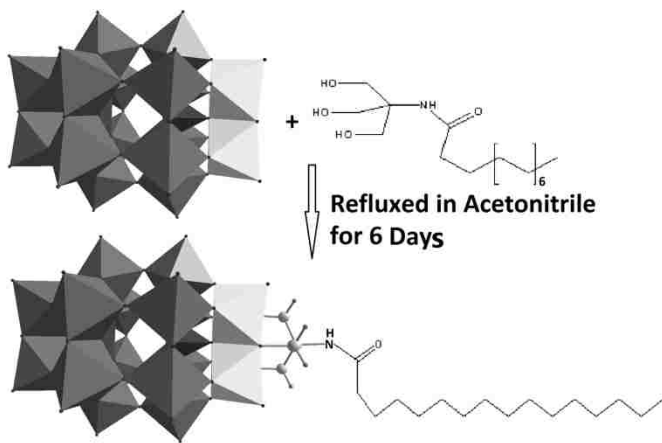


Figure 5.1 The synthesis of the surfactant **1** with Dawson type POMs as polar head group. Polyhedron color code: W, black; P, dark black; V, white. Reprinted with permission from ref. 28. Copyright 2012 Wiley-VCH.

Plate-like single crystals of TBA₂***2** were obtained from different crystallization strategies.

Although the X-ray diffraction intensities at high angles are very weak due to rather small

thickness of the crystals, the locations of all the atoms can be determined very accurately, which is rarely seen for compounds with such long alkyl chains. The space group of $\text{TBA}_2 \cdot \mathbf{2}$ is $P\bar{1}$ and there is an inversion center located at the center oxygen of hexavanadate in the structure of $\mathbf{2}$. The POM core can be considered as consisting two $[\text{RC}(\text{CH}_2\text{O})_3]^{3-}$ subunits bound to a $[\text{V}_6\text{O}_{13}]^{4+}$ core or, alternatively, as a hexametalate $[\text{V}_6\text{O}_{19}]^{8-}$ core connected to two $[\text{RC}(\text{CH}_2)_3]^{3+}$ subunits. The trisalkoxy ligands occupy opposite faces of the hexametalate octahedron. The conformation of long alkyl tails in crystals is close to the ideal zig-zag chain shape, which favors the parallel stacking of chains. The length of a single chain is *ca* 2.48 nm in crystalline state while the size of polar head is *ca* 0.76 nm, which is much larger than the sulfate group (*ca* 0.20 nm), the polar head of a common ionic surfactant SDS (sodium dodecyl sulfate) (Figure 5.2). DSC and TGA results indicate that the melting temperature of $\text{TBA}_2 \cdot \mathbf{2}$ is 90.82 °C and decomposition temperature is as high as 250°C.

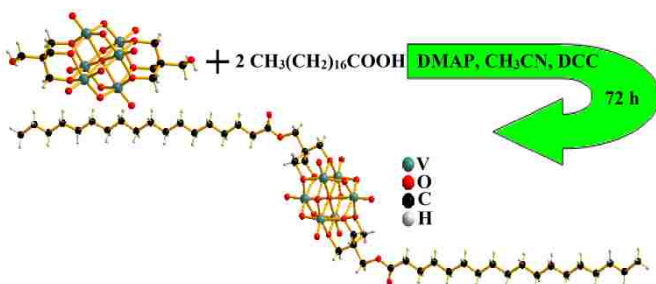


Figure 5.2 Reaction route for the synthesis of molecule $\mathbf{2}$. Reprinted with permission from ref. 20. Copyright 2011 Wiley-VCH.

In the packing diagram (Figure 5.3), *ab* plane ((001) lattice plane) was formed due to the close packing of TBA and V_6 . The distance between two neighboring lattice planes is 1.88 nm, which is filled by the alkyl chains. The non-polar tails tend to align side by side to strengthen the van der Waals interactions between their atoms, which is much weaker than ionic interaction in *ab* plane. The structural analysis indicates that the driving force for crystal growth is anisotropic and therefore, favors to growth in (001) lattice plane direction to form thin-plate shaped crystals.

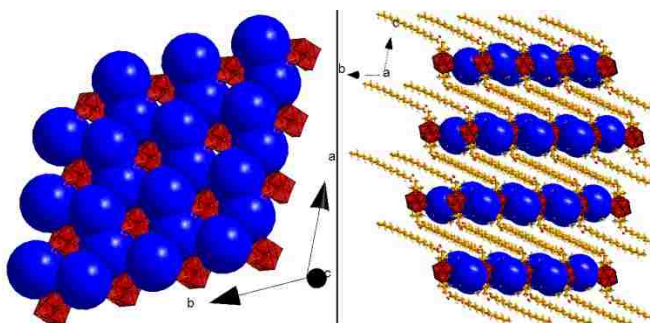


Figure 5.3 Packing diagram of TBA₂*1. (Left: ab plane or (001) lattice plane; right: bc plane or (100) lattice plane. Blue sphere represents TBA and red polyhedron represents hexavanadate.) Reprinted with permission from ref. 20. Copyright 2011 Wiley-VCH.

5.3.2 Critical association concentration (CAC)

The acetone solutions of TBA*1 with concentrations ranging from 0.002 to 0.5 mg/mL were prepared and monitored by static light scattering (SLS) at 90° scattering angle. It was expected that the scattered intensity would increase significantly if large self-assembled aggregates were formed in the solutions. Correspondingly, a sudden, drastic increase in the equilibrium scattered intensity at a given TBA*1 concentration would indicate the attainment of the critical association concentration (CAC), which was found to be 0.02 mg/mL in the present case. The solutions with concentrations below the CAC show very low scattered intensities (< 400 kcps; scattered intensity for benzene is 120 kcps), indicating the absence of large assemblies (Figure 5.4a). Dynamic light scattering (DLS) and SLS were applied to determine the hydrodynamic radius (R_h) and radius of gyration (R_g) of the assemblies, formed at different concentrations (Figure 5.4c). R_h values of the assemblies show narrow distributions and no angular dependence, suggesting spherical structure for the assemblies. The ratio of R_h/R_g is close to 1, indicating a hollow spherical structure. The vesicular structure and the sizes of the assemblies were confirmed by TEM studies (Figure 5.4d). Interestingly, contrary to the hexavanadate-based hybrid **2** whose self-assembly behavior and assembly sizes are concentration independent,²⁰ the vesicle size observed here increases from 50 nm to 115 nm as the concentration is raised from 0.02 to 0.5 mg/mL (Figure 5.4b).

The novel hybrid surfactant **2** with a giant polar head group can still decrease the surface tension of its aqueous solution with Na^+ being the counterions, showing a basic feature of surfactants. As the compound concentration increases, the surface tension decreases. Critical Micelle Concentration (CMC) is identified as 0.23 mg/mL from the surface tension results. The surface tension at the turning point is 45.4 mN/m, which is much lower than the surface tension of pure water at room temperature (Figure 5.5).

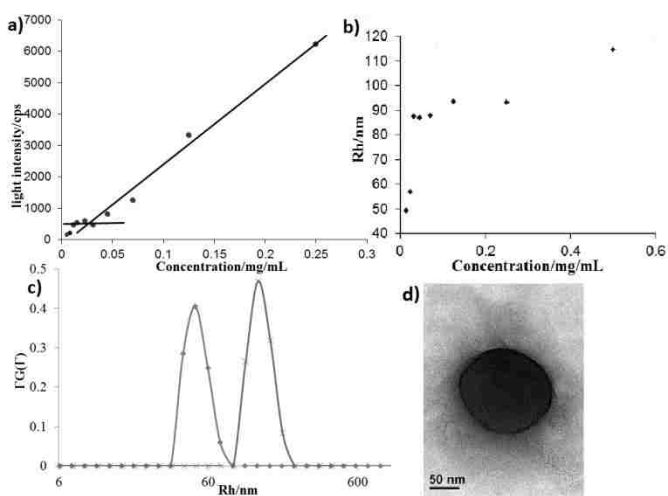


Figure 5.4 a) Scattered intensities at 90° scattering angle of the TBA*1 in acetone at different concentrations; b) hydrodynamic radius of the formed vesicle structures in the TBA*1 acetone solution depending on the concentration; c) DLS results of 0.5 (\times) and 0.03 (\diamond) mg/mL TBA*1's acetone solution at 30° scattering angle; d) TEM images of the vesicle structure from the 0.5 mg/mL TBA*1 in acetone solution. Reprinted with permission from ref. 28. Copyright 2012 Wiley-VCH.

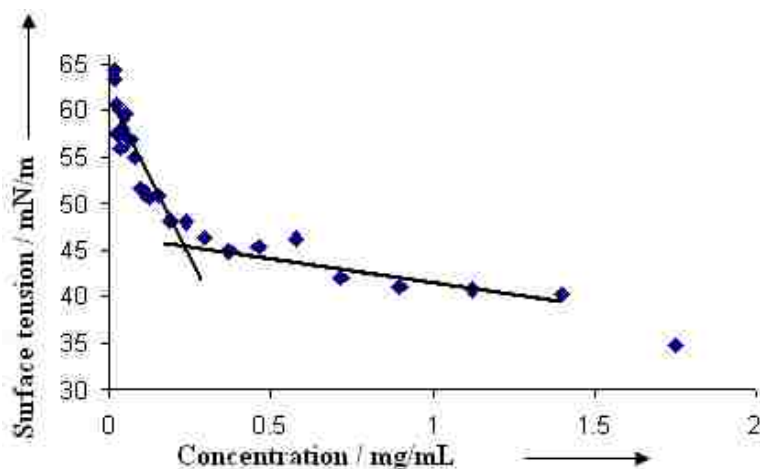


Figure 5.5 Concentration dependent surface tension of Na_2^*2 's aqueous solution. Reprinted with permission from ref. 20. Copyright 2011 Wiley-VCH.

5.3.3 Effect of solvent polarity

For solutions with a given POM-hybrid concentration, the vesicle size can be tuned by adjusting the solvent polarity. Solutions of 0.02 mg/mL TBA*1 in pure acetone, pure acetonitrile and acetone/water mixed solvents containing 95:5, 85:15, 65:35, and 50:50 vol% of acetone, respectively, were prepared. The vesicle sizes measured by DLS and TEM (Figure 5.6) show a linear relationship with the inverse of the dielectric constant of the solvent, indicating a charge-regulated process.⁵ The solvent-polarity dependent self-assembly can be explained by the dissociation of the TBA counterions from the POM surface, consequently increasing the hydrophilicity of the polar head groups. The counterion dissociation can clearly be observed by comparing the diffusion coefficients of counterions and the anionic hybrids in acetone and acetonitrile solutions by Diffusion Ordered Spectroscopy (DOSY) NMR technique. In polar solvents (acetonitrile), the TBA counterions diffuse much faster than the hybrid cluster, which leads to the TBA disassociation; however, the two parties show very close diffusion speed in the relatively nonpolar solvent, acetone, (Figure 5.7) indicating strong TBA association around the POM.

The vesicle size of {V₆} surfactant shows a similar dependence on the solvent polarity, but with a much more negative slope than that of TBA*1 (Figure 5.6a), which could be related to the less negative charge of {V₆} (-2) compared to the TBA*1 (-6).²⁰ The counterion disassociation is controlled by factors such as static charge interaction, solvent polarity and solvation of ions. Static charge force is proportional to the number of charges of the ions and thus, TBA could be easier to diffuse away from the surface of the {V₆} surfactant's polar head groups than from Dawson clusters (TBA*1). Therefore, the effective charge on the {V₆} surfactant increases more significantly when the solvent polarity increases, which finally results in a more negative slope in Figure 5.6a. For the {V₆} surfactant, vesicles could only be observed when 20~35 vol% of water was added to its acetone solution.²⁰ However, due to the high negative charge (-6) and much

larger polar head group, TBA*1 can form vesicle structures in less polar solvents such as pure acetone.

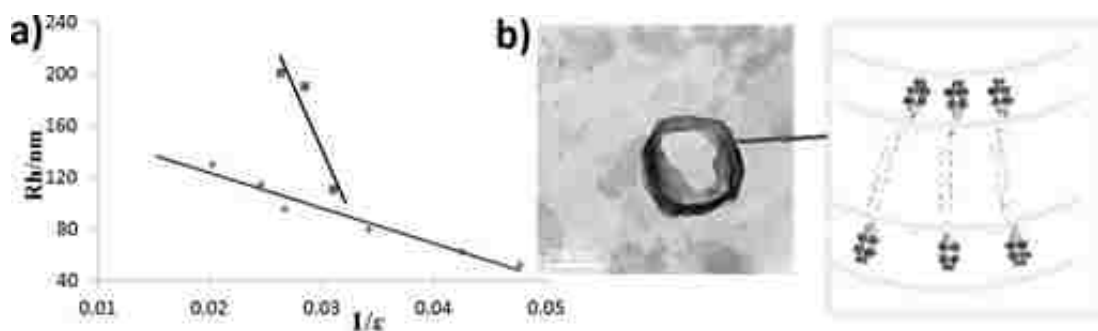


Figure 5.6 a) The plot of the hydrodynamic radius of vesicles vs. the inverse of the dielectric constant of the solvent. ◇ represents the data of Dawson-based surfactant while □ represents that of hexavanadate-based surfactant (V_6 surfactant); b) TEM images of the vesicle structure formed by TBA*1 in the mixture of water and acetone ($v/v=1/1$), with a proposed model for the bilayer structure. Reprinted with permission from ref. 28. Copyright 2012 Wiley-VCH.

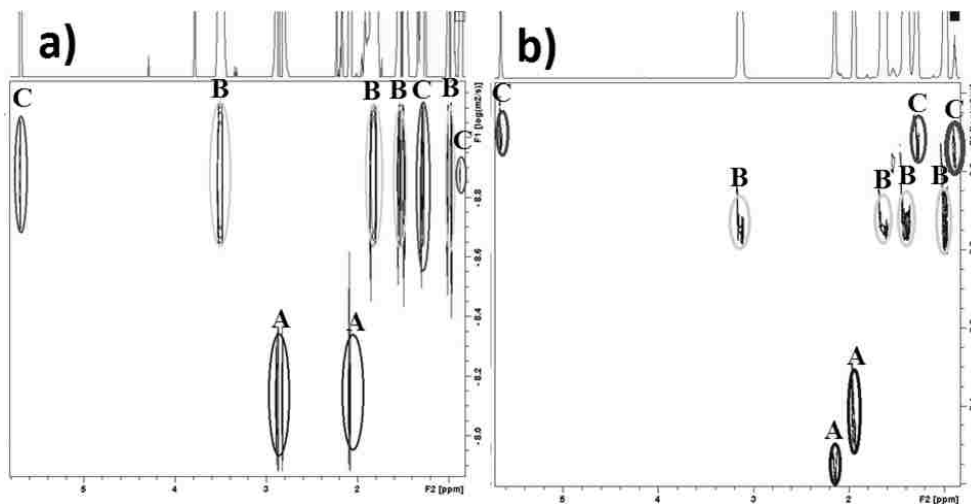


Figure 5.7 DOSY-NMR results of TBA*1 in acetone (a) and acetonitrile (b). A circle, solvent; B circle, tetrabutylammonium; C circle, surfactant anion. Reprinted with permission from ref. 28. Copyright 2012 Wiley-VCH.

5.3.4 Effect of counterions

Counterions play a critical role in colloid systems and biological systems, such as the folding of RNA molecules²⁹, the formation of virus capsid structures^{30,31}, and in the stabilization of biological macromolecules³². Due to their high charge density and hydrophilic nature, POMs exhibit strong counterion-dependent self-assembly, catalytic behavior and stability.⁷ In particular, counterion distribution around hydrophilic macroanions, and selective monovalent cation

association and exchange around Keplerate POM macroanions in dilute aqueous solutions are unique and directly related to their self-assembly process.³³⁻³⁵ On the other hand, counterions can also affect the behavior of common surfactants in aqueous solution, at air/solution interfaces or at solid/solution interfaces and in the micelle to vesicle transition processes.³⁶⁻³⁹ Therefore, the effect of counterions on the self-assembly of POM-containing hybrids is an interesting avenue, worth further investigation.

TBA*1 is not soluble in water, but soluble in polar organic solvents such as acetone and acetonitrile. Different salts, ZnCl₂, CuCl₂, NaI, tetrabutylammonium iodide (TBA*I) and dodecyltrimethylammonium bromide (DTMA*Br), which are soluble in acetonitrile, were added to acetonitrile solutions of TBA*1, respectively, to study the role of the counterions on the vesicle formation and vesicular sizes. The vesicle size decreased gradually with increasing concentration of ZnCl₂. Interestingly, the vesicle size remains unchanged at first upon addition of NaI, but gradually increases when the NaI concentration exceeds 0.03 mg/mL (Figure 5.8a). DOSY measurements indicated that the addition of NaI increases the diffusion coefficient (D) of TBA cations (without NaI, $D = 1.4 \times 10^{-9} \text{ m}^2/\text{s}$; with 0.1mg/mL NaI, $D = 2.0 \times 10^{-9} \text{ m}^2/\text{s}$), suggesting that the additional counterions replace the original TBA counterions around the Dawson clusters, and subsequently release TBA cations into the solution. ZnCl₂, which is quite solvated in acetonitrile, prefers coordinating to the terminal or bridging oxo ligands on the surface of the Dawson clusters, forcing the polar domains to be exposed to the solvent-environment, which in turn increases the curvature of the vesicle, i.e. the vesicle size becomes smaller. Upon the addition of NaI, on the other hand, the sodium ions contribute to shielding the high negative charges of the polar head groups from each other, and thus reduce the repulsion between the polar heads on the surface of the vesicle. The curvature of the vesicle decreases, and as a result the vesicle size increases. The same argument can be used to explain the formation of larger vesicles

from H*1 ($R_h = 110$ nm), compared to vesicles obtained from TBA*1 ($R_h = 75$ nm), both in acetonitrile.

The additions of CuCl_2 , TBA*I or DTMA*Br show no obvious effect on the vesicle size as those cations are not able to replace the TBA cations that surround the polar Dawson clusters. However, TBA*I and DTMA*Br were observed to cause the disassembly of the vesicles and this is confirmed by the fact that the scattered intensities from corresponding solutions drop increasingly when more of these salts were added (Figure 5.8b). Further, addition of TBA*I and DTMA*Br does not liberate the original TBA counterions, but results in a gradual accumulation of the hydrophobic cations around the hydrophilic Dawson clusters, causing a decrease in the hybrid molecule's amphiphilic nature. The TBA counterions dissociate the vesicle structures faster than DTMA, possibly due to the comparatively smaller volume of the TBA cations, which allows a larger amount of TBA cations to move closer to the POM, compared to the larger DTMA cations.

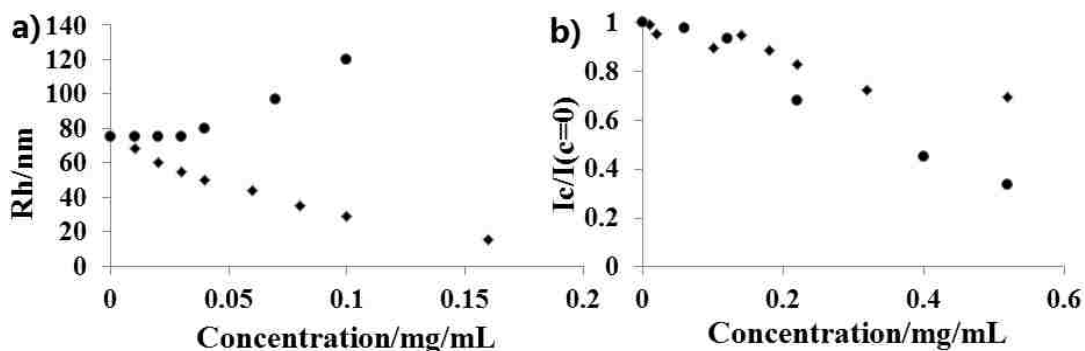


Figure 5.8 a) The plot of hydrodynamic radius vs. the concentration of added salt. Circle, NaI; Square, ZnCl_2 ; b) the plot of the reduced scattered intensity at 90° scattering angle vs. the concentration of added salt. Circle, TBA*I; Square, TMDA*Br. Reprinted with permission from ref. 28. Copyright 2012 Wiley-VCH.

5.3.5 Effect of pH

pH-sensitive vesicle structures are important for applications in sensing, imaging, and drug delivery systems.⁴⁰⁻⁴² $\{\text{Mo}_{72}\text{Fe}_{30}\}$, a POM macroanion, shows pH-controlled deprotonation in aqueous environment (like a weak acid) and results in pH-dependent assembled 'blackberry'

sizes.⁴³ H*1 is water soluble and its Dawson cluster polar head group behaves like a nanoacid, whose negative charges can be tuned by changing the pH of the solution.

The pH of a 1.0 mg/mL aqueous solution of H*1 is 2.99, corresponding to the release of ~ 4 protons per Dawson cluster. Vesicle structures with R_h of *ca.* 67 nm were observed from this solution by light scattering experiments. Interestingly, the R_h of the vesicle structures gradually decreased to 64 nm at pH = 5, while the R_h increased to 81 nm when pH = 1.5. A plateau area appears from pH = 5 to 9 with $R_h \sim 64$ nm. However, the R_h value decreased sharply to 38 nm when pH changed from 9 to 12 (Figure 5.9b). Further experiments indicate that the pH dependent self-assembly process can be done reversibly.

The increase of the pH value leads to further deprotonation of the polar head groups, which consequently increases their net charge. Therefore, the repulsion between the polar heads of the hybrids in the aggregates becomes stronger, resulting in significantly larger curvature of the vesicles, i.e. smaller size. The vesicles from the H*1 hybrids and the ‘blackberry’ structures formed by POM macroions show the same pH dependent self-assembly behavior.⁴³ However, the driving forces for the two aggregates are different. It is the solvophobic interaction that controls the assembly of the H*1 hybrid surfactant, whilst the counterion mediated attractive forces and the hydrogen bonding interactions are the major factors for the blackberry formation.

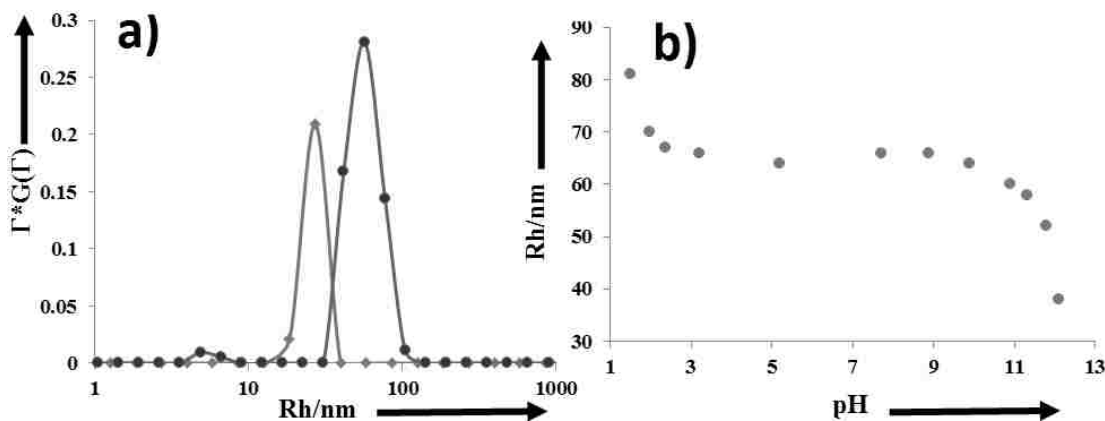


Figure 5.9 a) DLS results of H*1's aqueous solution at pH = 1.5 (●) and pH= 12 (◆) at 90° scattering angle; b) The plot of hydrodynamic radii of vesicles vs. pH of the hybrid aqueous solution. Reprinted with permission from ref. 28. Copyright 2012 Wiley-VCH.

5.3.6 Fluorescence

Interestingly, **2** shows strong blue luminescence in both aqueous and acetone solution when the counterions are protons. With an excitation at $\lambda=335\text{nm}$, both $\text{H}_2^*\mathbf{2}$ and $\text{Na}_2^*\mathbf{2}$ emit blue luminescence, peaked at 392nm, 409nm and 429nm (see Figure 5.10), respectively. Interestingly, the intensities of the first and the third peaks are higher than that of the second peak, which is different from the spectrum of $\text{H}_2^*\mathbf{2}$. The incident light with wavelength 300 - 420 nm can trigger such blue fluorescence. No emission is observed if the wavelength of the light is below 300nm. The excitation band for $\text{H}_2^*\mathbf{2}$ is around its Ligand (oxo) to Metal (vanadium) Charge Transfer (LMCT) absorption wavelength and it is possible that the origin of the emission involves an emission derived from an LMCT transition.⁴⁴

Admittedly, several other POMs were found to have photoluminescence properties in solid state at very low temperatures (e.g., 4K). A few of them retain the property in aqueous solution at room temperature.^[11] The photoluminescence mainly comes from the introduction of Eu^{3+} and most of POMs without Eu^{3+} do not have such property and even worse, they are usually considered as fluorescence quenchers due to their special ability to reserve electrons and stabilize fragile structures. $[\text{Et}_4\text{N}]_5[\text{V}_{14}\text{O}_{36}\text{Cl}]$ was observed to produce intense blue luminescence in

aqueous solution by Hong *et al.* who claimed that luminescence properties have rarely been reported for vanadium oxide clusters.⁴⁴

To further understand **2**'s luminescent properties, the fluorescence of $[\text{V}_6\text{O}_{13}\{(\text{OCH}_2)_3\text{COH}\}_2]^{2-}$ was tested with different counterions. Same luminescence, but with much lower intensity, is observed as **2** when protons are the counterions. Zubieta showed that minor structural change was observed in the $[\text{V}_6\text{O}_{13}\{(\text{OCH}_2)_3\text{CR}\}_2]$ core when protons associated with the bridge oxygen ligands, which might also lead to the red shift of the characteristic peak from 350 nm ($\text{TBA}_2*\mathbf{2}$) to 369 nm ($\text{H}_2*\mathbf{2}$) in their UV-Vis spectrum. It is possible that the minor structural change of the POM cores due to counterion exchange lead to the light emitting phenomenon.^[9] Moreover, the self-assembly of **2** and the presence of protons or sodium ions as counterions probably results in the higher luminescence intensity from **2**. The distances between polar heads should be very small due to the small sizes of proton and sodium ions in the assemblies and the interaction between POM polar head groups would become much stronger, which maybe strengthen the luminescence.

Excited at 410 nm, the aggregates of $\text{H}_2*\mathbf{2}$ in aqueous solution can be observed in a fluorescent microscope (Figure 5.10). Due to the small size of the aggregate, very tiny (diffraction limited size) dots can be seen. The intensity of the captured "dot" (Figure 5.10) did not show obvious decay in 30 min, which is totally different from the behaviour of organic fluorophores that exhibit photobleaching. The luminescence studies shown in Figure 3d indicate that the vanadate-hybrid does not break down under UV-light. Another possibility is that the alkyl tails might break from the POM while the POM head group stays intact. This is unlikely based on our detailed studies on the self-assembly of these hybrids below. The large assemblies (the microspheres observed under the fluorescent microscope) will not be stable after losing the alkyl chains. The possible connections between the hybrids' luminescence property and solution behaviors make us to explore the self-assembly of the hybrid in solution.

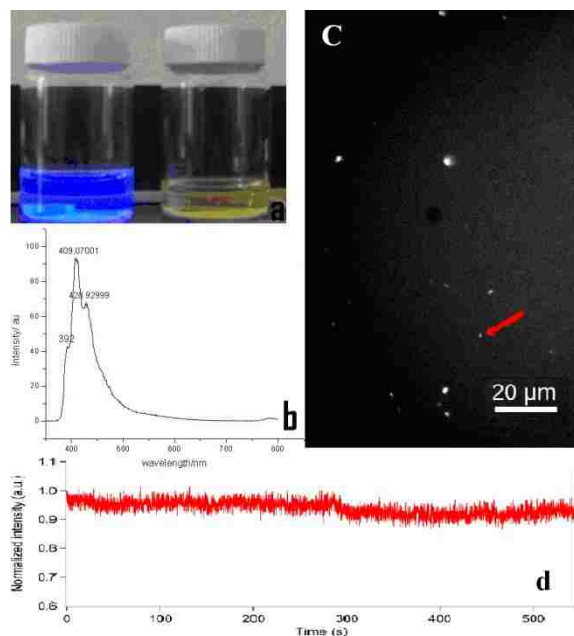


Figure 5.10 (a) H_2^*2 (left) and TBA_2^*2 (right) solution under UV light; (b) Fluorescence spectrum of H_2^*2 excited at 335 nm; (c) Fluorescent image of H_2^*2 in aqueous solution (By recording the intensity of the red arrow pointed assembly, we are able to analyze the decay of the normalized intensity over time); (d) Total intensity changes with time for a dot marked with an arrow in (c) demonstrating stability of 2's blue fluorescence. Reprinted with permission from ref. 20. Copyright 2011 Wiley-VCH.

5.3.7 Formation of nano-structures and the stability of the vesicles

The addition of divalent counterions to an aqueous solution of the H^*1 hybrid causes a decrease in the stability of the self-assembled structures. When 20 μL of 0.02 mg/mL CaCl_2 aqueous solution was added into a 5 mL aqueous solution of the H^*1 hybrid (~ 0.2 mg/mL), the solution became cloudy and the formation of a large amount of uniform macro-needle like structures was observed. SEM results indicate that the length of the needles is *ca.* 320 μm and the diameter of the cross section is *ca.* 2.7 μm , which is quite similar to the assemblies observed for Anderson-based surfactant on silicon substrate⁴⁵ (Figure 5.11). The micro-needle structures show high contrast from the iron substrate under SEM mode, suggesting that the polar head groups should be on the surface of the micro-structures. Known as the salting out effect⁴⁶, addition of Ca^{2+} leads to stronger interaction among the assemblies and the consequent coagulation of the assemblies.

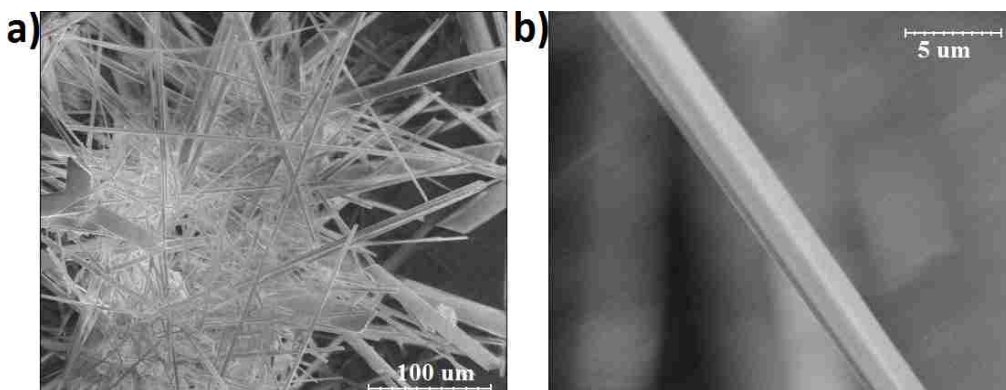


Figure 5.11 a) SEM image of the micro-needle structures; b) Zoom in image of one needle. Reprinted with permission from ref. 28. Copyright 2012 Wiley-VCH.

In water-acetone mixed solvent containing 20 vol% water of TBA*2, the average vesicle radius was around 180-220 nm for the compound concentrations from 0.375 to <1.5 mg/mL. SEM results indicate that the cloudy solution at 1.5 mg/mL contains similar micro-plate crystals described above (Figure 5.12).

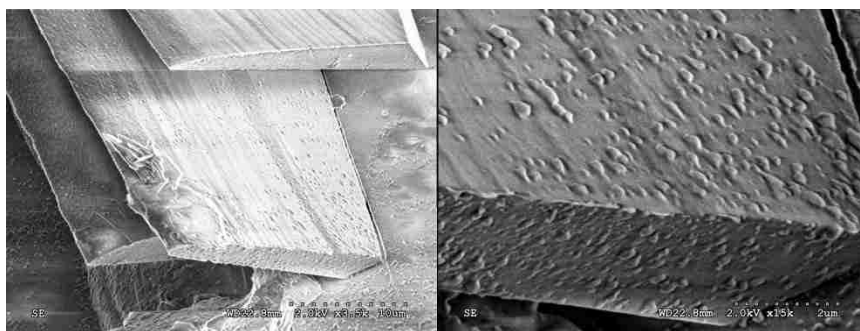


Figure 5.12 Left: SEM image of micro-sheet structure formed by 1. Right: Zoom in image of the surface of the micro-sheet. Reprinted with permission from ref. 20. Copyright 2011 Wiley-VCH.

5.4 Conclusion

Two organic-inorganic hybrid surfactants with the Dawson-type POM cluster and hexavanadate acting as the polar head groups, have been synthesized, which are able to self-assemble into vesicle structures in polar solvents. The size of the vesicles can be adjusted by hybrid concentration and the solvent polarity. In organic polar solvent, the vesicle formation and their corresponding sizes are dependent on the addition of salts: Zn^{2+} cations can decrease the vesicle

size, whilst Na⁺ and H⁺ cations can screen the repulsive interaction between POM polar head groups and thus increases the size of the vesicles. Due to the positive charge and hydrophobic properties of tetraalkylammonium ions, the addition of these can decrease the surfactant's amphiphilic features and eventually disassemble the vesicle structures. In aqueous solution, raising the solution pH can reversibly decrease the size of the vesicles by shielding the repulsion between polar head groups. The addition of Ca²⁺ triggers the collapse of vesicles into micro-needle structures.

Reference

- (1) Hill, C. L. *Chem. Rev.* **1998**, *98*, 1.
- (2) Long, D.-L.; Tsunashima, R.; Cronin, L. *Angew. Chem. Int. Ed.* **2010**, *49*, 1736.
- (3) Long, D.-L.; Cronin, L. *Chem. Eur. J.* **2006**, *12*, 3698.
- (4) Katsoulis, D. E. *Chem. Rev.* **1998**, *98*, 359.
- (5) Liu, T. B. *Langmuir* **2010**, *26*, 9202.
- (6) Liu, T. B.; Diemann, E.; Li, H. L.; Dress, A. W. M.; Muller, A. *Nature* **2003**, *426*, 59.
- (7) Yin, P.; Li, D.; Liu, T. *Isr. J. Chem.* **2011**, *51*, 191.
- (8) Cooper, G. J. T.; Cronin, L. *J. Am. Chem. Soc.* **2009**, *131*, 8368.
- (9) Pradeep, C. P.; Long, D.-L.; Newton, G. N.; Song, Y.-F.; Cronin, L. *Angew. Chem. Int. Ed.* **2008**, *47*, 4388.
- (10) Kojima, T.; Antonio, M. R.; Ozeki, T. *J. Am. Chem. Soc.* **2011**, *133*, 7248.
- (11) Zheng, S.-T.; Zhang, J.; Li, X.-X.; Fang, W.-H.; Yang, G.-Y. *J. Am. Chem. Soc.* **2010**, *132*, 15102.
- (12) Zhang, J.; Hao, J.; Wei, Y.; Xiao, F.; Yin, P.; Wang, L. *J. Am. Chem. Soc.* **2009**, *132*, 14.

- (13) Kang, J.; Xu, B.; Peng, Z.; Zhu, X.; Wei, Y.; Powell, D. R. *Angew. Chem. Int. Ed.* **2005**, *44*, 6902.
- (14) Han, J. W.; Hill, C. L. *J. Am. Chem. Soc.* **2007**, *129*, 15094.
- (15) Zheng, S.-T.; Zhang, J.; Yang, G.-Y. *Angew. Chem. Int. Ed.* **2008**, *47*, 3909.
- (16) Wang, Y. F.; Weinstock, I. A. *Dalton* **2010**, *39*, 6143.
- (17) Yan, Y.; Wu, L. *Isr. J. Chem.* **2011**, *51*, 181.
- (18) Yan, Y.; Wang, H.; Li, B.; Hou, G.; Yin, Z.; Wu, L.; Yam, V. W. W. *Angew. Chem. Int. Ed.* **2010**, *49*, 9233.
- (19) Landsmann, S.; Lizandara-Pueyo, C.; Polarz, S. *J. Am. Chem. Soc.* **2010**, *132*, 5315.
- (20) Yin, P.; Wu, P.; Xiao, Z.; Li, D.; Bitterlich, E.; Zhang, J.; Cheng, P.; Vezenov, D. V.; Liu, T.; Wei, Y. *Angew. Chem. Int. Ed.* **2011**, *50*, 2521.
- (21) Zhang, J.; Song, Y.-F.; Cronin, L.; Liu, T. *J. Am. Chem. Soc.* **2008**, *130*, 14408.
- (22) Zhang, J.; Song, Y.-F.; Cronin, L.; Liu, T. *Chem. Eur. J.* **2010**, *16*, 11320.
- (23) Giner-Casares, J. J.; Brezesinski, G.; Möhwald, H.; Landsmann, S.; Polarz, S. *J. Phys. Chem. Lett.* **2012**, *3*, 322.
- (24) Han, Y.; Xiao, Y.; Zhang, Z.; Liu, B.; Zheng, P.; He, S.; Wang, W. *Macromolecules* **2009**, *42*, 6543.
- (25) Hiemenz, P. C.; Rajagopalan, R. *Principles of Colloid and Surface Chemistry*; Marcel Dekker: New York, 1997.
- (26) Provencher, S. W. *Comput. Phys. Commun.* **1982**, *27*, 229.
- (27) Pradeep, C. P.; Misdrahi, M. F.; Li, F.-Y.; Zhang, J.; Xu, L.; Long, D.-L.; Liu, T.; Cronin, L. *Angew. Chem. Int. Ed.* **2009**, *48*, 8309.
- (28) Yin, P.; Pradeep, C. P.; Zhang, B.; Li, F.-Y.; Lydon, C.; Rosnes, M. H.; Li, D.; Bitterlich, E.; Xu, L.; Cronin, L.; Liu, T. *Chem. Eur. J.* **2012**, *18*, 8157.

- (29) Roh, J. H.; Behrouzi, R.; Briber, R. M.; Guo, L.; Thirumalai, D.; Woodson, S. A. *Biophys. J.* **2009**, *96*, 575a.
- (30) Zlotnick, A. *Virology* **2003**, *315*, 269.
- (31) Zlotnick, A.; Aldrich, R.; Johnson, J. M.; Ceres, P.; Young, M. J. *Virology* **2000**, *277*, 450.
- (32) Heilman-Miller, S. L.; Thirumalai, D.; Woodson, S. A. *J. Mol. Bio.* **2001**, *306*, 1157.
- (33) Pigga, J. M.; Kistler, M. L.; Shew, C. Y.; Antonio, M. R.; Liu, T. B. *Angew. Chem. Int. Ed.* **2009**, *48*, 6538.
- (34) Pigga, J. M.; Liu, T. *Inorg. Chim. Acta.* **2010**, *363*, 4230.
- (35) Pigga, J. M.; Teprovich, J. A.; Flowers, R. A.; Antonio, M. R.; Liu, T. B. *Langmuir* **2010**, *26*, 9449.
- (36) Bitting, D.; Harwell, J. H. *Langmuir* **1987**, *3*, 500.
- (37) Silbert, G.; Klein, J.; Perkin, S. *Faraday Discuss.* **2010**, *146*, 309.
- (38) Evans, D. F.; Evans, J. B.; Sen, R.; Warr, G. G. *J. Phys. Chem.* **1988**, *92*, 784.
- (39) Evans, J. B.; Evans, D. F. *J. Phys. Chem.* **1987**, *91*, 3828.
- (40) Chen, W.-J.; Li, G.-Z.; Zhou, G.-W.; Zhai, L.-M.; Li, Z.-M. *Chem. Phys. Lett.* **2003**, *374*, 482.
- (41) Long, P.; Song, A.; Wang, D.; Dong, R.; Hao, J. *J. Phys. Chem. B* **2011**, *115*, 9070.
- (42) Du, J.; Tang, Y.; Lewis, A. L.; Armes, S. P. *J. Am. Chem. Soc.* **2005**, *127*, 17982.
- (43) Liu, T. B.; Imber, B.; Diemann, E.; Liu, G.; Cokleski, K.; Li, H. L.; Chen, Z. Q.; Muller, A. *J. Am. Chem. Soc.* **2006**, *128*, 15914.
- (44) Chen, L.; Jiang, F.; Lin, Z.; Zhou, Y.; Yue, C.; Hong, M. *J. Am. Chem. Soc.* **2005**, *127*, 8588.

(45) Song, Y.-F.; McMillan, N.; Long, D.-L.; Thiel, J.; Ding, Y.; Chen, H.; Gadegaard, N.; Cronin, L. *Chem. Eur. J.* **2008**, *14*, 2349.

(46) Bockris, J. O. M.; Egan, H. *Trans. Faraday Soc.* **1948**, *44*, 151.

Chapter 6: Programmed Spontaneous Self-Assembly of Polyoxometalates-Organic Hybrid into Catalytic Active Nano-belt

6.1 Introduction

The self-assembly of molecules, nanoparticles, and colloids into well-defined micro- and macro-structures represents one of the key bottom-up protocols in building up artificial devices and functional units inside cells and viruses.¹⁻⁵ Single-component spontaneous self-assembly is usually adopted by nature due to the convenience in duplication and the need of limited genetic codes, e.g. viral capsids and cell membranes are composed of single capsid unit protein and single phospholipid molecule.^{6,7} However, multiple components are required to build artificial devices and moreover, the self-assembly process need to be triggered or directed by tuning the environment parameters or designing the interaction process between multiple species. Currently, limited research have been carried out to build artificial functional structures from spontaneous self-assembly because of the lack of knowledge in weak interactions that direct the self-assembly process and the design of functional building block.⁸⁻¹¹ Additionally, detailed study of self-assembly mechanism (e.g. kinetics and intermediate state) is rare although quite important to help us in understanding the weak interactions.¹²⁻¹⁶

Polyoxometalates (POMs) are a large group of metal oxide clusters with wide applications in catalysis, photo-electronic, and magnetic materials, medicine, and self-assembly research.¹⁷ The processing of POMs into nano-scaled materials could be applied to enhance their heterogeneous catalytic activity and build devices with varied functionalities.¹⁸ Specifically, one-dimensional (1D) nano-materials including nanotube, nanowire (nano-fiber), nanorod, and nanobelt are significant in designing electronic and optical devices, bioactive hydrogels, scaffolds in tissue engineering, and high-strength materials.¹⁹ However, rare studies on POM-based 1D nano-

material have been reported.^{20,21} Herein, we report the unique spontaneous self-assembly process of POM-organic hybrid into nano-belt structure based on the hydrophobic interaction and hydrogen bonding. Interestingly, it is the first time that micelle structures were observed as the intermediate state in the self-assembly process. Time-resolved small-angle X-ray scattering (SAXS) and TEM studies provide the detailed mechanism on the transformation of micelle to the nano-belt structures. Moreover, the resulted nano-belt is stable in aqueous and organic media. It is also a catalytically active against oxidation desulfurization reactions.

6.2 Experimental section

General. H₂O₂ (30% wt), n-octane, methyl *p*-tolyl sulfide, acetonitrile, D₂O, KOH, NaOH, LiOH, CsOH, NH₃*H₂O, and urea were purchased from Sigma-Aldrich and used without further purification. JEOL 2000 was used for TEM study and Hitachi 4300 was used for SEM study. Hewlett Packard 5890 Series II GC-MS was used to monitor the oxidation reactions of sulfide.

SAXS. The SAXS experiments were performed at 12-ID-B station with X-ray energy of 12 KeV at the Advanced Photon Source of the Argonne National Laboratory. The sample to detector distance was about 2 m. A 2D CCD detector was used to acquire images with typical exposure times in the range of 1.0 s.

Electron microscopy. Several drops of the solutions with target assemblies or aggregates were titrated onto the shiny surface of the copper grids, which were then dried in the air. The copper grids would be ready for TEM study after at least three days. While for SEM studies, the solutions were titrated to the surface of Al substrate (diameter, 25 mm) and dried in air for three days.

Atomic force microscopy (AFM). AFM imaging experiments were carried out on an MFP-3D-BIO atomic force microscope (Asylum Research, Santa Barbara, CA). The AFM images were taken in tapping mode in fluid with a closed-fluid cell. The FMR cantilevers used in the

experiments are on-contact mode high frequency silicon cantilevers, which are manufactured by Vista Probes (Phoenix, AZ). The image data were processed using Igor Pro (WaveMetrics, Inc. Lake Oswego, OR) with Asylum MFP-3D extension. The images were first flattened with an X-Y plane-fit to the scan lines. The images were then flattened with a second order polynomial fit to the scan lines after masking out the nano-belt area.

Catalytic reaction set up. 130 uL sulfide, 300 uL H₂O₂ (30%, wt), 65 uL octane and the catalysts (6 mg TBA***1** or different loading amount of the nanobelts, from 0 to 6 mg) were mixed in 3 mL acetonitrile. The reaction solution was kept at 40 °C through oil bath with stirring at 1000 rpm. GC-MS was used to monitor the reactions. Octane was used as standard to measure the relative concentration of reactant and products. Relative concentration of certain species was calculated as

$$c = \frac{I_t}{I_{\text{Octane,t}}} \bigg/ \frac{I_{\text{sulfide,o}}}{I_{\text{Octane,o}}}$$

6.3 Results and discussion

6.3.1 Synthesis and molecular structure of hybrid **1**

The synthesis of hybrid **1** has been done in our collaborators' laboratory and will be published separately. The molecular structure of the hybrid was showed in Figure 6.1a, which is a typical structure of single-tailed surfactant with hexavanadate as polar head groups. Different from our previous surfactants with POMs as polar head groups, two amine groups were incorporated into the molecular structure of **1**, which were designed to introduce inter-molecular hydrogen bonding interaction (amine can interaction with surface oxo ligands of POMs through hydrogen bonding).^{22,23} Single crystal X-ray diffraction analysis on TBA₂***1** (TBA, tetrabutyl ammonium) indicates that the POM clusters interact with neighbor cluster with double N-H...O hydrogen bonds to form 1D chain structures (Figure 6.1b). The 1D chain structures further pack with each other by counter-ion (TBA) mediated attractions to build 2D sheet structures. Since the inter-layer

is packed by alkyl tails, these two 2D sheets were stuck together by hydrophobic interactions to form A-B-A sandwich-type structures (Figure 6.1c). TBAs were used to fill the space between the A-B-A structures to finally pack into 3D crystals.

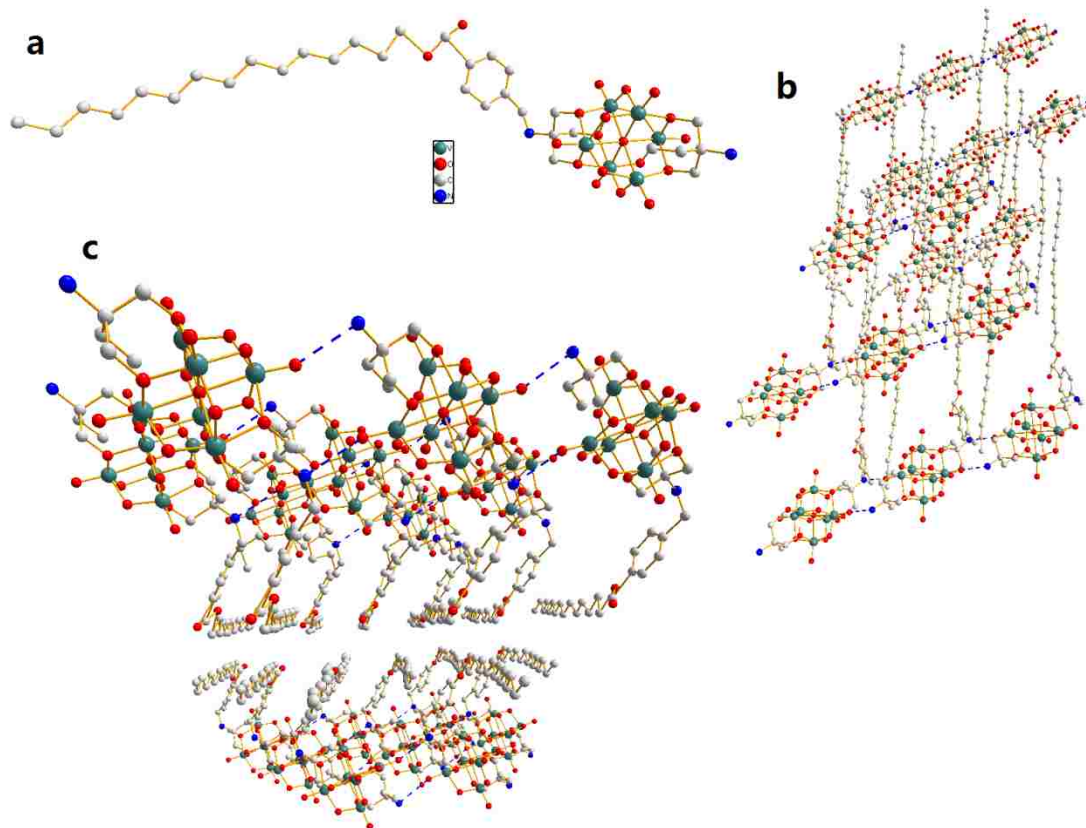


Figure 6.1 a) Ball-stick representation of the molecular structure of hybrid 1; b) top view of the A-B-A layer structures; c) side view of the A-B-A layer structure.

6.3.2 Morphological characterization of nano-belts

H₂*1 was dissolved in KOH solution with pH = 13.3 (surfactant concentration: 2.5 mg/mL). The obtained solution is clear solution, suggested by low scattered intensity at 90° from SLS studies (~ 100 kcps; scattered intensity for benzene, 113 kcps). However, the solution became cloudy several hours after the preparation without any external stimulus (Figure 6.2a). Large 1D aggregates were observed under optical microscope (Figure 6.2b). SEM and TEM studies suggest that these aggregates are uniform 1D nano-belts with thickness and width at nanometer scale while their lengths are at micrometer scale (Figure 6.2c, d, and e). High resolution TEM studies

on the nano-belt structures suggest the polar heads of surfactants interact with each other to form layered structures, which further pack together to form the nano-belts (Figure 6.2d and e). Atomic force microscopy confirmed the belt morphology of the aggregates under wet condition and was able to accurately determine the thickness of the nanobelts as ~ 20 nm (Figure 6.3). SAXS analysis on the nano-belts dispersed in solution shows three sharp peaks at $q = 0.202, 0.609,$ and 0.720 \AA^{-1} , corresponding to the inter-layer distance (3.11 nm) and inter-polar head groups distances (1.03 nm and 0.87 nm) when they pack in the layer (Figure 6.4).

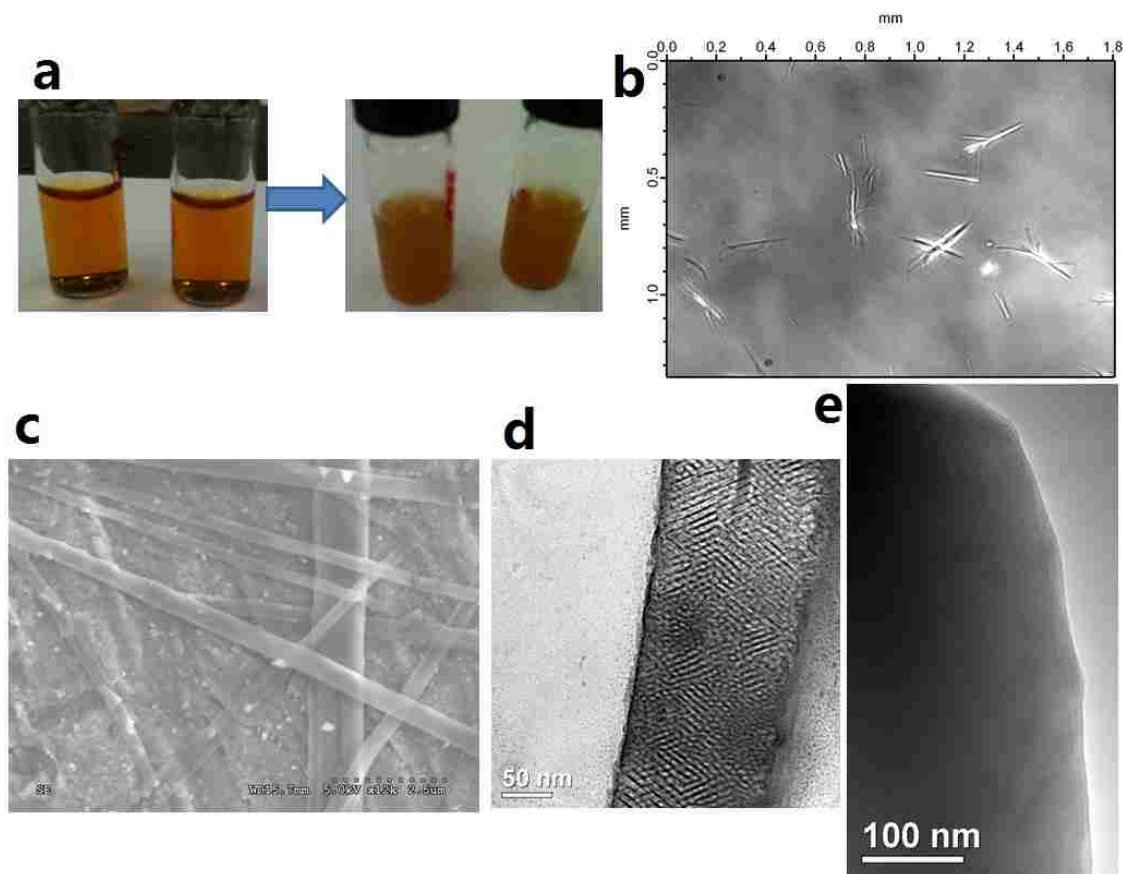


Figure 6.2 a) Pictures of the newly prepared solutions and the solutions became cloudy two hours after their preparation; b) optical microscopy images of the aggregates; c) SEM image of nano-belt structures; d) TEM image of the packing of polar heads on the surface of nano-belt; e) TEM images of the layer structures of nano-belt.

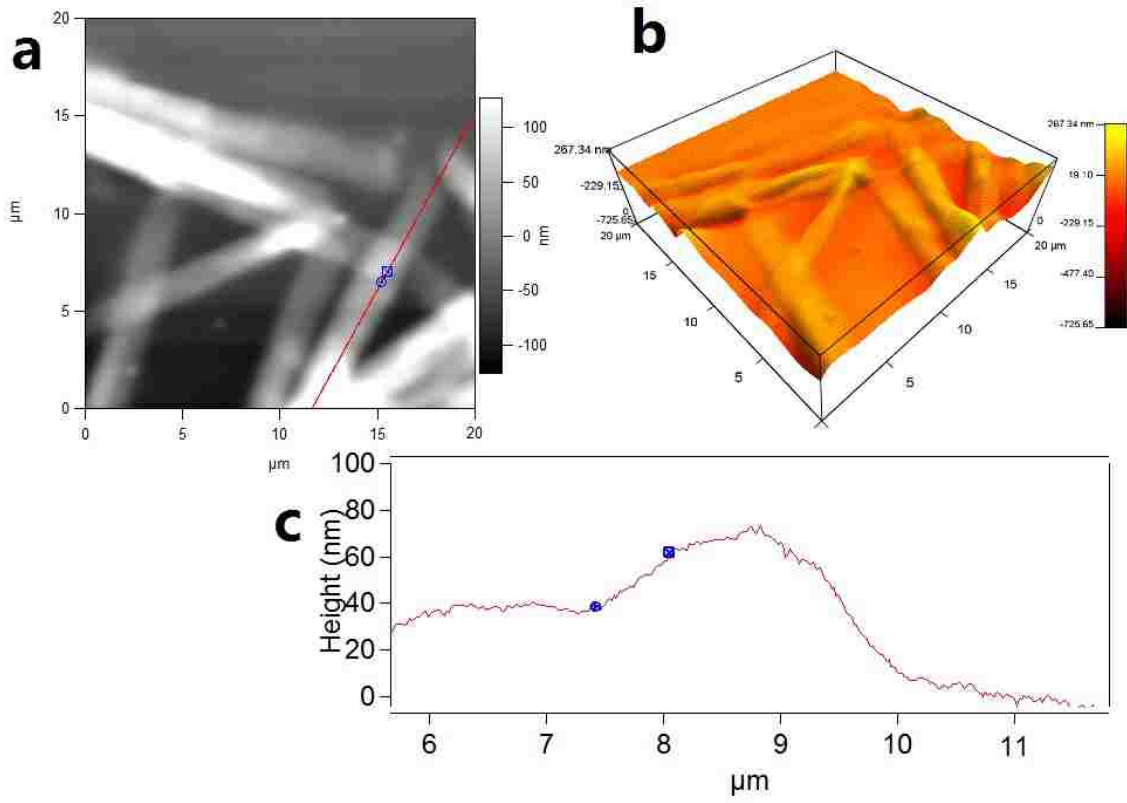


Figure 6.3 a) AFM images of nano-belts under wet condition; b) Z-direction graph of the features; c) Z-direction curve of the selected line.

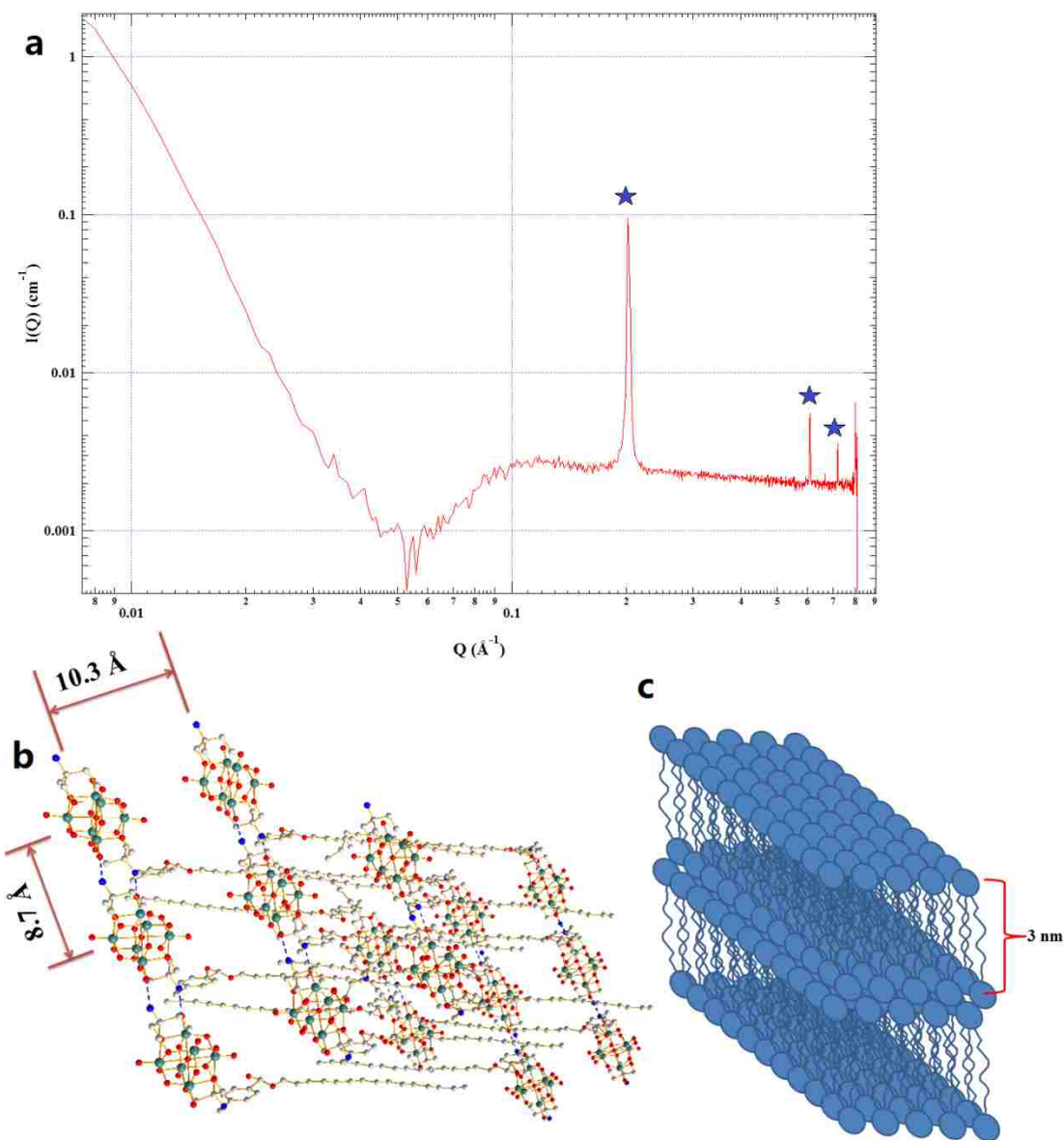


Figure 6.4 a) SAXS curve of the nano-belt dispersion solution; b) c) Models of the nanobelts.

6.3.3 Kinetics study of nano-belts formation

SAXS studies on the hybrid's 'real' solution when it was just dissolved in KOH solution show a typical curve of core-shell structures with radius, core size, and shell size are 4.19, 2.51, and 1.68 nm, respectively (Figure 6.5a and b). The core-shell assemblies actually represent the micelle structure of the hybrid with hydrophilic polar as the shell part and hydrophobic alkyl tails, which were confirmed by TEM images of the assemblies in the 'real' solution (Figure 6.5e). Time-resolved SAXS studies on the solutions indicate that three sharp peaks of belts appeared and

increased while at the same time the characteristic oscillation curve of micelle structure became weaker and weaker, and disappeared in 680 min (Figure 6.5c). Detailed SAXS kinetic study was summarized in Figure 6.5d by plotting the intensity of the first peak ($q = 0.202 \text{ \AA}^{-1}$) of the nanobelt and the intensity of micelle curve vs. time during 680 min period. Both of two plots show typical sigmoidal shape, suggesting a slow initial nucleation process of micelle structures at the beginning of the self-assembly process. It is believed that the micelles structures coagulate and form primary layer structures at the 60-min lag phase, suggested by the TEM studies at the lag phase period (Figure 6.5f). Due to the comparatively larger size of the initial assemblies, especially the micrometer-scaled length, the diffusion of the aggregates became much slower and the position for new micelle to be merged became larger, which accelerate growth rate of layer structures and the coagulation of micelles.

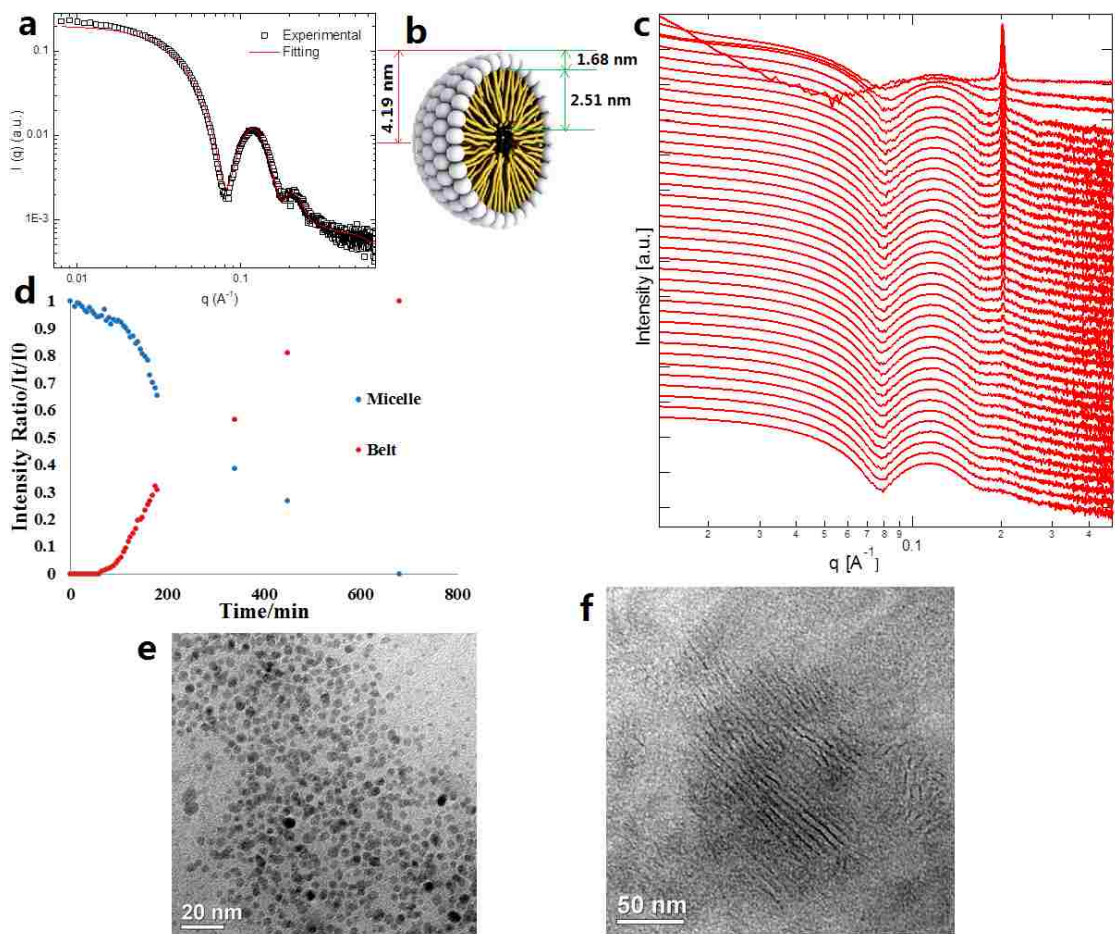


Figure 6.5 a) SAXS curve of initial solution and fitted with core-shell model; b) graphical representation of micelle structure; c) time-resolved SAXS results of the hybrid's solution; d) Plot of micelle peak and nano-belt peak vs. time; e) f) TEM images of micelle and primary lamellar phase structures, respectively.

The formation of nano-belt structures is highly dependent on solution pH, counter-ions, and hydrogen bonding. TEM studies on the aggregates of the hybrid dissolved in solution of pH ranging from 13.3 to 7.8 indicate that the rigidity of the belts decreased when pH decreased from 13.3 to 9.0. No regular structures were observed when the pH of aqueous solution < 8 (Figure 6.6). Moreover, SAXS studies on the hybrid solutions in LiOH, NaOH, KOH, and $\text{NH}_3 \cdot \text{H}_2\text{O}$ at almost the same pH value (ca. 12.6) show that regular nano-belts structures were only observed in KOH and $\text{NH}_3 \cdot \text{H}_2\text{O}$ solutions. On the other hand, the formation of nano-belts structures became significantly slower by adding urea in hybrid's KOH solution (urea concentration, 1 M) or replacing H_2O with D_2O in hybrid's KOH solution (more than 2 days). The summarization of the

above experimental results indicates the importance of charge interaction and hydrogen bonding in the formation of nano-belts. The low pH (< 8) value of aqueous solution makes the surfactant/micelle structures lowly charged and significantly weaken the charge interaction and lead to the irregular precipitation. Meantime, K^+ and NH_4^+ can lead to coagulation of micelles and further the forming of nano-belts. However, micelle structures are still stable in solution with Na^+ or Li^+ as counterions and no observation of the nano-belts.

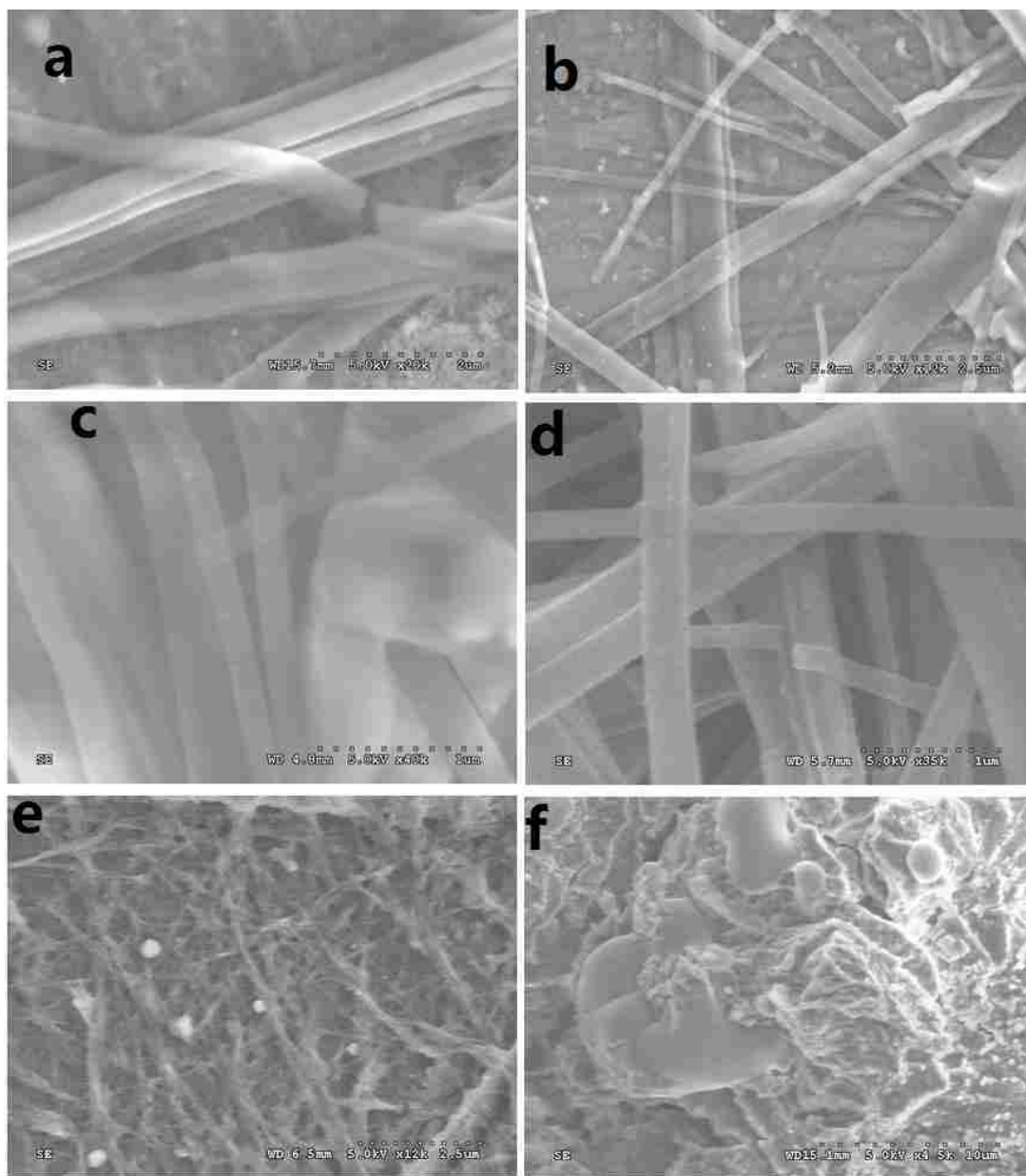


Figure 6.6 SEM images of the aggregates in solutions with pH as a) 11.9, b) 10.8, c) 10.5, d) 9.8, e) 9.0, and f) 7.8.

6.3.4 Oxidative desulfurization Catalysis by nano-belts

Hexavanadate, one of the catalytic active POMs in oxidation reactions, fully covers the surface of nano-belt structures and therefore, the nanobelts could work as heterogeneous catalysts. Herein, the catalytic efficiency of nanobelts was evaluated based on the catalyzed oxidative desulfurization reaction. The nanobelts structures were tested to be stable in acetonitrile and used to catalyze the oxidation of methyl *p*-tolyl sulfide with H₂O₂ (wt, 30%) (Figure 6.7a). The sulfide

were fully oxidized into sulfide mono-oxide and sulfone (molar ratio, 1:1) after running the reaction for 1.5 hrs at 40 °C with the loading of 6 mg of nano-belts (Figure 6.7b). Three hours after the sulfide is consumed, all the sulfide mono-oxide turned into sulfone. SEM studies on the catalysts after the reaction indicate that the belt structures remains stable after the reaction (Figure 6.7c). The catalysts were easily re-collected through centrifugation and further catalytic reactions proved that the catalysts did not lose catalytic efficiency for at least two more cycles. Moreover, catalytic reactions with homogeneous catalysts (6 mg) and different loading amounts of heterogeneous catalysts (0 ~ 6 mg) were carried out and the time it takes for the sulfide to be fully consumed was recorded for each case to generate a comparative study. The results indicate that the time it takes for the sulfide to get consumed is inversely proportional to the amount of heterogeneous catalyst added to the system to complete the reaction (Figure 6.7d). Even though the catalytic activity is better when the catalyst is used homogeneously (40 min), heterogeneous catalysis (1.5 hr) will still provide the option of catalyst recyclability, which is a great advantage.

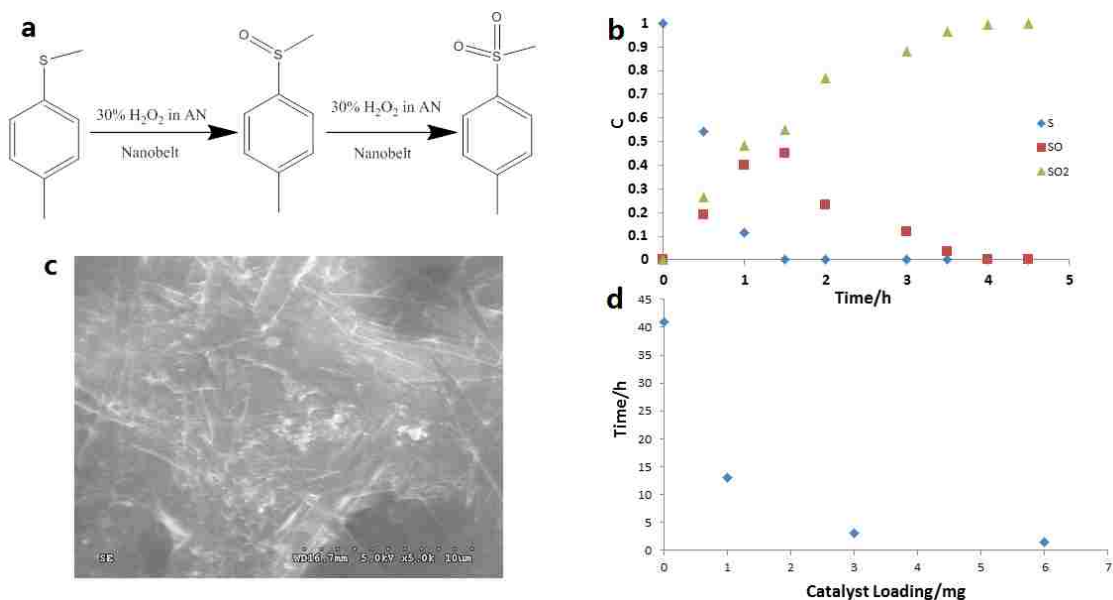


Figure 6.7 a) Reaction scheme for the oxidation of sulfide; b) kinetic curves of the concentrations of reactant and products in the reaction catalyzed by 6mg nano-belts; c) SEM images of the catalysts after the oxidation of sulfide reaction; d) reaction time of oxidation of sulfide reactions with different loading amount of nano-belts.

6.4 Conclusion

A new surfactant with hexavanadate as polar head groups were designed, synthesized, and programmed to self-assemble into 1D nano-belts structures. The formation mechanism was claimed to the coagulation of micelles into layered structures. The nanobelts were proved to high efficient heterogeneous catalysts for oxidation of sulfide.

Reference

- (1) Zhang, S.; Marini, D. M.; Hwang, W.; Santoso, S. *Current Opinion in Chemical Biology* **2002**, *6*, 865.
- (2) Lee, Y. S. In *Self-Assembly and Nanotechnology*; John Wiley & Sons, Inc.: 2007, p 183.
- (3) Whitesides, G. M.; Grzybowski, B. *Science* **2002**, *295*, 2418.
- (4) Yan, Y.; Chan-Park, M. B.; Zhang, Q. *Small* **2007**, *3*, 24.
- (5) *Molecular Self-Assembly Organic Versus Inorganic Approaches*; Fujita, M., Ed.; Springer: Berlin, 2000; Vol. 96.
- (6) Zlotnick, A.; Aldrich, R.; Johnson, J. M.; Ceres, P.; Young, M. J. *Virology* **2000**, *277*, 450.
- (7) Antonietti, M.; Förster, S. *Adv. Mater.* **2003**, *15*, 1323.
- (8) Desfougères, Y.; Croguennec, T.; Lechevalier, V. r.; Bouhallab, S. d.; Nau, F. o. *J. Phys. Chem. B* **2010**, *114*, 4138.
- (9) Shillcock, J. C. *Langmuir* **2011**, *28*, 541.
- (10) Suzuki, K.; Tsukidate, T.; Shimizu, M.; Ishiguro, A. In *Intelligent Robots and Systems, 2009. IROS 2009. IEEE/RSJ International Conference on 2009*, p 4343.
- (11) Villari, V.; Mineo, P.; Scamporrino, E.; Micali, N. *Chem. Phys.* **2012**, *409*, 23.
- (12) Zhao, Z.; Lu, W. *Phys. Rev. E* **2012**, *85*, 041124.

- (13) Lara, C. c.; Adamcik, J.; Jordens, S.; Mezzenga, R. *Biomacromolecules* **2011**, *12*, 1868.
- (14) Zhang, D.; Wang, J.; Chen, S.; Cheng, X.; Li, T.; Zhang, J.; Zhang, A. *Langmuir* **2012**, *28*, 16772.
- (15) Kang, S.-g.; Li, H.; Huynh, T.; Zhang, F.; Xia, Z.; Zhang, Y.; Zhou, R. *ACS Nano* **2012**, *6*, 9276.
- (16) Giacometti, A. *Centr.Eur.J.Phys.* **2012**, *10*, 540.
- (17) Long, D.-L.; Burkholder, E.; Cronin, L. *Chem. Soc. Rev.* **2007**, *36*, 105.
- (18) Song, Y.-F.; Tsunashima, R. *Chem. Soc. Rev.* **2012**, *41*, 7384.
- (19) Xia, Y.; Yang, P.; Sun, Y.; Wu, Y.; Mayers, B.; Gates, B.; Yin, Y.; Kim, F.; Yan, H. *Adv. Mater.* **2003**, *15*, 353.
- (20) Ritchie, C.; Cooper, G. J. T.; Song, Y.-F.; Streb, C.; Yin, H.; Parenty, A. D. C.; MacLaren, D. A.; Cronin, L. *Nature Chem.* **2009**, *1*, 47.
- (21) Nisar, A.; Zhuang, J.; Wang, X. *Adv. Mater.* **2011**, *23*, 1130.
- (22) Yin, P.; Pradeep, C. P.; Zhang, B.; Li, F.-Y.; Lydon, C.; Rosnes, M. H.; Li, D.; Bitterlich, E.; Xu, L.; Cronin, L.; Liu, T. *Chem. Eur. J.* **2012**, *18*, 8157.
- (23) Yin, P.; Wu, P.; Xiao, Z.; Li, D.; Bitterlich, E.; Zhang, J.; Cheng, P.; Vezenov, D. V.; Liu, T.; Wei, Y. *Angew. Chem. Int. Ed.* **2011**, *50*, 2521.

Chapter 7: Polyoxometalates-Organic Hybrid as Metal-Ion-Driven Molecular Switch with Reversible Folding and Assembly/Disassembly Behaviors

7.1 Introduction

Molecular switches are molecules that can be reversibly shifted between two or more stable states in response to environmental stimuli, e.g. pH, light, temperature, electrical current, and the presence of ligands or metal ions.¹⁻³ Metal-ion-driven molecular conformation change, as one of the major ideas in designing molecular switches,^{2,4,5} is vital in many biological behaviors, e.g. metal ion-directed protein folding and self-assembly, Ca^{2+} caused contraction or relaxation of human heart, Na^+ stimulated nerve impulses, and the Ca^{2+} -gated ion channel of K^+ inside cell membrane.⁶⁻⁹ However, it is still challenging to build artificial metal-ion-driven molecular switches based on relatively simple molecules that work as smart and powerful as the proteins. One of the major drawbacks is that only certain specific site or chemical bond related to the complexation of metal ions responses (e.g. rotates or bends) to introduction of metal ions, which limits the functionality of the molecular switches. Thus, the design of molecules switches with multiple responses to the stimuli is quite urgent since this behavior could mimic the folding process of bio-macromolecules expand their functionalities. Moreover, molecules switches, with metal-ion-responsive folding and self-assembly behavior, are simple models to understand the corresponding biological process of proteins and RNAs.

Polyoxometalates (POMs) are a large group of structurally well-defined molecular metal-oxide clusters (*ca.* 1 ~ 6 nm) with diverse physical properties and applications.¹⁰⁻¹³ Chemically grafting organic ligands/chains onto the POMs results in POM-organic hybrids, which can maintain or enhance/modify the optical-,¹⁴⁻¹⁶ electrical-,^{17,18} thermal-,¹⁹ and fluorescence²⁰⁻²² properties of the POMs. The functionality (e.g. self-assembly behavior and catalytic activity) of POM-based hybrids highly relies on their molecular conformation and therefore, the corresponding external

stimuli could be used as ‘switch’ signal for these functions. Moreover, POMs hybrids show specific biological activity, which might enhance the biocompatibility of molecular switch.²³⁻²⁵ Herein, we report, to the best of our knowledge, the first example of POMs-based metal-ion-driven molecular switch, which can be driven to fold by the stimuli of Zn²⁺ ions. The working cycles of the molecular switch were monitored by UV-Vis and ¹H-NMR. The folding process was uncovered by Small-Angle X-Ray Scattering (SAXS) and 2D Nuclear Overhauser Effect Spectroscopy (NOSY). More importantly, controllable metal ion translocation has been used to reversibly tune the packing parameter of POM-based amphiphile and its consequent self-assembly behaviour, which was studied by laser light scattering (LLS) and TEM.

7.2 Experimental section

General. Hybrid **1**, **2**, and the bipyridine ligand were synthesized according to previous literature.²⁶ DMSO, Methanol, anhydrous ZnCl₂, EDTA, aqueous solution of TBA*OH (40%, wt), and d₆-DMSO were purchased and used without further purification.

Synthesis of (TBA)₄*EDTA. 5 mL TBA*OH (40%,wt) solution was mixed with 0.274g EDTA. The mixture was kept sonicating until EDTA was fully dissolved. The obtained solution was kept at 50°C with reduce pressure for one week. Colorless ionic liquid was obtained.

UV-Vis monitoring the titration of hybrid 1 with ZnCl₂. 5 mg hybrid **1** was dissolved in 20 mL DMSO. 128 mg anhydrous ZnCl₂ was dissolved in 5 mL DMSO. UV-Vis was used to monitor 250-600 nm range results of the titration total volume of 5uL to 150 uL ZnCl₂ solution to the 20 mL **1**'s solution. UV-Vis measurements were done in Shimadzu UV-2101PC Spectrophotometer and pure DMSO solvent was used for background.

SAXS experimental section. The SAXS experiments were performed at 12-ID-B station with X-ray energy of 12 KeV at the Advanced Photon Source of the Argonne National Laboratory. The sample to detector distance was about 2 m. A 2D CCD detector was used to acquire images with typical exposure times in the range of 1.0 s.

TEM. The TEM images were taken on a JEOL JEM-2000 electron microscope operated at 200 kV. Samples for the TEM analysis were prepared by dropping a small volume of the solution sample onto a holey carbon film on copper grid.

Static light scattering. A commercial Brookhaven Instrument LLS spectrometer equipped with a solid-state laser operating at 532 nm was used for measurement of both SLS and DLS. SLS experiments were performed at scattering angles (θ) between 20 and 100°, at 2° intervals. However, due to the large fluctuations in scattered intensities at low scattering angles, we removed the data from 20-40° in the final analysis. Derived from Rayleigh-Gans-Debye equation²⁷, partial Zimm plot was used to analyze the SLS data to obtain the radius of gyration (R_g). The partial Zimm plot stems from the following approximate formula: $1/I = C(1+R_g^2*q^2/3)$. Here R_g is determined from the slope and the intercept of a plot of $1/I$ vs. q^2 .

Dynamic light scattering. DLS measures the intensity–intensity time correlation function by means of a BI-9000AT multi-channel digital correlator. The field correlation function $|g^{(1)}(\tau)|$ was analyzed by the constrained regularized CONTIN method²⁸ to yield information on the distribution of the characteristic line width Γ . The normalized distribution function of the characteristic line width, $G(\Gamma)$, so obtained, can be used to determine an average apparent translational diffusion coefficient, $D_{app} = \Gamma/q^2$. The hydrodynamic radius R_h is related to D via the Stokes–Einstein equation: $R_h = kT/(6\pi\eta D)$ where k is the Boltzmann constant and η the viscosity of the solvent at temperature T . From DLS measurements, we can obtain the particle-size distribution in solution from a plot of $\Gamma * G(\Gamma)$ versus R_h . The R_h of the particles is obtained by extrapolating $R_{h,app}$ to zero scattering angle. The normalized distribution function of the characteristic line width, $G(\Gamma)$, so obtained, can be used to determine an average apparent translational diffusion coefficient, $D_{app} = \Gamma/q^2$. The hydrodynamic radius R_h is related to D via the Stokes–Einstein equation: $R_h = kT/(6\pi\eta D)$ where k is the Boltzmann constant and η the viscosity of the solvent at temperature T . From DLS measurements, we can obtain the particle-size

distribution in solution from a plot of $\Gamma \cdot G(\Gamma)$ versus R_h . The R_h of the particles is obtained by extrapolating $R_{h,app}$ to zero scattering angle.

1D NMR and 2D DOSY, NOESY. All the NMR spectra were recorded on Bruker Avance 500 spectrometer equipped with a BBO probe at 25 °C. 2D NOESY were performed with mixing times ranging from 50 to 500 ms. The appropriate mixing time for trans-isomer and cis-isomer solution were determined to be 70 ms and 300 ms. Necessary phase corrections and baseline corrections were used to enhance the quality of the results.

DOSY was performed on a Bruker 500 MHz spectrometer with the magnetic field gradient (g) varying from 0 to 32 G/cm in 16 ~ 32 steps. The length of the gradient (d) was from 6000 ms to 8000 ms, and the time interval between two pulsedgradients (D) was from 0.1 s to 0.15 s. All spectra were taken at room temperature. After the data collection, FIDs were processed and analyzed with the NMR software TopSpin 2.0 provided by Bruker. Both T1/T2 relaxation and CONTIN methods were used to fit the raw data. The observed proton signal I in a standard DOSY spectrum is expressed through equation 1:

$$I = I_0 \exp \left[- (2\pi\gamma\delta)^2 \left(\Delta - \frac{\delta}{3} \right) D g^2 \right]$$

Equation (1)

where I_0 is the reference intensity, γ is the gyromagnetic ratio of the proton. If only one diffusive component exists in the solution, a straight line will occur in a plot of $\ln(I/I_0)$ versus g^2 , and the apparent diffusion coefficient (D) can be calculated from the slope using linear regression analysis.

Video for the folding process of hybrid molecule. The movie Hybrid_Movie was made by the author and based on NMR and SAXS results. The charge-free software Picasa 3 and windows movie maker are acknowledged here. The movie can be found as another supporting file or through the link <http://youtu.be/ZkIDe5z3Ils>. The addition of $ZnCl_2$ and the molecule of $ZnCl_2$ were omitted for clarity.

7.3 Results and discussion

7.3.1 Molecular structure of the hybrid molecular switch

Hybrid **1**, $\text{TBA}_{10}\text{H}_2[\{\text{P}_2\text{V}_3\text{W}_{15}\text{O}_{59}(\text{OCH}_2)_3\text{CNHCO}\}_2(\text{C}_5\text{H}_3\text{N})_2]$ (TBA, tetrabutylammonium), has been reported and fully characterized in previous literature.²⁶ It shows a dumbbell shape with two Dawson-type POMs at the two ends linked by a 2, 2'-bipyridine unit (Figure 7.1). The covalent but non-conjugated linkage between different building blocks makes the molecule quite stable while the functions of different components are maintained. The size of the molecule is *ca.* 1 X 1 X 4 nm³ and its molecular weight is *ca.* 10.6 kDa. 2, 2'-bipyridine is a key unit in designing smart molecules because of its metal-ion-induced controllable conformation around C-C single bond.²⁹⁻³² The purpose of designing hybrid **1** is to inherit the metal-ion-responsive behaviour from bipyridine to hybrid POMs. The POM units are bonded to the para-position of the heteroaromatic rings, which not only can extend the bipyridine unit's conformation change to the whole hybrid molecules, but also largely reduce the possible steric hindrance of POM units during the rotation process (Figure 7.2). Based on the above assumption, the hybrid can exist in two isomers: the trans-isomer in metal-ion-free environment and the cis-isomer when metal ions are added.

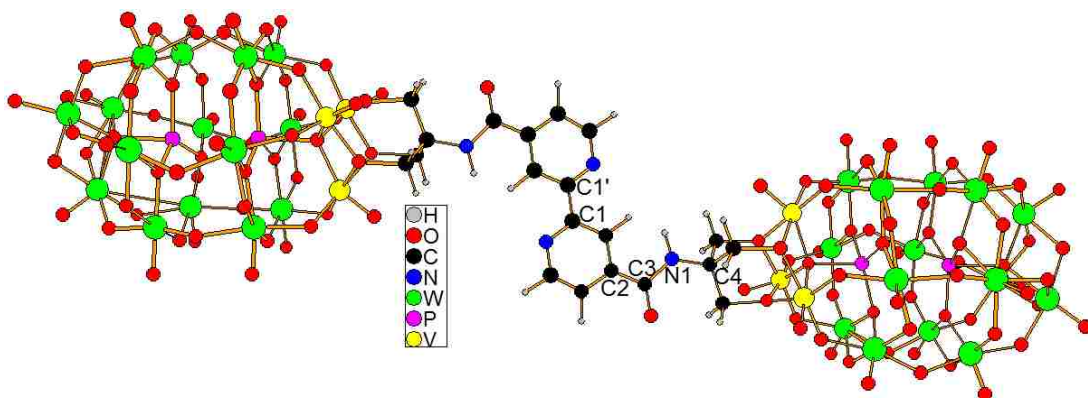


Figure 7.1 Ball-stick representation of molecular structure of anions in hybrid **1**.

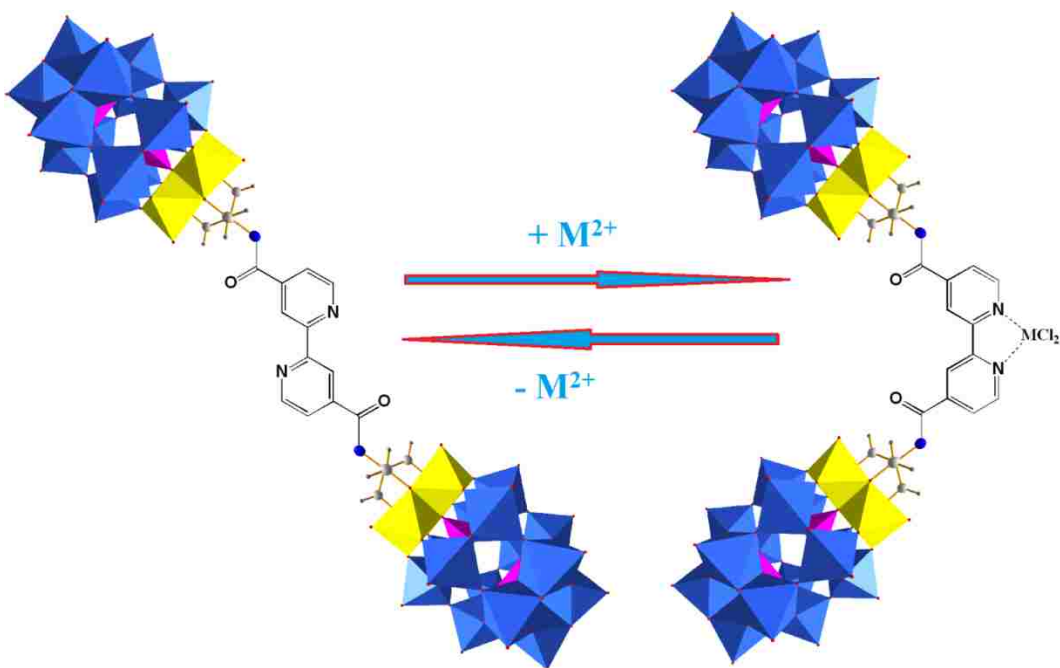


Figure 7.2 The reversible transformation process between trans-isomer and cis-isomer of **1**.

7.3.2 UV-vis monitoring the trans- to cis- isomer transformation process.

By titrating ZnCl_2 into the DMSO solution of the bipyridine ligand, a bathochromic shift of the bipyridine band from *ca.* 300 to 330 nm can be observed, which is resulted from the complexation between Zn^{2+} and the ligand (Figure 7.3 and Figure 7.4). The resolved absorption peak for bipyridine unit cannot be observed in the UV-Vis spectrum of hybrid **1** since it is immersed in the strong absorption peak of the POM unit. However, the similar bathochromic shift can be observed when Zn^{2+} is added to the DMSO solution of **1** (Figure 7.5). Control titration experiment on the bipyridine-free dumbbell-shape hybrids **2** (Figure 7.6 and Figure 7.7) shows no obvious change in its UV-Vis spectrum, ruling out the possibility that the interaction between the POM unit and Zn^{2+} contributes to the bathochromic shift. Therefore, the addition of Zn^{2+} can trigger the formation of Zn-bipyridine complex and change the conformation of the dumbbell structure from trans- to cis-.

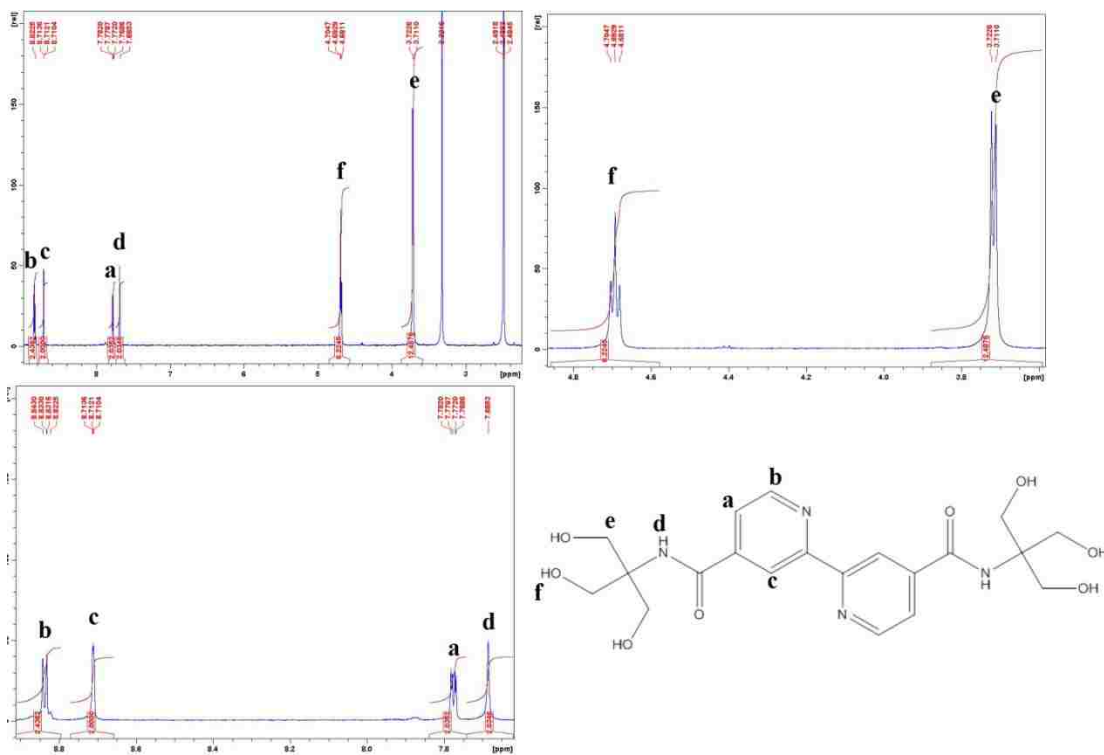


Figure 7.3 Molecular structure and NMR results of the bipyridine ligand.

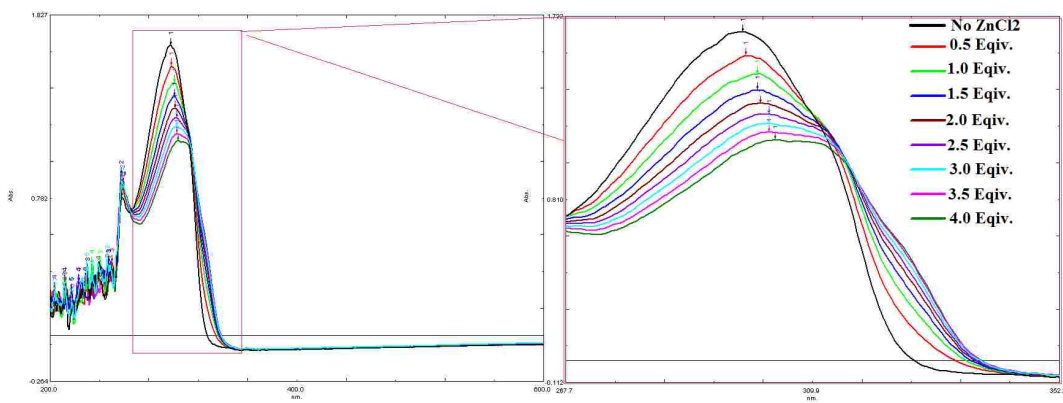


Figure 7.4 UV-Vis monitoring of the titration of ZnCl_2 into the DMSO solution of the bipyridine ligand. A bathochromic shift of the bipyridine band from ca. 300 to 330 nm can be observed, which is resulted from the complexation between Zn^{2+} and the ligand.

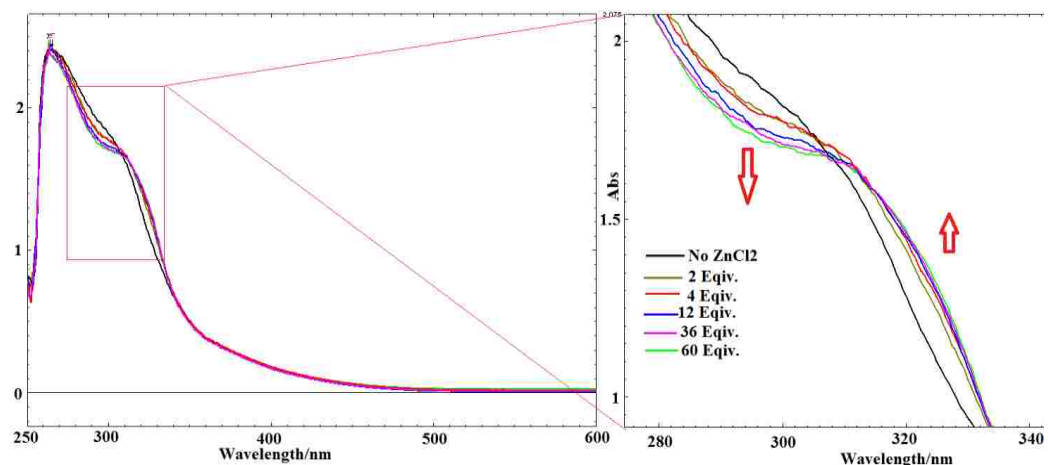


Figure 7.5 UV-Vis monitoring of hybrid 1 with the titration of ZnCl_2 in DMSO.

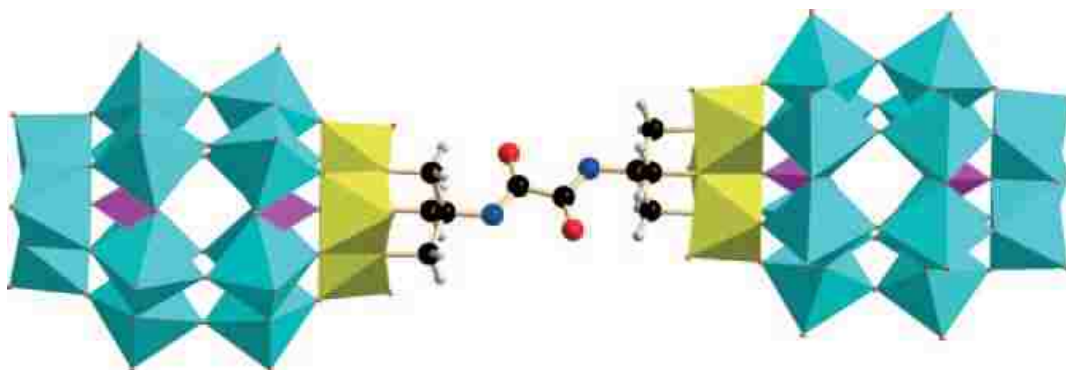


Figure 7.6 Molecular structure of hybrid 2. Cyan polyhedron, WO_6 ; yellow polyhedron, VO_6 ; purple polyhedron, PO_4 ; black sphere, carbon atom; blue sphere, nitrogen atom; red sphere, oxygen atom; gray sphere, hydrogen atom.

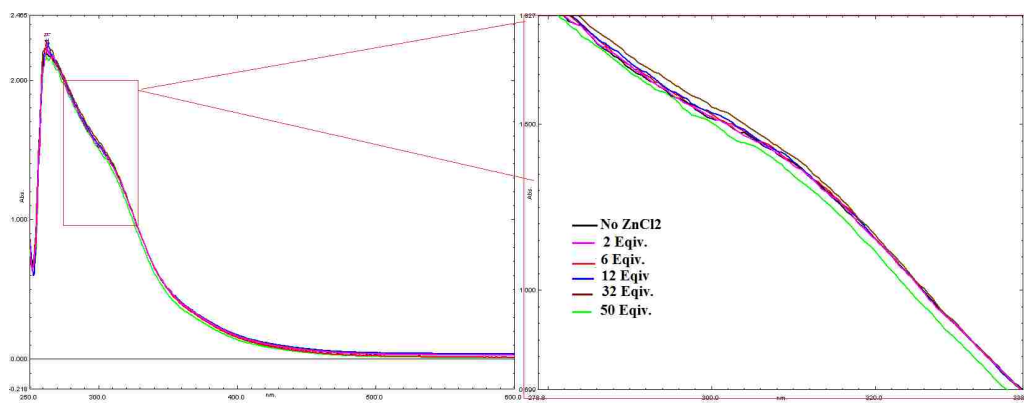


Figure 7.7 UV-Vis monitoring of the titration of ZnCl_2 into the DMSO solution of hybrid 2. No bathochromic shift were observed.

7.3.3 ¹H-NMR monitoring the reversible transformation process

¹H-NMR was further used to obtain detailed information and test the reversibility on the metal-ion-driven conformation change. Due to the strong induce effect of metal ions in their complexes, ¹H-NMR studies on the bipyridine ligands suggest that the corresponding peaks of the protons in heteroaromatic rings and amino groups show signal broadening and downfield shift when added Zn²⁺ reaches a molar ratio of 3.5:1 to bipyridine (i.e., 3.5 equivalents, Figure 7.8). The similar downshift and signal broadening of the peaks can be observed in the corresponding experiments of hybrid **1**. After titrating extra ZnCl₂ to the hybrid solution (5~18 equivalents), it can be clearly observed that the signal of H_a and H_c at 7.83 and 8.74 ppm, respectively, decrease gradually correlated with the appearance and increasing of two new peaks at 8.20 and 9.05 ppm (Figure 7.9 bottom, black line and green line correlated peak series), indication the Zn²⁺ controlled trans- to cis- transformation. Meantime, the peak of H_b and H_d at 8.46 and 8.84 ppm, respectively, continuously move downfield to 8.55 and 8.91 ppm, respectively (Figure 7.9 bottom, aqua line and pink line labelled peak series). As high as *ca.* 18 equivalents of ZnCl₂ is needed to fully transform the trans-isomers of hybrid **1** into cis-isomers probably due to the repulsive interaction between the giant Dawson clusters during the rotation process, which is confirmed by the fact that *ca.* 20 equivalents of HgCl₂ are needed for the transformation process of **1**. Interestingly, the downfield shifted peaks move upfield back to their original chemical shift after the adding of *ca.* 9 equivalents of (TBA)₄*EDTA (tetrabutylammonium*ethylenediaminetetraacetate, see experimental section), suggesting that the cis- conformation changes back to trans- conformation. EDTA is a strong chelating agent that can almost stoichiometrically coordinate with metal ions. In our case, EDTA can extract the Zn²⁺ from the cis-isomers, which become thermodynamically unstable and change back into trans-isomers. The addition of Zn²⁺ and later removal of it with EDTA in the DMSO solution of hybrid **1** is a running cycle of the molecular switch (Figure 7.2).

Further NMR studies confirm that the switch can work for at least 5 cycles through controlling the stimuli of Zn^{2+} without decomposition of the hybrids or dysfunctionality (Figure 7.10).

Additionally, the transformation from trans- to cis-isomer can lead to observable change of diffusion speed of the hybrid molecule in 2D diffusion ordered 1H -NMR spectroscopy (DOSY). DOSY results indicated that the diffusion coefficient (D) of trans-isomer is 7.927×10^{-11} m²/s (before adding $ZnCl_2$) and that of cis-isomer is 1.295×10^{-10} m²/s. Based on Stokes-Einstein diffusion equation (Equation in experimental section), hydrodynamic radii (R_h) of trans-isomer and cis-isomer can be calculated as 1.379 nm and 0.844 nm, respectively, suggesting the shrinking of the molecular size during the transformation process. The observation could be explained by the shorter distance between two Dawson-type POMs in cis-isomer than that of trans-isomer.

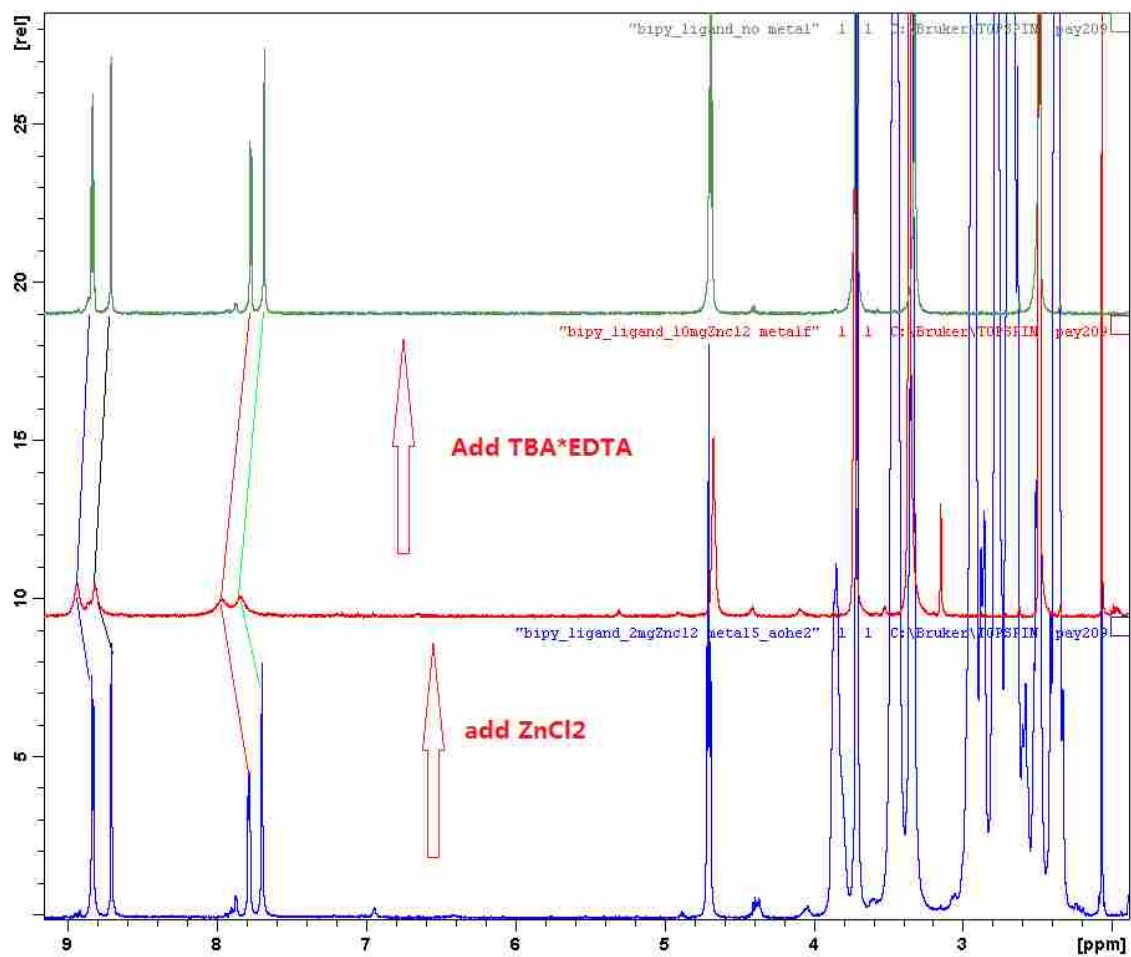


Figure 7.8 ¹H-NMR monitoring of bipyridine ligand with adding ZnCl₂ and TBA*EDTA. The downfield shift of hydrogen atom of bipyridine and N-H after the adding ZnCl₂ suggests the transformation of the trans- to cis-. After adding TBA*EDTA to the above solution, the chemical shift move upfield back to their original position, indicating the transformation of cis- to trans-.

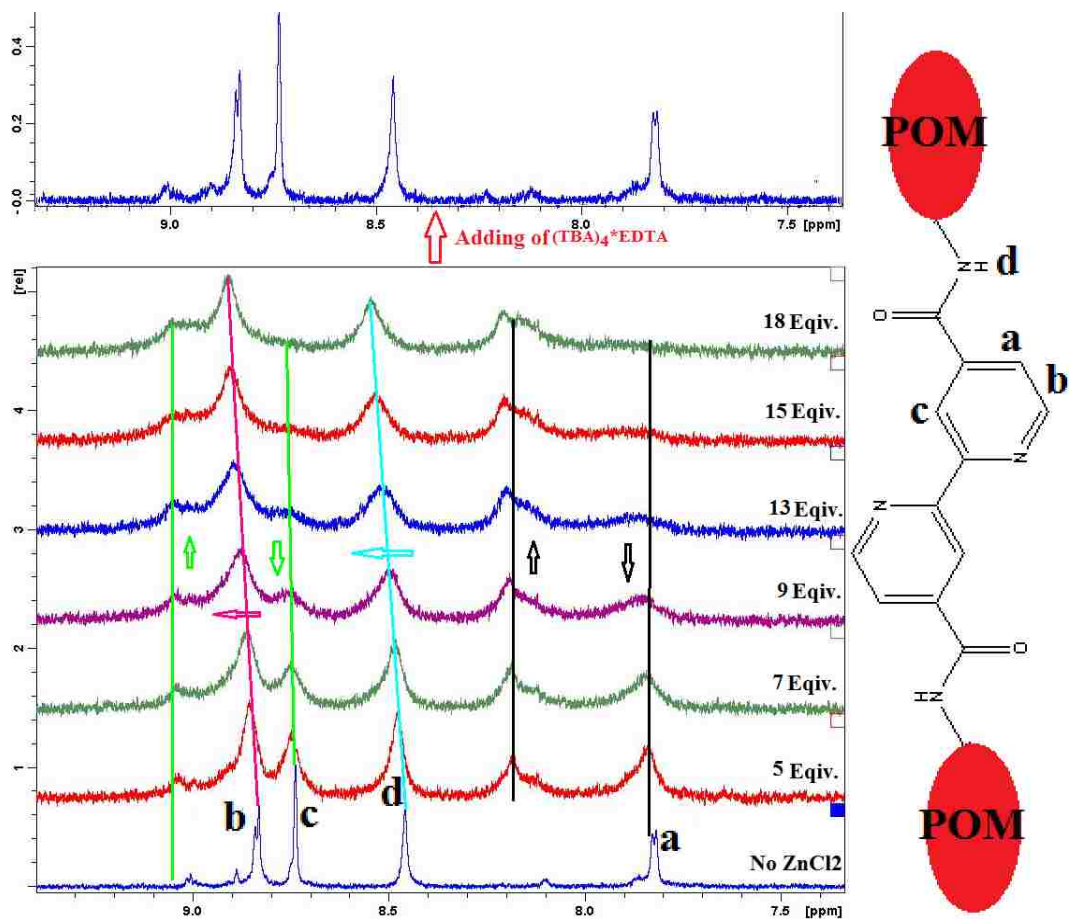


Figure 7.9 ¹H-NMR monitoring results of the titration of ZnCl₂ to the d₆-DMSO solution of 1 (bottom) and adding of (TBA)₄*EDTA after the titration of ZnCl₂ (top).

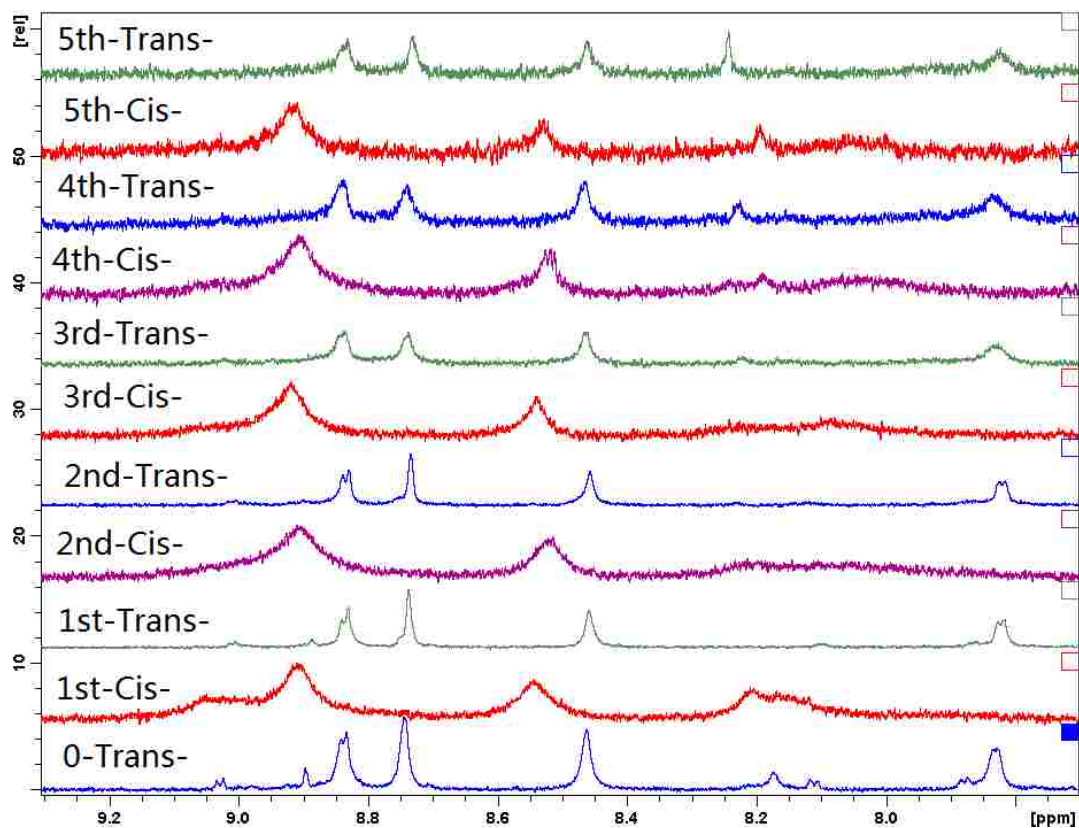


Figure 7.10 $^1\text{H-NMR}$ monitoring results of the five working cycles of the hybrid **1**.

7.3.4 The observation of folding behavior of hybrid during the transformation process in SAXS and NOESY.

Basically, the molecular framework of hybrid **1** is rigid and only five single bonds are allowed to rotate (the pair of C4-N1, the pair of C2-C3, C1-C1'), which might control the molecule's conformation. However, due to the symmetrical structure of Dawson-type POM, the pair of C4-N1 single bond have no effect in changing the hybrid's conformation. The rotation of C1-C1' highly relies on the complexation of bipyridine unit with metal ions and thus the study of hybrid's molecular conformation is heavily involved with C2-C3 bond. The amid groups and neighbouring heteroaromatic rings are forced to stay coplanarly because of the conjugative effect, which, therefore, limits the possible conformation number for both cis-isomer and trans-isomer to be only 3 (Figure 7.1 and Figure 7.11). SAXS, a powerful technique for characterizing nanostructures in solution, was used to determine the actual molecular conformation of hybrid **1**.³³⁻³⁷ The SAXS profiles of hybrid **1** before (open square) and after (open circle) adding ZnCl_2

(Figure 7.12a) are completely different, where they have peak maxima at $q = 0.27$, and 0.33 \AA^{-1} , respectively (Figure 7.12a). To further understand the structural cause of SAXS profile change, pair distance distribution functions (PDDF) in real space, $p(r)$, were obtained using program GNOM³⁸ as shown in Figure 7.12b. All PDDF exhibit dumbbell-type bimodal feature, where the first peak describes the intra-subunit (Dawson-type POM) distances and is same for all these three samples, while the second peak describes the inter-subunit pair distances. The position of the second peak roughly measures the center to center distance of the two subunit.³⁹ The second peak shifts its center from 28.5 \AA to 21.2 \AA after adding ZnCl_2 , resulting from the induced trans-to-cis isomerization and the shorter subunit separation in cis-isomer. In order to examine the correct molecular conformations, the PDDF for each conformation was calculated using program SolX^{40,41} and superimposed with the experimental PDDFs in Figure 7.12c. All the three trans-conformations fit well with experimental curve while only cisII fits the experimental data for cis-isomer.

To further examine those conformers, 2D NOESY measurements were employed. 2D NOESY is a NMR technology whose aim is to identify spins undergoing cross-relaxation and to measure the cross-relaxation rates.⁴² The intensity of NOESY is highly dependent on the distance between protons and normally a signal is only observed if their distance is smaller than 5 \AA .⁴² Therefore, NOESY results could be helpful to confirm the SAXS results and determine the right conformation by collecting information on the inter-proton distances in organic fragments. In NOESY result of **1**'s Zn^{2+} -free solution (trans-isomer), crosspeaks of amine proton (H_d) and H_c are observed (red rectangle) as well as that of H_a/H_b (aqua rectangle) and H_d/H_e (green rectangle), however, no crosspeaks of H_d/H_a shows up, which suggests that H_d is only close to H_c , implying transIII should be the correct model for trans-isomer (Figure 7.11 and Figure 7.13a). Meantime, NOESY results of the hybrid solution with Zn^{2+} (cis-isomer) suggests that H_d is close to both H_a and H_c by showing crosspeaks with both H_a (blue rectangle) and H_c (red rectangle), which confirm

the SAXS result that cisII is the right or the major conformation for cis-isomer (Figure 7.11 and Figure 7.13b). Theoretically, adding ZnCl_2 to drive the rotation of C1-C1' would change transIII into cisIII if C2-C3 bonds are frozed. However, the inter-POM distance (center to center) for cisIII is too close (1.2 nm) and the steric hinderence finally forces one of the C2-C3 bond to rotate 180° and make the distance further (2.0 nm) (Figure 7.11 and Figure 7.13c). The further roration of C2-C3 bond requires extra energy, which explains why excessive Zn^{2+} is needed for the transformation from trans- to cis-isomer. The smart behavior of **1** mimics the metal-ion-driven folding process of proteins, which directs the functionality of proteins.

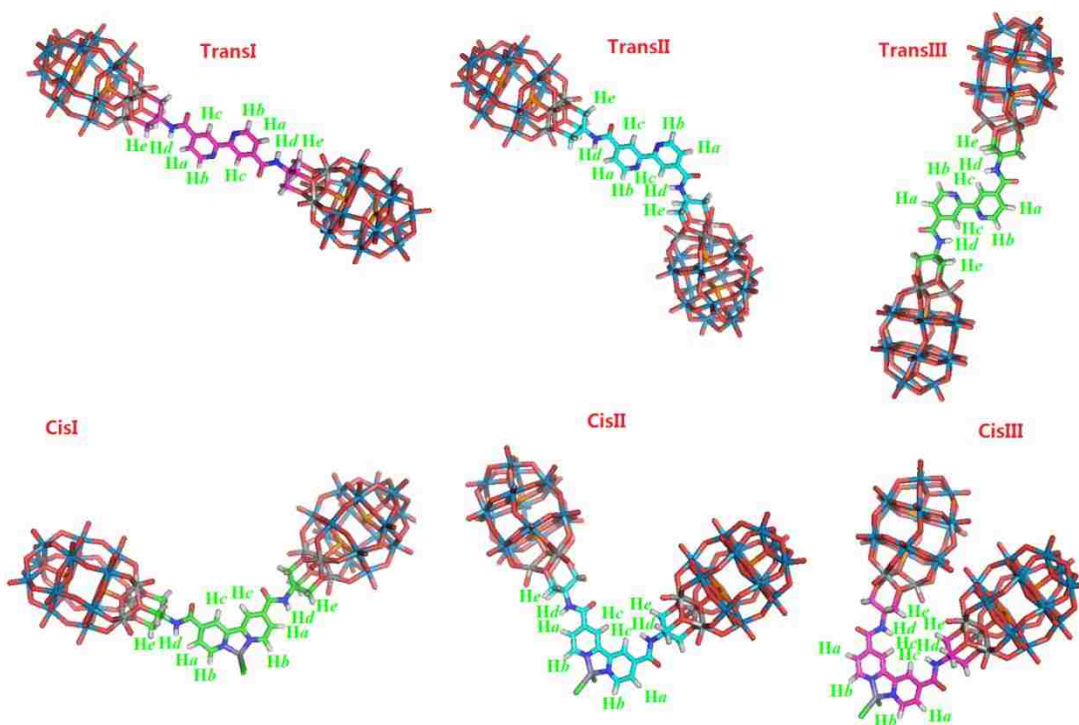


Figure 7.11 The possible conformations for trans-isomer and ciso-isomer, respectively.

SAXS was also used to confirm that the cis-isomers could be converted back to trans-isomers. After adding $(\text{TBA})_4\text{*EDTA}$, (shown in Figure 7.12a open triangle), the clusters are trans-isomers (open square), and the d spacing is around *ca.* 28 Å, based on the p (r) curve in Figure 7.12b, indicating a unfolding process for the hybrids (Figure 7.13c). It also should be noted that both trans- and cis- isomers are stable in solution after one month (Figure 7.14). In addition, from the

$p(r)$ curve, the minimum of trans-isomer is lower than 0, which is due to the lower density of organic linker compared to the buffer, DMSO. In the case of cis-isomer, because of the existence of heavy metal Zn^{2+} , their minimum is higher than 0.

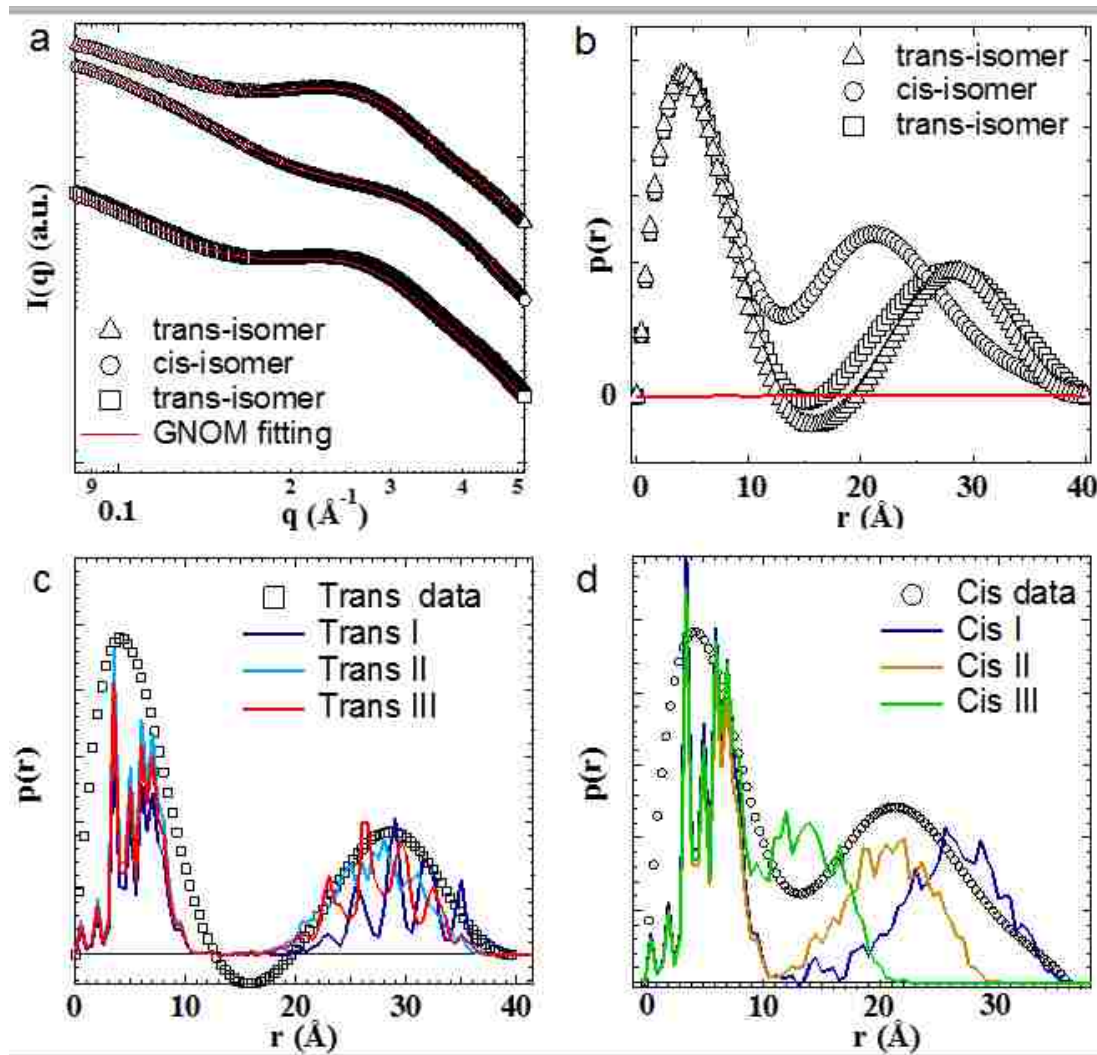


Figure 7.12 a) SAXS curve of trans-isomer without metal ions (open square), cis-isomer after adding $ZnCl_2$ (open circle), and trans-isomer after adding the EDTA into the cis-isomer solution (open triangle). SAXS profiles are vertically offset for clarity. b) Pair distance distribution function, $p(r)$, of the three samples obtained using program GNOM. c) The overlay of calculated $p(r)$ of the three trans-conformations and experimental $p(r)$ of trans-isomer. The calculated $p(r)$ were computed directly from the molecular coordinates using program SolX. d) The overlay of calculated $p(r)$ of the three cis-conformations and experimental $p(r)$ of cis-isomer.

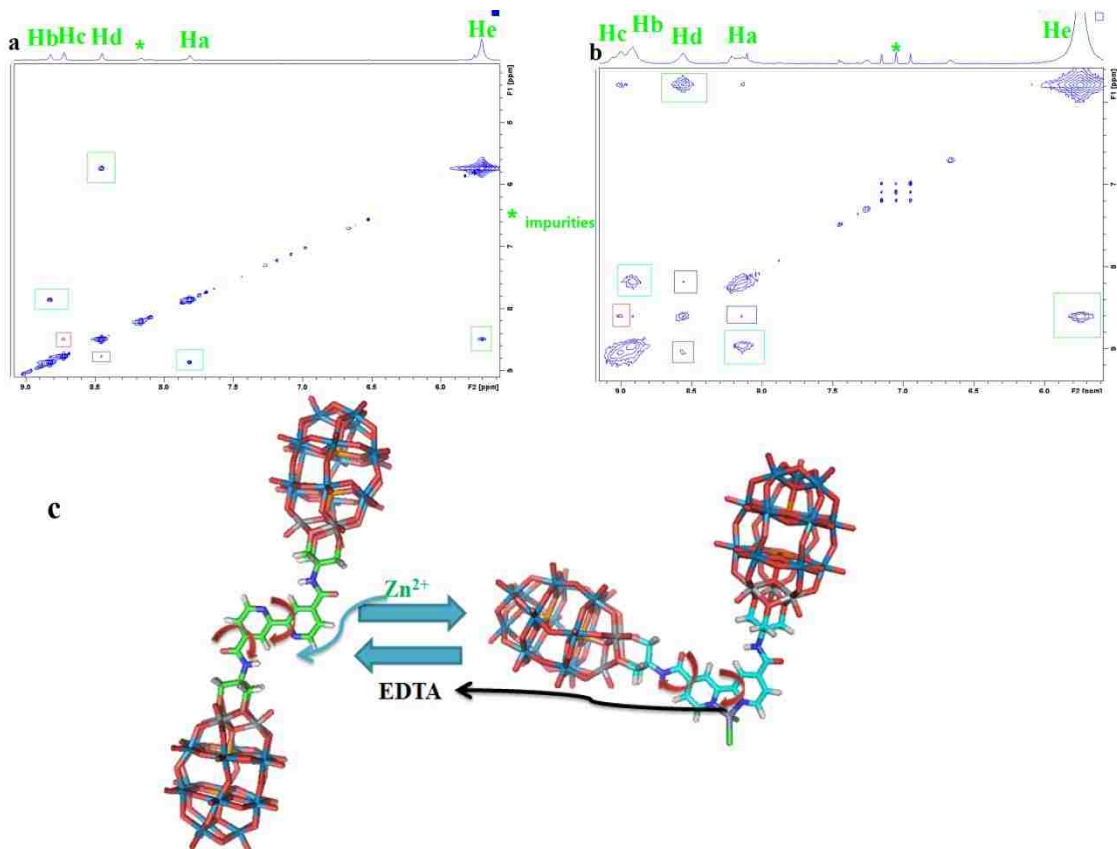


Figure 7.13 a) b) 2D NOESY result of hybrid 1's solution without and ZnCl₂, respectively. (retangle-crosspeak code: red, Hd/Hc; green, Hd/He; aqua, Ha/Hb; blue, Hd/Ha) c) Model for the folding and unfolding behavior of the hybrid stimulated by Zn²⁺.

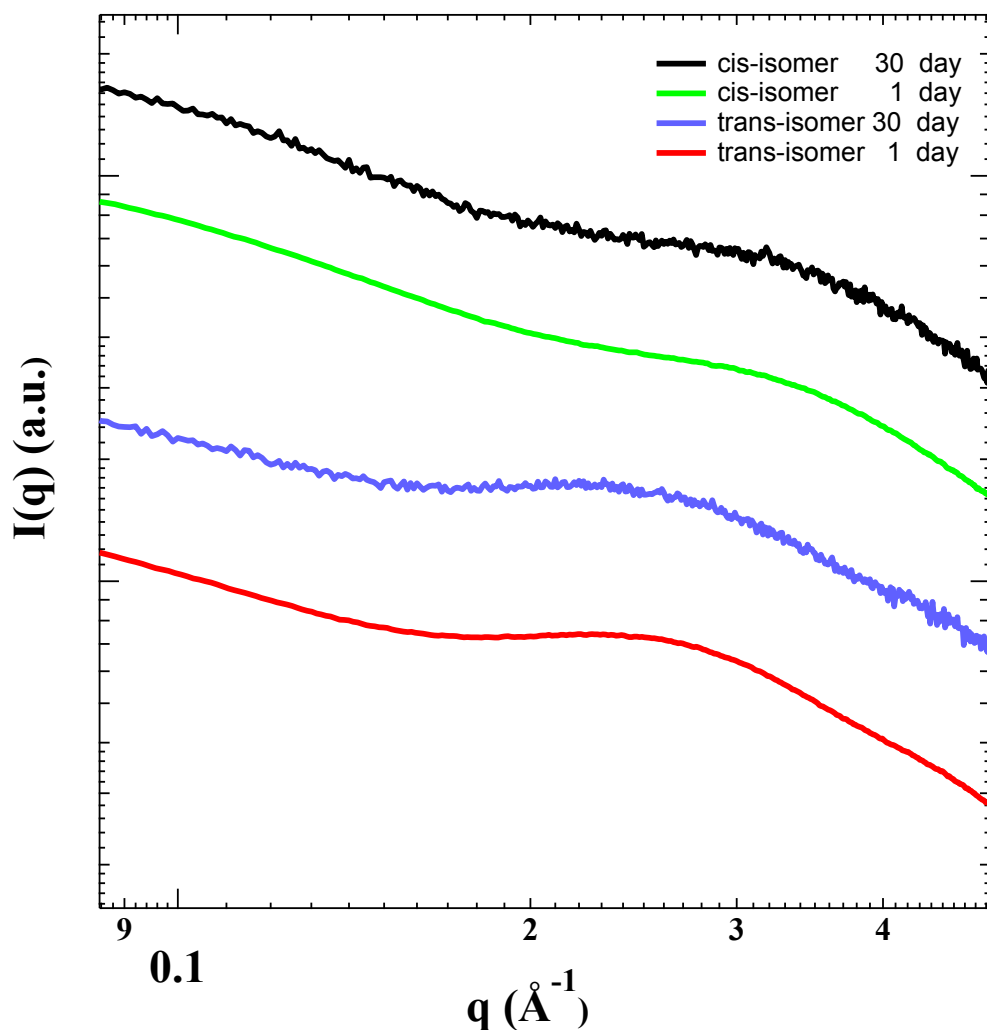


Figure 7.14 SAXS data of trans-isomer and cis-isomer measured at 1st day and 30 day. Data are arbitrarily scaled for clarity.

7.3.5 Metal-ion-driven self-assembly/disassembly behavior of hybrid in solution

The dumbbell hybrids are amphiphilic molecules⁴³⁻⁴⁵ and the metal-ion-driven conformation change of **1** can likely alter its packing parameter (P), which might be utilized to manipulate its solvophobic-driven self-assembly behaviour. The trans-isomers exist as discrete molecules in DMSO/methanol mixed solvents (1:1 volume ratio), suggested by the stable and low scattered intensity (*ca.* 40 kcps; scattered intensity for benzene is *ca.* 120 kcps) from the time-resolved SLS studies. However, the scattered intensity of **1**'s solution increased to *ca.* 9,000 kcps without any

precipitation after *ca.* 18 equivalents of ZnCl₂ were added, suggesting the formation of large structures. A typical CONTIN analysis from dynamic light scattering (DLS) study indicated the existence of assemblies with an average R_h of 138±7 nm with a narrow size distribution (Figure 7.15a). Radius of gyration (R_g) of the assemblies, obtained from the SLS measurement as 144±7 nm, was very close to R_h, suggesting a hollow spherical structure for the assemblies, which was confirmed by the TEM image (Figure 7.15b). The control experiment on hybrid **2** suggested that no assemblies were observed even as high as 54 equivalents Zn²⁺ were added, which ruled out the possibility that the POM-ZnCl₂ interaction led to the formation of large assemblies. The trans-isomer of **1** is of cylinder-shape with diameter as *ca.* 1 nm, and therefore the closest distance of the heteroaromatic ring in two nearest hybrid molecules should be no less than 1 nm based on the parallel-packing model (Figure 7.16).^{43,44} However, the distance for aromatic groups should achieve as short as 0.34 nm for face-to-face π-π stacking, which means that it is difficult for the hydrophobic organic linker of trans-isomer to directly interact with each other due to the steric hindrance of large-size POMs. In our previous study, vesicles were observed to form from **1**'s trans-isomers since TBAs were claimed to strongly interact with the organic linker in polar solvents (water/acetone mixtures) and fill up the solvophobic region^{43,44}. However, the interaction between TBAs and organic linkers became weaker in comparatively less polar solvent, e.g. DMSO/methanol mixtures, and therefore, no assemblies of **1**'s trans-isomer could be observed. The cis-isomer is a V-shaped molecule with the angle as 108° and *P* as 0.55, much large than that of trans-isomer, 0.40. In the packing model in figure 7c, two cis-isomers can strongly interact with each other through hydrophobic interaction and the π-π stacking of heteroaromatic ring with inter-POM distance > 2 nm, which enables two possible packing style of cis-isomers to form vesicles: 1) monolayer structure: two polar heads of **1** are on the outside surface and internal area surface, respectively with linker inside the shell of vesicle; 2) bilayer structure: the two polar heads are on the same side with linkers inside the shell. By removing ZnCl₂ from cis-isomer

through adding $(\text{TBA})_4\text{EDTA}$, the conformation of **1** change back to trans- and the vesicles disassemble, indicated by the dropping of scattered intensity to 47 kcps. This controllable self-assembly and disassembly processes can be repeated with the same sample by adding and removing ZnCl_2 for several cycles (Figure 7.17).

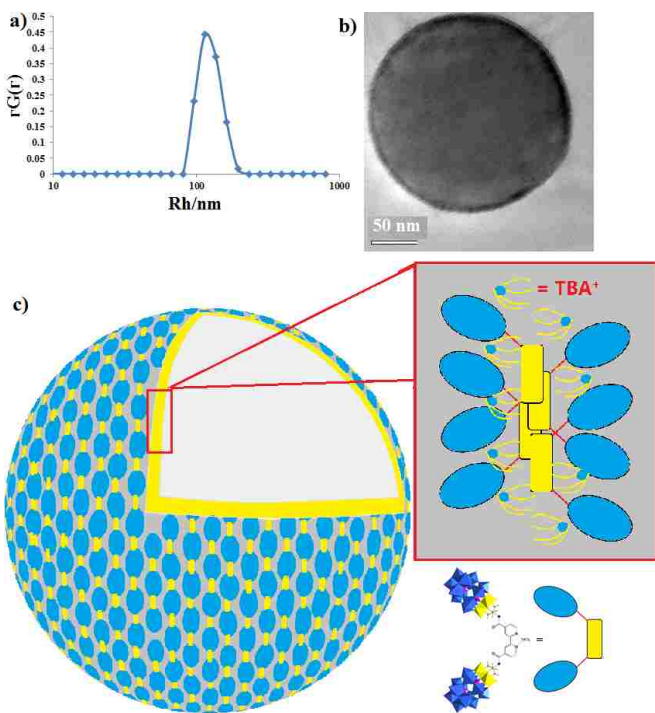


Figure 7.15 a) DLS results of the assemblies of Hybrid 1 in Methanol/DMSO mixed solvents at 45° scattering angle. b) TEM image of the large assembly. c) Model for the vesicle structure.

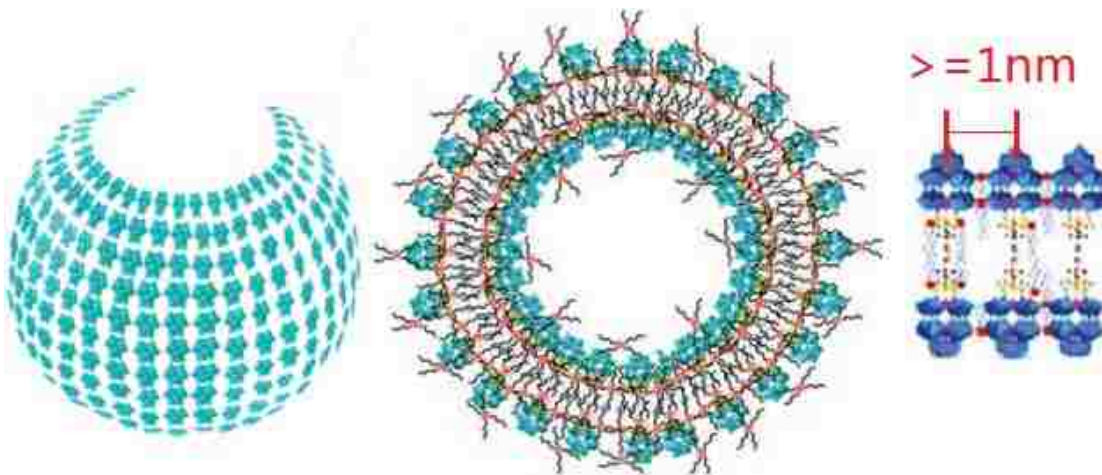


Figure 7.16 Model for the parallel packing of trans-isomer of **1**.

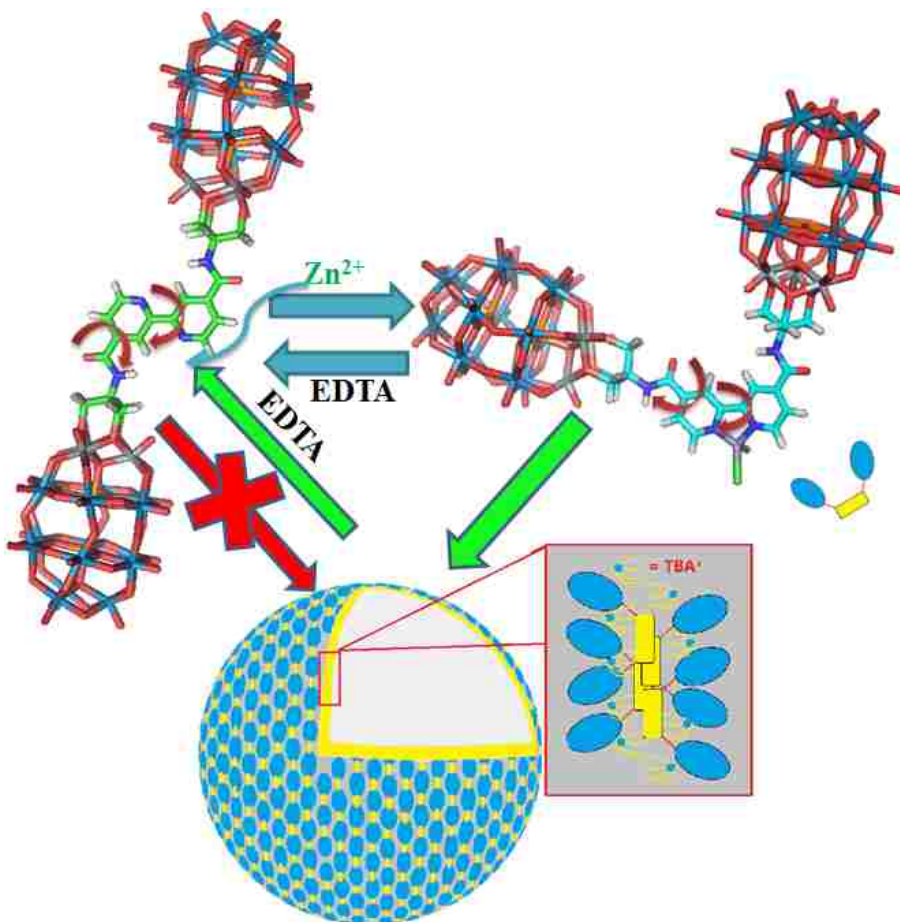


Figure 7.17 Graphical representation of the trans-isomer to cis-isomers to vesicle structures process.

7.4 Conclusion

In summary, the bipyridine-containing dumbbell-shape POM hybrid works as a Zn^{2+} -driven molecular switch. The hybrid exists as trans-isomer in metal ion-free solutions while it changes to cis-isomer when Zn^{2+} is added. The molecule can keep reversibly switching for multiple cycles if the adding and removing of Zn^{2+} in its DMSO solution can be controlled. As the first POM-based metal-ion-driven molecular switch that mimics the behaviour of metal ion-directed folding and assembly of proteins, the Zn^{2+} -controlled its conformation transformation can further utilized to manipulate its self-assembly behavior, which might be useful in delivery and control releasing.

Reference

- (1) Feringa, B. L. *Acc. Chem. Res.* **2001**, *34*, 504.

- (2) *Molecular Switches*; 2nd ed.; Feringa, B. L.; Browne, W. R., Eds.; Wiley-VCH: Weinheim, 2011; Vol. 1.
- (3) Feringa, B. L.; van Delden, R. A.; Koumura, N.; Geertsema, E. M. *Chem. Rev.* **2000**, *100*, 1789.
- (4) Amendola, V.; Fabbrizzi, L.; Mangano, C.; Pallavicini, P. *Acc. Chem. Res.* **2001**, *34*, 488.
- (5) Fabbrizzi, L.; Licchelli, M.; Pallavicini, P. *Acc. Chem. Res.* **1999**, *32*, 846.
- (6) *Metal ions in biology and medicine*; Centeno, J. A.; Collery, P.; Vernet, G.; Finkelman, R. B.; Gibb, H.; Etienne, J., Eds.; John Libbey Eurotext: Paris, France, 2000; Vol. 6.
- (7) Jiang, Y.; Lee, A.; Chen, J.; Cadene, M.; Chait, B. T.; MacKinnon, R. *Nature* **2002**, *417*, 515.
- (8) Salgado, E. N.; Radford, R. J.; Tezcan, F. A. *Acc. Chem. Res.* **2010**, *43*, 661.
- (9) *Protein folding and metal ions : mechanisms, biology and disease*; Gomes, C. M.; Wittung-Stafshede, P., Eds.; CRC Press: Boca Raton, FL, 2011.
- (10) Hill, C. L. *Chem. Rev.* **1998**, *98*, 1.
- (11) Long, D.-L.; Burkholder, E.; Cronin, L. *Chem. Soc. Rev.* **2007**, *36*.
- (12) Long, D.-L.; Tsunashima, R.; Cronin, L. *Angew. Chem. Int. Ed.* **2010**, *49*, 1736.
- (13) Proust, A.; Thouvenot, R.; Gouzerh, P. *Chem. Commun.* **2008**, 1837.
- (14) Thiel, J.; Yang, D.; Rosnes, M. H.; Liu, X.; Yvon, C.; Kelly, S. E.; Song, Y.-F.; Long, D.-L.; Cronin, L. *Angew. Chem. Int. Ed.* **2011**, *50*, 8871.
- (15) Yan, Y.; Wang, H.; Li, B.; Hou, G.; Yin, Z.; Wu, L.; Yam, V. W. W. *Angew. Chem. Int. Ed.* **2010**, *49*, 9233.
- (16) Yagai, S.; Ohta, K.; Gushiken, M.; Iwai, K.; Asano, A.; Seki, S.; Kikkawa, Y.; Morimoto, M.; Kitamura, A.; Karatsu, T. *Chem. Eur. J.* **2012**, *18*, 2244.

- (17) Li, H.; Pang, S.; Wu, S.; Feng, X.; Müllen, K.; Bubeck, C. *J. Am. Chem. Soc.* **2011**, *133*, 9423.
- (18) Yang, Y.; Xu, L.; Li, F.; Du, X.; Sun, Z. *J. Mater. Chem.* **2010**, *20*, 10835.
- (19) Rieger, J.; Antoun, T.; Lee, S.-H.; Chenal, M.; Pembouong, G.; Lesage de la Haye, J.; Azcarate, I.; Hasenknopf, B.; Lacôte, E. *Chem. Eur. J.* **2012**, *18*, 3355.
- (20) Yin, P.; Wu, P.; Xiao, Z.; Li, D.; Bitterlich, E.; Zhang, J.; Cheng, P.; Vezenov, D. V.; Liu, T.; Wei, Y. *Angew. Chem. Int. Ed.* **2011**, *50*, 2521.
- (21) Li, D.; Song, J.; Yin, P.; Simotwo, S.; Bassler, A. J.; Aung, Y.; Roberts, J. E.; Hardcastle, K. I.; Hill, C. L.; Liu, T. *J. Am. Chem. Soc.* **2011**, *133*, 14010.
- (22) Yin, P.; Jin, L.; Li, D.; Cheng, P.; Vezenov, D. V.; Bitterlich, E.; Wu, X.; Peng, Z.; Liu, T. *Chem. Eur. J.* **2012**, *18*, 6754.
- (23) Geng, J.; Li, M.; Ren, J.; Wang, E.; Qu, X. *Angew. Chem. Int. Ed.* **2011**, *50*, 4184.
- (24) Rhule, J. T.; Hill, C. L.; Judd, D. A.; Schinazi, R. F. *Chem. Rev.* **1998**, *98*, 327.
- (25) Song, Y.-F.; McMillan, N.; Long, D.-L.; Kane, S.; Malm, J.; Riehle, M. O.; Pradeep, C. P.; Gadegaard, N.; Cronin, L. *J. Am. Chem. Soc.* **2009**, *131*, 1340.
- (26) Pradeep, C. P.; Li, F.-Y.; Lydon, C.; Miras, H. N.; Long, D.-L.; Xu, L.; Cronin, L. *Chem. Eur. J.* **2011**, *17*, 7472.
- (27) Hiemenz, P. C.; Rajagopalan, R. *Principles of Colloid and Surface Chemistry*; Marcel Dekker: New York, 1997.
- (28) Provencher, S. W. *Comput. Phys. Commun.* **1982**, *27*, 229.
- (29) Haberhauer, G. *Angew. Chem. Int. Ed.* **2010**, *49*, 9286.
- (30) Zahn, S.; Reckien, W.; Kirchner, B.; Staats, H.; Matthey, J.; Lützen, A. *Chem. Eur. J.* **2009**, *15*, 2572.
- (31) Plitt, P.; Gross, D. E.; Lynch, V. M.; Sessler, J. L. *Chem. Eur. J.* **2007**, *13*, 1374.

- (32) König, B.; Hollnagel, H.; Ahrens, B.; Jones, P. G. *Angew. Chem. Int. Ed.* **1995**, *34*, 2538.
- (33) Li, T.; Winans, R. E.; Lee, B. *Langmuir* **2011**, *27*, 10929.
- (34) Macfarlane, R. J.; Lee, B.; Jones, M. R.; Harris, N.; Schatz, G. C.; Mirkin, C. A. *Science* **2011**, *334*, 204.
- (35) Antonio, M. R.; Nyman, M.; Anderson, T. M. *Angew. Chem. Int. Ed.* **2009**, *48*, 6136.
- (36) Pigga, J. M.; Kistler, M. L.; Shew, C. Y.; Antonio, M. R.; Liu, T. B. *Angew. Chem. Int. Ed.* **2009**, *48*, 6538.
- (37) Kojima, T.; Antonio, M. R.; Ozeki, T. *J. Am. Chem. Soc.* **2011**, *133*, 7248.
- (38) Svergun, D. *J. Appl. Crystallogr.* **1992**, *25*, 495.
- (39) Svergun, D. I.; Koch, M. H. J. *Rep. Prog. Phys.* **2003**, *66*, 1735.
- (40) Zuo, X.; Cui, G.; Merz, K. M.; Zhang, L.; Lewis, F. D.; Tiede, D. M. *Proc. Natl. Acad. Sci. USA* **2006**, *103*, 3534.
- (41) Zhang, R.; Thiyagarajan, P.; Tiede, D. M. *J. Appl. Crystallogr.* **2000**, *33*, 565.
- (42) R.R.Ernst; B.Bodenhausen; A.Wokaun *Principles of Nuclear Magnetic Resonances in One or Two Dimesnions*; Oxford University Press: Cambridge, 1992.
- (43) Misdrahi, M. F.; Wang, M.; Pradeep, C. P.; Li, F.-Y.; Lydon, C.; Xu, L.; Cronin, L.; Liu, T. *Langmuir* **2011**, *27*, 9193.
- (44) Pradeep, C. P.; Misdrahi, M. F.; Li, F.-Y.; Zhang, J.; Xu, L.; Long, D.-L.; Liu, T.; Cronin, L. *Angew. Chem. Int. Ed.* **2009**, *48*, 8309.
- (45) Yin, P.; Li, D.; Liu, T. *Chem. Soc. Rev.* **2012**, <http://dx.doi.org/10.1039/C2CS35176E>.

Chapter 8: Polyoxometalate-Organic Hybrid Molecules as Amphiphilic Emulsion Catalysts for Oxidation Reactions and Nanostructured Polyoxometalate-Polymer Latex Beads

8.1 Introduction

Polyoxometalates (POMs), a large series of discrete and stable nano-scaled metal oxide clusters with well-defined molecular structures, are optically and electrically active materials and have attracted increasing interest in recent years, especially as promising homogeneous and heterogeneous catalysts both in laboratory research and industrial processes.¹⁻⁶ Major limitations of the POM catalysts include the high cost for homogeneous catalysis (difficult to recycle the catalysts from the solution after the reaction) and the low catalytic efficiency for the heterogeneous catalysis (only surface layer of POM crystals are effective in catalytic reactions).² Mizuno, Hill, and Wang *et al.* developed the POM-incorporated porous crystalline framework for high efficient heterogeneous catalysis.⁷⁻¹⁰ Neumann and Mizuno *et al.* loaded POMs on the surface of micelles and positively charge substrate to obtain recyclable quasi-homogeneous catalysts.¹¹⁻¹⁵ However, the applications are limited for a few reaction systems. An additional issue is that the oxidation reactions in petroleum industry with POMs as catalysts often involve reactants in immiscible liquid phases, e.g., sulfur-containing and unsaturated organics in oil phase and oxidizing agent (H_2O_2) in aqueous phase.^{16,17} A possible scheme for solving these problems is to increase the interfacial area and try to locate catalyst at the interface. Such reaction systems provide an easy way to separate catalysts, excess reactants, and products from the reaction media which will therefore remain uncontaminated. This idea can be applied to environmental benign and green chemistry, organic synthesis, and industrial-scale reactions including biomass conversion, biofuel upgrade, and oxidation desulfurization.¹⁸ However, very few studies on the application of POMs as catalysts in the two-immiscible phase system has been reported since the reactions are usually slow, or even impossible because of the limited interfacial area where

reactants and catalyst interact. Neumann, Li, and co-workers successfully developed the so-called ‘emulsion catalyst’ by replacing the counterions of POMs with cationic surfactants.^{16,17} The electrostatic interaction between the POM anions and cationic surfactants leads to the formation of amphiphilic complexes which can be used to create emulsions. However, a large portion of POMs’ active surface area is covered by cationic surfactants, which lowers their catalytic activity and the stability of the corresponding emulsions. The relatively weak static charge interaction between the POMs and cationic surfactants might not be stable especially at low pH or at high ionic strength. Moreover, the lack of quantitative study on the mechanism and key factors that might control the catalytic activity hinders further improvement and practical applications.

Herein we report a new approach of forming functional emulsions by using POM-organic hybrid amphiphilic molecules. Chemically grafting functional organic chains/ligands to the POMs has been developed rapidly recently as these new materials can successfully expand the compatibility of the POMs in organic media, and also introduce more features to the POMs (e.g., controllable fluorescence properties).^{19,20} Long alkyl tails covalently functionalized hexavanadate was reported previously by us to demonstrate amphiphilic feature and form stable emulsions in the mixture of toluene and water.²¹ This kind of functionalized hexavanadate hybrids is electrically active and able to act as catalyst for oxidation reactions.^{8,22,23} We use two hexavanadate-based hybrid surfactants in oxidation desulfurization reactions to demonstrate quantitative study of the mechanism of the emulsion catalysis, as well as the effects of pH and hydrophobicity of the organic tails on their catalytic activity. To the best of our knowledge, it is the first example that catalysts can controllably form catalytic active emulsions and reverse emulsions, which can be applied to tune the phase transfer behavior of catalysts. Gas chromatography (GC) and GC-MS were utilized to monitor the reaction rate while laser light scattering (LLS), electron microscopy (EM), ¹H-NMR, and UV-Vis were applied to give direct and indirect information on the catalytic mechanism.

8.2 Experimental section

Synthesis of hybrid 2. 2 was prepared by heating a mixture of $(\text{TBA})_2[\text{V}_6\text{O}_{13}\{(\text{OCH}_2)_3\text{CCH}_2\text{OH}\}_2]$ (2.5g, 2mmol), steric anhydride(0.55g, 1mmol), DMAP(0.13g, 1.1mmol) and 40ml acetonitrile at 70°C for 24h. After the reaction, the mixture was cooled down to room temperature and filtrated. The solvent was then removed by rotary evaporation and the precipitates was dissolved in 20 ml chloroform and then filtrated to remove excess amounts of $(\text{TBA})_2[\text{V}_6\text{O}_{13}\{(\text{OCH}_2)_3\text{CCH}_2\text{OH}\}_2]$. Then the chloroform was removed by rotary and the crude products were dissolved in an acetone/water (4:1) mixture. When acetone was slowly evaporated in the open air, red platelet crystals was firstly appeared in the solution and removed by filtration. Finally the pure product was obtained as red needle-like crystals.

ESI-MS (MeCN, negative, m/z): 523.32(100%) $[\text{V}_6\text{C18}]^{2-}$, 1246.98 $\text{H}[\text{V}_6\text{C18}]^-$, 1288.19 $(\text{TBA})[\text{V}_6\text{C18}]^-$; IR(KBr, cm^{-1}): 2960(m, C-H vibration of $-\text{CH}_3$), 2923(s, C-H vibration of $-\text{CH}_2-$), 2853(m), 1752(m, C=O vibration), 1632(m), 1467(m), 1384(w), 1159(w), 1130(m), 1067(m, C-O vibration in esterified tris), 1039(m, C-O vibration in unesterified tris), 956(s), 944(vs, $\text{V}-\text{O}_t$ vibration), 811(m), 720(s, $\text{V}-\text{O}_b-\text{V}$ vibration), 582(m).

Catalytic reaction of desulfurization set-up. As a typical case, thiophene (50 μL) was dissolved in 4 mL hexanes. 8 mg hybrid surfactant or V_6 or SDS (4 mg) (proton as counterion) was dissolved in 2.5 mL water and mixed with 2.5 mL hydrogen peroxide (30%,wt). The pH value of the obtained aqueous solutions was tuned to the required value by carefully titrating HCl or NaOH solutions. The two solutions were then mixed with continuous stirring (1000 rpm) with water bath (35 ~ 40 $^\circ\text{C}$). The reaction progress was monitored by GC and GC-MS by collecting samples (1 μL) at different time intervals. The concentration of thiophene is calculated based on the ratio of the area integration of thiophene peak over the area integration of hexanes peaks. The

conversion ratio at any time interval can be calculated as: $(\text{Conversion})_t = (C_t - C_0)/C_0$, C_0 and C_t means the concentration of thiophene in organic phase at time 0 min and t min, respectively.

Synthesis of hybrid 3. 3-(Trimethoxysilyl) propyl methacrylate (1.5 mL, 6.3 mmol) was added to 200 mL of a solvent mixture of $\text{CH}_3\text{CN}/\text{H}_2\text{O}$ (150 mL/50 mL, v/v). The solution was acidified with 5 mL of 6 M aqueous HCl solution. To it was slowly added the precursor $\text{Na}_9[\text{A-PW}_9\text{O}_{34}] \cdot 15\text{H}_2\text{O}$ (it was synthesized according to previously published procedure²⁴) (2.7 g, 1.0 mmol) with a small portion. The resulting colourless clear solution was concentrated to ca. 60 mL in volume with a water bath at 80 °C. To it was added Bu_4NBr (3.0g, 9.3 mmol). After stirring for 30 min at room temperature, a white powder formed, was collected by centrifugation at 6000 rpm for 1 hr. The obtain compound was dissolved in acetonitrile and ran through proton exchange column. The solution passed through the column was collected and vacuumed to remove the solvent. The resulted white powder was directly used in my research.

8.3 Polyoxometalate-organic hybrid molecules as amphiphilic emulsion catalysts for deep desulfurization

Two hexavanadate-based hybrid surfactants were synthesized and their molecular structures were displayed in Figure 8.1. **1** has been reported recently²¹, while the synthesis of **2** is similar to that of **1** by controlling the molar ratio of stearic acid/hexavanadate which is less than **1**, leading to the formation of single-tailed POM hybrids. The original counterions of both hybrids, tetrabutylammonium (TBA), have been replaced with protons or sodium ions via ion-exchanger, making the hybrids soluble in aqueous solution (see experimental section). The critical micelle concentration (CMC) of $\text{Na} \cdot \mathbf{1}$ ($\text{Na} \cdot \mathbf{1}$ represents hybrid **1** with sodium as counterions) reported recently²¹ is used as the minimum concentration for creating emulsions.

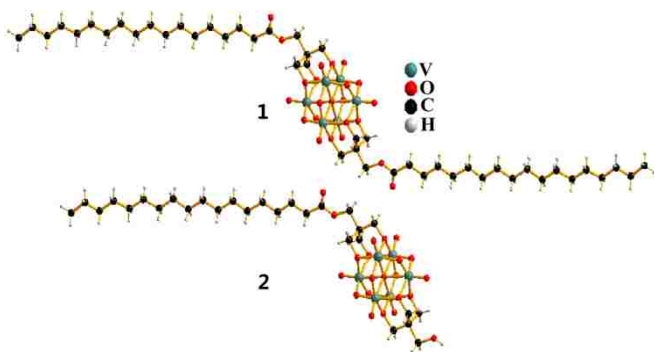


Figure 8.1 Molecular structures for hexavanadate-based hybrid surfactants, **1** and **2**. Reprinted with permission from ref.25. Copyright 2012 Wiley-VCH.

The oxidation of thiophene by hydrogen peroxide (H_2O_2) is used as the model reaction (Figure 8.2). H_2O_2 , an environmentally benign oxidizer, has been used widely for hazardous waste disposal, oxidation desulfurization, and organic synthesis.²⁶ Thiophene, the most inert compound against an oxidizing agent among all its derivatives, is poisonous to living bodies, environment, and noble metal catalysts for oil reforming in petroleum industry.²⁷ However, thiophene is immiscible with aqueous solution of hydrogen peroxide, making the oxidation of thiophene by H_2O_2 very difficult. Hence, this makes it an ideal model reaction not only to study the mechanism of the POM-based emulsion catalysis, but also to evaluate the potential practical applications of this approach in environmental chemistry and petroleum industry.

For a typical experiment, thiophene (50 μL) was dissolved in hexanes (4 mL) as a simple model for crude oil. Na***1** or Na***2** was dissolved in the aqueous solution of (*ca.* 1.6 mg/mL, 5 mL) H_2O_2 and mixed with the organic phase. The aqueous solution of the hybrid showed yellow color because of a strong UV-Vis absorption of the hexavanadate at 350 nm.²² Emulsions were formed in aqueous solution after stirring, which are stable for at least 2 days without further stirring (pH of the aqueous solution is *ca.* 6.0). Interestingly, the emulsion layer showed a deeper color than that of original aqueous solution; however, the aqueous solution at bottom is almost colorless (Figure 8.3a), suggesting most of the hybrids are at the water/hexanes interface. The hybrid surfactants are known to self-assemble into vesicle structures and be homogeneously distributed

in aqueous solution without the organic phase. When hexanes containing thiophene is added, the hybrids will stay at water/oil interface due to their amphiphilic feature and consequently stabilize the emulsions. As a result, almost all the catalytically active POM clusters are concentrated at the emulsion surface where two types of reactants can meet (Figure 8.3b and c). Dynamic light scattering (DLS) results indicated that the size of the emulsions is *ca.* 800 nm (Figure 8.4).

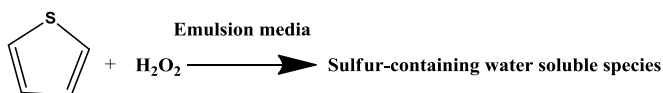


Figure 8.2 The equation for the catalytic oxidation reaction of thiophene. Reprinted with permission from ref.25. Copyright 2012 Wiley-VCH.

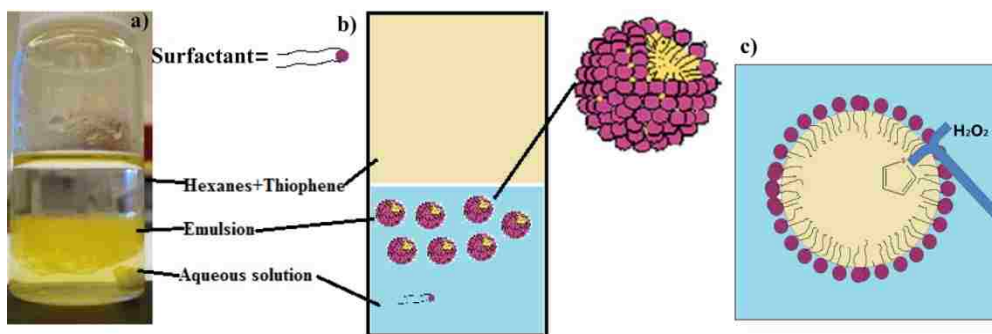


Figure 8.3 a) Picture of the emulsion catalytic system of surfactant with the pH of aqueous solution at 6; b) Models for the catalytic system; c) Model for the biphasic catalytic reactions. Reprinted with permission from ref.25. Copyright 2012 Wiley-VCH.

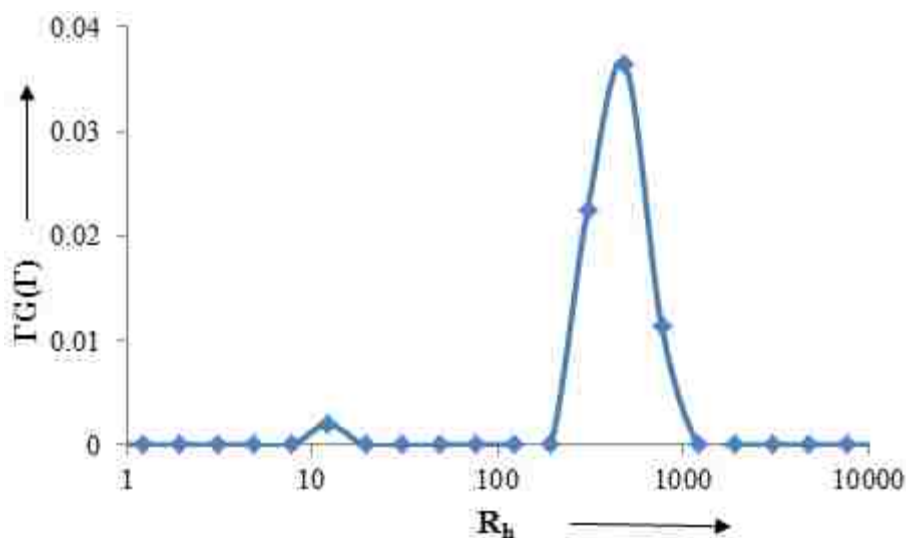


Figure 8.4 DLS results of the diluted emulsion solution. (R_h = *ca.* 400 nm). Reprinted with permission from ref.25. Copyright 2012 Wiley-VCH.

For a typical reaction, the concentration of thiophene in organic phase was monitored by GC and the reaction rate is evaluated by the decomposition conversion of thiophene after 80 min reaction. For all the reactions involving the emulsion catalysts, i.e., emulsions can be successfully created by using the hybrids, the conversion are much higher than those of the control experiments (the experiments with identical conditions but without adding any hybrids) within 80 min time interval (Figure 8.5 and Table 8-1). The synergetic effect of **1** and **2**'s amphiphilic and catalytic properties make them much better than either simple catalyst (e.g., hexavanadate, V_6) or conventional surfactant (SDS).

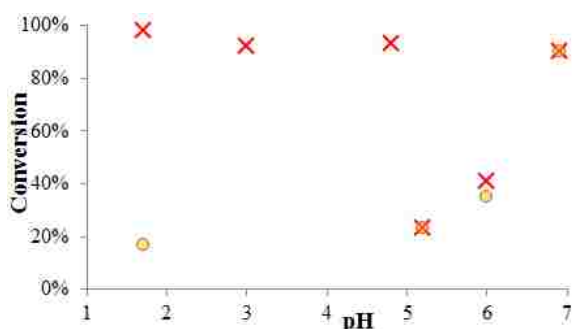


Figure 8.5 Oxidation decomposition conversion of thiophene for **1** and **2** catalyzed reactions at 80 min. (Control groups: V_6 as catalyst, the conversion is ca. 0% even after 1 day; SDS (sodium dodecyl sulfate) as catalyst, the conversion is ca. 6% at 80 min at pH = 1.7, 4.8, and 6.5, and achieved 40 % after 12 hrs.) Reprinted with permission from ref.25. Copyright 2012 Wiley-VCH.

Table 8-1 Oxidation decomposition conversion ratio of thiophene for **1** and **2** catalyzed experiments and control experiments at 80 min.

pH	1	2
6.9	90%	90%
6.0	41%	35%
5.2	23%	23%
4.8	93%	-----
3.0	92%	-----
1.7	98%	17%
Control 1: V_6 as catalyst, the conversion is ca. 0% even after 1 day.		
Control 2: SDS as catalyst, the conversion is ca. 6% at 80 min at pH = 1.7, 4.8, and 6.5, and achieved 40 % after 12 hrs.		

pH effect has been confirmed to play significant role in the self-assembly of POM-based hybrid surfactant in aqueous solution by changing the surface charge of POM polar head groups and,

consequently, their amphiphilic properties,²⁸ which could control the catalytic activity of the emulsion catalysts. H₂O₂ was tested to be quite unstable and would decompose immediately at pH>8 at 40 °C in the aqueous solution of the hybrids. A series of biphasic oxidation desulfurization catalytic reactions for both hybrid surfactants at different pH of aqueous solutions (from 1.0 to 6.9) were carried out at 35 ~ 40 °C (Figure 8.3). For catalytic experiments involving hybrid **2**, the oxidation decomposition conversion of thiophene became lower when the pH of aqueous solution dropped from 6.9 to 1.7 (Figure 8.5). The trend is consistent with the catalytic reactions of hybrid **1** when the corresponding pH decreased from 6.9 to 5.4 (Figure 8.5). It was experimentally confirmed that protons can covalently associate with hexavanadate clusters, which would significantly decrease its surface charge.²² Consequently, the static charge repulsion between the hexavanadates on emulsion surface became weaker, leading to much smaller curvature, i.e., larger emulsion sizes. In the current catalytic reactions, the emulsion sizes should become larger when the pH of aqueous solution is lower. Larger emulsions tend to lead to smaller total interfacial area when fix amount of surfactants are present in solution. Consequently, it will decrease the reaction rate. Static charge repulsion is expected to stabilize large particles by preventing them from collapse according to the DLVO theory.²⁹ Emulsions are not stable at very low pH since the hexavanadate clusters are weakly charged or neutral and therefore cannot stabilize the emulsions.

Interestingly, reverse emulsions can be observed in the hexanes phase for the pH range 4.8-1.7 in the catalytic reactions involving hybrid **1** (Figure 8.6 and Figure 8.7). Different from the oil-in-water emulsions, the reverse emulsions have the hexavanadate groups of the hybrids and the aqueous solution of H₂O₂ staying inside while thiophene and hexanes stay in the continuous phase (Figure 8.7d). The reverse emulsions can also work as catalytic centres with reactions carried out at the interface, which explains why hybrid **1** does not show decreased catalytic capability at lower pH (4.8-1.7) (Figure 8.5). As the indication of the reverse emulsion formation,

the organic phase turned to yellow in the reactions catalysed by hybrid **1** at low pH value (Figure 8.6), which was not observed in the reactions of hybrid **2**. UV-Vis spectrometry studies on organic phase indicated the existence of hybrid **1** at $\text{pH} < 5$, which confirmed the formation of reverse emulsions (Figure 8.7a). The concentration of reverse emulsions formed by hybrid **1** became higher in organic phase at lower pH by showing stronger UV-Vis absorption (Figure 8.7a). Interestingly, TEM studies confirmed that the reverse emulsions were not spherical, but rod-like structures with diameter and length as *ca.* 100 and 800 nm, respectively (Figure 8.7). When the pH in aqueous phase is lower than the critical value (*ca.* 5), the repulsion between the hexavanadate clusters is weak enough and the hydrophobic interaction is dominant, which drives the formation of reverse emulsions. However, no reverse emulsions were formed in the reactions of hybrid **2** since its hydrophobic part is not large enough to stabilize the hydrophilic domains in hexanes. The reverse emulsions of hybrid **1** are not stable and began to collapse to form precipitation with layer structures after *ca.* 1 hour without stirring and heating (Figure 8.7e and Figure 8.8). The hexanes phase separated from reaction system of **1** finally became colorless with precipitation in the bottom for overnight.

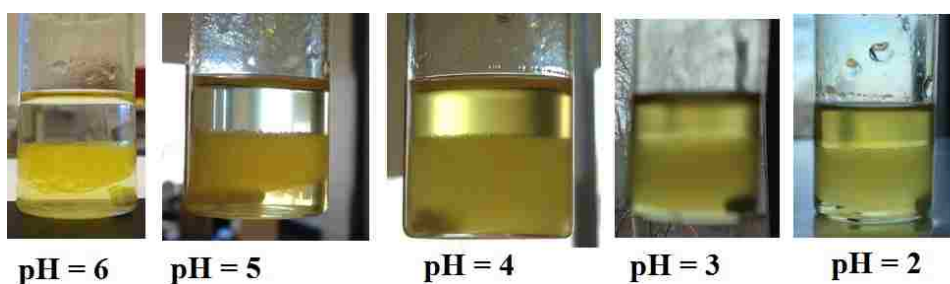


Figure 8.6 Pictures of hybrid **1**'s the catalytic systems with aqueous solutions at different pH values. The organic phases for $\text{pH} = 5$ and 6 are colorless while the pH is lower than 5 , the organic phases are of yellow color. Reprinted with permission from ref.25. Copyright 2012 Wiley-VCH.

The ultimate goal for desulfurization is not only oxidizing thiophene, but more importantly, removing all the sulfur-containing compounds from the oil phase. Most previous research on the oxidation desulfurization failed to achieve that and the oxidation products (sulfone) were left in the oil phase.^{16,17} In order to examine the existence of possible sulfur-containing product after our

reactions, the scanning temperature of GC was extended to up to 300 °C to search for possible products of the catalytic reactions. However, only hexanes and very tiny amount of unreacted thiophene (decomposition conversion is higher than 98%) were detected in the organic phase of the reactions with either **1** or **2** being the catalyst. For comparison, when using SDS as emulsifiers, a large amount of unreacted thiophene, together with thiophenoxide, thiophene and other unidentified organic molecules with high boiling temperatures can be observed in the hexanes phase. The unidentified organic compounds might be cyclo-addition products of thiophenoxide and thiophene.²⁷ The combination of the two GC results suggests that hybrid **1** and **2** catalyzed oxidation of thiophene produces water-soluble sulfur-containing species (sulfate) probably due to their highly efficient catalytic property. For practical applications this is very important since the emulsion catalysts are able to fully get rid of sulfur-containing species from the oil phase.

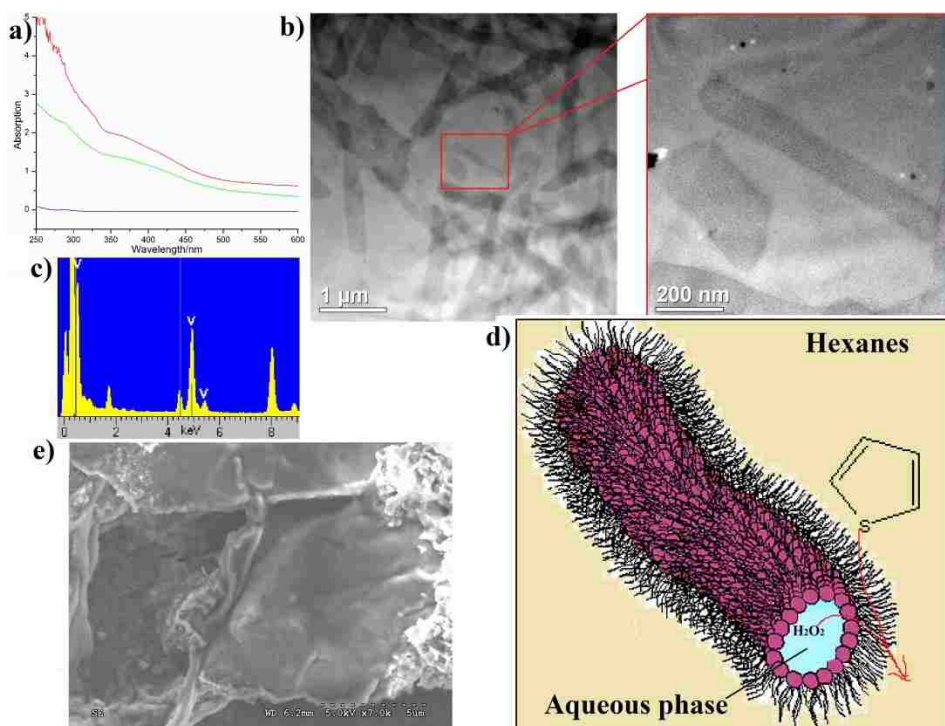


Figure 8.7 a) UV-Vis results of the hexanes phases with aqueous solutions at different pH values (Blue, pH=6; Green, pH=4; Red, pH=2); b) TEM images of the rod-like reverse emulsions; c) EDS results taken from the rod-like structures in b) in TEM, indicating large abundance of vanadium; d) Model for the rod-like reverse

emulsion; e) SEM images of the precipitation. Reprinted with permission from ref.25. Copyright 2012 Wiley-VCH.

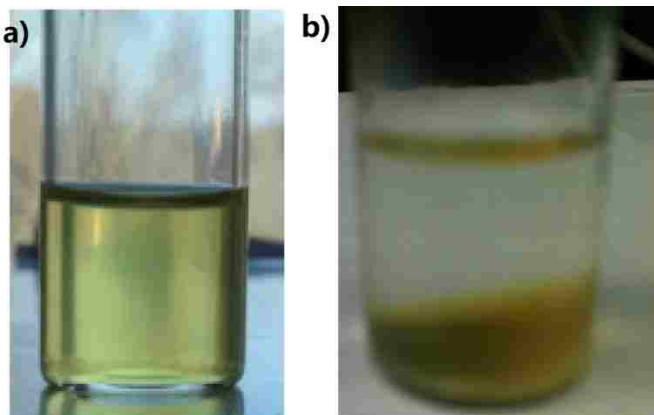


Figure 8.8 a) The freshly separated organic phase of catalytic reactions with the pH value of aqueous solutions as 2; b) sample a) overnight.

As claimed above, it is easy to separate reactants, products, and catalysts in such emulsion catalytic reactions. Organic phase and aqueous phase can be easily separated after demulsifying. The catalysts remained in aqueous solution were collected after the evaporation of water. $^1\text{H-NMR}$ results indicate that the hybrids are stable during the catalytic reaction. The emulsion catalyst can be recycled by running it through ion exchange column or evaporating the water solvent.

8.4 POMs-organic hybrid for building nanostructured POMs-polymer latex beads

Hybrid **3** is synthesized by covalently grafting four propyl methacrylate groups on the surface of phosphotungstate through multiple C-Si-O bonds.³⁰ The tri-lacunary POM is quite hydrophilic with three negative charges while the four organic groups form the hydrophobic part of the hybrid (Figure 8.9). In this project, amphiphilic hybrid **3** was utilized in the emulsion polymerization of styrene system. As a typical experiment for emulsion polymerization, hybrid **3** was used to stabilize the emulsion droplets of styrene in aqueous environment (Figure 8.10). Actually, the hybrid works also as co-monomer in the polymerization process of styrene since the organic

fragments are ended with C=C double bonds. The organic fragments are supposed to form random co-polymer with styrene because of their similar reactivity ratios.

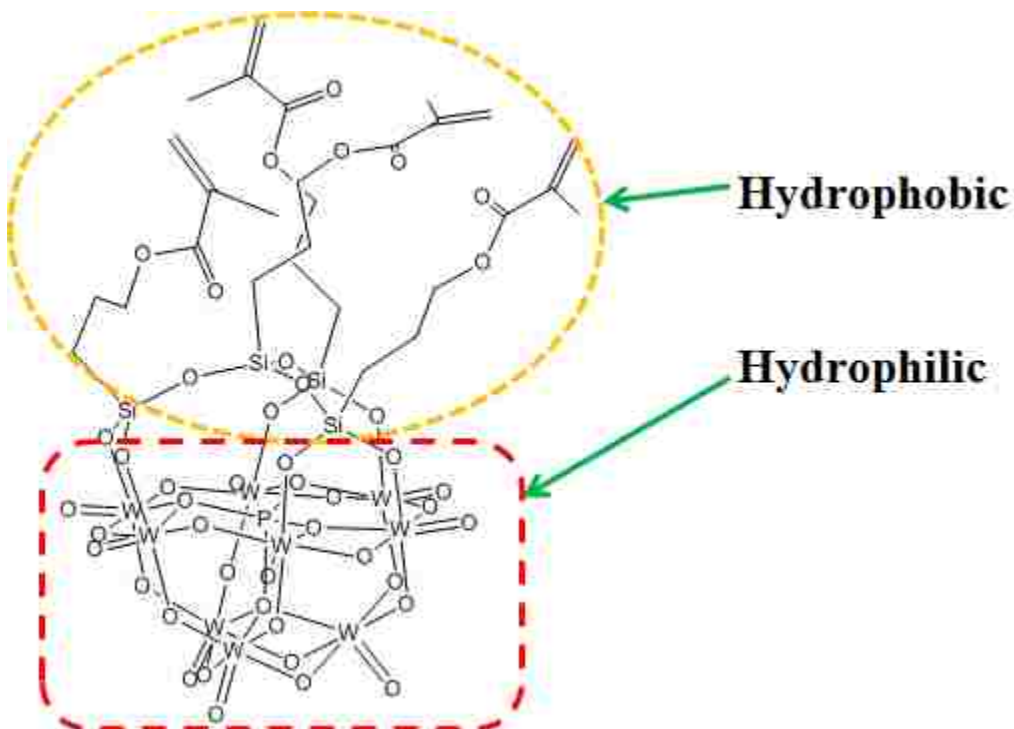


Figure 8.9 Molecular structure of hybrid 3.

The polymer reaction was carried out based on traditional emulsion polymerization protocol except we used hybrid 3 as surfactant.³¹ After 12 hrs polymerization reaction at 70 °C with potassium persulfate as initiator, the obtained milk-like solution was centrifuged and the obtained solid sample was washed with water. DLS results indicated Rh of the particles in the solution was ca. 100 nm. TEM confirmed that spherical particles with sizes as ca. 200 nm were the major assemblies in solution (Figure 8.11). More important, EDS analysis on the particle surface indicates that tungstate are concentrated on the surface of particles, suggesting POMs clusters cover the surface of the particles and stabilize them in solution. In that way, POMs can be easily and stably grafted on the surface of polymer latex, which provides a cheap way to produce POM-based heterogeneous catalysts.

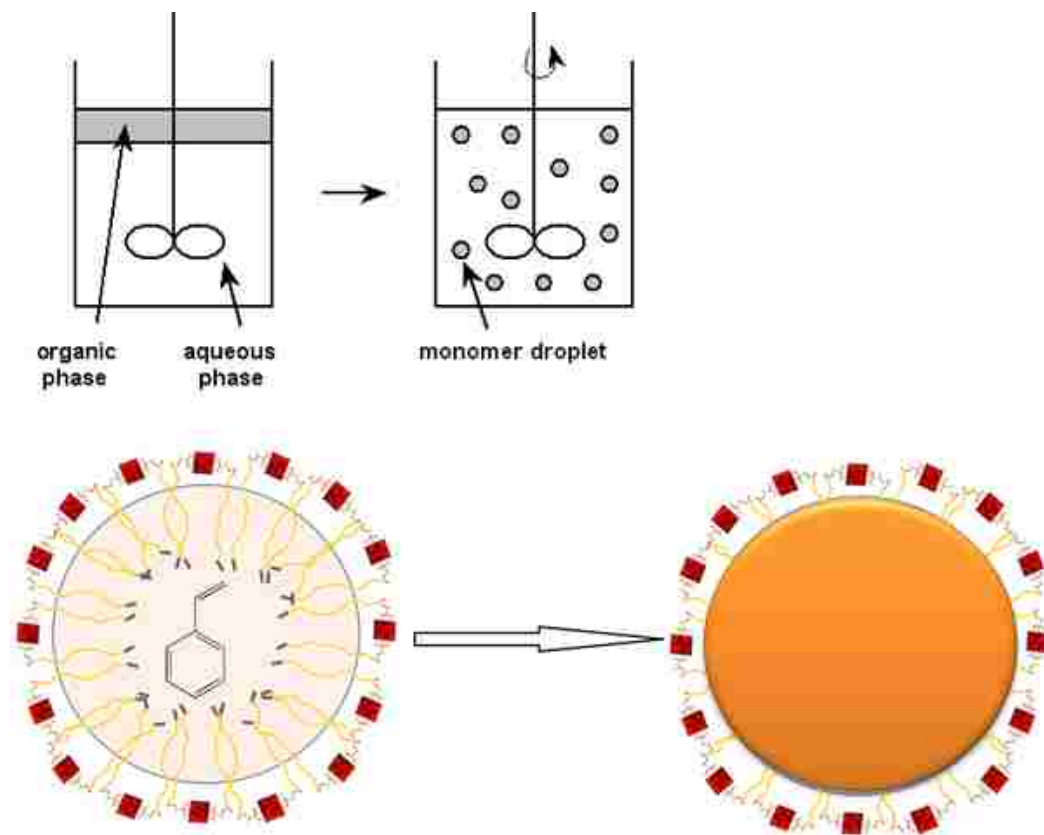


Figure 8.10 top) Typical experiment for emulsion polymerization; bottom) model for hybrid stabilized emulsion and the particles after polymerization.

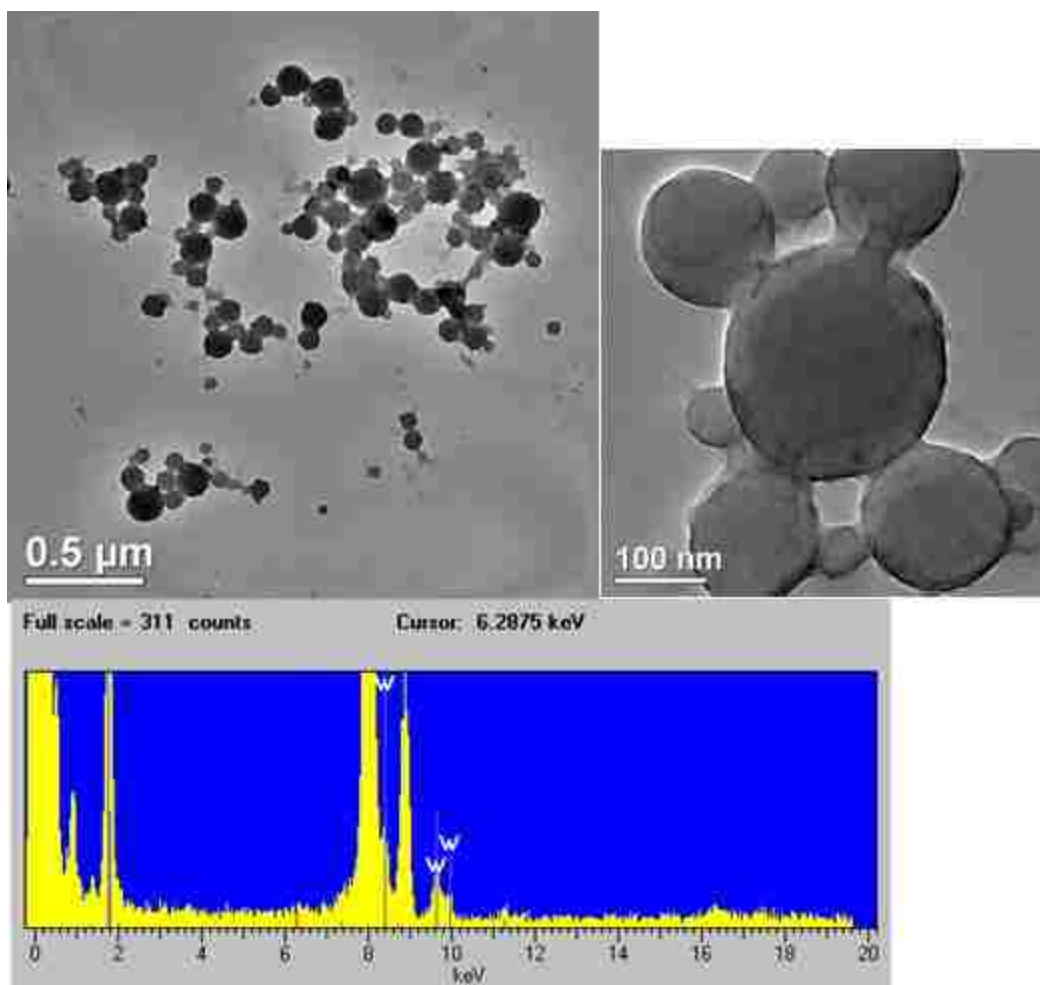


Figure 8.11 top) TEM images of the POM-polymer latex; bottom) EDS results of the surface area of the latex beads.

8.5 Conclusion

In summary, the amphiphilic hybrid hexavanadates are proven to be highly efficient emulsion catalysts with high stability for ultra-deep oxidation desulfurization. The hybrids can be used as amphiphiles to create emulsions with the catalytically active hexavanadate headgroups distributed at water/oil interface. The emulsion formation and the efficiency of the emulsion catalysts were monitored through time-resolved measurements. The conversion rate for the oxidation reaction of thiophene has been significantly improved since the catalysts at interface can connect the reactants in aqueous phase and oil phase. The pH of aqueous phase and the hydrophobicity of alkyl tails on the hybrids both play key roles in controlling the size of emulsion and the formation

reverse emulsions, which consequently determine the reaction rate. As an opening work on the emulsion catalytic behaviour of amphiphilic hybrid POMs, our research is supposed to extend the catalytic application of POMs and impose more controllability on their catalytic systems. The reported approach of emulsion catalysis can be easily expanded to other systems and to practical applications.

Reference

- (1) Ettetdgui, J.; Diskin-Posner, Y.; Weiner, L.; Neumann, R. *J. Am. Chem. Soc.* **2010**, *133*, 188.
- (2) Hill, C. L. *J. Mol. Catal. A* **2007**, *262*, 2.
- (3) Kamata, K.; Yonehara, K.; Sumida, Y.; Yamaguchi, K.; Hikichi, S.; Mizuno, N. *Science* **2003**, *300*, 964.
- (4) Long, D.-L.; Tsunashima, R.; Cronin, L. *Angew. Chem. Int. Ed.* **2010**, *49*, 1736.
- (5) Mizuno, N.; Misono, M. *Chem. Rev.* **1998**, *98*, 199.
- (6) Yin, Q.; Tan, J. M.; Besson, C.; Geletii, Y. V.; Musaev, D. G.; Kuznetsov, A. E.; Luo, Z.; Hardcastle, K. I.; Hill, C. L. *Science* **2010**, *328*, 342.
- (7) Du, D.-Y.; Qin, J.-S.; Wang, T.-T.; Li, S.-L.; Su, Z.-M.; Shao, K.-Z.; Lan, Y.-Q.; Wang, X.-L.; Wang, E.-B. *Chem. Sci.* **2012**, *3*.
- (8) Han, J. W.; Hill, C. L. *J. Am. Chem. Soc.* **2007**, *129*, 15094.
- (9) Mizuno, N.; Uchida, S.; Kamata, K.; Ishimoto, R.; Nojima, S.; Yonehara, K.; Sumida, Y. *Angew. Chem. Int. Ed.* **2010**, *49*, 9972.
- (10) Song, J.; Luo, Z.; Britt, D. K.; Furukawa, H.; Yaghi, O. M.; Hardcastle, K. I.; Hill, C. L. *J. Am. Chem. Soc.* **2011**, *133*, 16839.
- (11) Haimov, A.; Cohen, H.; Neumann, R. *J. Am. Chem. Soc.* **2004**, *126*, 11762.
- (12) Haimov, A.; Neumann, R. *J. Am. Chem. Soc.* **2006**, *128*, 15697.

- (13) Maayan, G.; Popovitz-Biro, R.; Neumann, R. *J. Am. Chem. Soc.* **2006**, *128*, 4968.
- (14) Neumann, R.; Cohen, M. *Angew. Chem. Int. Ed.* **1997**, *36*, 1738.
- (15) Yamaguchi, K.; Yoshida, C.; Uchida, S.; Mizuno, N. *J. Am. Chem. Soc.* **2004**, *127*, 530.
- (16) Li, C.; Jiang, Z.; Gao, J.; Yang, Y.; Wang, S.; Tian, F.; Sun, F.; Sun, X.; Ying, P.; Han, C. *Chem. Eur. J.* **2004**, *10*, 2277.
- (17) Lu, H.; Gao, J.; Jiang, Z.; Yang, Y.; Song, B.; Li, C. *Chem. Commun.* **2007**.
- (18) Crossley, S.; Faria, J.; Shen, M.; Resasco, D. E. *Science* **2010**, *327*, 68.
- (19) Dolbecq, A.; Dumas, E.; Mayer, C. d. R.; Mialane, P. *Chem. Rev.* **2010**, *110*, 6009.
- (20) Li, D.; Yin, P.; Liu, T. *Dalton* **2012**, *41*.
- (21) Yin, P.; Wu, P.; Xiao, Z.; Li, D.; Bitterlich, E.; Zhang, J.; Cheng, P.; Vezenov, D. V.; Liu, T.; Wei, Y. *Angew. Chem. Int. Ed.* **2011**, *50*, 2521.
- (22) Chen, Q.; Goshorn, D. P.; Scholes, C. P.; Tan, X. L.; Zubieta, J. *J. Am. Chem. Soc.* **1992**, *114*, 4667.
- (23) Mizuno, N.; Kamata, K. *Coord. Chem. Rev.* **2011**, *255*, 2358.
- (24) Domaille, P. J.; Hervéa, G.; Téazéa, A. In *Inorganic Syntheses*; John Wiley & Sons, Inc.: 2007, p 96.
- (25) Yin, P.; Wang, J.; Xiao, Z.; Wu, P.; Wei, Y.; Liu, T. *Chem. Eur. J.* **2012**, *18*, 9174.
- (26) *Catalytic oxidations with hydrogen peroxide as oxidant*; Strukul, G., Ed.; Kluwer Academic Publishers: the Netherlands, 1992.
- (27) Brown, K. N.; Espenson, J. H. *Inorg. Chem.* **1996**, *35*, 7211.
- (28) Li, D.; Song, J.; Yin, P.; Simotwo, S.; Bassler, A. J.; Aung, Y.; Roberts, J. E.; Hardcastle, K. I.; Hill, C. L.; Liu, T. *J. Am. Chem. Soc.* **2011**, *133*, 14010.

- (29) *Theory of the Stability of Lyophobic Colloids*; Verwey, E. J.; Overbeek, J. T. G., Eds.; Elsevier: Amsterdam, 1948.
- (30) Aoki, S.; Kurashina, T.; Kasahara, Y.; Nishijima, T.; Nomiya, K. *Dalton* **2011**, *40*, 1243.
- (31) Asua, J. M. *J. Polymer Sci. A: Polymer Chem.* **2004**, *42*, 1025.

Chapter 9: Supramolecular Assembly of Conjugated Polymers Containing POM-terminal Side Chains in Polar and Nonpolar Solvents

9.1 Introduction

Conjugated polymers are important materials with unique electrical and optoelectronic properties, which have found applications in a variety of molecular electronic devices including light-emitting diodes, solar cells, field effect transistors, photodetectors, sensors, and nonlinear optics.¹⁻

³ Polyoxometalates (POMs), a large group of metal oxide clusters consisting of early transition metal cations and oxo ligands, are also considered electrically active materials and have attracted increasing interest in recent years due to their outstanding properties in catalysis, medicine, and photo-electronic responses.⁴⁻⁶ Incorporating POM clusters covalently with conjugated polymers may lead to hybrid materials with not only value-adding properties but also synergistic effects. For example, POM-containing hybrid polymers have been found to be good candidates for photovoltaic cells, photocatalytic materials, and catalytic nanoparticles.⁷ While it is well known that the device performance of hybrid materials depends strongly on their aggregated micro- or nano-structures, there has been very few research on the aggregation of POM-containing conjugated polymers in both solution and solid states. Such studies are essential if POM-based controllable ordered structures are to be realized.

On the other hand, understanding the aggregation behavior of polyelectrolyte solutions has always been an important goal^{8,9,10} in polymer and biological sciences since it may help explain the behaviors of DNA^{11,12}, RNA¹³, and proteins¹⁴ in living cells and guide the design of polyelectrolyte-based functional materials³. However, due to the coexistence of complex inter- and intra-chain electrostatic interactions, the polyelectrolyte solutions are still poorly understood.¹⁵⁻¹⁸ Herein, we report the self-assembly behavior of conjugated polymers containing

POM-terminal side chains in polar and nonpolar solvents. As shown in Figure 1, such polymers have rigid rod-like structures due to the phenylene ethynylene backbone. The POM cluster, an organoimido derivatized hexamolybdate with size as ~ 1 nm and carrying two negative charges with two tetrabutyl ammonium (TBA) as the counter-cations, is covalently linked to the polymer backbone as the terminal of their side chains.

9.2 Experimental section

The syntheses of the four polymers have been previous reported.¹⁹ Toluene, acetone and DMSO were purchased from Aldrich-Sigma and were used without further purification. All solutions for light scattering experiments were filtered through a 200-nm filter, which was purchased from Millipore and used with a syringe. The UV-Vis absorption value of solutions with concentration ranging from 0.001 to 0.04 mg/mL were measured at 532 nm and used for absorption correction in CMC determination and molecular weight determination in light scattering experiments. The video for the fluorescence microscopy results can be watched through the following links:

Video for the aggregates of **1** in toluene: http://www.youtube.com/watch?v=kr64xGO_OBM

Video for the aggregates of **1** in acetone: http://www.youtube.com/watch?v=kr64xGO_OBM

Video for the rod-like aggregates of **1** in DMSO:
<http://www.youtube.com/watch?v=njObmpjjAuE>

Video for the co-existence of rod-like and dot-shape aggregates of **1** in DMSO:
<http://www.youtube.com/watch?v=LlaDQLbm66I>

Light scattering measurements for CMC determination in toluene: A toluene solution of polymer **1** with a concentration of 0.1 mg/mL was titrated with pure toluene while the scattering intensity of the solution at the 90° scattering angle was simultaneously monitored. Figure S1 shows how the scattering intensity changes as the concentration of the solution is lowered, from which the CMC can be determined to be 0.04 mg/mL.

Light scattering measurements for molecular weight determination: solutions with concentrations from 0.001 mg/mL to 0.04 mg/mL in toluene were prepared. The dn/dc for polymer 1 in toluene was determined to be 0.273 mL/g within the above concentration range.

Static light scattering: A commercial Brookhaven Instrument LLS spectrometer equipped with a solid-state laser operating at 532 nm was used for measurement of both SLS and DLS. SLS experiments were performed at scattering angles (θ) between 20 and 100°, at 2° intervals. However, due to the large fluctuations in scattered intensities at low scattering angles, we removed the data from 20-40° in the final analysis. Derived from Rayleigh-Gans-Debye equation²⁰, partial Zimm plot was used to analyze the SLS data to obtain the radius of gyration (R_g). The partial Zimm plot stems from the following approximate formula: $1/I = C(1 + R_g^2 * q^2/3)$. Here R_g is determined from the slope and the intercept of a plot of $1/I$ vs. q^2 .

Dynamic light scattering: DLS measures the intensity–intensity time correlation function by means of a BI-9000AT multi-channel digital correlator. The field correlation function $|g^{(1)}(\tau)|$ was analyzed by the constrained regularized CONTIN method²¹ to yield information on the distribution of the characteristic linewidth Γ from $|g^{(1)}(\tau)| = \int G(\Gamma) e^{-\Gamma \tau} d\Gamma$. The normalized distribution function of the characteristic linewidth, $G(\Gamma)$, so obtained, can be used to determine an average apparent translational diffusion coefficient, $D_{app} = \Gamma/q^2$. The hydrodynamic radius R_h is related to D via the Stokes–Einstein equation: $R_h = kT/(6\pi\eta D)$ where k is the Boltzmann constant and η the viscosity of the solvent at temperature T . From DLS measurements, we can obtain the particle-size distribution in solution from a plot of $\Gamma * G(\Gamma)$ versus R_h . The R_h of the particles is obtained by extrapolating $R_{h,app}$ to zero scattering angle. $= \int G(\Gamma) e^{-\Gamma \tau} d\Gamma$. The normalized distribution function of the characteristic linewidth, $G(\Gamma)$, so obtained, can be used to determine an average apparent translational diffusion coefficient, $D_{app} = \Gamma/q^2$. The hydrodynamic radius R_h is related to D via the Stokes–Einstein equation: $R_h = kT/(6\pi\eta D)$ where k is the Boltzmann constant and η the viscosity of the solvent at temperature T . From DLS measurements, we can

obtain the particle-size distribution in solution from a plot of $\Gamma \cdot G(\Gamma)$ versus R_h . The R_h of the particles is obtained by extrapolating $R_{h,app}$ to zero scattering angle.

Transmission electric microscopy studies. The TEM images were taken on a JEOL JEM-2000 electron microscope operated at 200 kV. Samples for the TEM analysis were prepared by dropping a small volume of the solution sample onto a holey carbon film on copper grid.

9.3 Results and discussion

9.3.1 Molecular weight determination

Polymers **1–4**, $(C_{140}H_{203}Mo_6N_3O_{28})_n$, $(C_{212}H_{299}Mo_6N_3O_{36})_n$, $(C_{148}H_{223}Mo_6N_3O_{30})_n$, and $(C_{18}H_{24}O_2)_n$ (Figure 9.1), were synthesized according to literature¹⁹ and they have been fully characterized. They are insoluble in water, but can be easily dissolved in some common organic solvents with different polarities (e.g., toluene, acetone, and DMSO). Polymers **1**, **2**, and **3** all possess the same type of POM clusters, but with different side chain lengths and/or POM cluster loading ratios, making them ideal models for understanding such hybrid polymers. Polymer **4**, without any POM in polymer chain, is used for control study in order to clarify the importance of POMs in the solution behaviors of these copolymers. Due to the low polarity of toluene, the counter-cations, TBAs, are expected to be associated firmly with the cluster anions to neutralize the charges on polymers, a situation which is suitable for determining the polymer's molecular weight. Polymer **1** is observed to self-assemble in toluene, with the critical micelle concentration (CMC) being 0.040 mg/mL according to static light scattering (SLS) studies (Figure 9.2). The determination of the weight average molecular weight ($\overline{M_w}$) must be done below the CMC in toluene. It is calculated to be 28,000 g/mol for polymer **1** from SLS studies (Figure 9.3), corresponding to 9-10 repeating units ($n=9\sim 10$). The length of each repeating unit is *ca.* 5.3 nm. Therefore, the contour length of the polymer chain should be *ca.* 50 nm. Interestingly, the chain structure of Polymer **1** can be clearly observed when studying its film with atomic force microscope (AFM) (Figure 9.4).

Polymer **2** has fewer POM-containing side chains (lower POM loading ratio) than Polymer **1** does, while polymer **3** possesses the same POM-loading ratio as Polymer **1** but through a longer and more flexible bridge. Polymers **2** and **3** is expected to have similar contour length as polymer **1** based on the previous characterization.¹⁹

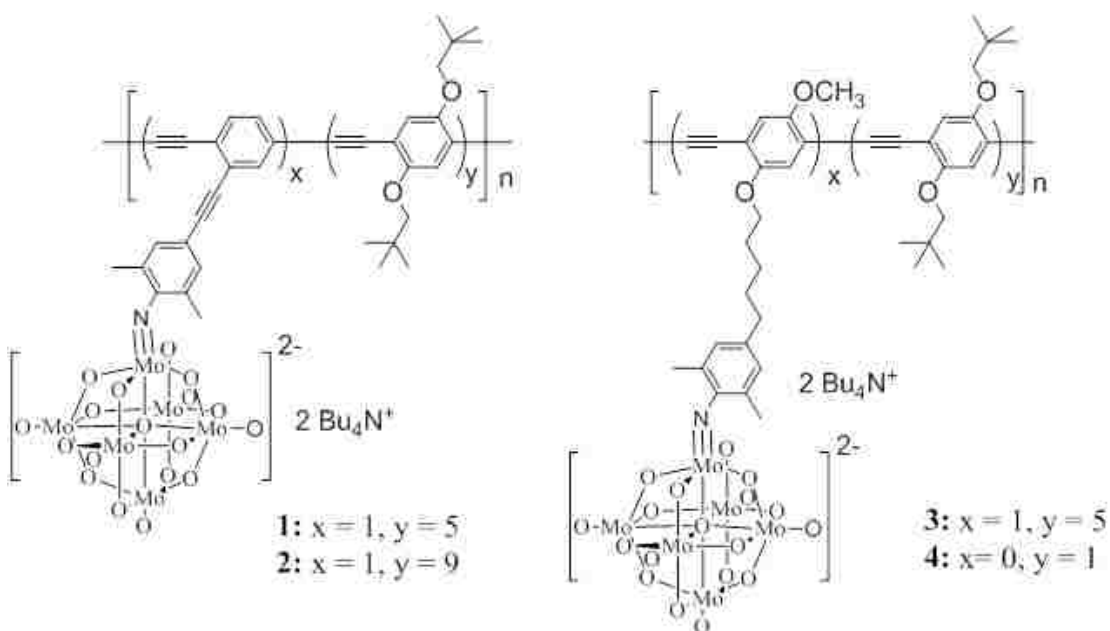


Figure 9.1 Molecular structures of polymers 1, 2, 3, and 4. Reprinted with permission from ref.22. Copyright 2012 Wiley-VCH.

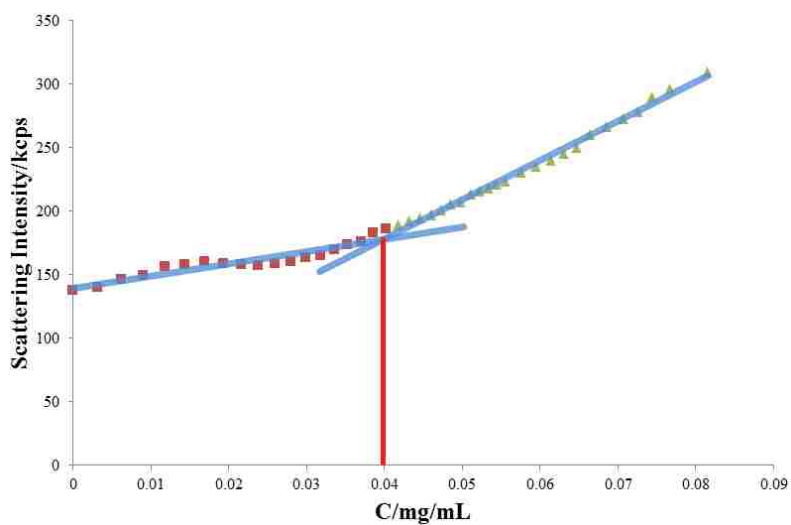


Figure 9.2 The change in scattered intensities monitored at 90° scattering angle as the concentration of polymer **1** in toluene is continuously lowered through solvent titration. The CMC was determined to be 0.04 mg/mL.

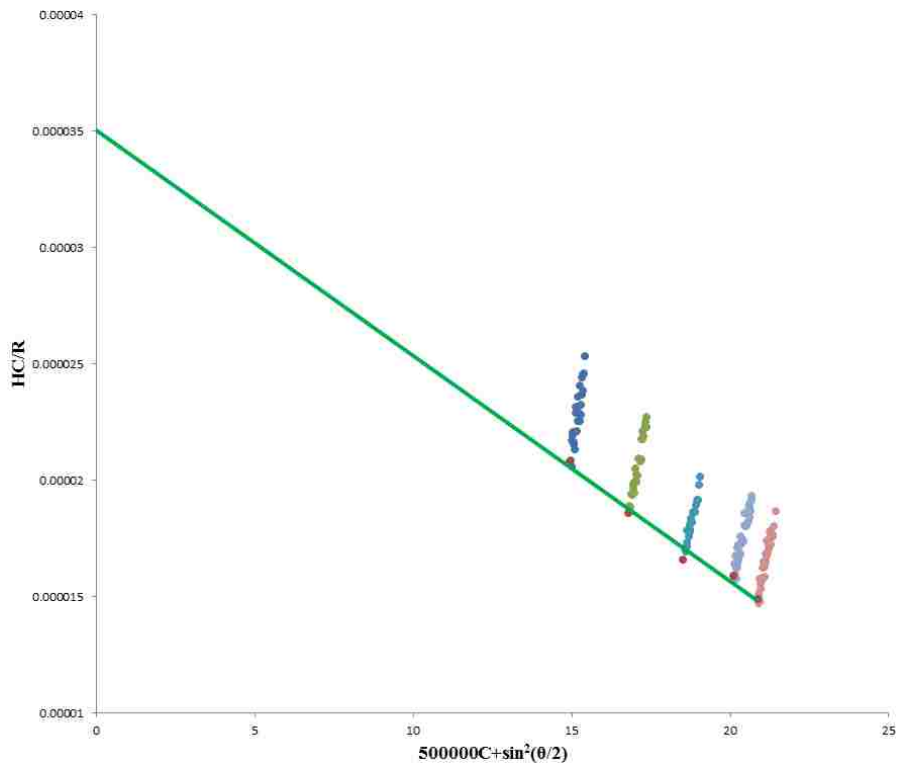


Figure 9.3 Zimm plot for the calculation of molecular weight of polymer 1.

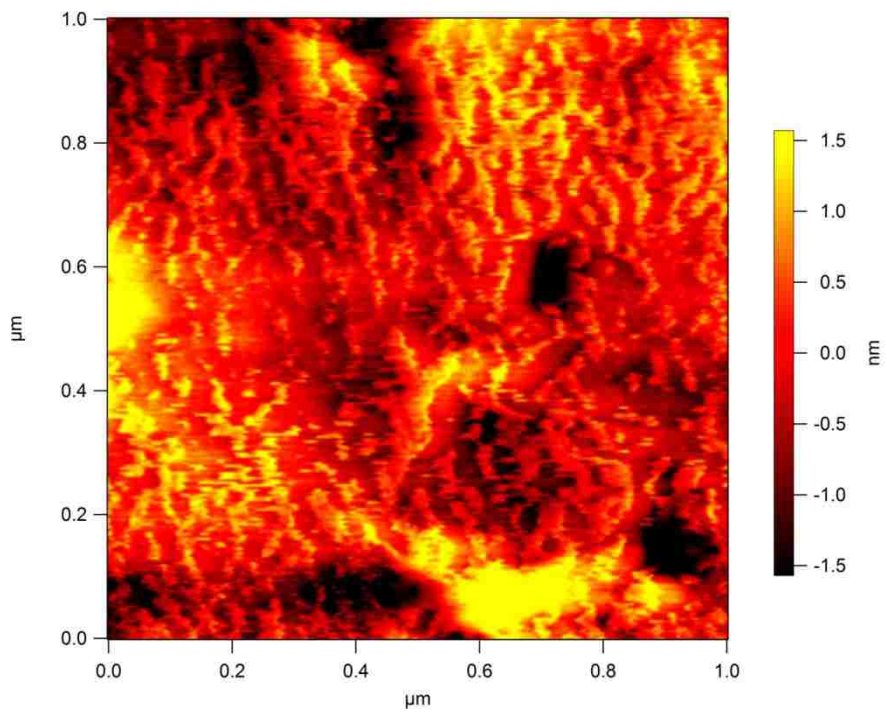


Figure 9.4 Topography of the surface of a spin-coated polymer 1 film.

9.3.2 Self-assembly of the polymers in nonpolar solvent

Polymer **1** shows amphiphilic property in toluene since the polymer backbone is solvophilic while the POM clusters are solvophobic. In a freshly prepared 0.1 mg/mL toluene solution of **1**, dynamic light scattering (DLS) indicates the coexistence of two species with hydrodynamic radii (R_h) of *ca.* 5 ± 1 nm and 44 ± 3 nm, respectively (Figure 9.5a). The smaller species can be assigned to single polymer chains and the larger ones are likely the assemblies. Time-resolved SLS study monitored at 90° scattering angle shows that the scattering intensity keeps increasing with time and reaches equilibrium after 20 days (Figure 9.5b), suggesting the formation of supramolecular structures. However, the average R_h of the aggregates does not change with time, suggesting that it is the number, not the size of supramolecular aggregates that increases with time. The R_h value does not show angular dependence, indicating spherical structures for the aggregates. The average radius of gyration, R_g , is calculated to be 43 ± 3 nm from the SLS studies. The ratio of R_h/R_g is ~ 1 , suggesting a hollow spherical structure for the aggregates, which is also confirmed by TEM results (Figure 9.6a). Interestingly, a large number of assemblies can be directly observed in solution under fluorescence microscope as large dots (Figure 9.6b). Based on the analysis of the amphiphilic properties of **1**, the assemblies are presumed to be reverse vesicles with polymer backbones exposing to the solvent while the POMs forming the solvophobic interior (Figure 9.6c).

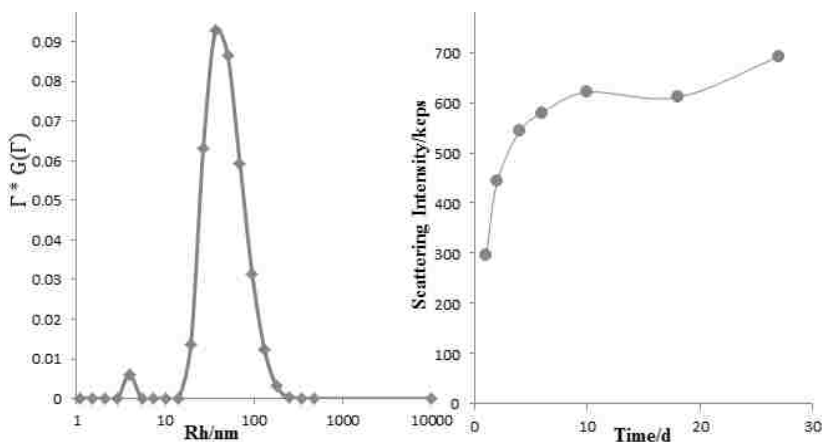


Figure 9.5 a) CONTIN analysis results of DLS data of polymer 1's 0.1 mg/mL toluene solution at the scattering angle of 30°; b) the scattering intensities versus time monitored at 90° scattering angle for polymer 1's 0.1 mg/mL toluene solution. Reprinted with permission from ref.22. Copyright 2012 Wiley-VCH

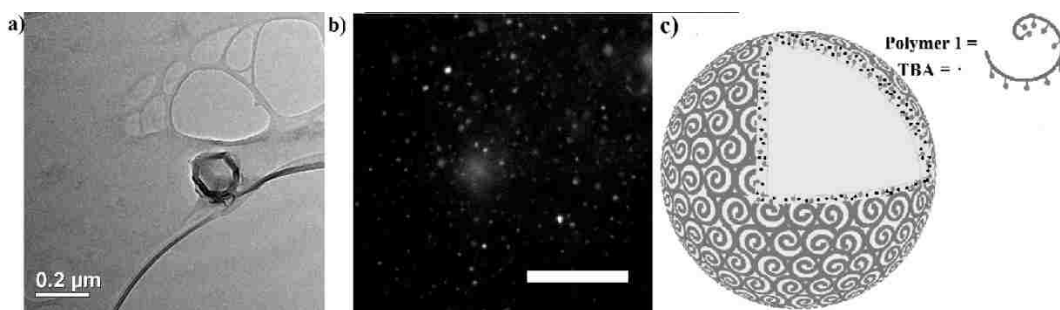


Figure 9.6 a) TEM image of the assembly of polymer 1 in toluene; b) fluorescence microscope image of a 0.1 mg/mL toluene solution of polymer 1 (scale bar, 30 μm); c) model of the reverse vesicle structure in toluene. Reprinted with permission from ref.22. Copyright 2012 Wiley-VCH

Similar to Polymer 1, Polymers 2 and 3 in toluene form vesicular assemblies as well, but with much larger sizes ($R_h = R_g = ca. 200$ nm for 2 and $ca. 110$ nm for 3, respectively, Figure 9.7). Without POM clusters in the side chain, polymer 4 shows very low scattered intensity with small average R_h values (less than 10 nm) in toluene, indicating negligible inter-polymer aggregation. The similar assembly behavior of the three POM-based polymers, coupled with the lack of supramolecular structure formation of polymer 4, suggests that both the hydrophobic backbone and the POMs on side chains play crucial roles in the reverse vesicle formation. The size difference among these vesicles can be attributed to the extent of imbalance between solvophilic/solvophobic components of the polymers. With lower POM loading ratio or longer flexible organic linkage on the side chain, the backbones of polymers 2 and 3 are more flexible

than that of **1**, consequently easier for them to bend toward the solvent part, which will reduce the area of solvophilic components and lead to smaller curvature, i.e., larger vesicle size.

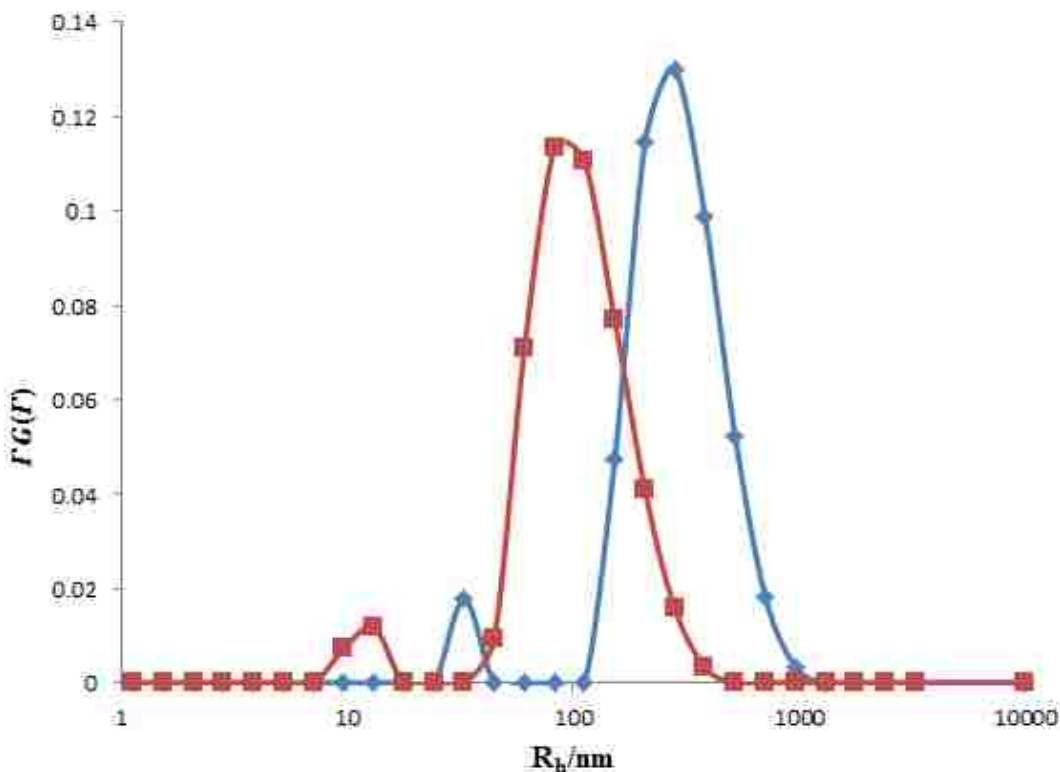


Figure 9.7 Dynamic light scattering (DLS) results of **2** (blue) and **3** (red) at scattering angle of 30 degree. $R_h=R_g=200$ nm for **2** and $R_h=R_g=110$ nm for **3**.

9.3.3 Self-assembly of the polymers in polar solvents

In a polar solvent such as acetone or DMSO, the TBA counter-cations may dissociate from the surface of cluster anions and make the POM clusters charged. The charged clusters render these polymers polyelectrolyte properties, as confirmed by Zeta-potential measurements. The Zeta-potential values recorded in 0.5 mg/mL acetone and DMSO solutions of polymer **1** are -23.9 and -24.0 mV, respectively. These polyelectrolytes further assemble. SLS and DLS results show that the average R_h and R_g of the assemblies in acetone solution are 15 and 48 nm, respectively, and those of the assemblies in the DMSO solution are 43 and 60 nm, respectively. The assembly sizes remain the same when the solution is diluted even down to 0.1 mg/mL. For both assemblies, their average R_g value is much larger than their corresponding R_h value, suggesting anisotropic

(possibly rod-like) structures for the assemblies. These rod-like assemblies with very uniform sizes can be directly observed under fluorescence microscope (Figure 9.8). Tiny dots can be found around the rod structures in the solutions, which might be due to the existence of polymer **1** single chains or oligomers (Figure 9.9). Interestingly, corresponding TEM studies not only confirm the rod structures of the assemblies, but also show their hollow feature, e.g., from the broken rods shown in Figure 9.10. Strong contrast between the dark, solid shell and the light hollow centre can be observed in the collapsed rod structure (Figure 9.10). The thickness of the wall is *ca.* 4 nm. The diameters (*D*) for the tube structures formed in acetone and DMSO are 30 nm and 38 nm, respectively. Energy-dispersive X-ray spectroscopy (EDS) studies indicate the existence of molybdenum in the features, which confirms that the building units of the tube-like structures are indeed polymer **1** (Figure 9.11). POM-based microtubular structures have been obtained in solution state and crystalline state²³⁻²⁵; however, the report on POM-based single-wall nanotube structures (SWNTs) is rare²⁶.

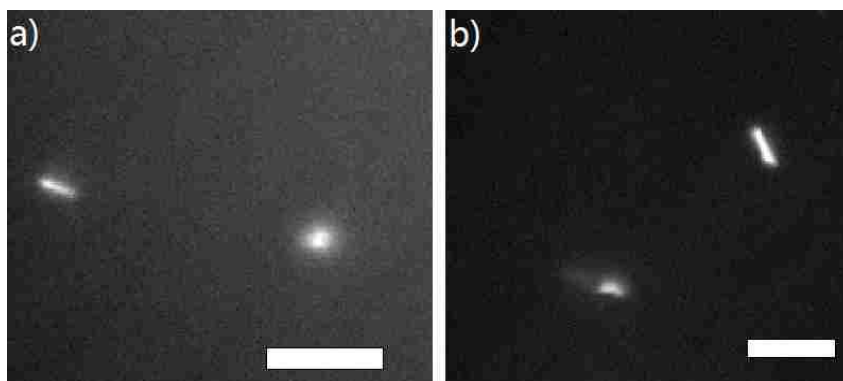


Figure 9.8 Images taken under fluorescence for a) assemblies in **1**'s 0.1 mg/mL acetone solution; b) assemblies in **1**'s 0.1 mg/mL DMSO solution. Scale bar, 10 μ m. Reprinted with permission from ref.22. Copyright 2012 Wiley-VCH

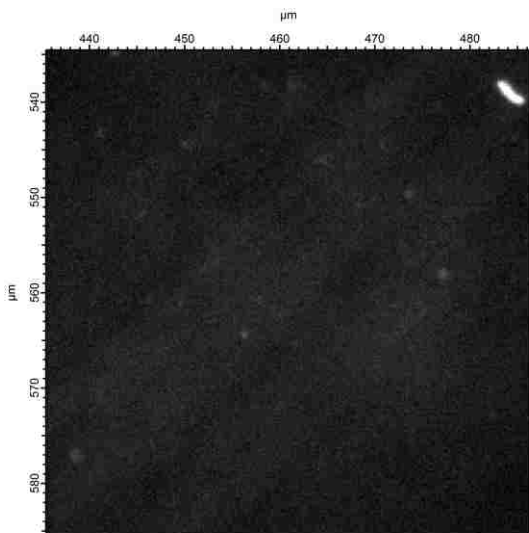


Figure 9.9 Fluorescence image of a DMSO solution of polymer 1, showing the rod structure (up right corner) and small dots of single chains.

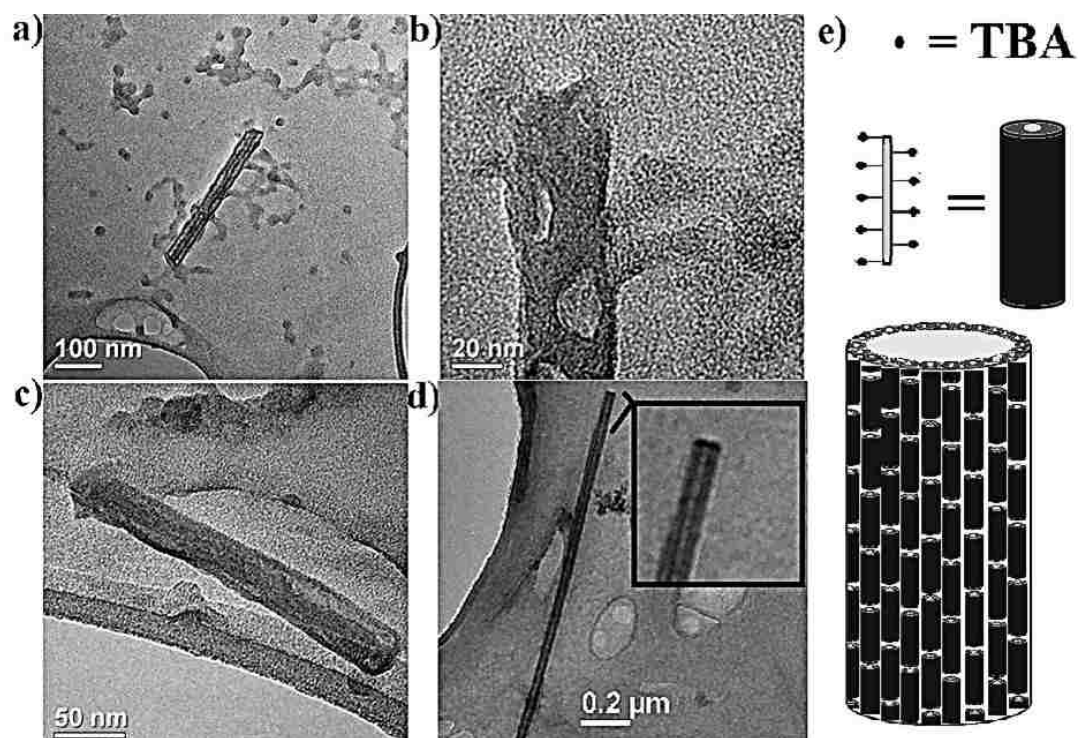


Figure 9.10 TEM images for a) assemblies in acetone; b) zoom in image of the feature in a); c) another rod structure in acetone; d) assemblies in DMSO (inset: zoom in image for the tube structure). e) Model for the tube-like assemblies. Reprinted with permission from ref.22. Copyright 2012 Wiley-VCH

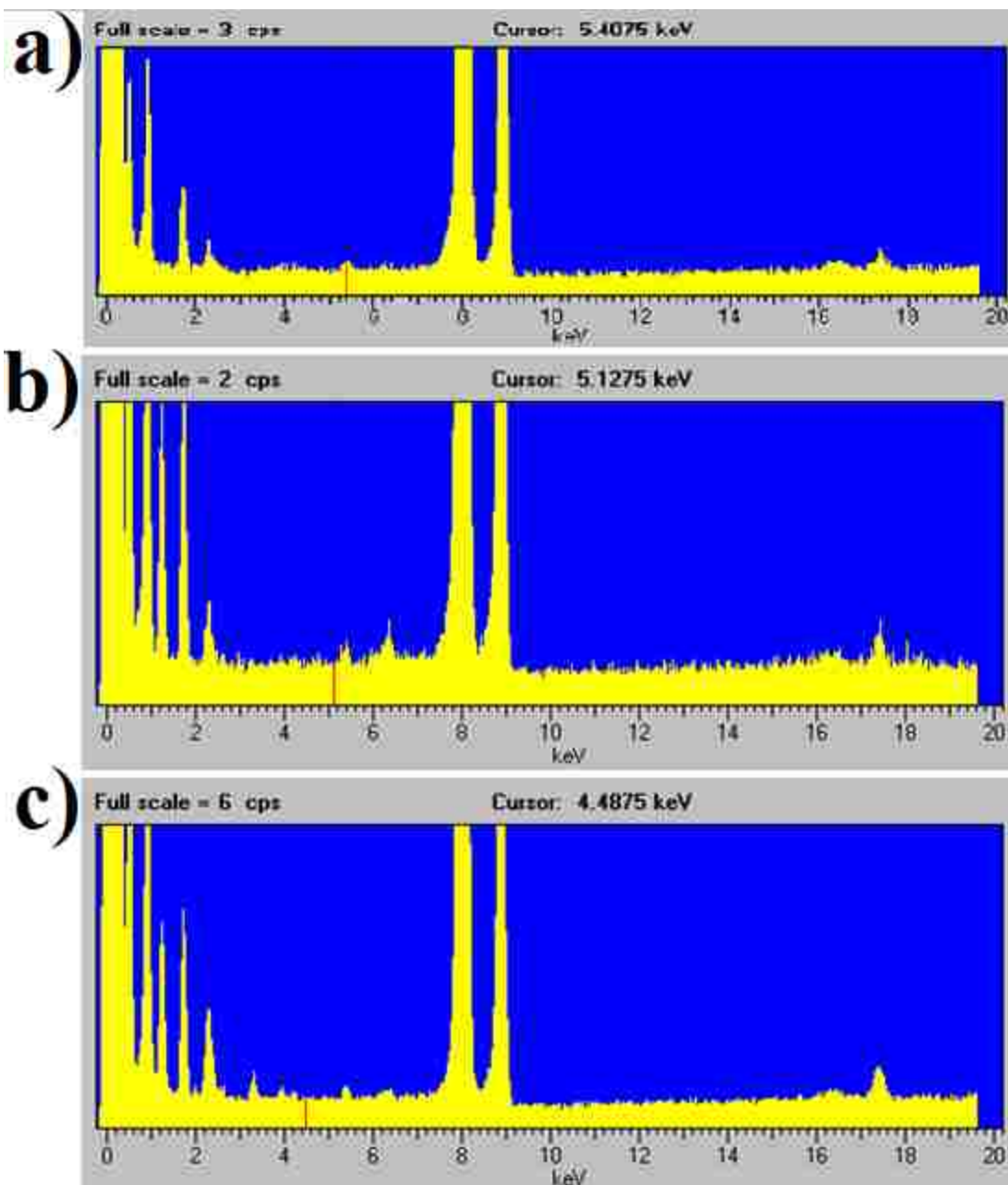


Figure 9.11 EDS taken under TEM for a) aggregates in toluene; b) aggregates in acetone; c) aggregates in DMSO. The peak at 17.4 KeV indicates the existence of Mo.

The tubular assemblies are found to be counterion dependent. Light scattering and TEM results indicate that the diameter of the tubes increases in the presence of ZnCl_2 ($D = 58 \text{ nm}$) or tetramethyl ammonium bromide ($D = 55 \text{ nm}$) (Figure 9.12 and Figure 9.13). However, the wall thickness does not change, suggesting the obvious role of counterions and the charge-regulated

mechanism for the self-assembly behavior. The additions of tetrapropyl ammonium bromide and tetrabutyl ammonium bromide have no effect on the sizes of the supramolecular structure.

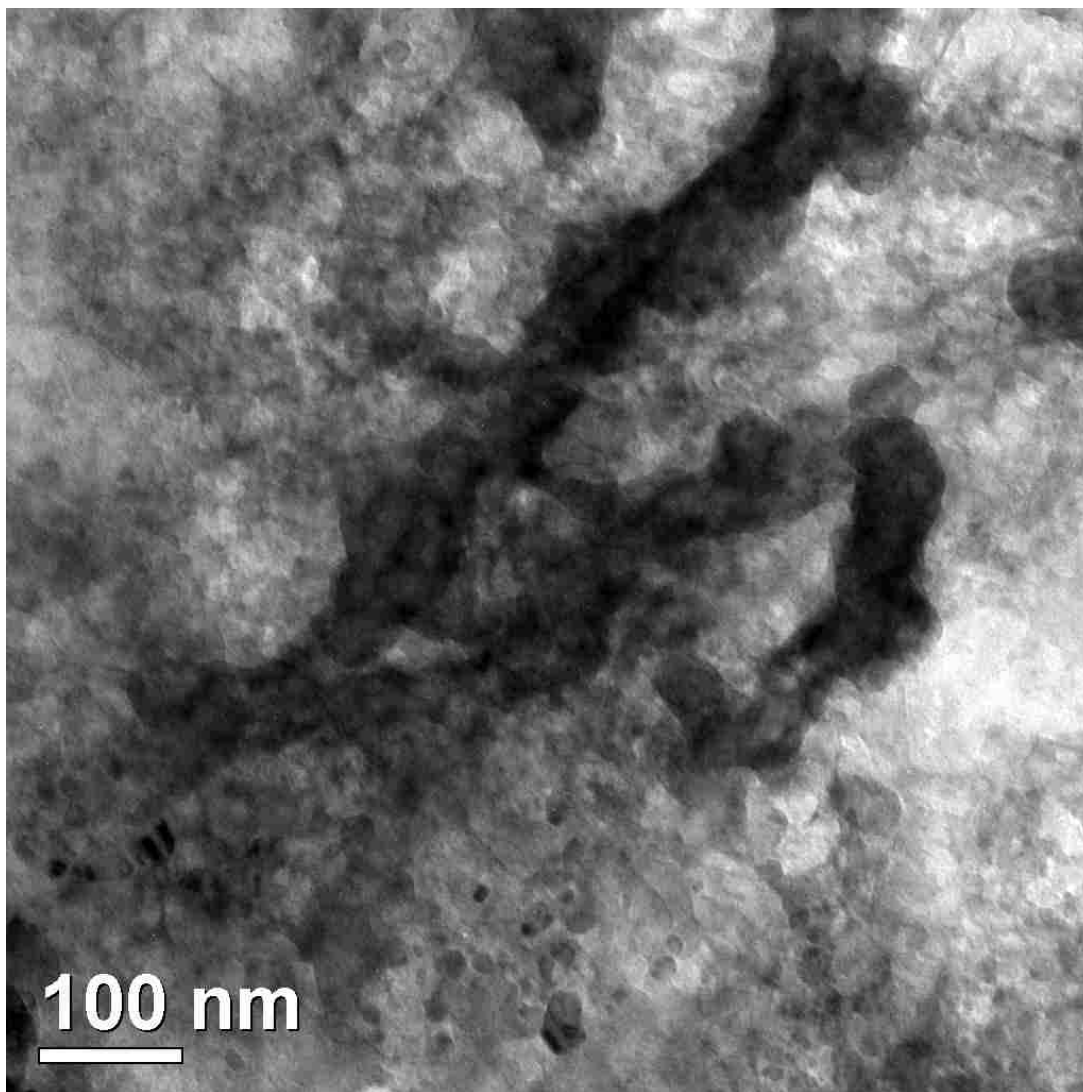


Figure 9.12 TEM images for the tube-like structures in 1's 10 mL 0.5 mg/mL DMSO solution with 0.5 mg ZnCl_2 . Diameter = 58 nm. Light Scattering results indicate the R_h and R_g values for the aggregates being 69 nm and 80 nm, respectively.

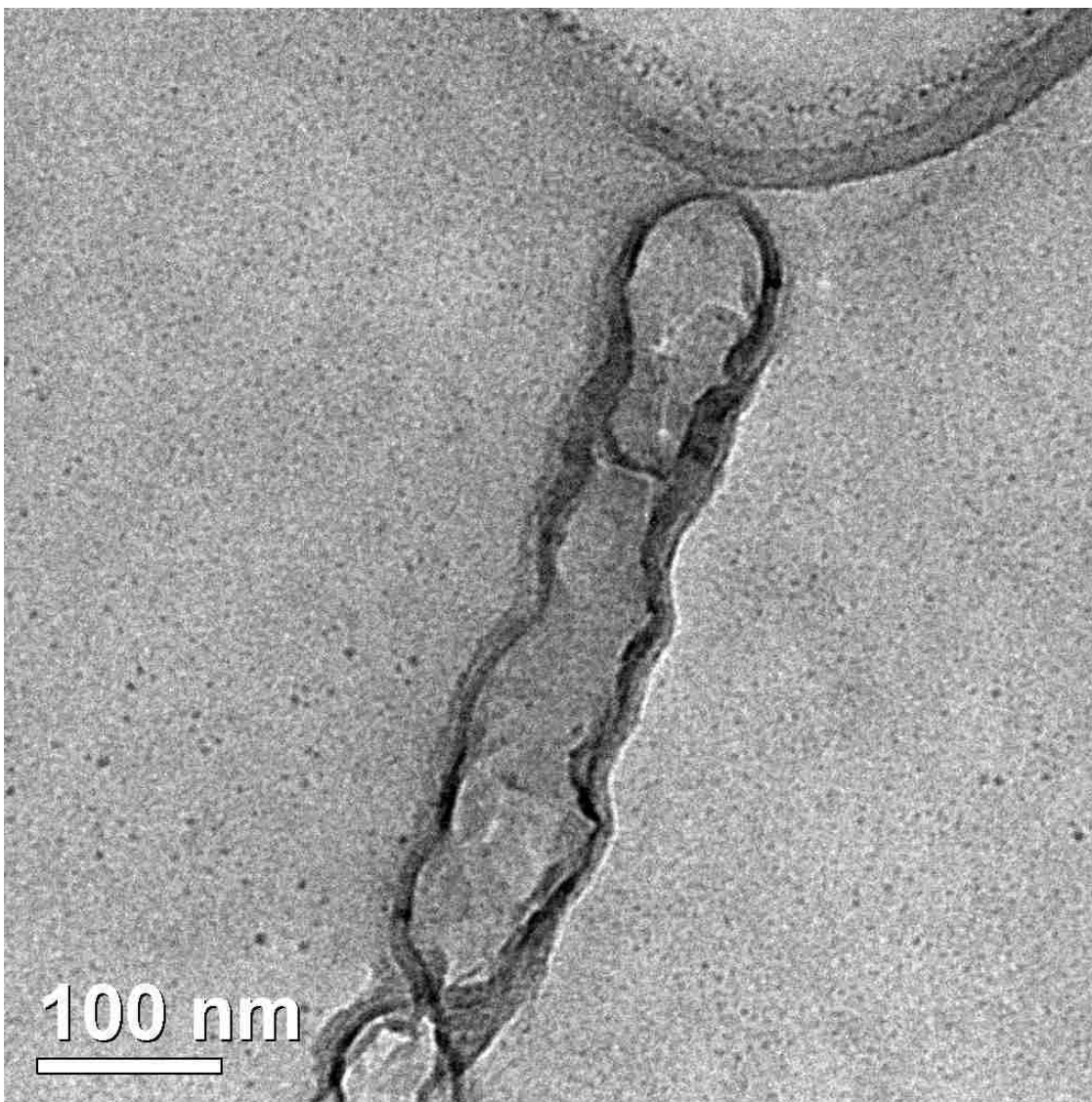


Figure 9.13 TEM images for the tube-like structures in 1's 10 mL 0.5 mg/mL DMSO solution with 2 mg tetramethyl ammonium bromide. Diameter = 55 nm. Light Scattering results indicate R_h and R_g values for the aggregates are 60 nm and 73 nm, respectively.

Polymers **2** and **3** show similar behavior in DMSO by also forming anisotropic structures. The R_h values are almost identical for the three polymers, while the R_g value for the assemblies formed by polymer **2** (67 nm) is higher than polymer **1** (60 nm) and polymer **3** (52 nm). In other words, the assemblies of polymer **2** seem to adopt a more rigid-rod like morphology, presumably due to its lower POM content in the polymer. On the other hand, the tubular structures formed by polymers **1** and **3** can be more easily bent due to the presence of more POM clusters. Polymer **4** is

not soluble in DMSO, but slightly soluble in acetone. The acetone solution of Polymer **4** shows no supramolecular structure formation, confirming again the important role that POMs play on the solution behavior of such copolymers.

A model is presented here to explain the assembly formation in polar solvents. The electrostatic interaction between the polymer chains, mediated by counter-ions, leads to the formation of tube-like structures. Due to the solvophobic and rigid rod nature of the polymer backbone, the polymer chains may aggregate through π - π stacking to grow the tube along length direction (Figure 9.10e). The π - π stacking of the poly(phenylene ethynylene) (PPE) backbones is supported by the observation that both the excitation and the emission spectra bathochromically shift when the polymer concentration increases (e.g., from 0.005 to 0.1 mg/mL in any of three solvents, Figure 9.14, Figure 9.15, Figure 9.16, and Figure 9.17).²⁷ This is similar to the case reported by Wegner et al. in the formation of micelle structure of another type of rigid-rod polyelectrolyte and the bundle structures due to the metal ions induced aggregation of the micelle structures.^{28,29}

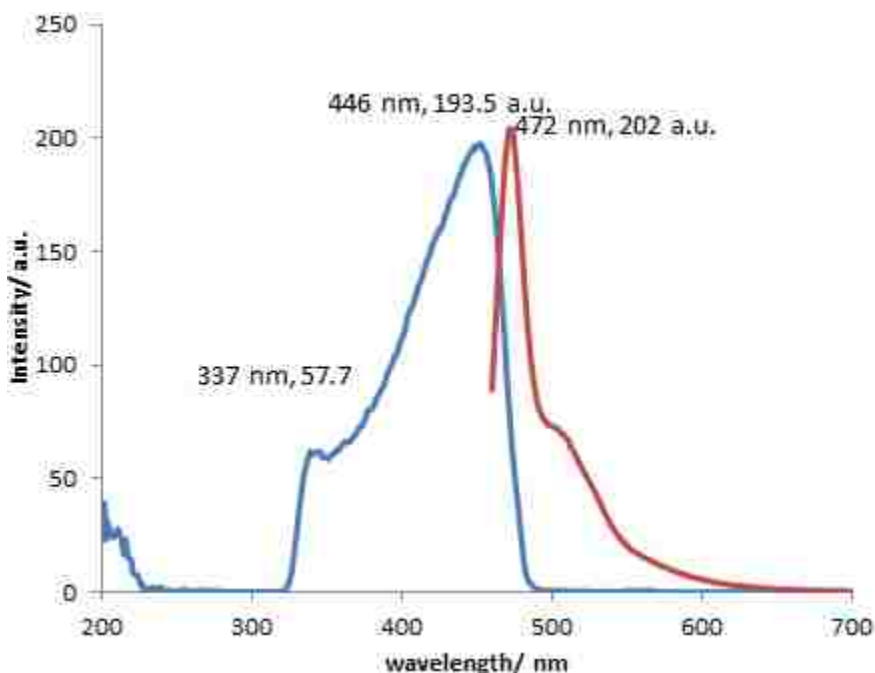


Figure 9.14 Excitation (blue) and emission (red) spectra of 0.005 mg/mL solution of **1** in acetone.

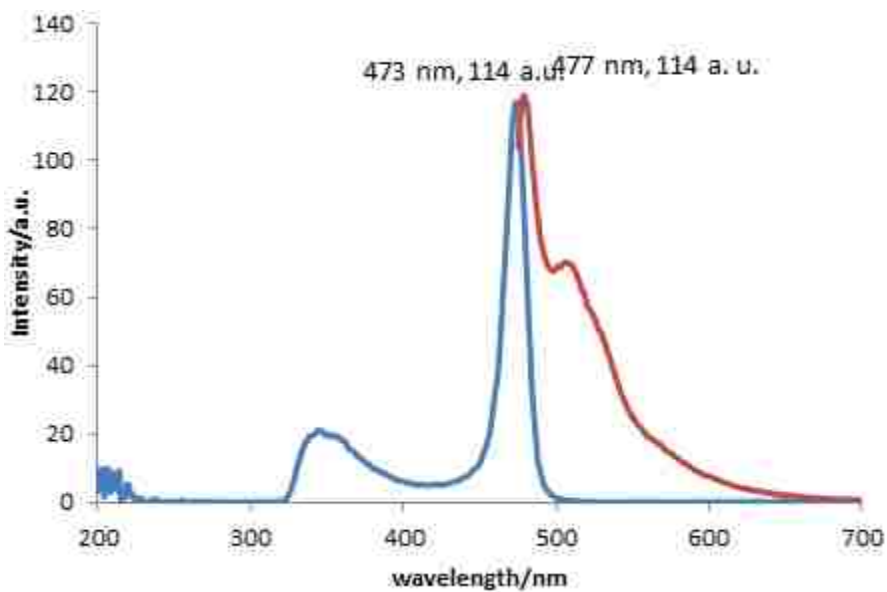


Figure 9.15 Excitation (blue) and emission (red) spectra of 0.1 mg/mL solution of 1 in acetone.

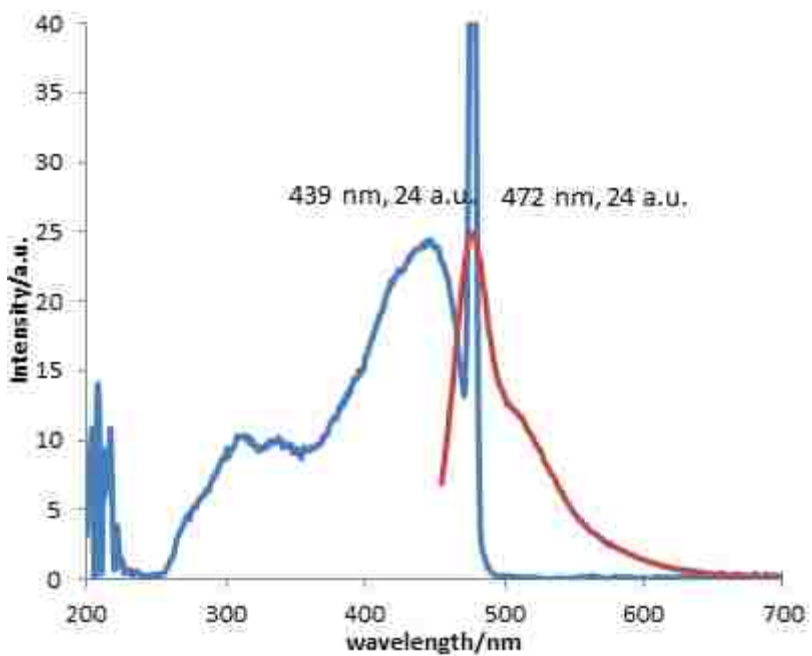


Figure 9.16 Excitation (blue) and emission (red) spectra of 0.005 mg/mL of 1 in DMSO solution.

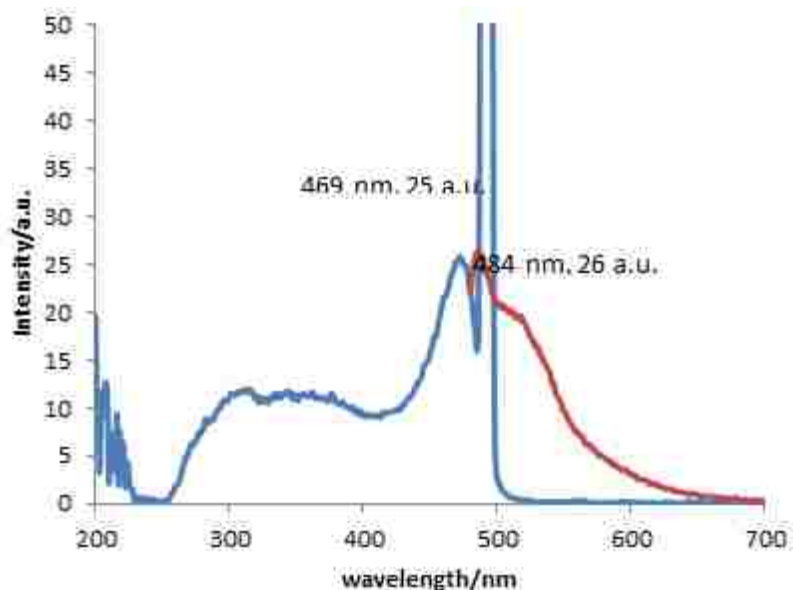


Figure 9.17 Excitation (blue) and emission (red) spectra of 0.1 mg/mL of 1 in DMSO solution.

The assembly of the three hybrid polymers appears to mimic the solution behavior of inorganic macroions. We have previously demonstrated that macroions, including POM anions, with large sizes (2-6 nm) and moderate charge density, tend to self-assemble into large vesicle-like single-layered blackberry-type structures, with counterion-mediated attraction and hydrogen bonding as the major driving forces.³⁰⁻³² As we mentioned before, the macroions, in fact, are simple models of 0-D polyelectrolytes with well-defined shape, size and adjustable charge.³⁰ The rod-shaped polymers can be treated as 1-D linear polyelectrolytes, and consequently form 1-D hollow tubular structures, as shown schematically in Figure 9.10e.

9.4 Conclusion

In summary, the assembly behavior of three conjugated polymers containing POM-terminal side chains in both nonpolar and polar solvents has been studied. In nonpolar solvents such as toluene, the polymers show amphiphilic characteristics and self-assemble into reverse vesicles. In polar solvents, the POM side chains are charged and consequently the polymers show polyelectrolyte properties by forming tubular structure which might mimic the behavior of inorganic macroions.

Their different aggregation performance will be helpful in developing POM-based functional devices.

Reference

- (1) *Handbook of Conducting Polymers*; 3rd ed.; CRC, Boca Raton: FL, 2007; Vol. 1.
- (2) *Handbook of Conducting Polymers*; 3rd ed.; CRC, Boca Raton: FL, 2007; Vol. 2.
- (3) Jiang, H.; Taranekar, P.; Reynolds, J. R.; Schanze, K. S. *Angew. Chem. Int. Ed.* **2009**, *48*, 4300.
- (4) Dolbecq, A.; Dumas, E.; Mayer, C. d. R.; Mialane, P. *Chem. Rev.* **2010**, *110*, 6009.
- (5) Hill, C. L. *Chem. Rev.* **1998**, *98*, 1.
- (6) Long, D.-L.; Burkholder, E.; Cronin, L. *Chem. Soc. Rev.* **2007**, *36*, 105.
- (7) Qi, W.; Wu, L. *polym. Int.* **2009**, *58*, 1217.
- (8) Dias, R. S.; Pais, A. A. C. C. *Adv. Colloid Interface Sci.* **2010**, *158*, 48.
- (9) Liu, T.; Rulkens, R.; Wegner, G.; Chu, B. *Macromolecules* **1998**, *31*, 6119.
- (10) Stevens, M. J. *Phys. Rev. Lett.* **1999**, *82*, 101.
- (11) Crozier, P. S.; Stevens, M. J. *J. Chem. Phys.* **2003**, *118*, 3855.
- (12) Stevens, M. J. *Biophys. J.* **2001**, *80*, 2075.
- (13) Schroeder, R.; Barta, A.; Semrad, K. *Nat. Rev. Mol. Cell Biol.* **2004**, *5*, 908.
- (14) Salgado, E. N.; Radford, R. J.; Tezcan, F. A. *Acc. Chem. Res.* **2010**, *43*, 661.
- (15) Henle, M. L.; Pincus, P. A. *Phys. Rev. E* **2005**, *71*, 060801.
- (16) Mukherjee, A. K.; Schmitz, K. S.; Bhuiyan, L. B. *Langmuir* **2003**, *19*, 9600.
- (17) Sedlak, M. *J. Chem. Phys.* **2002**, *116*, 5256.
- (18) Rulkens, R.; Wegner, G.; Thurn-Albrecht, T. *Langmuir* **1999**, *15*, 4022.

- (19) Xu, B. B.; Lu, M.; Kang, J. H.; Wang, D.; Brown, J.; Peng, Z. H. *Chem. Mater.* **2005**, *17*, 2841.
- (20) Hiemenz, P. C.; Rajagopalan, R. *Principles of Colloid and Surface Chemistry*; Marcel Dekker: New York, 1997.
- (21) Provencher, S. W. *Comput. Phys. Commun.* **1982**, *27*, 229.
- (22) Yin, P.; Jin, L.; Li, D.; Cheng, P.; Vezenov, D. V.; Bitterlich, E.; Wu, X.; Peng, Z.; Liu, T. *Chem. Eur. J.* **2012**, *18*, 6754.
- (23) Cooper, G. J. T.; Cronin, L. *J. Am. Chem. Soc.* **2009**, *131*, 8368.
- (24) Shen, Y.; Peng, J.; Pang, H.; Zhang, P.; Chen, D.; Chen, C.; Zhang, H.; Meng, C.; Su, Z. *Chem. Eur. J.* **2011**, *17*, 3657.
- (25) Kang, Z.; Wang, E.; Jiang, M.; Lian, S.; Li, Y.; Hu, C. *Eur. J. Inorg. Chem.* **2003**, *2003*, 370.
- (26) Wang, R. Y.; Jia, D. Z.; Zhang, L.; Liu, L.; Guo, Z. P.; Li, B. Q.; Wang, J. X. *Adv. Funct. Mater.* **2006**, *16*, 687.
- (27) Halkyard, C. E.; Rampey, M. E.; Kloppenburg, L.; Studer-Martinez, S. L.; Bunz, U. H. F. *Macromolecules* **1998**, *31*, 8655.
- (28) Kroeger, A.; Belack, J.; Larsen, A.; Fytas, G.; Wegner, G. *Macromolecules* **2006**, *39*, 7098.
- (29) Zaroslov, Y. D.; Gordeliy, V. I.; Kuklin, A. I.; Islamov, A. H.; Philippova, O. E.; Khokhlov, A. R.; Wegner, G. *Macromolecules* **2002**, *35*, 4466.
- (30) Liu, T. *Langmuir* **2009**, *26*, 9202.
- (31) Liu, T.; Diemann, E.; Li, H.; Dress, A. W. M.; Muller, A. *Nature* **2003**, *426*, 59.
- (32) Yin, P.; Li, D.; Liu, T. *Isr. J. Chem.* **2011**, *51*, 191.

Chapter 10 : Conclusion

Macroions, as the major research area in our lab, have been claimed to fill the gap between simple ion solutions and colloid suspensions in the research of electrolyte solutions.^{1,2} Polyoxometalates (POMs) were selected as simple models to study the solution behaviors of macroions, especially, inter-macroions forces. More importantly, the study of POMs' solution behaviors could be instructive in understanding the functionality of biopolymers, e.g. proteins, RNAs, and DNAs. Part of my PhD research is specifically focusing on the self-recognition and chiral recognition behavior of macroions during their self-assembly process in dilute solutions. Self/chiral-recognition behavior is universal phenomenon and considered to play dominant role in multiple biological processes.¹⁻³

On the other hand, POMs are photo-electronic, catalytic, biologic, and magnetic active metal oxide molecular clusters and the assemblies of POMs could be design into functional devices. Due to weak interaction (e.g. hydrophobic interaction, hydrogen bonding, π - π interaction, and static charge interaction), the designed POM-organic hybrid molecules can be deliberately assembled into aggregates with different morphologies with size scale ranging from nm to um, which were studied as their potential application in functional materials and devices.^{2,4,5}

The project of self-recognition between molecular rods in their self-assembly process contributes to not only the mechanism of weak interaction resulted self-assembly, but also the advanced ideas on how to characterize/judge the self-recognition behavior. The self-recognition between two molecular rods with different encapsulated central metal ions or different organic functional groups demonstrates that different charge distribution and hydrophobic interaction/ π - π interaction are strong enough to lead self-recognition behavior. Meanwhile, the combination of TEM and energy dispersive X-ray spectrum (EDS) is powerful tool to characterize the self-recognition behavior by analyzing individual assemblies with different sizes and compositions besides traditional SLS and DLS technologies. What is more, the disassociation of the assemblies by

removing/replacing the counter-ions could be used to confirm the self-assembly behavior as well as the importance of counter-ion in forming and stabilizing the assemblies by measuring the stability/toughness of the assemblies during the disassociation process.

The project of self-recognition between chiral POMs and chiral discrimination/selection of chiral POMs induced by small organic molecules in their self-assembly process in dilute solution pushes the limit of similarity between POMs in self-recognition study and provides possible mechanisms for chiral recognition and chiral selection in biological systems. Chiral macropolyoxoanions were observed to show chiral recognition behavior by forming homogeneous blackberry structure of the individual enantiomers in their racemic mixtures. Their self-assembly behavior can be tuned by adding of lactic acid with the ‘like’-pairs and ‘dislike’-pair rules. The study on chiral recognition and chiral discrimination provides us with insightful ideas on the nature of interaction between macroions, which not only sheds light on the basic research on homo-chirality and chiral selection, but also provides new way for chiral separation and sensing.

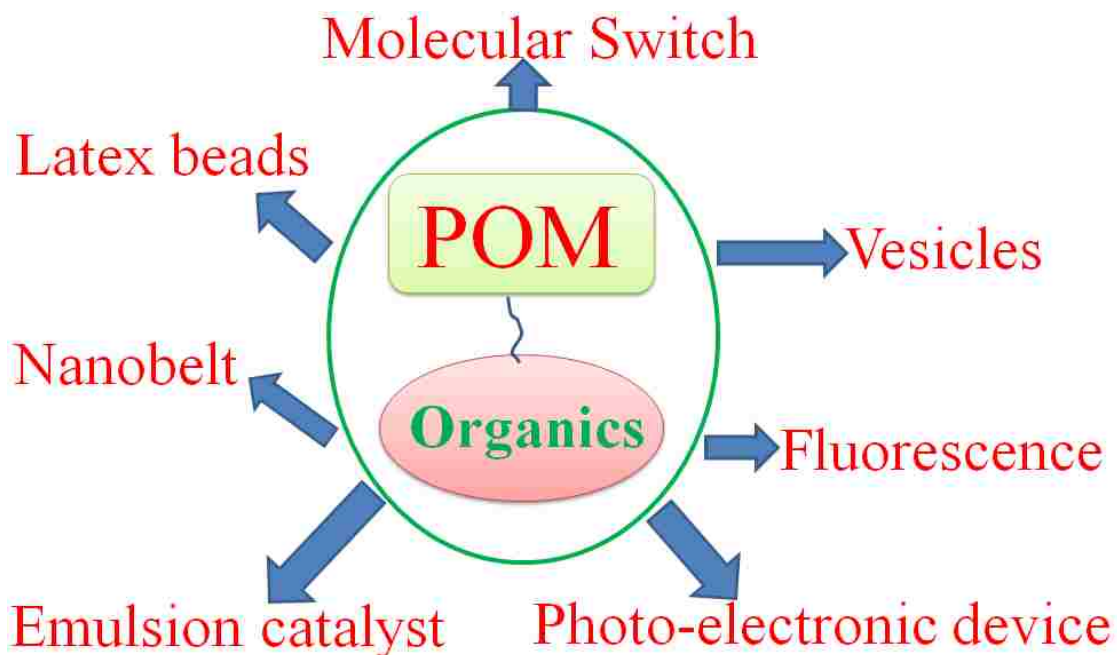


Figure 10.1 Different functional devices derived from the assemblies of POM-organic hybrids.

POM-organic hybrids with different functional groups could be designed to self-assemble into varied devices with wide applications (Figure 10.1). Surfactants with POMs as polar head groups are able to self-assemble into vesicles with tunable sizes and fluorescence due to hydrophobic interaction and the interaction between POMs.^{6,7} Conjugated polymers with POMs in their side chains can form reverse vesicle and 1D nanotube structures with potential application in photo-electronic devices.⁸ Two Dawson-type POMs linked by one 2, 2'-bipyridine unit works as metal-ion-responsive dumbbell-shape molecular switch, which shows multiple responses to the adding/removing of metal ions and the controlled self-assembly/disassembly behavior. POMs based surfactant with multiple amine groups was programmed to spontaneously assemble into 1D nano-belt structures, which show high efficient heterogeneous catalytic activity against the oxidation reaction of sulfide. Due to the amphiphilic properties of POM-organic hybrids and their catalytic active polar head groups, they can be used in emulsion catalysis and emulsion polymerization.⁹

Reference

- (1) Liu, T. B. *Langmuir* **2010**, *26*, 9202.
- (2) Yin, P.; Li, D.; Liu, T. *Chem. Soc. Rev.* **2012**, *41*, 7368.
- (3) Yin, P.; Li, D.; Liu, T. *Isr. J. Chem.* **2011**, *51*, 191.
- (4) Song, Y.-F.; Tsunashima, R. *Chem. Soc. Rev.* **2012**, *41*, 7384.
- (5) Li, D.; Yin, P.; Liu, T. *Dalton* **2012**, *41*, 2853.
- (6) Yin, P.; Cronin, L.; Liu, T. *Chem. Eur. J.* **2012**, DOI: 10.1002/chem.201200362.
- (7) Yin, P.; Wu, P.; Xiao, Z.; Li, D.; Bitterlich, E.; Zhang, J.; Cheng, P.; Vezenov, D. V.; Liu, T.; Wei, Y. *Angew. Chem. Int. Ed.* **2011**, *50*, 2521.
- (8) Yin, P.; Jin, L.; Li, D.; Cheng, P.; Vezenov, D. V.; Bitterlich, E.; Wu, X.; Peng, Z.; Liu, T. *Chem. Eur. J.* **2012**, DOI: 10.1002/chem.201103782.

(9) Yin, P.; Wang, J.; Xiao, Z.; Wu, P.; Wei, Y.; Liu, T. *Chem. Eur. J.* **2012**, *18*, 9174.

Author Vita

PANCHAO YIN

13 DUH Dr. APT 114, Bethlehem, PA 18015 | +610-597-6932 | pay209@lehigh.edu

EDUCATION

Lehigh University

Admitted as PhD student in Department of Chemistry in 2009, expected graduation in February, 2013

Advisor: Prof. Dr. Tianbo Liu

Tsinghua University in Beijing

Bachelor of Engineering, in polymer Science & Engineering in Department of Chemical Engineering, from Aug, 2005 to July, 2009

GRADUATE RESEARCH, LEHIGH UNIVERSITY (ADVISOR: PROF. DR. TIANBO LIU)

Major Research Project:

- 1, Self-recognition of chiral polyoxometalates and rod-like polyoxometalates in their self-assembly process**
- 2, Counterion distribution around capsid proteins**
- 3, Self-assembly and catalytic behavior of surfactant with POMs as polar head groups**
- 4, Synthesis and catalytic behavior of polyoxometalates-containing polymer beads**

TEACHING

1, Teaching assistant of physical chemistry lab (2009, 2012) in chemistry department of Lehigh University

2, As adult supervisor of high school student, Joy Wang in 2012 Intel International Science and Engineering Fair (fourth award in chemistry) and 2013 Intel Science Talent Search (currently, final)

SKILLS

1, Data collection and analysis of Laser light scattering, Small-Angle X-ray Scattering, TEM, and SEM.

2, Data collection and crystal structure refinement for single-crystal X-ray diffraction.

3, Performing experiments and analysis of the data of UV-Vis, NMR, FT-IR, CD, GC, TGA, DSC and GC-MS.

AWARDS

Department Fellowship from Department of chemistry, Lehigh University, 2012
Kenneth A. Earhart Award from Emulsion polymer institute, Lehigh University, 2012
Outstanding undergraduate student from Tsinghua University, July, 2009

PUBLICATIONS

Corresponding author

1, Wu, P.; Chen, J.; **Yin, P.***; Xiao, Z.; Zhang, J.; Bayaguud, A.; Wei, Y.*; Solvent-induced supramolecular chirality switching of bis-(trisalkoxy)-hexavanadates. *Polyhedron* <http://dx.doi.org/10.1016/j.poly.2012.06.007>.

2, Wu, P.; **Yin, P.***; Zhang, J.; Hao, J.; Xiao, Z.; Wei, Y.*; Single-Side Organically Functionalized Anderson-Type Polyoxometalates. *Chem. Eur. J.* **2011**, *17* (43), 12002-12005.

3, Wei, W.; **Yin, P.***; Wei, Z.; Hao, J. Hydrogen Bonding Deduced α and β Polymorphs of Bis(tetrabutylammonium) Bis(cyclohexylammonium) β -Octamolybdate, $[\beta\text{-Mo}_8\text{O}_{26}]^{4-}$. *J. Chem. Crystallogr.* **2011**, *41*, 364-369.

First author & Co-first author

1, **Yin, P.**; Li, D.; Liu, T.* Solution behaviors and self-assembly of polyoxometalates as models of macroions and amphiphilic polyoxometalate-organic hybrids as novel surfactants. *Chem. Soc. Rev.* **2012**, *41*, 7368-7383.

2, **Yin, P.**; Wang, J.; Xiao, Z.; Wu, P.; Wei, Y.*; Liu, T.* Polyoxometalate–Organic Hybrid Molecules as Amphiphilic Emulsion Catalysts for Deep Desulfurization. *Chem. Eur. J.* **2012**, *18*, 9174-9178.

3, **Yin, P.**; Pradeep, C. P.; Zhang, B.; Li, F.-Y.; Lydon, C.; Rosnes, M. H.; Li, D.; Bitterlich, E.; Xu, L.; Cronin, L.*; Liu, T.* Controllable Self-Assembly of Organic–Inorganic Amphiphiles Containing Dawson Polyoxometalate Clusters. *Chem. Eur. J.* **2012**, *18*, 8157-8162.

4, **Yin, P.**; Jin, L.; Li, D.; Cheng, P.; Vezenov, D. V.; Bitterlich, E.; Wu, X.; Peng, Z.*; Liu, T.* Supramolecular Assembly of Conjugated Polymers Containing Polyoxometalate Terminal Side Chains in Polar and Nonpolar Solvents. *Chem. Eur. J.* **2012**, *18*, 6754-6758.

5, **Yin, P.**; Li, D.; Liu, T.* Counterion Interaction and Association in Metal-Oxide Cluster Macroanionic Solutions and the Consequent Self-Assembly. *Isr. J. Chem.* **2011**, *51*, 191-204.

6, **Yin, P.**; Wu, P.; Xiao, Z.; Li, D.; Bitterlich, E.; Zhang, J.; Cheng, P.; Vezenov, D. V.; Liu, T.*; Wei, Y.* A Double-Tailed Fluorescent Surfactant with a Hexavanadate Cluster as the Head Group. *Angew. Chem. Int. Ed.* **2011**, *50*, 2521-2525.

7, Wang, L.[†]; **Yin, P.**[†]; Zhang, J.; Hao, J.; Lv, C.; Xiao, F.; Wei, Y.* χ -Octamolybdate $[\text{Mo}^{\text{V}}_4\text{Mo}^{\text{VI}}_4\text{O}_{24}]^{4-}$: An Unusual Small Polyoxometalate in Partially Reduced Form from Nonaqueous Solvent Reduction. *Chem. Eur. J.* **2011**, *17*, 4796-4801. ([†] these two authors contribute equally to this paper)

Other Publications

1, Zhang, J.; **Yin, P.**; Hao, J.; Xiao, F.; Chen, L.; Wei, Y.* Synthesis and Assembly of a Difunctional Core POM Cluster with Two Appended POM Cluster Caps. *Chem. Eur. J.* **2012**, *18*, 13596-13599.

2, Li, D.; **Yin, P.**; Liu, T.* Supramolecular architectures assembled from amphiphilic hybrid polyoxometalates. *Dalton* **2012**, *41*, 2853-2861.

3, Li, Q.; **Yin, P.**; Shi, L.; Wei, Y.* Syntheses, Crystal Structures, and Spectroscopic Studies of Aromatic Ester Derivatives of Hexamolybdate. *Eur. J. Inorg. Chem.* **2009**, *2009*, 5227-5232.

4, Li, D.; Song, J.; **Yin, P.**; Simotwo, S.; Bassler, A. J.; Aung, Y.; Roberts, J. E.; Hardcastle, K. I.; Hill, C. L.*; Liu, T.* Inorganic–Organic Hybrid Vesicles with Counterion- and pH-Controlled Fluorescent Properties. *J. Am. Chem. Soc.* **2011**, *133* (35), 14010-14016.

5, Haso, F.; Fang, X.; **Yin, P.**; Li, D.; Ross, J. L.; Liu, T.* The self-assembly of a macroion with anisotropic surface charge density distribution. *Chem. Commun.* **2013**, *49*, 609-611.

6, Hao, J.; Zhang, J.; **Yin, P.**; Xiao, Z.; Xiao, F.; Wei, Y.* Unprecedented Organoimido-Derivatized Lacunary Polyoxometalates. *Chem. Eur. J.* **2012**, *18*, 2503-2506.

7, Biboum, R. N.; Doungmene, F.; Keita, B.; de Oliveira, P.; Nadjjo, L.*; Lepoittevin, B.; Roger, P.; Brisset, F.; Mialane, P.; Dolbecq, A.; Mbomekalle, I. M.; Pichon, C.; **Yin, P.**; Liu, T.;

Contant, R., Poly(ionic liquid) and macrocyclic polyoxometalate ionic self-assemblies: new water-insoluble and visible light photosensitive catalysts. *J. Mater. Chem.* **2012**, *22* (2), 319-323.

8, Xiao, F.; Misdrahi, M. F.; Zhang, J.; **Yin, P.**; Hao, J.; Lv, C.; Xiao, Z.; Liu, T.; Wei, Y.*; Buildup of Amphiphilic Molecular Bola from Organic–Inorganic Hybrid Polyoxometalates and Their Vesicle-Like Supramolecular Assembly. *Chem. Eur. J.* **2011**, *17* (43), 12006-12009.

9, Wu, P.; Xiao, Z.; Zhang, J.; Hao, J.; Chen, J.; **Yin, P.**; Wei, Y.* DMAP-catalyzed esterification of pentaerythritol-derivatized POMs: a new route for the functionalization of polyoxometalates. *Chem. Commun.* **2011**, *47*, 5557-5559.

10, Zhu, Y.; Xiao, Z.; Wang, L.; **Yin, P.**; Hao, J.; Wei, Y.*; Wang, Y. Monosubstituted arylimido hexamolybdates containing pendant amino groups: synthesis and structural characterization. *Dalton* **2011**, *40*, 7304-7309.

11, Li, Q.; Wu, P.; **Yin, P.**; Zhang, J.; Shi, L.; Wei, Y.* Synthesis, Characterization and Structure of An α -Octamolybdate-Supported Compound Formed During the Diffuse Process. *J. Cluster Sci.* **2010**, *21*, 181-186.

12, Xiao, F.; Hao, J.; Zhang, J.; Lv, C.; **Yin, P.**; Wang, L.; Wei, Y.* Polyoxometalato-cyclophanes: Controlled Assembly of Polyoxometalate-Based Chiral Metallamacrocycles from Achiral Building Blocks. *J. Am. Chem. Soc.* **2010**, *132*, 5956-5957.

13, Zhang, J.; Hao, J.; Wei, Y.*; Xiao, F.; **Yin, P.**; Wang, L. Nanoscale Chiral Rod-like Molecular Triads Assembled from Achiral Polyoxometalates. *J. Am. Chem. Soc.* **2009**, *132*, 14-15.

14, Wang, L.; Zhu, L.; **Yin, P.**; Fu, W.; Chen, J.; Hao, J.; Xiao, F.; Lv, C.; Zhang, J.; Shi, L.; Li, Q.; Wei, Y.* From 0D dimer to 2D Network—Supramolecular Assembly of Organic Derivatized Polyoxometalates with Remote Hydroxyl via Hydrogen Bonding. *Inorg. Chem.* **2009**, *48*, 9222-9235.

15, Zhu, Y.; Wang, L.; Hao, J.; **Yin, P.**; Zhang, J.; Li, Q.; Zhu, L.; Wei, Y.* Palladium-Catalyzed Heck Reaction of Polyoxometalate-Functionalised Aryl Iodides and Bromides with Olefins. *Chem. Eur. J.* **2009**, *15*, 3076-3080.

16, Li, Q.; Wang, L.; **Yin, P.**; Wei, Y.*; Hao, J.; Zhu, Y.; Zhu, L.; Yuan, G. Convenient syntheses and structural characterizations of mono-substituted alkylimido hexamolybdates: $[\text{Mo}_6\text{O}_{18}(\text{NR})]^{2-}$ (R = Me, Et, n-Pr, i-Pr, n-Bu, t-Bu, Cy, Hex, Ode). *Dalton* **2009**, 1172-1179.

17, Hao, J.; Xia, Y.; Wang, L.; Ruhlmann, L.; Zhu, Y.; Li, Q.; **Yin, P.**; Wei, Y.*; Guo, H. Unprecedented Replacement of Bridging Oxygen Atoms in Polyoxometalates with Organic Imido Ligands. *Angew. Chem. Int. Ed.* **2008**, *120*, 2666-2670.

CONFERENCE

1, **Yin, P.**; Liu, T.; Wang, J. In Amphiphilic polyoxometalate-organic hybrid molecules as pH-sensitive emulsion catalysts for ultra-deep desulfurization, Abstracts of Papers, 244th ACS National Meeting & Exposition, Philadelphia, PA, United States, August 19-23, 2012.

2, **Yin, P.**; Li, D.; Bitterlich, E.; Liu, T.; Cronin, L., Surfactant with Dawson type polyoxometalates as polar head: a concentration and water dependent single-layer vesicle to multilayer vesicle transition. Dec, 18th, 2010 in International Chemical Congress of Pacific Basin Societies, Hawaii.